Ball, Thomas James (2008) *Development of new methods in solid-state NMR.*
PhD thesis.

http://theses.gla.ac.uk/385/

Development of New Methods

In Solid-State NMR

Submitted in partial fulfilment of the requirements

for the degree of Doctor of Philosophy

Thomas James Ball

University of Glasgow

Department of Chemistry

June 2008

Abstract

Many chemically important nuclei are quadrupolar with half-integer spin (i.e., spin I = 3/2, 5/2, etc.) The presence of quadrupolar broadening for such nuclei can limit the information that may be extracted using NMR. MAS is able to remove first-order quadrupolar broadening but can only reduce the second-order contribution to the linewidth. The MQMAS and STMAS techniques have enabled high-resolution NMR spectra of half-integer quadrupolar nuclei in the solid state to be obtained by two-dimensional correlation under MAS conditions. Both of these experiments have several well-known limitations. One is that the conversion pulses in particular are very inefficient and the other is that the longer acquisition times required for two-dimensional experiments can be a limiting factor. Both of these disadvantages are addressed in this thesis.

For the former case, existing composite pulse schemes designed to improve the efficiency of the conversion of multiple-quantum coherences are compared using ^{27}Al and ^{87}Rb MQMAS NMR of a series of crystalline and amorphous materials. In the latter case, a new experiment, named STARTMAS, is introduced that enables isotropic spectra of spin I = 3/2 nuclei to be obtained in real time. The theoretical basis of the technique is explained and its applicability demonstrated using ^{23}Na and ^{87}Rb NMR of a wide range of solids.

The nuclear Overhauser effect (NOE) is one of the most widely exploited phenomena in NMR and is now widely used for molecular structure determination in solution. NOEs in the solid state are rare and those to quadrupolar nuclei rarer still, this being due to the general absence of motion on the correct timescale and the usual efficiency of quadrupolar T_1 relaxation, respectively. In this thesis, ^{11}B{^{1}H} transient NOE results are presented for a range of solid borane adducts. A comparison is made of the ^{11}B NMR enhancements observed under MAS and static conditions and a rationale is proposed for the behaviour in the latter case.

Declaration

This thesis is available for library use on the understanding that it is copyright material and that no quotation from the thesis may be published without proper acknowledgement.

I certify that all material in this thesis that is not my own work has been identified and that no material has previously been submitted and approved for the award of a degree by this or any other university.

....

Thomas James Ball

June 2008

Acknowledgements

First, I would like to thank my supervisor, Prof Steve Wimperis, for the guidance and tuition he has given me, and the patience he has shown, during the course of my PhD studies. I am also grateful to Dr Sharon Ashbrook and Dr Nick Dowell for teaching me how to use the spectrometers and assisting me with my first projects during the early period of my PhD. I am also thankful to the EPSRC for funding a studentship and to Dr Stefan Steuernagel for assistance in the acquisition of the first STARTMAS NMR spectra.

My doctoral studies have been made all the more enjoyable with the presence of my dearest Marica, who has brought considerable Mediterranean fervour to my life and has been a great friend to me both in and out of the lab. I hope that I have taught her how to be a proper English lady! I am grateful also to Teresa Kurkiewicz; her joyful demeanour and seemingly endless energy never failed to make me smile and helped to make my time in Glasgow all the more memorable. I must also thank Dr Michael Thrippleton for sparing the time to read some of the early drafts of this thesis and for always being willing to answer my questions. I am also indebted for his assistance in teaching other group members our finest English! I made numerous friends during my time in Exeter and am eternally grateful to all of them for the fun we had. One especially strong friendship has emerged from my time in Devon; this person knows who they are — they have been incredible over the past three and a half years in providing relentless support and advice, and for just being there. My gratitude can never be enough.

Finally, I would be nowhere without the support, both financial and emotional, of my family. Thanks to my sister, Sarah, for welcoming me to Leeds on several occasions during the past few years and to my parents for helping me to maintain strong inner belief and resolve. The successful accomplishment of a PhD is testament to your immense contribution. This thesis is for you.

Contents

Appendices   **204**

Simulation Program Source Code

Accompanying folder containing source code of programs used in this thesis.

Chapter 1

Introduction

1.1   Thesis Overview

Since the first measurement of nuclear magnetic moments in 1938 [1, 2] and the subsequent first demonstration in the bulk phase [3–6], where the ^{1}H spectra of solid paraffin [3] and water [6] were acquired, nuclear magnetic resonance (NMR) has become one of the most widely used techniques for determining structure and observing dynamics. Virtually all elements in the Periodic Table possess nuclides that are accessible to NMR and, in addition, it can be used for solving a wide range of chemical problems prevalent in the three principal phases of matter. In the liquid state, the presence of rapid molecular motion typically leads to spectra featuring narrow, well-resolved lineshapes. The narrowness of these lineshapes is the result of the motional averaging of mechanisms that may be a source of line broadening, such as dipolar coupling and chemical shift anisotropy (CSA) [7]. The general absence of such motion in the solid state typically leads to anisotropically broadened lineshapes that are several orders of magnitude broader than their solution-state counterparts. The existence of broadenings resulting from several mechanisms thus leads to broad, poorly-resolved lineshapes in solid-state NMR spectra. Such lineshapes are, however, a consequence of an abundance of

information rather than a lack of it. Consequently, the development of methods in solid-state NMR has focussed on ways of obtaining high-resolution isotropic spectra in which all anisotropic line broadening has been removed.

The first technique devised to remove anisotropic line broadenings was magic angle spinning (MAS) in 1958 [8–10], in the first example of which line narrowing was observed in the ^{23}Na NMR spectrum of a single crystal of sodium chloride [8]. In MAS, the sample is spun in a rotor inclined at an angle of $54.74°$ with respect to the applied magnetic field, B_0. This introduces a time dependence to the anisotropic interactions that mimics the effects of the motion observed in liquids. MAS is able to removing broadenings resulting from heteronuclear dipolar couplings and CSA. Similar success is not seen for the case of homonuclear dipolar couplings, however. This has posed particular problems for the case of homonuclear dipolar couplings involving ^{1}H and ^{19}F nuclei, which commonly have a magnitude in excess of 30 kHz. The different capabilities of MAS when removing line broadenings arise because interactions such as CSA and heteronuclear dipolar coupling are "inhomogeneous" interactions [11], whilst homonuclear dipolar coupling is a "homogeneous" interaction [11]. This distinction may be explained as follows: for inhomogeneous interactions such as heteronuclear dipolar coupling, the Hamiltonian describing the coupling between a particular pair of spins commutes with that describing the coupling between a different pair. In the case of homogeneous interactions, this commutation relation does not hold.

The inability of MAS to remove large homonuclear dipolar couplings led

to the development of the Lee-Goldburg experiment [12] in which the spins are irradiated by a radiofrequency field inclined at the magic angle in the rotating frame. This has the effect of averaging the homonuclear dipolar interaction, to a first-order approximation, to zero. The heteronuclear dipolar coupling and CSA are scaled by this experiment. In 1968, Waugh and co-workers devised a multiple-pulse method that averages the homonuclear dipolar coupling, to a second-order approximation, to zero [13, 14]. This experiment, referred to as WAHUHA, consists of repeated cycles of four on-resonance 90° pulses, with relative phases of +x, +y, −x and −y in the rotating frame. A vast array of multiple-pulse methods have since been developed and a combination of these with MAS, in a technique known as combined rotation and multiple-pulse sequence (CRAMPS) [15], has enabled high-resolution [1]H [16] and [19]F [15] spectra to be obtained.

In 1972 it was shown that the signal from a dilute spin such as ^{13}C may be enhanced by cross polarisation (CP) from an abundant spin such as [1]H [17, 18]. CP NMR has since been widely used under both static [17, 19] and MAS conditions [20–23]. The combination of MAS and proton decoupling [24, 25] to remove broadening due to [1]H-^{13}C heteronuclear dipolar couplings, with cross polarisation, has greatly facilitated the acquisition of high-resolution ^{13}C spectra at natural abundance. Whilst cross-polarisation was developed initially to enhance the signal of dilute spin I = 1/2 nuclei, the technique has now been applied to a variety of quadrupolar nuclei [26, 27], such as [11]B [28], [17]O [29, 30], [23]Na [31, 32], [27]Al [33], [43]Ca [34] and [95]Mo [35], although the variation in

nutation frequency observed for the range of crystallite orientations present in a powder means that the resultant lineshapes are often very distorted [33, 36].

The methods described above have all been devised to narrow spectral lines of spin $I = 1/2$ nuclei. For many elements, the only NMR-accessible nuclei are quadrupolar, i.e., they have a spin quantum number $I > 1/2$. Common examples are oxygen (^{17}O is spin $I = 5/2$), sodium (^{23}Na is spin $I = 3/2$) and aluminium (^{27}Al is spin $I = 5/2$), with all of these elements being prevalent amongst a wide range of inorganic materials and oxygen being present amongst an even greater range of compounds. The success of MAS as a line-narrowing method for spin $I = 1/2$ nuclei [37] led to its application to half-integer quadrupolar nuclei (those with $I = n/2$, where n can take odd-integer values greater than 1). The inability of MAS to remove, to a second-order approximation, line broadening due to the quadrupolar interaction [38, 39] means that the resultant spectra still possess significant residual second-order quadrupolar broadening of the central transition. In the cases where there are several crystallographically inequivalent sites present and/or where the quadrupolar interaction is large, the resolution and signal intensity observed under MAS can be very poor.

In 1988, a study by Llor and Virlet of the effect of sample spinning with a time-dependent spinning angle led to the development of two methods that achieve complete removal of second-order quadrupolar broadening [40]. These techniques, known as double rotation (DOR) [41, 42] and dynamic angle spinning (DAS) [43–45], involve spinning the sample about two angles either

simultaneously (DOR) or sequentially (DAS). DOR is a one-dimensional experiment and so has the advantage over DAS (a two-dimensional experiment) that isotropic spectra may be obtained in a much shorter acquisition time, although the resultant spectra possess an abundance of spinning sidebands as a consequence of the slow spinning speed of the outer rotor. Both experiments have significant limitations. The requirement for specialist hardware and the technical demands of both techniques has meant that they have found limited use as methods for obtaining high-resolution NMR spectra of half-integer quadrupolar nuclei. A more general technique, known as variable angle spinning (VAS) was also devised [46, 47]. In this experiment, in which the sample may be spun at any angle with respect to B_0, a substantial reduction in the quadrupolar broadening observed under MAS may be obtained. This is only observed, however, if CSA and dipolar coupling effects are negligible, and given the fact that this is typically not the case, VAS has not been widely used.

In 1995, a method was introduced that enables high-resolution NMR spectra of half-integer quadrupolar nuclei to be obtained using conventional MAS hardware [48, 49]. This experiment, known as multiple-quantum magic angle spinning (MQMAS), is a two-dimensional method in which multiple-quantum coherences are correlated with single-quantum coherences under MAS conditions. The resultant increase in resolution enables the facile differentiation of crystallographically inequivalent sites in a solid. The ease with which this experiment may be performed has led to it being used to study a

wide range of crystalline and amorphous materials.

In 2000, Gan introduced a two-dimensional technique which, like MQMAS, enables the acquisition of high-resolution spectra of half-integer quadrupolar nuclei under MAS conditions [50–53]. In this method, known as satellite-transition magic angle spinning (STMAS), single-quantum (satellite-transition) coherences are correlated with single-quantum (central-transition) coherences. This experiment has not been used to the same extent as MQMAS, although it has been shown to possess great potential for the study of low-γ nuclei [54] and to be a very sensitive probe of dynamics [55].

One of the major limitations of the MQMAS and STMAS methods is that the mixing or conversion step in each case, namely the conversion of multiple-quantum coherences to central-transition coherences in MQMAS [56], and of satellite- to central-transition coherences in STMAS [53, 54], is a very inefficient process. Consequently, the sensitivity of these experiments can be poor. Several methods have been developed to address this weakness, focussing mainly on MQMAS. Amongst these methods are fast amplitude-modulated (FAM) [57] and soft-pulse added mixing (SPAM) [58] pulses, which have been successfully used to increase the efficiency of the conversion step in MQMAS. FAM pulses have been applied to a range of half-integer quadrupolar nuclei, although the enhancements reported for nuclei with higher spin-quantum numbers have been much less than those observed for spin I = 3/2 nuclei. FAM pulses have been used more widely than other techniques devised to enhance multiple-quantum to single-quantum coherence transfer, primarily as a consequence of

the ease with which they may be implemented.

The observation by Overhauser in 1953 of the polarisation of nuclear spins in a metal by the saturation of the electron resonances [59] led to the discovery of the nuclear Overhauser effect (NOE) [60–62]. The NOE occurs as a result of spin-lattice relaxation that is driven by random modulation of the dipole-dipole interaction between two nuclear spins. The increase or attenuation in signal intensity observed for one spin upon inversion or saturation of the populations of the nuclear spin energy levels of a spin with close spatial proximity has led to this effect becoming a very useful probe of internuclear distances. The NOE is now a widely used method for structure determination for molecules in solution [63]. In the solid state, however, NOEs are rarely observed [64–66], primarily as a consequence of a lack of motion on the required timescale. NOEs to quadrupolar nuclei are not usually observed either, as quadrupolar spin-lattice relaxation is typically much more efficient than dipole-dipole cross-relaxation [67].

This thesis is concerned with (i) methods for obtaining high-resolution NMR spectra of half-integer quadrupolar nuclei and (ii) the use of NMR as a probe of molecular motion in solids, via the nuclear Overhauser effect. Chapter 2 describes the NMR phenomenon and the Fourier transform method used in all modern-day NMR experiments. The density operator and tensor operator formalisms are introduced and the major mechanisms that lead to line broadening in NMR spectra are described. Finally, a description of two-dimensional NMR is given and the types of experiment commonly used are

explained.

In Chapter 3, the theoretical basis of the quadrupolar interaction is given and its effect on NMR spectra of quadrupolar nuclei is shown. Techniques are described that may be used to obtain high-resolution spectra of half-integer quadrupolar nuclei. Particular attention is given to the MQMAS and STMAS methods and to the information contained within the two-dimensional spectra that they produce.

The efficiency of coherence transfer processes is considered in Chapter 4. Selective and non-selective pulses are introduced and their behaviour in the presence of a quadrupolar interaction is shown. The efficiency of multiple-quantum excitation and conversion is then demonstrated and coherence transfer enhancement schemes designed to improve the efficiency of the latter process are introduced. A comparison is then made of the utility of FAM and SPAM pulses for enhancing the conversion step in MQMAS experiments of spin $I = 3/2$ and spin $I = 5/2$ nuclei, using ^{87}Rb NMR of rubidium nitrate, ^{27}Al NMR of aluminium acetylacetonate and ^{27}Al NMR of bayerite as examples. In addition, the performance of FAM and SPAM pulses in enhancing the $+2 \rightarrow +1$ coherence transfer step in DQF-STMAS is considered.

Chapter 5 introduces a new technique, known as STARTMAS, as a method for acquiring isotropic spin $I = 3/2$ NMR spectra in the solid state. The experiment is described and computer-simulated spectra that illustrate the data sampling schemes that may be used are presented. Experimental spectra are

presented using examples from four powdered solids, namely the ^{87}Rb STARTMAS NMR of rubidium nitrate, and the ^{23}Na STARTMAS NMR of dibasic sodium phosphate, sodium citrate dihydrate and sodium oxalate. The ability of STARTMAS to produce "ultrafast" NMR spectra is illustrated using rubidium nitrate as an example and the potential of the technique to produce isotropic-isotropic correlation spectra is also shown.

In Chapter 6, a ^{11}B (spin I = 3/2) NMR study of NOEs of a series of borane adducts in the solid state is presented. The nuclear Overhauser effect is described in detail and ^{11}B{^{1}H} NOE enhancements are shown for a range of borane adducts. Enhancements to the central, satellite and triple-quantum transitions of ^{11}B are given and a comparison of the increase in signal intensity observed under static and MAS conditions is made. A rationale for the differences observed is then proposed with theoretical calculations being used to consider the effect of rapid rotation of the BH_3 group on the ^{11}B{^{1}H} dipolar coupling and the ^{11}B{^{1}H} NOE. Variable-temperature ^{11}B NMR studies of the ^{11}B{^{1}H} NOE in borane triphenylphosphine are also shown and the significance of this for the molecular motion present in these borane adducts is considered.

1.2 Experimental Details

The experimental results presented in this thesis were acquired using Bruker Avance 200 and Bruker Avance 400 spectrometers, equipped with 4.7 T and 9.4 T superconducting magnets, respectively. Some of the spectra in

Chapter 5 were acquired with the assistance of Dr S. Steuernagel (Bruker BioSpin GmbH, Rheinstetten, Germany), using a Bruker Avance II spectrometer equipped with a widebore 11.7 T magnet. All static and MAS NMR experiments were performed using conventional MAS probes, with the samples packed into 2.5- or 4.0-mm rotors. Rotation speeds of 10–33 kHz were typically used. Radiofrequency field strengths were calibrated independently on a range of samples and only approximate values are quoted. All samples were obtained from commercial suppliers and used without further purification.

In-house computer programs, some written and developed by myself, were used for generating simulated spectra, and for processing some of the spectra shown in this thesis. Many of the spectra shown in Chapter 5 were generated and/or processed using MATLAB software written by Dr M. J. Thrippleton. Source codes of the Fortran, Mathematica and MATLAB programs used for simulating and processing NMR data are included in a folder which accompanies this thesis. In two-dimensional contour plots, positive and negative contours are shown using bold and dashed lines, respectively, and the contour levels used are given in the figure captions.

Chapter 2

Fundamentals of NMR

2.1   The Zeeman Interaction

Atomic nuclei possess an intrinsic angular momentum, known as spin. This angular momentum has a magnitude, $|\mathbf{I}|$, given by

$$|\mathbf{I}| = \hbar\sqrt{I(I + 1)} \; ,$$ (2.1)

where I is the magnetic quantum number. I can be zero, or take positive integer or half-integer values. Nuclei with spin $I = 0$ are unobservable by NMR. The projection of this angular momentum onto an axis, typically the z axis, is quantized in units of $\hbar$:

$$\mathbf{I}_z = m_I \hbar \; .$$ (2.2)

The azimuthal quantum number, m_I, can take $2I + 1$ values, varying from $-I$ to $+I$ in integer steps. These values correspond (in the absence of a magnetic field) to the $2I + 1$ degenerate states for the spin angular momentum.

For nuclei with spin $I > 0$, there is an associated magnetic dipole moment, $\boldsymbol{\mu}$. This dipole moment is directly proportional to the spin angular momentum, $\mathbf{I}$:

$$\boldsymbol{\mu} = \gamma\mathbf{I} , \qquad\qquad (2.3)$$

where the constant of proportionality is γ, the gyromagnetic ratio (units rad s^{-1} T^{-1}). When an external magnetic field, B_0, is applied, the degeneracy of the $2I + 1$ states is removed. The interaction of the magnetic dipole moment with the applied magnetic field is known as the Zeeman interaction. The energy of this interaction is given by (assuming that B_0 is applied along the z axis):

$$E = -\mu_z B_0 , \qquad\qquad (2.4)$$

and the $2I + 1$ states now have energies, E_{m_I}, given by

$$\begin{aligned} E_{m_I} &= -\gamma I_z B_0 \\ &= -\gamma m_I \hbar B_0 \end{aligned} \qquad\qquad (2.5)$$

For a spin $I = 1/2$ nucleus, the two states with $m_I = +1/2$ and $-1/2$ thus have energies given by $-(1/2)\gamma\eta B_0$ and $+(1/2)\gamma\eta B_0$ and are commonly labelled α and β, respectively. The energy of a transition, ΔE, between these states is thus $\gamma\eta B_0$ and this may be expressed in terms of the frequency ν_0 (in units of Hz) as

$$\nu_0 = \frac{\gamma B_0}{2\pi} . \qquad\qquad (2.6)$$

This frequency is known as the Larmor frequency and it may also be expressed in angular frequency units (rad s^{-1}) as ω_0, where $\omega_0 = 2\pi\nu_0$. The effect of the Zeeman interaction is shown in Fig. 2.1 for spin $I = 1/2$ and spin $I = 3/2$ nuclei.

At thermal equilibrium, the nuclear spin energy levels are populated

a **b**

$m_I = -1/2$ $m_I = -3/2$

$m_I = +1/2$ $m_I = -1/2$

ω_0 ω_0

ω_0

$m_I = +1/2$

ω_0

$m_I = +3/2$

No applied With applied No applied With applied
field field field field
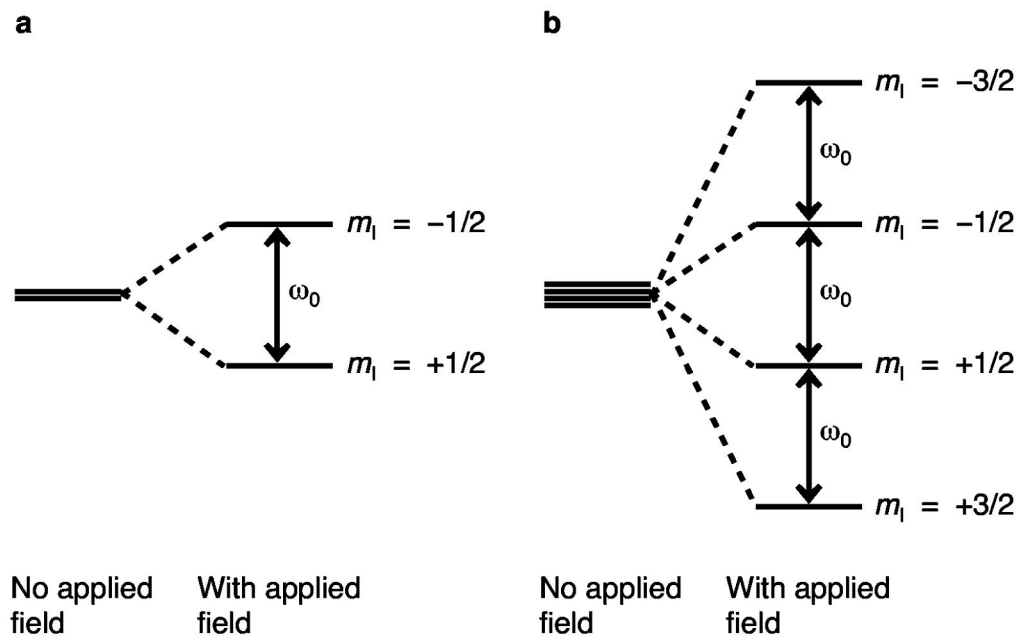
Figure 2.1. The effect of the Zeeman interaction on the energy levels of (a) a spin $I = 1/2$ nucleus and (b) a spin $I = 3/2$ nucleus.

according to the Boltzmann distribution, leading to a slight excess of spins in the lower energy α state (assuming $\gamma > 0$). This leads to a greater number of dipole moments aligned parallel to the field and, consequently, a bulk magnetization, M, is present in the sample. It is this magnetization which is manipulated in NMR.

2.2   The Vector Model

Whilst quantum mechanics is required to describe the behaviour of isolated spin-1/2 nuclei, classical mechanics may be used to describe the behaviour of an ensemble of spins that is present in a macroscopic sample. This may be achieved, at least in the case of simple NMR experiments, by using the "vector model" [68].

The bulk magnetization, M, present in a macroscopic sample at thermal equilibrium may be conveniently represented by a vector **M** oriented parallel to the z axis. When a radiofrequency (rf) pulse is applied, a linearly oscillating B_1 field exists in the transverse (xy) plane. This field oscillates at a frequency, ω_{rf}, chosen to be close to the Larmor frequency of the spins being observed. In a static reference frame, known here as the laboratory frame, the B_1 field may be considered to be the sum of two fields, one rotating at a frequency of $+\omega_{rf}$ and the other at $-\omega_{rf}$. The field rotating at a frequency of $-\omega_{rf}$ is far away from the Larmor frequency of the spins and so its effects may be disregarded. The effect on the bulk magnetization that results from its interaction with both the B_0 and B_1 fields is difficult to visualise in the laboratory frame. Consequently, this effect is visualised by changing to a coordinate system that is rotating about the z axis at a frequency ω_{rf}. In this frame of reference, known as the rotating frame, the $+\omega_{rf}$ part of the B_1 field appears static.

In the rotating frame, the apparent Larmor frequency of precession is given by $\Omega = \omega_0 - \omega_{rf}$, where Ω is known as the offset frequency. Consequently, the field present along the z axis in the rotating frame, known as the reduced field, ΔB, is given by

$$\Delta B = -\frac{\Omega}{\gamma} \, . \tag{2.7}$$

There are thus two orthogonal fields to consider in the rotating frame, ΔB and B_1. Whereas in the laboratory frame the magnetization precesses at its Larmor
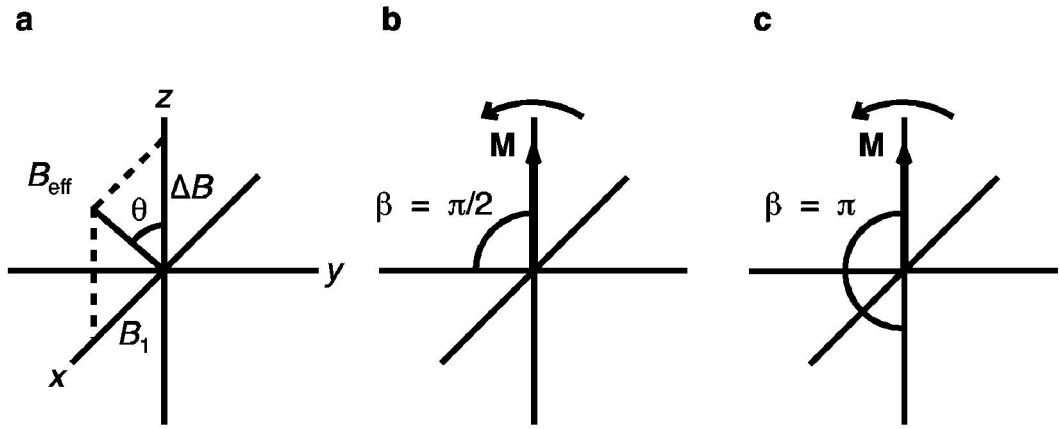
Figure 2.2. Vector model depiction of (a) the magnetic fields present in the rotating frame and (b) and (c) the effect of an rf pulse applied about the *x* axis with $\Delta B = 0$ for the values of β indicated.

frequency about the B_0 field, in the rotating frame the magnetization precesses about the effective field, B_{eff}, which is defined as the resultant of the ΔB and B_1 fields and has a magnitude given by:

$$B_{\text{eff}} = \sqrt{(\Delta B)^2 + (B_1)^2} \; . \tag{2.8}$$

The presence of these fields in the rotating frame is depicted in Fig. 2.2a, where the angle θ, known as the tilt angle, is given by

$$\theta = \tan^{-1}\left(\frac{B_1}{\Delta B}\right). \tag{2.9}$$

When viewed in the rotating frame, the effect of a radiofrequency pulse applied along the *x* axis is that the magnetization nutates in the *yz* plane until it is switched off. The angle through which the magnetization nutates during the pulse is known as the flip angle, β, defined (in radians) as

15

$$\beta = \omega_{rf}\tau \,, \tag{2.10}$$

where τ is the duration of the pulse (in seconds). For an on-resonance pulse, that is, one for which the offset frequency is zero, the effective field is coincident with the B_1 field ($\theta = \pi/2$). In such a case, a pulse applied along the rotating frame x axis with $\beta = \pi/2$ will cause a nutation of the magnetization in the yz plane, onto the $-y$ axis, whilst one with $\beta = \pi$ (known as an inversion pulse) will lead to the magnetization nutating to the $-z$ axis. This is illustrated in Figs. 2.2b and 2.2c, respectively.

After a pulse has been applied, the magnetization precesses about the rotating frame z axis at a frequency Ω (with the exception of an inversion pulse, which leaves the magnetization vector aligned along the $-z$ axis). This precession does not continue indefinitely, however, and it is damped by relaxation processes which return the magnetization vector to its orientation at thermal equilibrium, along the z axis. The loss of magnetization from the xy plane (the return to its equilibrium value of zero) is known as transverse relaxation and is quantified by an exponential time constant T_2, whilst the return of the z-magnetization to its equilibrium value is known as longitudinal relaxation and is described by an exponential time constant T_1.

As the magnetization precesses about the z axis a current is induced in a receiver coil oriented in the xy plane. This decaying current is referred to as the free induction decay (FID) and it is this which forms the time-domain signal that is detected in an NMR experiment. The FID is subjected to a Fourier

transform, which, as described in the next section, produces a frequency-domain signal.

2.3   Fourier Transform NMR

The FID acquired in NMR, denoted s(t), typically takes the following form for a simple one-pulse experiment:

$$s(t) \; = \; C \; \exp(\, i\Omega t) \; \exp(-t \, / \, T_2) \; , \quad\quad\quad (2.11)$$

where C represents the amplitude of the time-domain signal. A single detector is unable to determine the sense of precession (i.e., the sign of Ω) in the rotating frame. To overcome this problem, a method known as quadrature detection is used [69]. In this method, two datasets are collected for each FID that are $\pi/2$ radians out of phase with respect to one another. This method yields signals of the form $\cos(\Omega t)$ and $\sin(\Omega t)$; these correspond to the x- and y- (real and imaginary) components of the transverse magnetization in the rotating frame.

When quadrature detection is used, the FID is sampled at intervals of Δ seconds, such that, in accordance with the Nyquist theorem [70], the resultant spectrum covers a frequency range given by SW = $1/\Delta$, where SW is the spectral width in units of Hz.

A Fourier transform [71, 72] may be used to convert a time-dependent signal, s(t), into one which is frequency dependent, S(ω), where

$$S(\omega) = \int_0^\infty s(t)\exp(-i\omega t)\mathrm{d}t \ . \qquad\qquad (2.12)$$

This method converts a dataset that is a function of time to one which is a function of frequency and so, assuming $T_2 = \infty$, produces a frequency-dependent spectrum that has an amplitude proportional to C when $\omega = \Omega$ and that is zero for all other frequencies.

The FID consists of real and imaginary components and hence, Fourier transformation of this signal will produce a spectrum that contains real and imaginary parts. The expression for S(ω) yielded by the Fourier transform of Eq. (2.12) takes the form

$$S(\omega) = C(A(\omega) + iD(\omega)) \ , \qquad\qquad (2.13)$$

where A(ω) and D(ω) consititute the real and imaginary parts of the spectrum and represent absorptive and dispersive Lorentzian functions, respectively:

$$A(\omega) = \frac{R}{R^2 + (\omega - \Omega)^2}$$
$$D(\omega) = -\frac{(\omega - \Omega)}{R^2 + (\omega - \Omega)^2} \qquad\qquad (2.14)$$

where $R = 1/T_2$ is the rate constant for transverse relaxation expressed in units of Hz. The C factor merely leads to a scaling of the spectrum and so is omitted. These functions are shown in Fig. 2.3, where the absorptive lineshape shown in Fig. 2.3a has a peak intensity of 1/R and a width at half-height, $\Delta v_{1/2}$, of 2R rad s^{-1} (or R/π Hz), whereas the dispersive lineshape in Fig. 2.3b has an intensity of
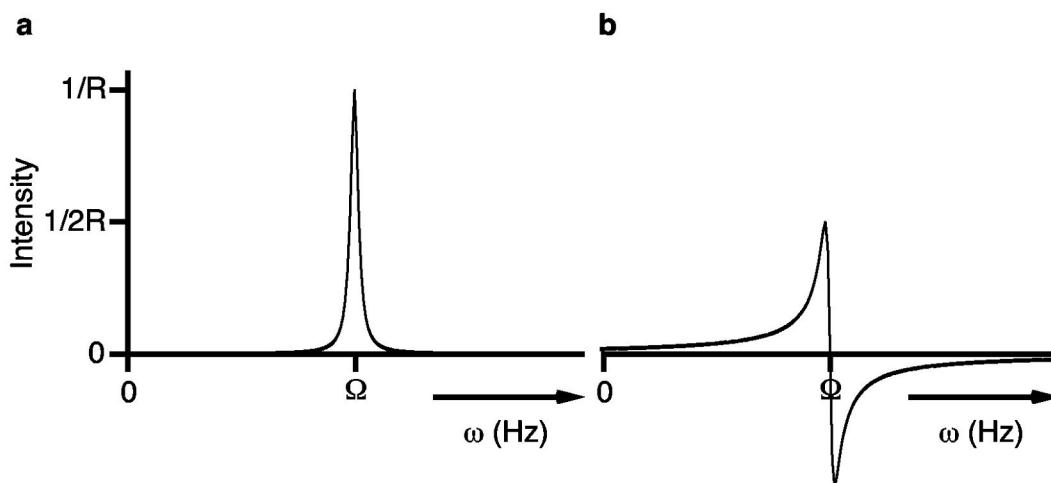
Figure 2.3. The (a) absorptive and (b) dispersive Lorentzian lineshapes that comprise the real and imaginary parts of the spectrum obtained by Fourier transformation of a signal acquired using quadrature detection. The spectral width is 10 kHz and the linewidth at half-height, $\Delta v_{1/2}$, is 200 Hz.

$1/2R$ and a width at half-height of ~ 7.5 R rad s^{-1}. The reduced intensity and greater breadth of the dispersive lineshape makes it much less desirable in NMR spectra and so usually only the real part of the spectrum, i.e., that comprising the absorptive Lorentzian, is shown.

2.4   Density Operator Formalism

The theory of quantum mechanics states that individual spins may be described by a wavefunction, $\Psi(t)$ [73], which can be written as the linear combination of an orthogonal set of basis functions, ϕ_n:

$$\Psi(t) = \sum_n c_n(t)\phi_n \quad , \tag{2.15}$$

where $c_n(t)$ are time-dependent coefficients. In a macroscopic sample there are

many such spins present and so computing the wavefunction for every spin quickly becomes rather laborious. Conveniently, there exists a method that overcomes this difficulty. This uses the density operator, ρ, which is defined as [74]

$$\rho = \overline{\left| \Psi(t) \right\rangle \left\langle \Psi(t) \right|} , \tag{2.16}$$

where the overbar indicates an ensemble average. If, for a nucleus with spin $I = 1/2$ it is assumed that each spin has a wavefunction that is a superposition of the α and β eigenstates in the Zeeman basis set, then $\left| \Psi(t) \right\rangle$ and $\left\langle \Psi(t) \right|$ are given by:

$$\begin{aligned} \left| \Psi(t) \right\rangle &= c_\alpha(t) \left| \alpha \right\rangle + c_\beta(t) \left| \beta \right\rangle \\ \left\langle \Psi(t) \right| &= c_\alpha^*(t) \left\langle \alpha \right| + c_\beta^*(t) \left\langle \beta \right| \end{aligned} , \tag{2.17}$$

where $c_\alpha^*(t)$ and $c_\beta^*(t)$ are complex conjugates of the coefficients $c_\alpha(t)$ and $c_\beta(t)$.

An operator Q may be expressed in matrix form using a set of basis functions such that the element in row i and column j is given by the integral

$$Q_{ij} = \int \phi_i^* Q \phi_j dt , \tag{2.18}$$

which may also be written in Dirac notation as

$$Q_{ij} = \left\langle i \left| Q \right| j \right\rangle . \tag{2.19}$$

In the case that $Q = \rho$, the density operator thus has a matrix representation

whose elements, ρ_{ij}, are given by:

$$\rho_{ij} = \overline{c_i^*(t)c_j(t)} .$$

(2.20)

The density operator may thus be expressed in matrix form as:

$$\rho = \begin{pmatrix} \overline{\langle \alpha |\rho| \alpha \rangle} & \overline{\langle \alpha |\rho| \beta \rangle} \\ \overline{\langle \beta |\rho| \alpha \rangle} & \overline{\langle \beta |\rho| \beta \rangle} \end{pmatrix}$$
$$= \begin{pmatrix} \rho_{11} & \rho_{12} \\ \rho_{21} & \rho_{22} \end{pmatrix}$$

(2.21)

Note that the use of two basis functions yields a 2 × 2 matrix representation of the density operator. The diagonal elements, ρ_{11} and ρ_{22}, correspond to the probabilities of the spins being found in the α and β states of the Zeeman Hamiltonian and so simply represent the relative populations of these states. The off-diagonal elements correspond to coherent superpositions of the α and β eigenstates and are termed coherences. At thermal equilibrium, the density matrix, ρ_{eq}, is directly proportional to I_z, the z-component of the spin angular momentum operator, and so is given by [74]:

$$\rho_{eq} = I_z = \begin{pmatrix} \dfrac{1}{2} & 0 \\ 0 & -\dfrac{1}{2} \end{pmatrix} .$$

(2.22)

In the case of a spin $I = 1/2$ nucleus, the off-diagonal elements correspond to coherences that have $\Delta m_I = \pm 1$ (they are said to have coherence order $p = \pm 1$) and are the only coherences observed directly in NMR. By convention,

however, only $p = -1$ coherences are observed when quadrature detection is used. The equilibrium density matrices of nuclei with larger spin quantum numbers contain off-diagonal elements corresponding to coherences with $|p| > 1$. Whilst such coherences are not directly observable in NMR, they form a crucial part of many experiments, some of which are described in Chapter 3.

In order to obtain the value of an observable, the expectation value of the corresponding operator, Q, is needed. This is given by

$$\langle Q \rangle = \overline{\rangle \Psi(t) |Q| \Psi(t) \langle} = \sum_i \sum_j \overline{c_i^*(t)c_j(t) \rangle j |Q| i \langle}$$
$$= \sum_i \sum_j \overline{\rangle i |\rho| j \langle \rangle j |Q| i \langle} \tag{2.23}$$

This can be shown to be equal to the trace (the sum of the diagonal elements) of the matrix product of the operator with the density operator:

$$\overline{\langle \Psi(t) |Q| \Psi(t) \rangle} = \text{Tr}\{\rho Q\} . \tag{2.24}$$

As was described in Section 2.3, the real and imaginary components of the observed signal in an NMR experiment correspond to the x- and y-components of the magnetization vector in the rotating frame. These are proportional to I_x and I_y, the x- and y-components of the spin angular momentum, the matrix representations of which are given in Appendix A. Consequently, the trace of the product of ρ with I_x and I_y will yield the real and imaginary components of the observable signal.

To use the density operator to predict the course of an NMR experiment, its evolution with time needs to be considered. This is achieved using the Liouville-von Neumann equation [75], which is derived from the time-dependent Schrödinger equation:

$$\frac{d\rho(t)}{dt} = -i\big[H(t), \rho(t)\big]$$
$$= -i\big(H(t)\rho(t) - \rho(t)H(t)\big)$$

(2.25)

where $\rho(t)$ is the density operator at time t and $H(t)$ is the Hamiltonian describing the spin system at time t. If the Hamiltonian is, or can be made to appear, time-independent then the solution to Eq. (2.25) is given by:

$$\rho(t) = \exp\big(-iHt\big)\rho(0)\exp\big(+iHt\big),$$

(2.26)

where $\rho(0)$ is the value of the density operator at time $t = 0$. The Hamiltonian under which the spin system is evolving can be chosen to represent a range of interactions, such as the resonance offset, chemical shift, and quadrupolar interactions. The Hamiltonian describing a particular interaction may, like the density operator, be described in matrix form, and so determining the value of $\rho(t)$ simply involves the multiplication of three matrices.

Take, for example, the effect of a $\pi/2$ pulse aligned along the rotating frame x axis on the equilibrium magnetization of a spin $I = 1$ nucleus. The equilibrium density matrix, defined to be the density matrix at time $t = 0$, is given by:

$$\rho(0) = I_z = \begin{pmatrix} 1 & 0 & 0 \\ 0 & 0 & 0 \\ 0 & 0 & -1 \end{pmatrix}. \tag{2.27}$$

The pulse Hamiltonian is given by $H(t) = \omega_1 I_x$ and, as the flip angle of the pulse is equivalent to $\omega_1 \tau$, Eq. (2.26) becomes

$$\rho(\tau) = \exp\left(-i\frac{\pi}{2}I_x\right)I_z \exp\left(+i\frac{\pi}{2}I_x\right). \tag{2.28}$$

The density matrix at time zero is diagonal, that is, only its diagonal elements are non-zero. The matrix representation of the operator I_x is diagonalised using a matrix U and its transpose, U^T, given, in this case, by:

$$U = U^T = \frac{1}{\sqrt{2}}\begin{pmatrix} \frac{1}{\sqrt{2}} & 1 & \frac{1}{\sqrt{2}} \\ 1 & 0 & -1 \\ \frac{1}{\sqrt{2}} & -1 & \frac{1}{\sqrt{2}} \end{pmatrix}, \tag{2.29}$$

which leads to

$$U I_x U^T = \begin{pmatrix} 1 & 0 & 0 \\ 0 & 0 & 0 \\ 0 & 0 & -1 \end{pmatrix} = I_z. \tag{2.30}$$

Now that the pulse Hamiltonian has been diagonalised, Eq. (2.28) becomes

$$\rho(\tau) = U \exp\left(-i\frac{\pi}{2}I_z\right)U^T I_z U \exp\left(+i\frac{\pi}{2}I_z\right)U^T. \tag{2.31}$$

The exponential of a diagonal matrix is simply a matrix consisting of the exponentiated diagonal elements and so it is then a simple matter to arrive at the solution:

$$\rho(\tau) = \frac{i}{\sqrt{2}} \begin{pmatrix} 0 & 1 & 0 \\ -1 & 0 & 1 \\ 0 & -1 & 0 \end{pmatrix} = -I_y \ . \tag{2.32}$$

This result shows that the effect of a $\pi/2$ pulse aligned along the x axis on the z-component of the bulk magnetization is to convert it into the $-y$-component of the magnetization. This is equivalent to a rotation of the bulk magnetization vector **M** from the z axis onto the $-y$ axis, and so is in accordance with the vector model description in Section 2.2.

2.5   Tensor Operators

Whilst the density matrix formalism is a convenient way of observing the effect on the magnetization of, for example, an rf pulse, it can become rather unwieldy for larger spin quantum numbers, as the density matrix of a single spin I nucleus (which has dimensions of $2I + 1 \times 2I + 1$) quickly increases in size. This problem may be alleviated by instead expressing the density operator as the linear combination of a sum of operators, A_i:

$$\rho(t) = \sum_i a_i(t) A_i \ . \tag{2.33}$$

25

For a pair of spin $I = 1/2$ nuclei, operators derived from the products of Cartesian spin angular momentum operators have been used very successfully [76]. For quadrupolar nuclei, however, the density operator is commonly expressed in terms of irreducible spherical tensor operators, $T_{l,p}$ [77]:

$$\rho(t) = \sum_{l=0}^{2I} \sum_{p=-l}^{l} a_{l,p}(t)T_{l,p} \, ,$$ (2.34)

where $T_{l,p}$ is a spherical tensor of rank l which can take the values 0, 1, 2, ..., $2I$ and where p, the coherence order, can take the values $-l$, $-l + 1$, ..., $+l$. The matrix representations of these operators are given in Appendix B. $T_{1,0}$ represents a state with coherence order zero, that is, it describes a population state [77]. This operator is proportional to the z-component of the spin angular momentum:

$$T_{1,0} \propto I_z \, .$$ (2.35)

Likewise, the x- and y-components of the spin angular momentum, described using the angular momentum operators I_x and I_y, may be expressed in terms of tensor operators of rank 1 and coherence order +1 and −1:

$$\begin{aligned} I_x &\propto \left(T_{1,-1} - T_{1,+1}\right) \\ I_y &\propto \left(T_{1,-1} + T_{1,+1}\right) \end{aligned}$$ (2.36)

The behaviour of tensor operators when evolving under the effects of an offset frequency Ω, a quadrupolar splitting ω_Q and an rf pulse may be simply

expressed. In the presence of an offset, tensor operators evolve for a time τ according to [77]

$$T_{l,p} \xrightarrow{\quad \Omega\tau \quad} T_{l,p}e^{-ip\Omega\tau} \ , \tag{2.37}$$

Evolution under an offset thus has the effect of altering neither the rank nor coherence order of the tensor operator, instead changing the phase. In many modern experiments the effect of the offset can be ignored as the presence of a π pulse refocuses the chemical shift interaction.

Under the influence of a pulse, tensor operators evolve according to [77]

$$T_{l,p} \xrightarrow{\quad \beta(I_y \cos \phi - I_x \sin \phi) \quad} \sum_{p'} T_{l,p'}d^l_{p',p}(\beta)e^{-i\Delta p\phi} \ , \tag{2.38}$$

where β is the flip angle of the pulse, ϕ is the phase of the pulse (zero for a pulse aligned along the y axis), and $\Delta p = p' - p$ is the change in coherence order. Reduced Wigner rotation matrix elements are represented by $d^l_{p',p}(\beta)$ and their values may be found in Appendix C for $l = 1, 2$ and 4. Eq. (2.38) reveals that a pulse changes the coherence order, but not the rank, of a tensor operator. Consider, for example, the effect on the z-magnetization of a $\pi/2$ pulse aligned along the rotating frame y axis. The z-magnetization, described by the tensor operator $T_{1,0}$, evolves as follows:

$$T_{1,0} \xrightarrow{\quad (\pi/2)_y \quad} \frac{1}{\sqrt{2}} \{T_{1,-1} - T_{1,1}\} \ . \tag{2.39}$$

The combination of tensor operators of rank 1 and coherence order +1 and −1 is proportional to the x-component of the spin angular momentum, I_x. This result thus agrees with that predicted by the vector model.

In the presence of a first-order quadrupolar interaction, tensor operators evolve in the following way for a time, τ:

$$T_{l,p} \xrightarrow{\;\;\omega_Q\tau\;\;} \sum_{l'=l}^{2l} c_{l',l}^{p}(\tau) T_{l',p} \;, \tag{2.40}$$

where ω_Q is the quadrupolar splitting parameter and the values of the coefficients $c_{l',l}^{p}(\tau)$ are given in Appendix D. Free precession in the presence of a quadrupolar interaction thus changes the rank, but not the coherence order, of a tensor operator. It is the combination of this evolution and that under an rf pulse that can lead to the creation of multiple-quantum coherences. In the case of triple-quantum coherence, the operators $T_{3,-1}$, $T_{3,+1}$, $T_{3,-3}$ and $T_{3,+3}$ are created and are present (with the exception of $T_{3,-1}$ and $T_{3,+1}$, which are removed by phase cycling) during the t_1 period of the triple-quantum MAS experiment described in Chapter 3.

Using the tensor operator formalism, it is thus easy to show the effect of a pulse and of evolution under a quadrupolar splitting or offset. The well-defined behaviour of tensor operators under these conditions provides a convenient way in which to consider the effects of the more complex NMR experiments for which a vector model description is inadequate.

2.6 Line Broadening Mechanisms

There exist several mechanisms that can lead to line broadening in NMR spectra in the solid state. Two of the most significant, the chemical shift and dipolar coupling, are introduced in this section and their effect on solid-state NMR spectra is described. Another major source of line broadening in the case of quadrupolar nuclei is the quadrupolar interaction. This will be described in detail in Chapter 3.

2.6.1 Chemical Shift

When a magnetic field is applied, electrons begin a circulatory motion about a nucleus. This motion creates a magnetic field that can either increase or decrease the magnetic field experienced by the nucleus. This shielding is the origin of the chemical shift and has the effect of modifying the Larmor frequency defined in Eq. (2.6) to [78]:

$$\omega_0 = -\gamma B_0 (1 - \sigma) . \qquad (2.41)$$

In Eq. (2.41), σ is the chemical shielding tensor. The chemical shielding has the properties of a second-rank Cartesian tensor and as such may be represented by a 3×3 matrix. This is also the case for the dipolar interaction (described in Section 2.6.2) and the first-order quadrupolar interaction (described in Chapter 3) and in each case, the tensor is defined with respect to a frame of reference such that this matrix is diagonal. This reference frame is

29

known as the principal axis system (PAS). In such a reference frame, the tensor is defined by three quantities, referred to as the principal values describing the interaction. For chemical shielding, these are defined as σ_{XX}^{PAS}, σ_{YY}^{PAS} and σ_{ZZ}^{PAS} and correspond to the principal values of the interaction associated with the PAS X, Y and Z axes, respectively. The chemical shielding tensor may thus be represented by the following matrix in its PAS:

$$\sigma = \begin{pmatrix} \sigma_{XX}^{PAS} & 0 & 0 \\ 0 & \sigma_{YY}^{PAS} & 0 \\ 0 & 0 & \sigma_{ZZ}^{PAS} \end{pmatrix}, \qquad (2.42)$$

where these principal values may be used to define an isotropic value of the chemical shielding tensor, σ_{iso}, an anisotropy, Δ, and an asymmetry, η:

$$
\begin{aligned}
\sigma_{iso} &= \frac{1}{3}\left(\sigma_{XX}^{PAS} + \sigma_{YY}^{PAS} + \sigma_{ZZ}^{PAS}\right) \\
\Delta &= \sigma_{ZZ}^{PAS} - \sigma_{iso} \\
\eta &= \frac{\sigma_{XX}^{PAS} - \sigma_{YY}^{PAS}}{\Delta}
\end{aligned}
\qquad (2.43)
$$

In NMR, absolute frequencies are not measured; instead, frequencies are quoted as chemical shifts with respect to a reference material. The chemical shift, δ_{iso}, is thus defined as follows [79]:

$$\delta_{iso} = \frac{\omega_0 - \omega_0(\text{ref})}{\omega_0(\text{ref})} = \frac{\left(\sigma_{iso}(\text{ref}) - \sigma_{iso}\right)}{1 - \sigma_{iso}(\text{ref})}, \qquad (2.44)$$

where ω_0(ref) and σ_{iso}(ref) are the Larmor frequency and isotropic value of the chemical shielding tensor of the reference sample, respectively. The chemical shift, defined in Eq. (2.44), also has the properties of a second-rank Cartesian tensor and as such may be defined by three principal values in its PAS, δ_{XX}^{PAS}, δ_{YY}^{PAS} and δ_{ZZ}^{PAS}. Using these principal values, the isotropic chemical shift, δ_{iso}, the chemical shift anisotropy, Δ_{CS}, and the chemical shift asymmetry, η_{CS}, are defined as

$$\delta_{iso} = \frac{1}{3}\left(\delta_{XX}^{PAS} + \delta_{YY}^{PAS} + \delta_{ZZ}^{PAS}\right)$$

$$\Delta_{CS} = \delta_{ZZ}^{PAS} - \delta_{iso} \qquad\qquad . \qquad (2.46)$$

$$\eta_{CS} = \frac{\delta_{XX}^{PAS} - \delta_{YY}^{PAS}}{\Delta_{CS}}$$

The observed chemical shift, δ, is defined as the sum of isotropic and anisotropic contributions:

$$\delta = \delta_{iso} + \frac{1}{2}\Delta_{cs}\{3\cos^2\theta - 1 + \eta_{cs}\sin^2\theta\cos 2\phi\}, \qquad (2.47)$$

where θ and ϕ are polar angles that define the orientation of the B_0 field in the PAS of the chemical shielding tensor. In the solution state, rapid molecular tumbling averages the anisotropic component of the chemical shift to zero and so only the isotropic component is observed. In the solid state, however, the general lack of motion means that the anisotropic component of the chemical shift is no longer averaged to zero. This means that, due to the range of orientations observed in a powder, each crystallite has a different chemical shift

and so a "powder pattern" is observed in the spectrum.

2.6.2   Dipolar Coupling

There exists an interaction between the magnetic moments of nuclei that are close in space. This through-space interaction is referred to as the dipolar interaction and, for the case of a homonuclear IS spin pair, is defined by the following first-order average Hamiltonian, H_{dd}^{hom}, expressed in the rotating frame [80]:

$$H_{dd}^{hom} = \omega_D(3I_zS_z - I \cdot S), \tag{2.48}$$

where $I \cdot S = I_xS_x + I_yS_y + I_zS_z$ and ω_D is the dipolar coupling parameter, given by:

$$\omega_D = \frac{\omega_D^{PAS}}{2}\left(3\cos^2\theta - 1\right), \tag{2.49}$$

where θ is the angle between the I-S internuclear vector and B_0. ω_D^{PAS} is the dipolar coupling parameter in the principal axis system of the dipolar coupling tensor and is defined as [81, 82]:

$$\omega_D^{PAS} = -\frac{\mu_0\gamma_I\gamma_S\hbar}{4\pi r_{IS}^3}, \tag{2.50}$$

with γ_I and γ_S being the gyromagnetic ratios of the I and S spins and r_{IS} their internuclear distance.

Like the chemical shielding interaction described in Section 2.6.1, the dipolar coupling has the properties of a second-rank Cartesian tensor. In contrast to the chemical shielding, however, the dipolar coupling tensor is traceless and so its isotropic value, D_{iso}, is zero. In addition, the dipolar coupling tensor is always axially symmetric ($\eta = 0$).

In the solution state, the presence of molecular motion averages the dipolar coupling to its isotropic value. This means that, if residual linewidths are ignored, no evidence of the presence of the dipolar coupling is seen in the spectrum. In the solid state, however, the general lack of motion means that the averaging seen in the solution state is not observed. The angular dependence of ω_D means that, in a powdered solid, a range of dipolar couplings exists, so producing a powder pattern in the NMR spectrum.

As shown in Eq. (2.50), the strength of the dipolar interaction between two nuclei I and S is proportional to $\gamma_I \gamma_S$. The effect of the Hamiltonian in a multi-spin homonuclear system is to remove the degeneracy of the many Zeeman levels that have the same net azimuthal quantum number. This arises because of the homogeneous nature of this interaction [11] and leads to a very large range of transition frequencies in the NMR spectrum of such a spin system. For homonuclear dipolar couplings between nuclei such as ^{1}H and ^{19}F, this means that the resultant spectra commonly contain linewidths of up to 30kHz.

The dipolar interaction between two non-equivalent spin species I and S is characterised by the following first-order rotating frame average Hamiltonian:

$$H_{dd}^{het} = 2\omega_D m_I m_S I_z S_z \, . \qquad\qquad (2.51)$$

If the I and S spins are assumed to be spin $I = 1/2$ nuclei, then this has the effect of shifting the energies of the four Zeeman levels by $\pm\omega_D/2$. The two transitions of each of the I and S spins, that have equal frequencies in the absence of a dipolar coupling, are thus shifted by $\pm\omega_D$. The orientational dependence of ω_D leads to a powder pattern in the spectrum, and as the dipolar coupling has, like the chemical shift, the properties of a second-rank Cartesian tensor, this powder pattern consists of two overlapping axially symmetric CSA patterns (one for each transition) that are mirror images of one another. Line broadening due to heteronuclear dipolar coupling can be removed by, in addition to MAS [37], a technique known as decoupling [25]. This involves applying high-power continuous irradiation at the Larmor frequency of the spin that is being decoupled (typically the S spin). This causes rapid transitions between the S-spin Zeeman states such that the observed (I) spin transitions are once again degenerate and a single peak at the I-spin frequency, from which anisotropic line broadening due to the dipolar interaction has been removed, is observed.

2.7   Two-Dimensional NMR

Many routine NMR experiments are two-dimensional in nature. They differ from their one-dimensional counterparts in that they comprise two time periods during which the magnetization evolves, conventionally labelled t_1 and t_2. The typical form of a two-dimensional NMR experiment [83, 84] is shown in

Fig. 2.4.

An initial pulse of phase ϕ_1 excites transverse magnetization that is then allowed to evolve during the t_1 period. Another pulse (or commonly, a sequence of pulses) of phase ϕ_2 then converts this magnetization to $p = -1$ central-transition coherence that is detected during the t_2 period. This process is typically repeated 64–256 times, with the t_1 period being incremented each time.

This yields a time-domain signal, $s(t_1, t_2)$, that is a function of two time periods, and that commonly (though not always) is cosine modulated during the t_1 period:

$$s(t_1, t_2) = \cos(\omega_1 t_1) \exp(-R_1 t_1) \exp(i\omega_2 t_2) \exp(-R_2 t_2) , \qquad (2.52)$$

where R_1 and R_2 are transverse relaxation rate constants during the t_1 and t_2 periods, respectively. Performing a Fourier transformation in both dimensions then yields a two-dimensional spectrum that, like its one-dimensional analogue, contains real and imaginary components. The two dimensions, ω_2 and ω_1, are known as the direct and indirect dimensions, respectively. For two-dimensional experiments to be useful, it is a necessity that the real part of the spectrum contains lineshapes that are purely absorptive in both dimensions; that is, they contain none of the highly undesirable dispersive character that was described in Section 2.3.
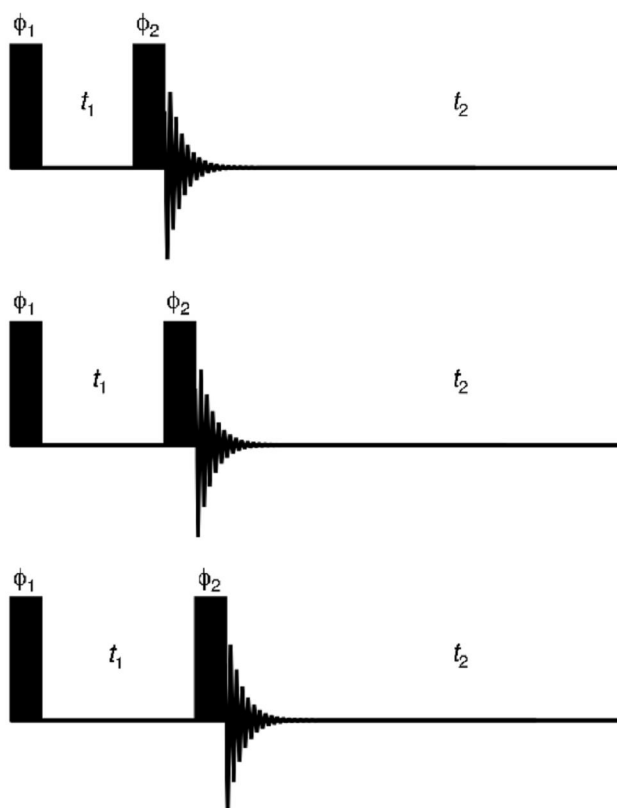
Figure 2.4. The typical form of a two-dimensional NMR experiment. The t_1 period is incremented in successive one-dimensional experiments such that a signal is produced in which the magnetization has evolved during two time periods.
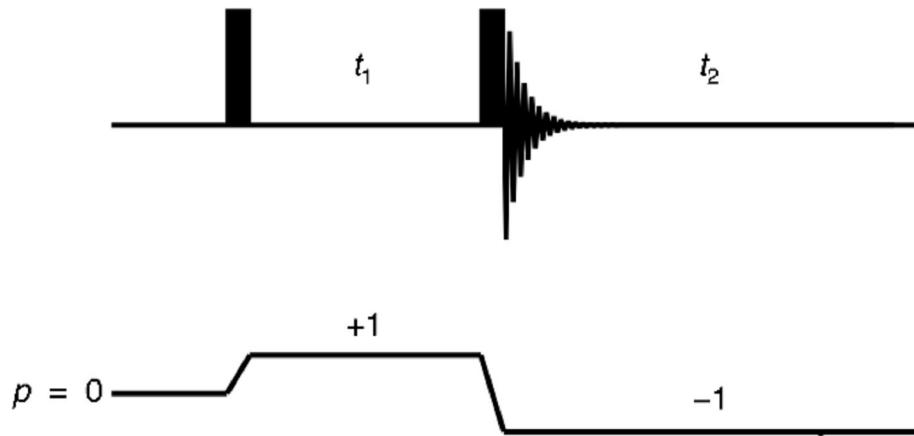
2.7.1   Phase Modulation

In Section 2.3 it was shown how the Fourier transform converts a dataset that is a function of time to one which is a function of frequency:

$$s(t) \xrightarrow{\quad FT \quad} S(\omega) \, , \tag{2.53}$$

where $S(\omega)$ may be expressed as the sum of its absorptive and dispersive Lorentzian components:

$$S(\omega) = A(\omega) + iD(\omega) \, . \tag{2.54}$$

Figure 2.5. Pulse sequence and coherence transfer pathway for the N-type COSY experiment.

Consider, for example, a simple two-pulse N-type COSY experiment [85]. The coherence transfer pathway and pulse sequence for this experiment are shown in Fig. 2.5. As is now customary for many modern two-dimensional experiments, phase cycling is used to ensure the correct coherence transfer pathway is selected [86, 87]. A two-dimensional experiment of this form, in which only one coherence transfer pathway is selected during the t_1 period, yields a time-domain signal of the form:

$$s(t_1, t_2) = \exp(-i\omega_1 t_1) \exp(-R_1 t_1) \exp(i\omega_2 t_2) \exp(-R_2 t_2) \, . \tag{2.55}$$

A function of the form $\exp(i\omega t)$ is not an even function, that is, $\exp(i\omega t) \neq \exp(-i\omega t)$. Consequently, a time-domain dataset of the form in Eq. (2.55) is sensitive to the sign of the offset and is said to be frequency discriminated. Fourier transformation in the t_2 dimension leads to the following dataset:

$$s(t_1, \omega_2) = \exp(-i\omega_1 t_1) \exp(-R_1 t_1)\{A(\omega_2) + iD(\omega_2)\} \, . \tag{2.56}$$

Inspection of the spectrum obtained in the ω_2 dimension reveals that the phase

of the lineshape varies as a function of t_1. Two-dimensional experiments producing time-domain data in the form of Eq. (2.55) are thus said to be phase modulated.

A second Fourier transformation, in the t_1 dimension, leads to the two-dimensional dataset

$$S(\omega_1, \omega_2) = \{A(\omega_1) + iD(\omega_1)\}\{A(\omega_2) + iD(\omega_2)\}$$
$$= [A(\omega_1)A(\omega_2) - D(\omega_1)D(\omega_2)] \qquad . \qquad (2.57)$$
$$+i[D(\omega_1)A(\omega_2) + A(\omega_1)D(\omega_2)]$$

Equation (2.57) reveals that the real part of the spectrum contains a mixture of doubly-absorptive and doubly-dispersive contributions. The lineshape arising from such contributions is known as a phase-twist lineshape, and, on account of it having both positive and negative parts, it is thus unsuitable for high-resolution NMR. Performing an experiment in which $p = -1$ coherences are selected during the t_1 period (known as a P-type COSY experiment [85]) produces a time-domain signal, which, after Fourier transformation in both dimensions, yields a dataset that differs from that in Eq. (2.57) only in the sign of the frequency in the ω_1 dimension. Phase-modulated experiments thus achieve the desired frequency discrimination, but have the undesirable by-product of a phase-twist lineshape.

2.7.2 Amplitude Modulation

Many two-dimensional NMR experiments involve the selection of more than one coherence transfer pathway during the t_1 period. An example of this is the double-quantum filtered (DQF)-COSY experiment [88], the pulse sequence of which is shown in Fig. 2.6. Experiments such as this yield a time-domain signal of the form

$$
\begin{aligned}
s(t_1, t_2) &= \frac{1}{2} \{\exp(+i\omega_1 t_1) + \exp(-i\omega_1 t_1)\} \\
&\quad \times \exp(-R_1 t_1) \exp(i\omega_2 t_2) \exp(-R_2 t_2) \qquad . \qquad (2.58) \\
&= \cos(\omega_1 t_1) \exp(-R_1 t_1) \exp(i\omega_2 t_2) \exp(-R_2 t_2)
\end{aligned}
$$

Such a signal is said to be amplitude modulated, as variation of t_1 modifies only its amplitude, and not its phase. The Fourier transform of a function of the form $\cos(\omega t)\exp(-Rt)$ (a cosine Fourier transform) yields an absorptive Lorentzian, $A(\omega)$. The resulting spectrum thus contains, in contrast to the Fourier transform of a complex exponential function, only real components. Consequently, a two-dimensional Fourier transform of the time-domain signal in Eq. (2.58) yields a dataset of the form:

$$
S(\omega_1, \omega_2) = A(\omega_1)\{A(\omega_2) + iD(\omega_2)\} . \qquad (2.59)
$$

The real part of this signal is of the form $A(\omega_1)A(\omega_2)$ and so yields a doubly-absorptive lineshape. Amplitude-modulated experiments thus produce spectra containing not the phase-twist lineshapes observed with phase-modulated experiments, but lineshapes whose doubly-absorptive nature makes them far
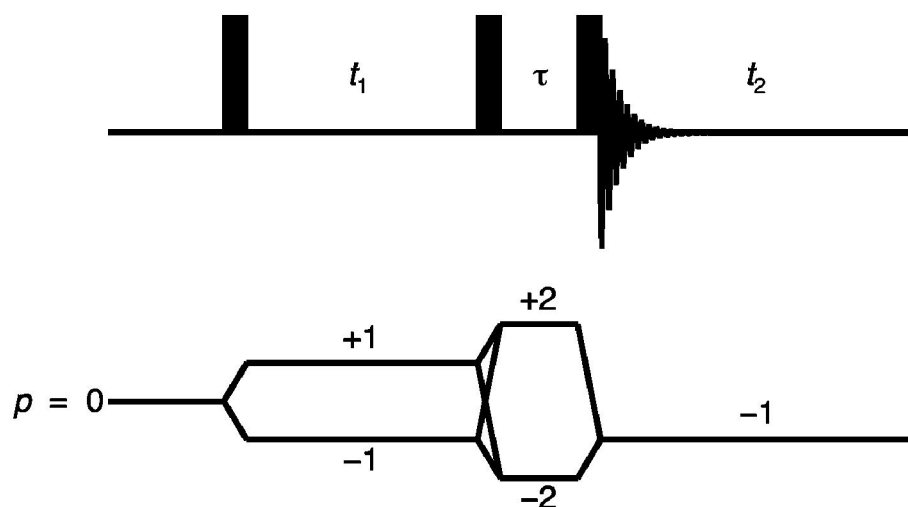
Figure 2.6. Pulse sequence and coherence transfer pathway for the DQF-COSY experiment.

more conducive to high-resolution NMR. However, amplitude-modulated data lack the frequency discrimination possessed by phase-modulated data. This is a direct consequence of the relations

$$\begin{aligned}\cos(\omega_1 t_1) &= \cos(-\omega_1 t_1)\\ \sin(\omega_1 t_1) &= -\sin(-\omega_1 t_1)\end{aligned}. \qquad (2.60)$$

This lack of frequency discrimination is a drawback of acquiring amplitude-modulated data. The following section describes methods that allow both frequency discrimination to be achieved and doubly-absorptive lineshapes to be obtained.

2.7.3   States-Haberkorn-Ruben and TPPI Methods

A phase shift of $\pi/2$ radians of a cosine function yields a sine function. The States-Haberkorn-Ruben (SHR) method [89] achieves frequency discrimination

by using both cosine- and sine-modulated time-domain signals. When a Fourier transform is performed in the t_2 dimension, time-domain signals that have sine and cosine modulation in t_1, denoted $S_{sin}(t_1, \omega_2)$ and $S_{cos}(t_1, \omega_2)$ respectively, are obtained:

$$S_{cos}(t_1, \omega_2) = \cos(\omega_1 t_1) \exp(-R_1 t_1)\{A(\omega_2) + iD(\omega_2)\}$$
$$S_{sin}(t_1, \omega_2) = \sin(\omega_1 t_1) \exp(-R_1 t_1)\{A(\omega_2) + iD(\omega_2)\}$$
(2.61)

In the SHR method, a new dataset is formed, $S_{SHR}(t_1, \omega_2)$, in which the real and imaginary components are the real parts of the cosine- and sine-modulated datasets, respectively:

$$S_{SHR}(t_1, \omega_2) = \cos(\omega_1 t_1) \exp(-R_1 t_1) A(\omega_2) +$$
$$i \sin(\omega_1 t_1) \exp(-R_1 t_1) A(\omega_2)$$
(2.62)

This may also be expressed as:

$$S_{SHR}(t_1, \omega_2) = \exp(i\omega_1 t_1) \exp(-R_1 t_1) A(\omega_2) ,$$
(2.63)

which, after Fourier transformation in the indirect dimension gives:

$$S_{SHR}(\omega_1, \omega_2) = \{A(\omega_1) + iD(\omega_1)\}A(\omega_2)$$
$$= A(\omega_1)A(\omega_2) + iD(\omega_1)A(\omega_2)$$
(2.64)

The real part of this signal is doubly absorptive and so is of the required form for high-resolution two-dimensional NMR.

There exists an alternative technique for achieving frequency

discrimination, known as time proportional phase incrementation (TPPI) [90]. This method is similar to the SHR method and operates by shifting the phase of the pulse, or group of pulses, that preceed the t_1 period, for each increment of t_1. This phase shift, equal to $\pi/(2|p|)$, where p is the order of coherence evolving during the t_1 period, leads to the following dataset, after Fourier transformation in the t_2 dimension:

$$S_{\text{TPPI}}(t_1, \omega_2) = \cos\{(\omega_1 + (2\pi)(SW_1 / 2))t_1\} \exp(-R_1 t_1)A(\omega_2) , \qquad (2.65)$$

where $1/SW_1$ is equal to the t_1 increment. In this method, the spectral width in the ω_1 dimension is doubled and so, in accordance with the Nyquist theorem, the sampling interval in the indirect dimension (the t_1 increment) is halved.

Chapter 3

Quadrupolar Interaction

3.1   Introduction

The dominant interaction for nuclei with spin $I > 1/2$ is usually that which arises between the nuclear electric quadrupole moment and the electric field gradient [91–93]. This quadrupolar coupling commonly has a magnitude of the order of megahertz and is responsible for the large quadrupolar splittings observed in solid-state NMR spectra of quadrupolar nuclei. In liquids, the quadrupolar interaction is also responsible for efficient quadrupolar relaxation. The major source of line broadening for quadrupolar nuclei is the inhomogeneous contribution arising from the quadrupolar coupling and it is this which determines the appearance of the resultant NMR spectra in the solid state. In this section, the origin of this quadrupolar broadening will be described, as will the equations describing its effects and the implications for the appearance of the spectra.

3.2   The Quadrupolar Coupling

In addition to the magnetic dipole moment that is characteristic of all NMR-active nuclei, nuclei with spin $I > 1/2$ possess an electric quadrupole

moment, *eQ*. The electric quadrupole moment takes a fixed value and is characteristic of the nucleus. The presence of a non-spherical distribution of electrons around a nucleus leads to an electric field gradient (EFG). The electric field gradient is a three-dimensional entity which can be described using the EFG tensor, V. This tensor can be described by three components in its PAS. These are denoted V_{XX}^{PAS}, V_{YY}^{PAS} and V_{ZZ}^{PAS} and correspond to the principal values of the electric field gradient associated with the X, Y and Z PAS axes, respectively. These components satisfy the conditions

$$V_{XX}^{PAS} + V_{YY}^{PAS} + V_{ZZ}^{PAS} = 0$$
$$\left| V_{ZZ}^{PAS} \right| \geq \left| V_{XX}^{PAS} \right| \geq \left| V_{YY}^{PAS} \right| \qquad (3.1)$$

The EFG tensor is traceless and so its isotropic value is zero. This means that its anisotropy is equal to V_{ZZ}^{PAS} and so is given by *eq*, where *e* is the magnitude of the electron charge. The coupling of the quadrupole moment (*eQ*) and the EFG (*eq*) leads to an interaction that is quantified, in units of Hertz, using a quadrupolar coupling parameter C_Q [94]:

$$C_Q = \frac{e^2 qQ}{h}, \qquad (3.2)$$

and the cross-sectional shape of the EFG tensor parallel to the $X^{PAS}Y^{PAS}$ plane is characterised by an asymmetry parameter, η, which can take values between 0 and 1, and is given by:

$$\eta = \frac{V_{XX}^{PAS} - V_{YY}^{PAS}}{V_{ZZ}^{PAS}} . \tag{3.3}$$

3.3 The Quadrupolar Interaction

3.3.1 The First-Order Quadrupolar Interaction

The Hamiltonian describing a quadrupolar nucleus can be expressed, neglecting the effects of CSA and any homonuclear and heteronuclear dipolar couplings, as follows:

$$H = H_Z + H_Q , \tag{3.4}$$

where the Hamiltonian H_Z (equal to $\omega_0 I_z$) expresses the effect of the Zeeman interaction and H_Q that of the quadrupolar interaction. Whilst the quadrupolar interaction can in some cases be very large, it is typically at least an order of magnitude smaller than the Zeeman interaction. This means that its effect on the energy levels can be considered as a perturbation of the dominant Zeeman term and so time-independent perturbation theory may be used [95]. The quadrupolar Hamiltonian is given by the following equation, expressed in the PAS of the EFG tensor [96]:

$$H_Q^{PAS} = \omega_Q^{PAS} \left[I_Z^2 - \frac{1}{3} I(I + 1) + \frac{\eta}{3} \left(I_X^2 - I_Y^2 \right) \right] , \tag{3.5}$$

where I_X, I_Y and I_Z are analogous to the operators I_x, I_y and I_z defined in Chapter

2. ω_Q^{PAS} is defined as the magnitude of the quadrupolar interaction in the PAS of the EFG tensor and is given, in units of rad s^{-1}, by

$$\omega_Q^{PAS} = \frac{3\pi C_Q}{2I(2I-1)} \,.$$ (3.6)

In the laboratory frame, a quadrupolar splitting parameter, ω_Q, is defined, in units of rad s^{-1}:

$$\omega_Q = \frac{\omega_Q^{PAS}}{2} (3 \cos^2 \beta - 1 + \eta \sin^2 \beta \cos 2\gamma) \,,$$ (3.7)

where β and γ are angles relating the PAS of the EFG tensor to B_0. Equation (3.7) reveals the quadrupolar splitting to be orientationally dependent. For a powdered solid, this means that each crystallite orientation will experience a different quadrupolar splitting, so giving rise to a powder pattern.

Equation (3.5) may also be expressed using spherical tensor operators (for a spin $I = 3/2$ nucleus) as:

$$H_Q^{PAS} = 2\omega_Q^{PAS} \left(T_{2,0} + \frac{\eta}{\sqrt{6}} \left(T_{2,2} + T_{2,-2} \right) \right),$$ (3.8)

or in matrix form as:

$$H_Q^{PAS} = \omega_Q^{PAS} \begin{pmatrix} 1 & 0 & \dfrac{\eta}{\sqrt{3}} & 0 \\ 0 & -1 & 0 & \dfrac{\eta}{\sqrt{3}} \\ \dfrac{\eta}{\sqrt{3}} & 0 & -1 & 0 \\ 0 & \dfrac{\eta}{\sqrt{3}} & 0 & 1 \end{pmatrix} . \tag{3.9}$$

To determine the effects of the quadrupolar interaction, the Hamiltonian must first be transformed to the laboratory frame. As tensor operators have well-defined properties under rotation, the quadrupolar Hamiltonian defined in Eq. (3.8) is used. A tensor of rank l and coherence order p, denoted $T_{l,p}$, transforms from one frame of reference to another via a rotation $R(\alpha, \beta, \gamma)$ as [97]:

$$R(\alpha, \beta, \gamma) T_{l,p} R^{-1}(\alpha, \beta, \gamma) = \sum_{p'=-l}^{l} D_{p',p}^{l}(\alpha, \beta, \gamma) T_{l,p'} , \tag{3.10}$$

where α, β and γ are the Euler angles [98] that relate the two frames of reference and $R^{-1}(\alpha, \beta, \gamma)$ is the inverse of the rotation operator $R(\alpha, \beta, \gamma)$. The Euler angles, α, β and γ, are defined as rotations of α about the laboratory frame x axis, of β about the laboratory frame y axis and of γ about the laboratory frame z axis, respectively. $D_{p',p}^{l}(\alpha, \beta, \gamma)$ are Wigner rotation matrix elements and are defined as [99]

$$D_{p',p}^{l}(\alpha, \beta, \gamma) = d_{p',p}^{l}(\beta) \exp\{-i(\alpha p' + \gamma p)\} , \tag{3.11}$$

where $d_{p',p}^{l}(\beta)$ are reduced rotation matrix elements [100]. Consequently, in the

47

laboratory frame the quadrupolar Hamiltonian, H_Q, is expressed as:

$$H_Q = 2\omega_Q^{PAS} \sum_{p'=-2}^{2} [(D_{p',0}^2(\alpha, \beta, \gamma) + \frac{\eta}{\sqrt{6}} \{D_{p',2}^2(\alpha, \beta, \gamma) + D_{p',-2}^2(\alpha, \beta, \gamma)\} \mathbb{T}_{2,p'} \tag{3.12}$$

which may also be expressed in matrix form:

$$H_Q = 2\omega_Q^{PAS} \begin{pmatrix} A & -B^+ & C^+ & 0 \\ B^- & -A & 0 & C^+ \\ C^- & 0 & -A & B^+ \\ 0 & C^- & -B^- & A \end{pmatrix}, \tag{3.13}$$

where

$$A = \left| \frac{1}{2} D_{00}^2(\alpha, \beta, \gamma) + \frac{\eta}{2\sqrt{6}} (D_{0,2}^2(\alpha, \beta, \gamma) + D_{0,-2}^2(\alpha, \beta, \gamma)) \right|$$

$$B^+ = \left[\frac{1}{\sqrt{2}} D_{1,0}^2(\alpha, \beta, \gamma) + \frac{\eta}{\sqrt{12}} \left(D_{1,2}^2(\alpha, \beta, \gamma) + D_{1,-2}^2(\alpha, \beta, \gamma) \right) \right]$$

$$B^- = \left[\frac{1}{\sqrt{2}} D_{-1,0}^2(\alpha, \beta, \gamma) + \frac{\eta}{\sqrt{12}} \left(D_{-1,-2}^2(\alpha, \beta, \gamma) + D_{-1,2}^2(\alpha, \beta, \gamma) \right) \right]. \tag{3.14}$$

$$C^+ = \left[\frac{1}{\sqrt{2}} D_{2,0}^2(\alpha, \beta, \gamma) + \frac{\eta}{\sqrt{12}} \left(D_{2,2}^2(\alpha, \beta, \gamma) + D_{2,-2}^2(\alpha, \beta, \gamma) \right) \right]$$

$$C^- = \left[\frac{1}{\sqrt{2}} D_{-2,0}^2(\alpha, \beta, \gamma) + \frac{\eta}{\sqrt{12}} \left(D_{-2,2}^2(\alpha, \beta, \gamma) + D_{-2,-2}^2(\alpha, \beta, \gamma) \right) \right]$$

The first-order perturbation to an energy level, $E_{m_I}^{(1)}$, is given by [95]

$$E_{m_I}^{(1)} = \langle m_I | H_Q | m_I \rangle . \tag{3.15}$$

Hence, taking the example of the energy level with $m_I = 3/2$, this is equivalent
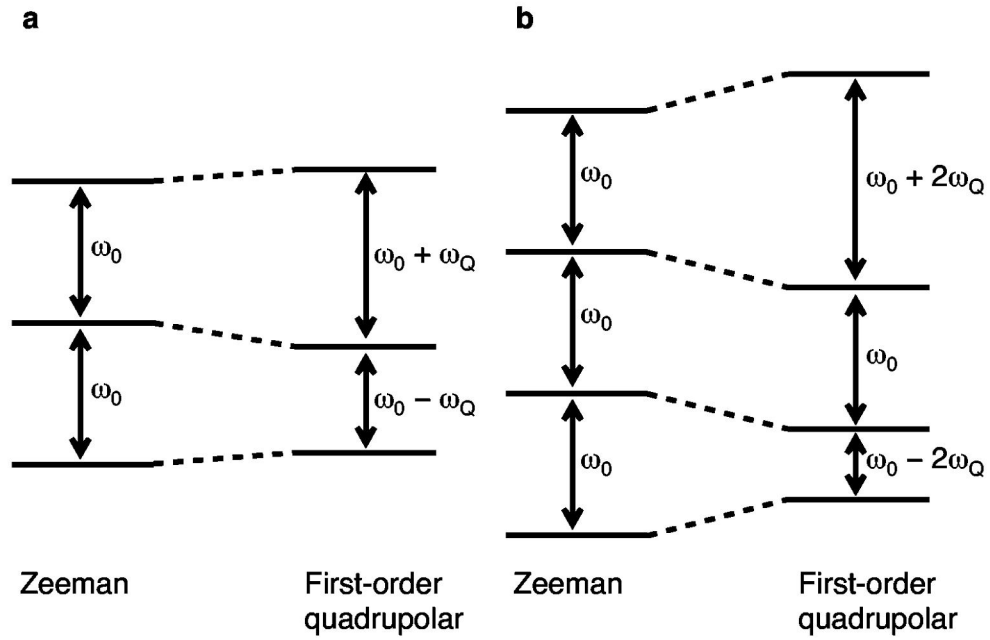
Figure 3.1. The first-order perturbation to the energy levels of a spin (a) $I = 1$ and (b) $I = 3/2$ nucleus by the quadrupolar interaction.

to the element in the first row and first column (i.e., the first diagonal element) in the matrix representation of the quadrupolar Hamiltonian. The four Zeeman states of a spin $I = 3/2$ nucleus are thus perturbed as follows:

$$E_{3/2}^{(1)} = E_{-3/2}^{(1)} = \frac{\omega_Q^{PAS}}{2}\left(3\cos^2\beta - 1\right) = \omega_Q$$

$$E_{1/2}^{(1)} = E_{-1/2}^{(1)} = -\frac{\omega_Q^{PAS}}{2}\left(3\cos^2\beta - 1\right) = -\omega_Q \tag{3.16}$$

The first-order perturbation to the energies of the Zeeman states is shown in Figs. 3.1a and 3.1b for the case of spin $I = 1$ and spin $I = 3/2$ nuclei, respectively.

Figure 3.1 reveals that, for a spin $I = 1$ nucleus, the frequency of the ($m_I = +1 \leftrightarrow -1$) transition (the double-quantum (DQ) transition) is unaffected to first

order by the quadrupolar interaction. For a spin $I = 3/2$ nucleus, the frequencies of the ($m_I = +1/2 \leftrightarrow -1/2$) and ($m_I = +3/2 \leftrightarrow -3/2$) transitions, known as the central (CT) and triple-quantum (TQ) transitions respectively, are unaffected to first order. In general, all symmetric transitions are unperturbed by the first-order quadrupolar interaction. Figure 3.1b shows that for a spin $I = 3/2$ nucleus, the frequencies of the ($m_I = +3/2 \leftrightarrow +1/2$) and ($m_I = -1/2 \leftrightarrow -3/2$) transitions, the so-called satellite transitions (ST), are given by $\omega_0 - 2\omega_Q$ and $\omega_0 + 2\omega_Q$, respectively. For half-integer nuclei with spin $I > 3/2$, there is more than one set of satellite transitions and these are labelled ST_1 (the $m_I = \pm3/2 \leftrightarrow \pm1/2$ transitions), ST_2 (the $m_I = \pm5/2 \leftrightarrow \pm3/2$ transitions), and so on. The orientational dependence of ω_Q means that, in a powdered solid, a powder pattern is observed in the NMR spectrum. The absence of an isotropic component in Eq. (3.16) means that the powder pattern remains centred about ω_0. Owing to the absence of a first-order perturbation to the frequency of the central transition, the resultant powder pattern features a narrow line and it is for this reason that much solid-state NMR of quadrupolar nuclei has focussed on observation of solely this transition. The central transition is, however, affected by a smaller second-order perturbation and so the magnitude of this effect needs to be determined.

3.3.2   *The Second-Order Quadrupolar Interaction*

Time-independent perturbation theory states that the second-order

q	$A^0(I, q)$	$B^2(I, q)$	$C^4(I, q)$
1/2	−2/5	−8/7	54/35
3/2	6/5	0	−6/5

Table 3.1. Values of the zeroth-, second- and fourth-rank coefficients in Eqs. (3.22) and (3.23) for the $m_I = \pm q \leftrightarrow \mu q$ transitions of a spin $I = 3/2$ nucleus.

perturbation to an energy level, $E^{(2)}_{m_I}$, is given by [95]

$$E^{(2)}_{m_I} = \sum_{n \neq m} \frac{\langle m | H_Q | n \rangle \langle n | H_Q | m \rangle}{E^{(0)}_m - E^{(0)}_n} \, , \tag{3.17}$$

where m and n take the values (for a spin $I = 3/2$ nucleus) +3/2, +1/2, −1/2 and −3/2. $E^{(0)}_m - E^{(0)}_n$ is the energy of the transition between energy levels m and n when these energy levels are perturbed solely by the Zeeman interaction. To proceed with this calculation, the multiplication of Wigner rotation matrix elements is required, the result of which is described by [98]

$$D^a_{p',p}(\alpha, \beta, \gamma) D^b_{q',q}(\alpha, \beta, \gamma) = \sum_c \rangle ap, bq | cr \langle \rangle ap', bq' | cr' \langle D^c_{r',r}(\alpha, \beta, \gamma)) \, , \tag{3.18}$$

where c takes the values $|a - b|$, $|a - b + 1|$, ... $|a + b|$, $r' = p' + q'$, $r = p + q$ and $\rangle ap, bq | cr \langle \rangle ap', bq' | cr' \langle$ are Clebsch-Gordon coefficients [100]. For the energy level of a spin $I = 3/2$ nucleus with $m_I = 1/2$, Eq. (3.17) is thus

$$E^{(2)}_{1/2} = \frac{\rangle 1 | H_Q | 2 \langle \rangle 2 | H_Q | 1 \langle}{\omega_0} + \frac{\rangle 4 | H_Q | 2 \langle \rangle 2 | H_Q | 4 \langle}{\omega_0} \, , \tag{3.19}$$

which is equal to

$$E^{(2)}_{1/2} = -\frac{B^+B^-}{\omega_0} + \frac{C^-C^+}{\omega_0} \,. \tag{3.20}$$

Using Eq. (3.18) this can be shown to be equal to

$$E^{(2)}_{1/2} = \frac{(\omega_Q^{PAS})^2}{2\omega_0}\left[-\frac{2}{5} - \frac{8}{7}\,D^2_{0,0}(\alpha,\beta,\gamma) + \frac{54}{35}\,D^4_{0,0}(\alpha,\beta,\gamma)\right], \tag{3.21}$$

which may be expressed more generally as:

$$E^{(2)}_{m_I} = \frac{(\omega_Q^{PAS})^2}{2\omega_0}\Big[A^0(I,q)Q^0(\eta) + B^2(I,q)Q^2(\alpha,\beta,\gamma,\eta) \\ +C^4(I,q)Q^4(\alpha,\beta,\gamma,\eta)\Big], \tag{3.22}$$

and consequently, the second-order perturbation to the frequency of a transition $m_I \leftrightarrow -m_I$ is given by

$$E^{(2)}_{m_I \leftrightarrow -m_I} = \frac{(\omega_Q^{PAS})^2}{\omega_0}\Big[A^0(I,q)Q^0(\eta) \\ +B^2(I,q)Q^2(\alpha,\beta,\gamma,\eta) + C^4(I,q)Q^4(\alpha,\beta,\gamma,\eta)\Big], \tag{3.23}$$

where
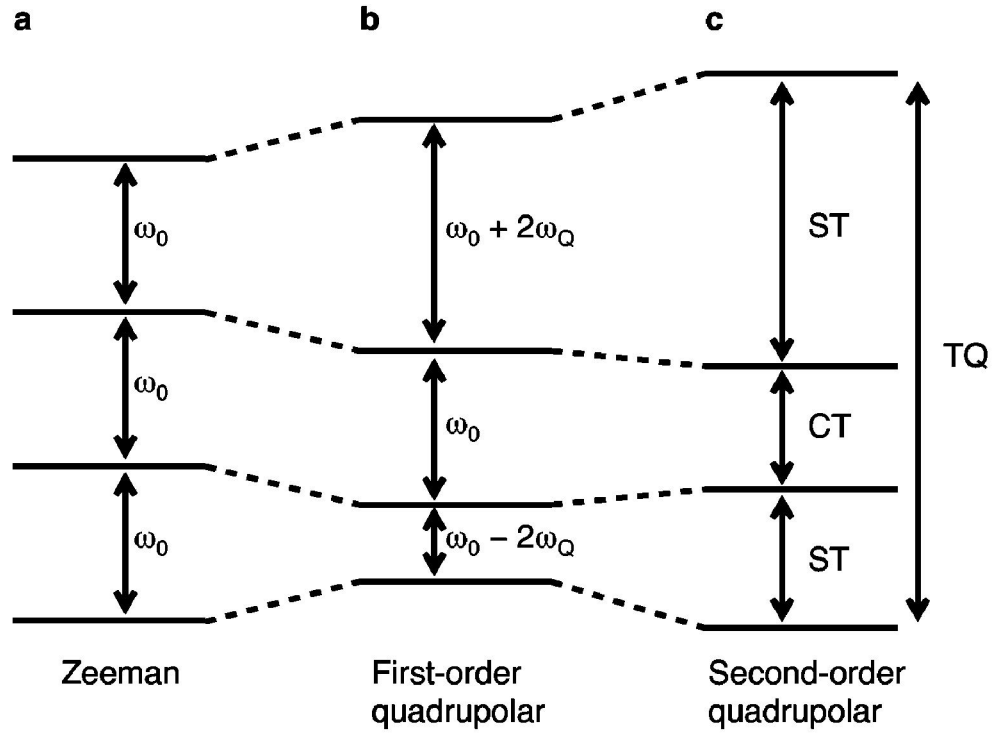
Figure 3.2. The energy levels of a spin $I = 3/2$ nucleus when successively perturbed by the (a) Zeeman, (b) first-order quadrupolar and (c) second-order quadrupolar interactions.

$$Q^0(\eta) = \left(1 + \frac{\eta^2}{3}\right)$$

$$Q^2(\alpha, \beta, \gamma, \eta) = \left(1 - \frac{\eta^2}{3}\right)D_{0,0}^2(\alpha, \beta, \gamma) - \sqrt{\frac{2}{3}}\eta\{D_{0,2}^2(\alpha, \beta, \gamma)$$

$$Q^4(\alpha, \beta, \gamma, \eta) = \left(1 + \frac{\eta^2}{18}\right)D_{0,0}^4(\alpha, \beta, \gamma) + \frac{\sqrt{10}}{6}\eta\{D_{0,2}^4(\alpha, \beta, \gamma)$$

$$+D_{0,-2}^4(\alpha, \beta, \gamma)\} + \frac{35}{18\sqrt{70}}\{D_{0,4}^4(\alpha, \beta, \gamma) + D_{0,-4}^4(\alpha, \beta, \gamma)\}$$

$\qquad\qquad (3.24)$

and $A^0(I, q)$, $B^2(I, q)$ and $C^4(I, q)$ are zeroth-, second- and fourth-rank coefficients that depend on I and m_I. The values of these coefficients for the central and satellite transitions of a spin $I = 3/2$ nucleus are shown in Table 3.1; a complete listing of these coefficients for spin $I = 3/2$ and spin $I = 5/2$ nuclei is given in Appendix E. It should be noted that, as a consequence of Eq. (3.11) and the fact

that all the Wigner rotation matrix elements, $D^l_{p',p}(\alpha, \beta, \gamma)$, in Eq. (3.24) have p' = 0, only the β and γ angles are required to describe the rotation of the PAS of the EFG tensor into the laboratory frame. If the further simplification that the asymmetry parameter η = 0, is made, then only Wigner rotation matrrix elements with p = 0 are needed and so only the angle β is required.

The effect of the quadrupolar interaction on the energy levels of a spin I = 3/2 nucleus is shown in Fig. 3.2. Figure 3.2 shows that the central transition experiences a second-order perturbation (proportional to $(\omega_Q^{PAS})^2/\omega_0$) that is considerably smaller than the first-order interaction (proportional to ω_Q^{PAS}) that affects the satellite transitions.

3.3.3   Effect of Sample Spinning

The expressions derived in Sections 3.3.1 and 3.3.2 that describe the perturbations arising from the first- and second-order quadrupolar interactions are applicable under "static" (non-spinning) conditions. It has been well documented that magic angle spinning (MAS) is able to considerably reduce the anisotropic broadening present in solid-state NMR spectra of quadrupolar nuclei [8–10]. This leads to improved resolution and so facilitates spectral interpretation when there are overlapping powder patterns from inequivalent sites present. In this section, the origin of the line-narrowing effect of MAS is shown. The implications of MAS for the perturbation of the energy levels is described and the way that these effects manifest themselves in second-order

quadrupolar broadened MAS spectra is considered.

In deriving Eq. (3.12), the quadrupolar Hamiltonian in the laboratory frame, transformation of the Hamiltonian between two frames of reference was required. This transformation, from the PAS of the EFG tensor to the laboratory frame, needed just a single set of Euler angles, α, β and γ. Under conditions of sample spinning, the transformation proceeds via an intermediate frame of reference, known as the rotor-fixed frame. In this frame of reference, the z axis is coincident with the sample rotation axis. Two sets of angles are thus required to define the rotation from the PAS of the EFG tensor to the laboratory frame:

$$\text{PAS} \xrightarrow{\text{R}(\alpha', \beta', \gamma')} \text{Rotor} \xrightarrow{\text{R}(0, \chi, -\omega_R t + \xi)} \text{Lab} \; , \quad (3.25)$$

where α', β' and γ' are angles relating the PAS of the EFG tensor to the rotor-fixed frame, and $(-\omega_R t + \xi)$ and χ are the angles describing the rotation of the rotor frame onto the laboratory frame, where χ is the angle between the spinning axis and B_0 and ξ indicates the crystallite orientation relative to the rotor axis at time $t = 0$. ω_R is the spinning frequency (in units of rad s^{-1}), which may also be expressed in units of Hertz as ν_R, where $\nu_R = \omega_R/2\pi$. The transformation from the rotor-fixed frame to the laboratory frame is seen to require only 2 angles, which is due to the same reason as in the case of the static second-order quadrupolar interaction described at the end of the previous section. By splitting the transformation from the PAS to the laboratory frame of reference into two rotations, the Wigner rotation matrix elements given in Eq.

(3.24), $D_{0,r}^c(\alpha, \beta, \gamma)$, are modified to

$$D_{0,r}^c(\alpha, \beta, \gamma) = \sum_{m=-c}^{c} D_{0,m}^c(0, \chi, -\omega_R t + \xi) D_{m,r}^c(\alpha', \beta', \gamma') , \qquad (3.26)$$

where c = 2 or 4. Sample spinning has thus introduced a time dependence that conflicts with the time-independent perturbation theory that was used in the previous sections. However, this theory remains valid if an integer number of rotor periods is assumed. Using Eq. (3.11), the Wigner rotation matrix elements

$D_{0,m}^c(0, \chi, -\omega_R t + \xi)$ may be written as

$$D_{0,m}^c(0, \chi, -\omega_R t + \xi) = d_{0,m}^c(\chi) \exp(im\omega_R t) \exp(-im\xi) . \qquad (3.27)$$

The presence of Wigner rotation matrix elements with p' = 0 means that, as in the case described in the previous section, only two angles are required for the transformation from the rotor-fixed frame to the laboratory frame. Over the course of an integer number of rotor periods, t will vary from 0 to $(2n\pi/\omega_R)$ s, where n is the number of rotor periods, and under such conditions, the integral of the term $\exp(im\omega_R t)$ is only non-zero when m = 0. Consequently, only Wigner rotation matrix elements of the form $D_{0,0}^c(0, \chi, -\omega_R t + \xi)$ and $D_{0,r}^c(\alpha', \beta', \gamma')$ are required and so Eq. (3.26) may be simplified to

$$D_{0,r}^c(\alpha, \beta, \gamma) = d_{0,0}^c(\chi) D_{0,r}^c(\alpha', \beta', \gamma') , \qquad (3.28)$$

and in so doing is made time-independent. Assuming an integer number of rotor periods, Eq. (3.23) thus becomes:

$$E^{(2)}_{m_1 \leftrightarrow -m_1} = \frac{(\omega_Q^{PAS})^2}{\omega_0}\Big[A^0(I, q)Q^0(\eta) + B^2(I, q)d^2_{0,0}(\chi)Q^2(\beta', \gamma', \eta)$$

$$+C^4(I, q)d^4_{0,0}(\chi)Q^4(\beta', \gamma', \eta)\Big] \tag{3.29}$$

where

$$Q^0(\eta) = \left(1 + \frac{\eta^2}{3}\right)$$

$$Q^2(\beta', \gamma', \eta) = \left(1 - \frac{\eta^2}{3}\right)d^2_{0,0}(\beta') - \sqrt{\frac{8}{3}}\eta d^2_{2,0}(\beta')\cos 2\gamma'$$

$$Q^4(\beta', \gamma', \eta) = \left(1 + \frac{\eta^2}{18}\right)d^4_{0,0}(\beta') + \frac{\sqrt{10}}{3}\eta d^4_{2,0}(\beta')\cos 4\gamma' \tag{3.30}$$

$$+ \frac{35}{9\sqrt{70}}\eta^2 d^4_{4,0}(\beta')\cos 4\gamma'$$

Notice that the second- and fourth-rank contributions in Eq. (3.29) are independent of α'. If the assumption of axial symmetry is made, then the angle γ' is no longer required.

The dependence of the reduced rotation elements in Eq. (3.30) on χ is given by

$$d^2_{0,0}(\chi) = \frac{1}{2}\left(3\cos^2\chi - 1\right), \tag{3.31}$$

and

$$d^4_{0,0}(\chi) = \frac{1}{8}\left(35\cos^4\chi - 30\cos^2\chi - 1\right). \tag{3.32}$$

57

These elements equal zero when $\chi = 54.74°$ in Eq. (3.31) and 30.56° or 70.12° in Eq. (3.32). This means that spinning at the magic angle completely removes the second-rank contribution to the anisotropic broadening, but only reduces the fourth-rank contribution. The absence of a common root to the equation

$$\mathrm{d}_{0,0}^{l}(\chi) = 0 \, , \tag{3.33}$$

for the cases of $l = 2$ and $l = 4$ means that spinning about a single angle χ is incapable of removing both second- and fourth-rank anisotropic broadenings.

3.3.4   Second-Order Quadrupolar Broadened Spectra

Inspection of Eq. (3.29) reveals that the second-order perturbation to the frequency of the transitions of a quadrupolar nucleus contains both isotropic and anisotropic components. The zeroth-rank component, $A^0(I, q)Q^0(\eta)$, leads to an isotropic shift in the spectrum, whilst the second- and fourth-rank anisotropic terms, $B^2(I, q)Q^2(\beta', \gamma', \eta)$ and $C^4(I, q)Q^4(\beta', \gamma', \eta)$, are responsible for anisotropic line broadening. Figure 3.3 shows simulated central-transition lineshapes under MAS conditions for a spin $I = 3/2$ nucleus, simulated with $\eta = 0, 0.5$ and 1, respectively. The orientationally dependent second- and fourth-rank terms in Eq. (3.29) lead to the observed broadening and the effect of the zeroth-rank term is evident in the shift of the powder pattern (in this case to lower frequency) from the centre of the spectrum.
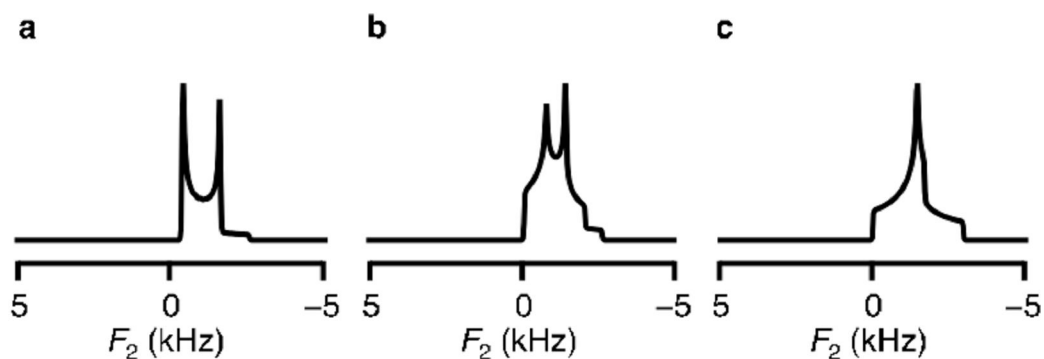
Figure 3.3. Computer-simulated MAS second-order quadrupolar central-transition lineshapes of a spin I = 3/2 nucleus, simulated using η = (a) 0, (b) 0.5 and (c) 1, respectively. The quadrupolar coupling parameter C_Q = 2 MHz, the Larmor frequency is 100 MHz and the spectra were generated by averaging over 5760 values of the angles β' and γ'. The MAS rate is 40 kHz.

3.3.5   Spinning Sidebands

The assumption made in Section 3.3.3 was that sampling over an integer number of rotor periods and spinning at the magic angle leads to complete removal of second-rank anisotropic broadening. This method of data sampling, in which the free induction decay is sampled at the start of every rotor period, ("rotor-synchronization"), is not the usual method of data acquisition in NMR. Consequently, the time dependence of the rotation matrix elements given in Eq. (3.26) needs to be considered. If axial symmetry is assumed, then only the elements with r = 0 are required and so Eq. (3.23) becomes:

$$
E^{(2)}_{m_I \leftrightarrow -m_I} = \frac{(\omega_Q^{PAS})^2}{\omega_0} \Big[A^0(I, q) + B^2(I, q) \sum_{m=-2}^{2} D^2_{0,m}(0, \chi, -\omega_R t + \xi)
$$

$$
D^2_{m,0}(0, \beta', \gamma') + C^4(I, q) \sum_{m=-4}^{4} D^2_{0,m}(0, \chi, -\omega_R t + \xi) \qquad , \quad (3.34)
$$

$$
D^2_{m,0}(0, \beta', \gamma') \Big]
$$

where the following relations have been used for deriving the second- and fourth-rank contributions to Eq. (3.34):

$$D_{0,0}^2(\alpha, \beta, \gamma) = \sum_{m=-2}^{2} D_{0,m}^2(0, \chi, -\omega_R t + \xi)D_{m,0}^2(0, \beta', \gamma')$$

$$D_{0,0}^4(\alpha, \beta, \gamma) = \sum_{m=-4}^{4} D_{0,m}^4(0, \chi, -\omega_R t + \xi)D_{m,0}^4(0, \beta', \gamma') \qquad (3.35)$$

If the Wigner rotation matrix elements are expanded according to Eq. (3.11), the second-rank contribution is thus given by

$$
\begin{aligned}
D_{0,0}^2(\alpha, \beta, \gamma) = {} & d_{0,0}^2(\chi)d_{0,0}^2(\beta') - 2d_{0,1}^2(\chi)d_{0,1}^2(\beta')\big[\cos \omega_R t \cos \xi \\
& + \sin \omega_R t \sin \xi\big] + 2d_{0,2}^2(\chi)d_{0,2}^2(\beta')\big[\cos 2\omega_R t \cos 2\xi \\
& + \sin 2\omega_R t \sin 2\xi\big]
\end{aligned} \qquad (3.36)
$$

whilst the fourth-rank contribution is given by

$$
\begin{aligned}
D_{0,0}^4(\alpha, \beta, \gamma) = {} & d_{0,0}^4(\chi)d_{0,0}^4(\beta') - 2d_{0,1}^4(\chi)d_{0,1}^4(\beta')\big[\cos \omega_R t \cos \xi \\
& + \sin \omega_R t \sin \xi\big] + 2d_{0,2}^4(\chi)d_{0,2}^4(\beta')\big[\cos 2\omega_R t \cos 2\xi \\
& + \sin 2\omega_R t \sin 2\xi\big] - 2d_{0,3}^4(\chi)d_{0,3}^4(\beta')\big[\cos 3\omega_R t \cos 3\xi \\
& + \sin 3\omega_R t \sin 3\xi\big] + 2d_{0,4}^4(\chi)d_{0,4}^4(\beta')\big[\cos 4\omega_R t \cos 4\xi \\
& + \sin 4\omega_R t \sin 4\xi\big]
\end{aligned} \qquad (3.37)
$$

As a consequence of the presence of the Wigner rotation matrix elements with p = 0 (i.e., $D_{m,0}^2(0, \beta', \gamma')$ and $D_{m,0}^4(0, \beta', \gamma')$ in Eq. (3.35)), the angle γ' does not appear in Eq. (3.37).

The implication of Eq. (3.37) is that the static powder pattern, to which the

time-independent term in these equations contributes, is broken up into a series of spinning sidebands [101] that have the same phase [102] and that are separated by the spinning frequency, ω_R. The spinning sidebands are a consequence of the time-dependent terms in Eqs. (3.36) and (3.37). If the sample is spun at a frequency which is small with respect to the width of the static powder pattern (i.e., small with respect to the anisotropy of the quadrupolar interaction) then the spinning sideband manifold closely resembles the envelope of the powder pattern. As the spinning rate is increased, this similarity is lost to the point where, in the case that the spinning frequency greatly exceeds the width of the powder pattern, a centreband is observed at the isotropic frequency [37].

The time-independent terms in Eqs. (3.36) and (3.37) represent the narrowing of the anisotropically-broadened static powder pattern that can be achieved by spinning. As shown in Section 3.3.3, spinning at the magic angle removes second-rank broadening as $d_{0,0}^2(54.7^0) = 0$, whilst the fourth-rank contribution is not removed by MAS as $d_{0,0}^4(54.7^0) \neq 0$. This means that, under MAS conditions, any static powder pattern that arises from an interaction that is solely second-rank in nature will be split into a centreband and series of sidebands whose linewidth has no inhomogeneous contribution. For the case of a second-order quadrupolar interaction, there will thus be a fourth-rank contribution to the linewidth of the centreband and sidebands.

The effect of MAS on the powder patterns of second-order quadrupolar broadened central-transition spectra of half-integer quadrupolar nuclei is

61
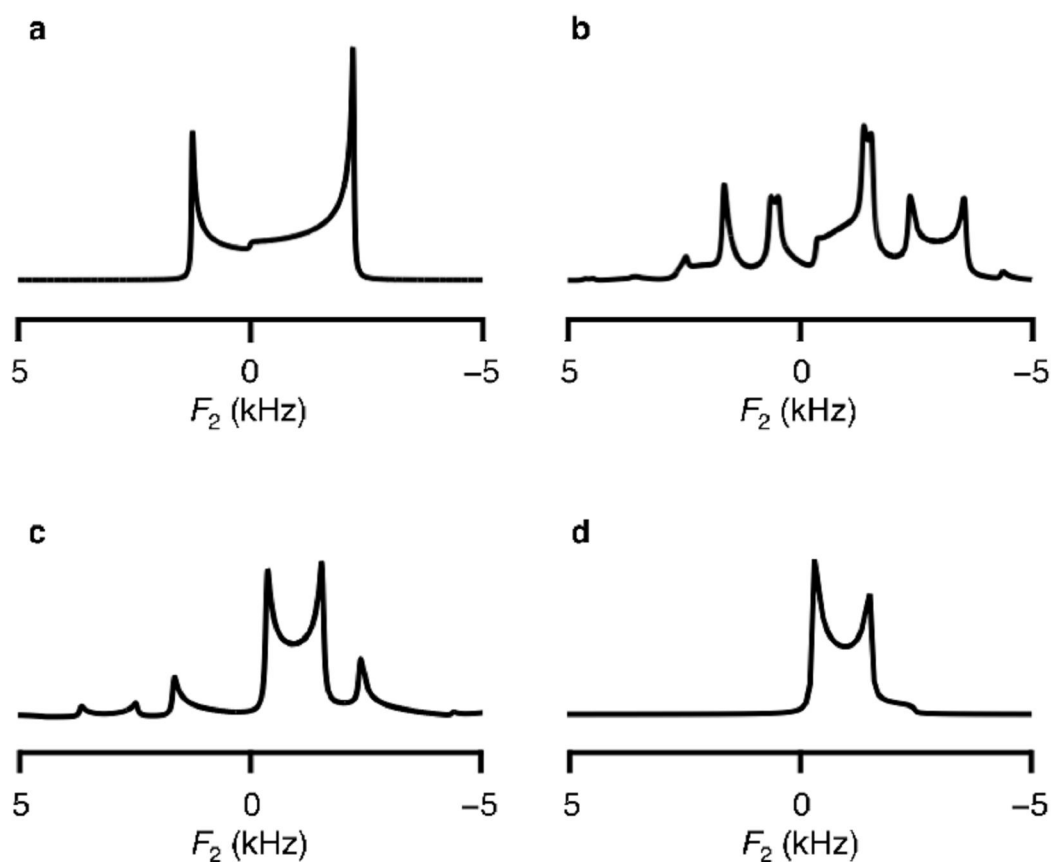
Figure 3.4. Simulated central-transition second-order quadrupolar broadened powder patterns for a spin $I = 3/2$ nucleus, shown for when the spinning frequency is (a) 0, (b) 1 kHz, (c) 2 kHz and (d) 40 kHz. The quadrupolar coupling parameter $C_Q = 2$ MHz, the Larmor frequency is 100 MHz and axial symmetry is assumed. In (a) the spectrum was generated using 500 equally-spaced values of the angle β, whilst in (b)–(d) the spectra were simulated by averaging over 720 values of the angles β' and ξ.

demonstrated in Fig. 3.4, where simulated spectra of a spin $I = 3/2$ nucleus are shown. The spectra show how, at low spinning frequencies, the sideband envelope remains similar to the static powder pattern. However, as the spinning rate increases, these sidebands are spaced further apart and progressively lose intensity until, at a spinning speed much greater than the width of the static powder pattern, a centreband containing fourth-rankanisotropic broadening remains. Note that the centreband is not always the most intense peak. It should also be noted that the spectra in Figs. 3.4b–3.4d are

not normalised relative to each other so as to enable the structure of the spinning sidebands to be clearly seen; the integrated areas of these spectra are, of course, identical and independent of the spinning frequency.

3.4   High-Resolution Methods

3.4.1   Introduction

It was shown in the previous section that MAS removes line broadening arising from interactions which have solely second-rank contributions and in so doing improves considerably the resolution of solid-state NMR spectra. Interactions such as CSA, dipolar coupling and the first-order quadrupolar interaction are described in terms of second-rank components alone and so MAS is able to split the static powder patterns into a manifold of narrow spinning sidebands. The failure of MAS to have the same effect on interactions containing a fourth-rank contribution is arguably its greatest limitation and the methods developed to overcome this are introduced in the next section.

3.4.2   Double Rotation and Dynamic Angle Spinning

The inability of MAS to completely remove broadening due to the fourth-rank component of the second-order quadrupolar interaction means that, in cases where there is an overlap of the powder patterns of inequivalent sites, unambiguous spectral assignment becomes very difficult. Several methods

have been proposed to remove completely the residual effects of the quadrupolar interaction, amongst them double rotation (DOR) [41, 42] and dynamic angle spinning (DAS) [43–45]. As mentioned in Section 3.3.3, no single angle can simultaneously remove the second- and fourth-rank contributions to the quadrupolar broadening. For this to be achieved, the following condition needs to be satisfied:

$$d_{0,0}^2(\chi) = d_{0,0}^4(\chi) = 0 \ . \tag{3.38}$$

DOR and DAS satisfy this condition by spinning about two angles.

In DAS, a two-dimensional experiment is performed in which the sample is spun sequentially about two angles during the two time periods, t_1 and t_2. The rotor angle is switched between these two periods, during which time the magnetization is stored as a population state. In this experiment, the angles χ_1 and χ_2 need to be chosen such that the following equations are fulfilled:

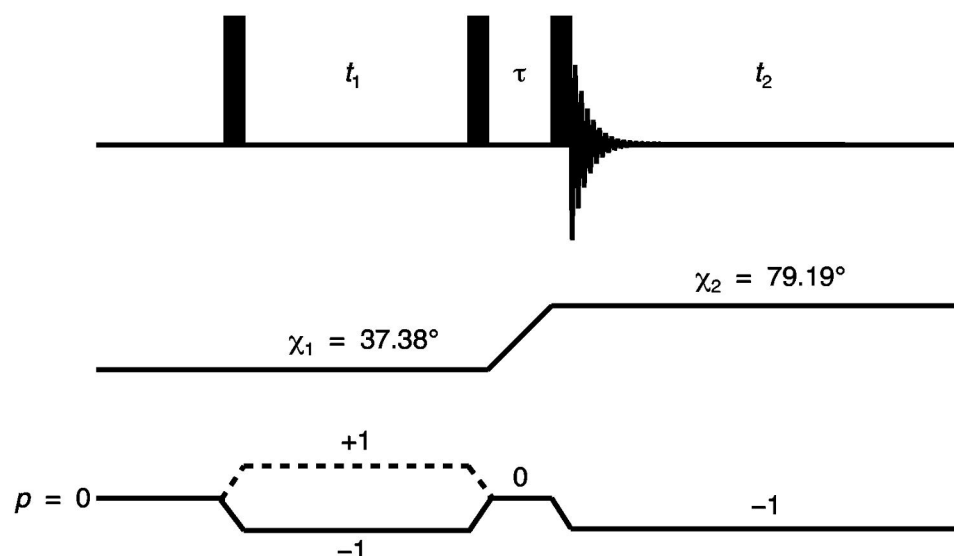$$a\,d_{0,0}^2(\chi_1) + b\,d_{0,0}^2(\chi_2) = 0 \ , \tag{3.39}$$

$$a\,d_{0,0}^4(\chi_1) + b\,d_{0,0}^4(\chi_2) = 0 \ , \tag{3.40}$$

and

$$a + b = 1 \ . \tag{3.41}$$

There are many solutions to Eqs. (3.39–3.40), but the most commonly used sets

Figure 3.5. Pulse sequence for dynamic angle spinning. The acquisition of both $p = +1$ and $p = -1$ pathways during t_1 ensures purely absorptive lineshapes are obtained.

of angles are $\chi_1 = 37.38°$ and $\chi_2 = 79.19°$, with a = b = 0.5.

The inhomogeneous broadening is refocussed at a time $t_2 = (a/b)t_1$ and this yields a two-dimensional spectrum possessing anisotropically broadened lineshapes that have a gradient of a/b. An "isotropic" spectrum that is free of inhomogeneous quadrupolar broadening may then be obtained by a projection onto an axis orthogonal to the ridge; this may be accomplished using a shearing transformation. The pulse sequence for DAS is shown in Fig. 3.5. There have been several variants of this sequence devised, with one removing the need for a shearing transformation. This modification, which also involves a second angle hop to 54.74°, has the consequence that the quadrupolar interaction is refocussed at $t_2 = 0$ for all values of t_1. The resultant spectrum thus contains ridges that are not only parallel to the ω_2 axis, but that are free of broadenings due to CSA and dipolar couplings.

DAS has two major limitations. One is that the periods in which the
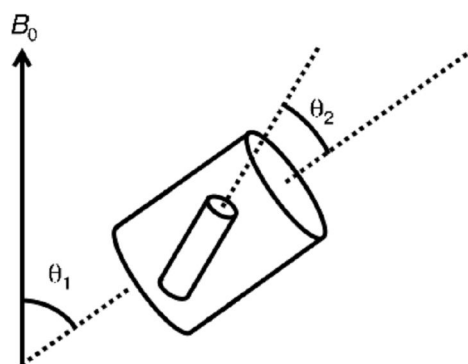
Figure 3.6. The arrangement of rotors that forms the basis of the double rotation experiment. In this experiment, $\theta_1 = 54.74°$ and $\theta_2 = 30.56°$.

magnetization is stored as a population state require long T_1 relaxation times, so making it unsuitable for the many cases in which the T_1 relaxation of a quadrupolar nucleus is very efficient. This has a particularly large effect when a second angle hop is required for acquisition under MAS conditions. The other drawback of DAS is that specialist hardware is required for its implementation, a fact which has limited the applicability of the technique. Nevertheless, several examples of its utility in ^{11}B [103] and ^{17}O [104–109] NMR have been reported.

In DOR, refocussing of the quadrupolar interaction is achieved by spinning simultaneously about two angles. This is usually achieved by spinning the sample in an inner rotor that is itself inside an outer rotor. The outer rotor is inclined at the magic angle whilst the inner rotor is inclined at an angle of 30.56° to the outer rotor axis. This is shown in Fig. 3.6.

In contrast to DAS, DOR is a one-dimensional experiment. The technique has major limitations, however. The most significant one arises from the fact that the outer rotor can usually only be spun at speeds of 1–2 kHz and so the resultant spectrum is crowded with spinning sidebands that can greatly hinder

interpretation. In addition, DOR requires a specialist probe which, as in the case of DAS, is prone to mechanical problems. In spite of this, DOR has been successfully applied in [17]O [110–115], [23]Na [116–123] and ^{27}Al [124–127] NMR.

3.4.3 Multiple-Quantum MAS

3.4.3.1 Introduction

A method was developed in 1995 that achieves complete refocusing of the second-order quadrupolar interaction [48, 49], and which, unlike DOR and DAS, may be performed using conventional MAS hardware. This experiment, known as MQMAS, operates by taking advantage of the fact that the fourth-rank coefficients of the second-order quadrupolar interaction perturbing the central and multiple-quantum (usually $m_I = +3/2 \leftrightarrow -3/2$) transitions of a half-integer quadrupolar nucleus differ by a scaling factor. Consequently, a two-dimensional experiment correlating single-quantum central-transition coherences and multiple-quantum (MQ) coherences, performed under MAS conditions, will lead to complete removal of the effects of the quadrupolar interaction to second order. This is achieved by an experiment in which MQ coherences are excited and then allowed to evolve in the t_1 period before subsequent conversion to observable central-transition coherences that evolve during the t_2 period. The resultant two-dimensional spectrum contains, after shearing, a second-order quadrupolar broadened central-transition powder lineshape parallel to the ω_2 axis and an isotropic spectrum devoid of

quadrupolar broadening parallel to the ω_1 axis (although fourth-rank broadenings that are not quadrupolar in origin remain in ω_1) [128, 129].

3.4.3.2 Non Pure-phase Methods

The original MQMAS experiment involved excitation of either $p = -3$ or $p = +3$ coherences that evolve during the t_1 period before their subsequent conversion to observable central-transition coherence ($p = -1$) [49]. The pulse sequence for this experiment is shown in Fig. 3.7, where the two coherence transfer pathways that may be selected are indicated. In this experiment, single-pulse excitation has been shown to be better than the two-pulse method [49, 130, 131] used in solution-state NMR [84].

The time-domain signal acquired by the experiment in Fig. 3.7, when performed on a spin $I = 3/2$ nucleus, neglecting chemical shift effects, and using the solid coherence transfer pathway, is given by:

$$s(t_1, t_2) = \exp\left\{ i\, \frac{\left(\omega_Q^{PAS}\right)^2}{\omega_0} \left(\frac{6}{5}\, Q^0(\eta) - \frac{6}{5}\, d_{0,0}^4(\chi) Q^4(\beta', \gamma', \eta) \right) t_1 \right\} \times$$

$$\exp\left\{ i\, \frac{\left(\omega_Q^{PAS}\right)^2}{\omega_0} \left(-\frac{2}{5}\, Q^0(\eta) + \frac{54}{35}\, d_{0,0}^4(\chi) Q^4(\beta', \gamma', \eta) \right) t_2 \right\} \quad \text{(3.42)}$$

Equation (3.42) thus shows that the fourth-rank contribution to the second-order quadrupolar broadening is refocussed with the formation of an echo when
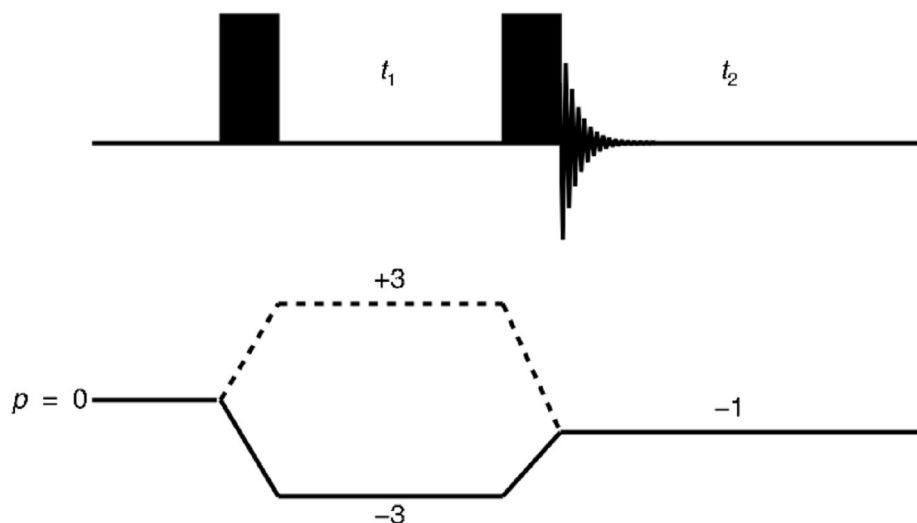
Figure 3.7. Pulse sequence and corresponding coherence transfer pathways for the two-pulse triple-quantum MAS experiment. The $+3 \rightarrow -1$ and $-3 \rightarrow -1$ pathways correspond to the antiecho and echo pathways for a spin $I = 3/2$ nucleus, respectively.

$$\left(-\frac{6}{5}t_1 + \frac{54}{35}t_2\right) = 0 \ , \tag{3.43}$$

i.e., when $t_2 = (6/5)(35/54)t_1 = (7/9)t_1$. The position in t_2 at which the echo forms thus depends on the ratio of the fourth-rank coefficients defined in Eq. (3.22), this is referred to as the MQMAS ratio, $R(I, q)$, and is defined as:

$$R(I, q) = \frac{C^4(I, q)}{C^4(I, 1/2)} \ , \tag{3.44}$$

where q is the coherence order of the transition evolving during the t_1 period and so takes the value $\pm 3/2$ for a triple-quantum MAS experiment.

When $t_1 = 0$, the quadrupolar interaction is refocussed as a half-echo, i.e., its signal decreases from its maximum to zero. As t_1 increases, the echo moves progressively forward in t_2 until, at a sufficient value of t_1, a whole echo is

formed. The $-3 \rightarrow -1$ pathway is, for a spin $I = 3/2$ nucleus, referred to as the echo pathway because the echo formed by the refocussing of the residual second-order quadrupolar interaction moves forward in t_2 as t_1 increases. Conversely, the $+3 \rightarrow -1$ pathway is known as the antiecho pathway, in which case the echo moves backwards in t_2 as t_1 increases. For a spin $I = 5/2$ nucleus, the situation is reversed. More generally, if the MQMAS ratio is negative, then the $-3 \rightarrow -1$ coherence transfer pathway is the echo pathway, whilst if it is positive, then the $+3 \rightarrow -1$ pathway is the echo pathway. The MQMAS ratios for triple-quantum MAS experiments of spin $I = 3/2$, $5/2$ and $7/2$ nuclei are given in Appendix F.

Two-dimensional Fourier transformation of the data in Eq. (3.42) yields a two-dimensional spectrum containing an anisotropically broadened ridge lineshape inclined at a gradient of $-7/9$ with respect to the ω_2 axis. The spectrum obtained by Fourier transformation of the signal arising from the $+3 \rightarrow -1$ (antiecho) pathway contains a ridge lineshape inclined at a gradient of $7/9$. In each case, an isotropic spectrum may then be obtained by projection onto an axis orthogonal to this ridge, in a manner exactly analogous to DAS that was described earlier.

Inspection of Eq. (3.42) shows that the signal yielded from these two-pulse MQMAS methods is phase modulated and hence, the resultant two-dimensional spectrum contains lineshapes that are not pure-phase (i.e., they contain the highly undesirable phase-twist). Consequently, these experiments are not suitable for modern NMR spectroscopy and are no longer routinely

used.

3.4.3.3 Pure-phase Methods

It has been observed that for a spin $I = 3/2$ nucleus, the $-3 \rightarrow -1$ and $+3 \rightarrow -1$ conversions are equally efficient when a hard pulse with an inherent flip angle of $\beta = 90°$ is used [132]. By performing a two-dimensional experiment in which the $-3 \rightarrow -1$ and $+3 \rightarrow -1$ coherence transfer pathways are simultaneously selected such that $p = -3$ and $p = +3$ coherences evolve during the t_1 period, a spectrum containing absorption-mode lineshapes may be obtained [132]. There is, however, no pulse flip angle which can perform these coherence transfer processes with equal efficiency for nuclei with spin $I > 3/2$ and consequently, such an experiment has not been widely used.

A modification of the experiment described above that can lead to absorption-mode two-dimensional lineshapes for all values of I was suggested in 1996. This experiment also involves simultaneous evolution of $p = +3$ and $p = -3$ coherences during the t_1 period, but their conversion to observable central-transition coherences is achieved using two pulses that proceed via a population state ($p = 0$). This method, known as a z-filter [133–135], achieves the acquisition of purely absorption-mode lineshapes by utilising the fact that the $+3 \rightarrow 0$ and $-3 \rightarrow 0$ conversions are always equally efficient. The pulse sequence and coherence transfer pathway is shown in Fig. 3.8a, where the last pulse is a 90° pulse selective for the central transition. The acquisition of both p
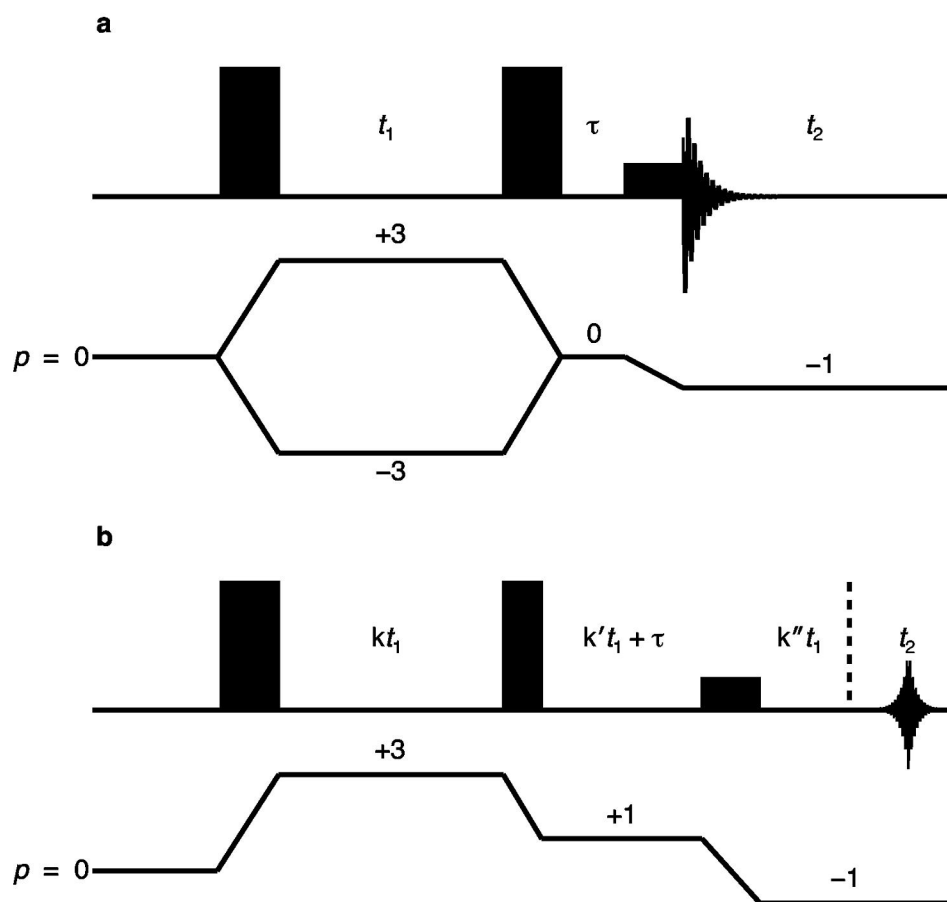
Figure 3.8. Pulse sequence and coherence transfer pathways for the (a) z-filter and (b) split-t_1 whole-echo triple-quantum MAS experiments. The τ interval in (a) is of short duration (typically 3 μs).

$= +3$ and $p = -3$ coherences during t_1 leads to an increase in signal intensity with respect to the original experiment of Frydman and Harwood, and this signal intensity is maximised by reducing the radiofrequency field strength of the final pulse.

Another route to obtaining purely absorptive two-dimensional lineshapes in MQMAS spectra was devised that involves the appendage of a spin-echo unit, consisting of an inversion pulse that is selective for the central transition. In the resultant experiment, known as a "shifted-echo" or "whole-echo" experiment [136–138], when the echo pathway is selected, the echo is shifted

forward in t_2 by a time τ, where τ is the echo interval. This means that, assuming a sufficiently long value of τ is chosen, the residual second-order quadrupolar interaction is refocussed as a whole echo for every value of t_1. In addition, the echo is no longer formed at $t_2 < 0$ for the antiecho pathway.

The fact that a choice of echo interval can be made such that the quadrupolar interaction is refocussed as a whole echo for all values of t_1 means that this experiment yields a spectrum containing purely absorptive two-dimensional lineshapes. This occurs as a result of the properties of whole echoes. Whole echoes contain real and imaginary components that are symmetric and anti-symmetric about the midpoint, respectively. The Fourier transform of such a time-domain signal yields a lineshape in which the real part is purely absorptive and the imaginary part is zero. It is for this reason that such a modification to the experiment has become routine as a way of obtaining pure-phase two-dimensional lineshapes in MQMAS. It should be noted that the symmetry properties of a whole echo only hold in cases where the inhomogeneous broadening exceeds the homogeneous broadening [136]. This is typically the case for crystalline materials but in amorphous or disordered materials this is often not observed and, in such cases, whole-echo methods are not the optimum choice.

It was shown in Section 3.4.3.2 that the residual fourth-rank quadrupolar broadening is refocussed, when the echo pathway is selected, when $t_2 = -(C^4(I, 3/2)/C^4(I, 1/2))t_1$, so leading to a spectrum with an anisotropically broadened ridge aligned along a gradient equal to the MQMAS ratio. To obtain an

isotropic spectrum it is necessary to perform a shearing transformation; this produces a spectrum in which the ridge is parallel to the ω_2 axis and an isotropic spectrum is then obtained directly from a projection onto the ω_1 axis [139]. However, a further modification to the MQMAS experiment has been devised which directly produces a spectrum in which the quadrupolar broadened ridge is parallel to the ω_2 axis, so avoiding the need for a shearing transformation. This is achieved by performing a shifted-echo experiment in which the t_1 period is split into periods of multiple-quantum and central-transition evolution [134, 137, 138]. In such an experiment, the inhomogeneous broadening is refocussed at the end of the t_1 period and a whole echo formed at $t_2 = \tau$ for all values of t_1. To illustrate this, consider the example of a spin $I = 3/2$ nucleus. The MQMAS ratio in this case has the value $-7/9$; that is, the fourth-rank contribution to the inhomogeneous broadening from the triple-quantum transition is $-7/9$ of that arising from the central transition. Consequently, if the t_1 period is split into periods of triple-quantum and central-transition evolution in the ratio 9:7, the fourth-rank contribution to the second-order quadrupolar interaction will be refocussed at the end of t_1 for all values of t_1.

The division of the t_1 period into periods of triple-quantum and central-transition evolution is the basis of so-called "split-t_1" acquisition in MQMAS experiments. The pulse sequence for these experiments is shown in Fig. 3.8b. Split-t_1 acquisition is usually combined with the shifted-echo method so as to produce an experiment that yields both ridge lineshapes parallel to the F_2 axis and pure-phase two-dimensional lineshapes. The experiment shown in Fig. 3.8b

is thus referred to as a split-t_1 whole-echo MQMAS experiment and is applicable to all the multiple-quantum transitions of every half-integer quadrupolar nucleus. The values of the constants k, k′ and k′′ in Fig. 3.8b are given, for spin I = 3/2, 5/2 and 7/2 nuclei, in Appendix G. For nuclei possessing triple-quantum transitions with a positive MQMAS ratio, the period of central-transition evolution during t_1 has p = −1 (i.e., k′ = 0), as in such cases, a correlation between triple-quantum and single-quantum transitions of opposite sign is required for refocussing of the fourth-rank inhomogeneous broadening to occur at t_2 > 0.

The MQMAS experiment is now a routine method for obtaining high-resolution NMR spectra of quadrupolar nuclei and there have been numerous examples demonstrating its applicability to nuclei with a range of spin quantum numbers, such as [11]B [140–145], [17]O [146–161], [23]Na [162–173], [25]Mg [174, 175], [27]Al [176–194], [43]Ca [195–198], [45]Sc [199, 200], [51]V [201, 202], [55]Mn [203], [59]Co [204, 205], [63]Cu [206], [87]Rb [136, 207, 208] and [93]Nb [209–214].

3.4.4   Satellite-Transition MAS

Another method that facilitates the acquisition of isotropic spectra of quadrupolar nuclei is the STMAS experiment, introduced in 2000 [50]. This experiment operates in an analogous manner to MQMAS, but instead uses a correlation of satellite-transition coherences with central-transition coherences to achieve refocussing of the residual fourth-rank quadrupolar broadening. The
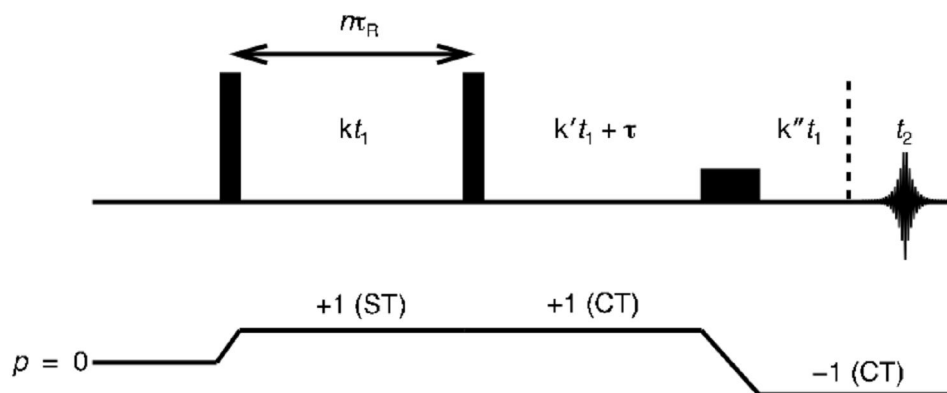
Figure 3.9. Pulse sequence and coherence transfer pathway for the phase-modulated whole-echo STMAS experiment. Split-t_1 acquisition is used and the constants k, k′ and k″ are given in Appendix G.

acquisition of whole echoes is typically used to ensure the acquisition of absorption-mode two-dimensional lineshapes. The resultant two-dimensional spectrum, if obtained using split-t_1 acquisition, consists of an ST $\rightarrow$ CTcorrelation ridge for each inequivalent site in the solid, each of which is broadened by the residual second-order quadrupolar interaction parallel to the ω_2 axis and that is free from quadrupolar broadening parallel to the ω_1 axis.

In Section 3.3.3 it was shown that rotor-synchronized MAS removes the effects of any second-rank interaction, such as the first-order quadrupolar interaction. Consequently, as the satellite transitions in a quadrupolar nucleus are subject to a large first-order quadrupolar perturbation, very accurate rotor-synchronization is required during the t_1 period. To fully remove the effects of the first-order quadrupolar interaction, the magic angle must also be set very precisely (within $\pm 0.003°$) [53].

STMAS spectra are typically acquired using the phase-modulated split-t_1 whole-echo pulse sequence in Fig. 3.9. This experiment yields a two-

dimensional spectrum containing pure-phase two-dimensional lineshapes that are anisotropically broadened along an axis parallel to the ω_2 axis in an analogous manner to the MQMAS experiment shown in Fig. 3.8b. STMAS spectra also feature an additional peak not observed in their MQMAS analogues which arises from CT → CT transfer. This peak is aligned along a gradient of +1 and is an inevitable consequence of an experiment involving excitation of solely single-quantum coherences and it cannot be removed by phase cycling alone. This peak may overlap with ST → CT correlation peaks of sites with small quadrupolar interactions and so hinder spectral interpretation.

It has been shown that STMAS can offer significant sensitivity advantages over MQMAS [53] and the technique has been widely used for a variety of quadrupolar nuclei such as ^{11}B [53], ^{17}O [53], ^{23}Na [50, 51, 53, 215], ^{27}Al [52, 53, 216, 217], ^{45}Sc [52, 53], ^{59}Co [52, 53, 218], ^{87}Rb [52, 53, 215] and ^{93}Nb [52]. This gain in sensitivity has been shown to hold also for low-γ nuclei (for which the achievable radiofrequency field strengths are much less) and has been demonstrated in the acquisition of STMAS spectra of ^{25}Mg (spin I = 5/2) and ^{39}K (spin I = 3/2) at natural abundance [54]. The ability of STMAS to yield high-resolution NMR spectra of low-γ quadrupolar nuclei has been demonstrated extensively for ^{17}O in a wide range of minerals [53, 55, 190, 194, 219, 220].
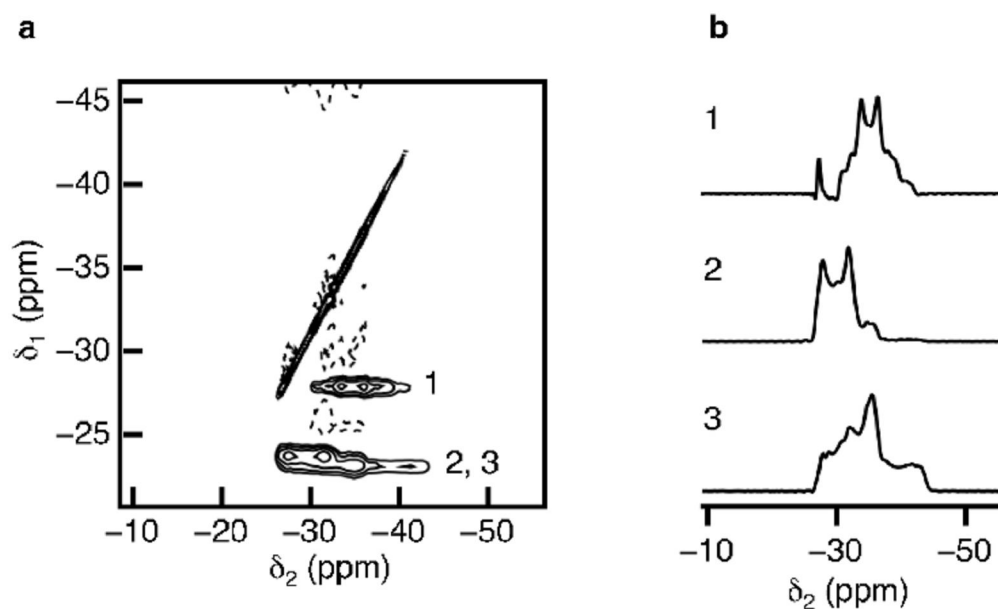
Figure 3.10. (a) Two-dimensional ^{87}Rb STMAS NMR spectrum of rubidium nitrate recorded at B_0 = 9.4 T and a MAS rate of 10 kHz. (b) Cross-sections taken parallel to the δ_2 axis of the spectrum in (a) for each of the three ^{87}Rb sites. Contours are shown at 8, 16, 32 and 64% of the maximum intensity.

3.4.5   Appearance of MQMAS and STMAS Spectra

Both MQMAS and STMAS yield two-dimensional spectra that contain considerable information. By projecting the two-dimensional spectra onto an axis orthogonal to the ridge lineshapes, isotropic spectra that are free of inhomogeneous quadrupolar broadening may be obtained. These isotropic spectra enable the number of crystallographically inequivalent sites in a solid to be determined. Using these spectra to obtain information on the relative populations of these sites should be done with caution however — the non-uniform excitation and conversion of multiple-quantum coherences (in MQMAS) [56] and of satellite-transition coherences (in STMAS) [52], means that

78

these techniques are not quantitative. This is discussed in greater detail in Chapter 4. A typical spectrum of a crystalline material obtained using these methods is presented in Fig. 3.10, where the [87]Rb STMAS NMR spectrum of rubidium nitrate, RbNO$_3$, is shown. The two-dimensional spectrum in Fig. 3.10a shows the expected ST $\rightarrow$ CT ridges for each of the three sites [221] present, along with the superfluous CT $\rightarrow$ CT correlation ridge. Cross-sections taken parallel to the δ_2 axis for each of the three sites yield second-order quadrupolar broadened lineshapes whose width, shape and position in the two-dimensional spectrum are dependent on the values of C_Q and η of each of the sites in this material [136].

MQMAS and STMAS have the great advantage over one-dimensional high-resolution methods such as DOR that the resultant spectra possess two dimensions in which quadrupolar information is retained [136]. Quadrupolar parameters may be extracted from MQMAS and STMAS spectra by analysis of the position of the centre of gravity of each ridge lineshape in the ω_1 and ω_2 dimensions. These positions depend on the isotropic chemical shift, δ_{CS}, and δ_Q, the isotropic second-order quadrupolar shift, which is given by

$$\delta_Q \;=\; \frac{\left(\omega_Q^{PAS}\right)^2}{\omega_0}\left(1 + \frac{\eta^2}{3}\right),\qquad (3.45)$$

expressed as a ppm shift. It can be shown that for a spin $I \;=\; 3/2$ nucleus the peak positions in the ω_1 and ω_2 dimensions of a sheared or split-t_1 triple-quantum MAS spectrum are given by:

$$\delta_1 = \frac{17}{8}\delta_{CS} + \frac{1}{2}\delta_Q \ , \tag{3.46}$$

and

$$\delta_2 = \delta_{CS} - \frac{2}{5}\delta_Q \ , \tag{3.47}$$

and by rearranging:

$$\delta_{CS} = \frac{8\delta_1 + 10\delta_2}{27} \ , \tag{3.48}$$

and

$$\delta_Q = \frac{216\delta_1 - 459\delta_2}{160} \ . \tag{3.49}$$

The expressions in Eqs. (3.46) and (3.47) are different for spectra obtained by non-split-t_1 methods or for those that have not been subject to a shearing transformation and these are shown, for both MQMAS and STMAS experiments of spin $I = 3/2$ and $I = 5/2$ nuclei, in Appendix H. If the peak positions in the two dimensions are known, then the quadrupolar parameters δ_{CS} and δ_Q may be determined. It is not possible to obtain C_Q and η independently from δ_Q, however, the quadrupolar product P_Q, defined as [107]:

$$P_Q = C_Q \sqrt{\left(1 + \frac{\eta^2}{3}\right)} \ , \tag{3.50}$$

may be determined from δ_Q by

$$P_Q = \frac{2I(2I - 1)\omega_0 \sqrt{\delta_Q}}{3\pi \times 10^3} \, .$$

(3.51)

3.4.5.1   Spectra of Amorphous Materials

In unsheared MQMAS and STMAS spectra, or spectra acquired from non-split-t_1 methods, the anisotropically broadened ridge lineshapes lie along an axis given by the MQMAS or STMAS ratio, typically known as the anisotropic (A) axis. In amorphous and disordered materials, the lineshapes may be broadened along additional axes due to a distribution of isotropic chemical shifts and second-order quadrupolar shifts [222]. Where there is a distribution of isotropic chemical shifts, the ridges are broadened along an axis that has a gradient of +1 in the case of STMAS and +3 for triple-quantum MAS. This axis is usually referred to as the chemical shift (CS) axis. If there is also a range of second-order quadrupolar broadenings, then the lineshape will also be broadened along an axis with a gradient given by the ratio

$$\frac{A^0(I, q)}{A^0(I, 1/2)} \, ,$$

(3.52)

where $A^0(I, q)$ and $A^0(I, 1/2)$ are the spin- and transition-dependent zeroth-rank coefficients introduced in Section 3.3.2. This axis is known as the quadrupolar shift (QS) axis.

The ability of MQMAS and STMAS to identify distributions of isotropic chemical shifts and isotropic second-order quadrupolar shifts demonstrates the great utility of these techniques when considering the structure of amorphous materials.

Chapter 4

Coherence Transfer Enhancement

4.1   Selective and Non-Selective Pulses

An important parameter in NMR is the inherent nutation frequency, ω_1, related to the radiofrequency field strength, B_1, by $\omega_1 = -\gamma B_1$. When an NMR experiment is performed, it is desirable to have a nutation frequency much greater than the range of resonance frequencies being studied. Under such conditions the effective field, B_{eff}, experienced by all the spins whose frequencies are in the range being studied, is virtually constant. Using the vector model description of NMR described in Section 2.2, this means that the magnetization vectors of all the spins are rotated through the same flip angle by the pulse. A pulse that has this effect is known as a "hard" or non-selective pulse. In the context of quadrupolar nuclei, a hard pulse is one for which the following condition is satisfied:

$$\omega_1 \gg \omega_Q . \tag{4.1}$$

For half-integer quadrupolar nuclei in the solid state, however, this is rarely the case. In a powdered sample, ω_Q takes values ranging from zero to ω_Q^{PAS}. Consequently, Eq. (4.1) is not satisfied for the majority of the crystallites, even with the highest radiofrequency field strengths currently attainable (typically

300 kHz), and so the following condition now applies:

$$\omega_1 \ll \omega_Q,$$

in which case the pulse is referred to as "soft" or selective and only the central transition is excited. For the majority of crystallites, the ratio ω_Q/ω_1 is thus much greater than unity. In this section, the effect of the range of values of ω_Q/ω_1 on single-pulse single-quantum coherence excitation is shown, whilst in the subsequent sections the coherence transfer processes present in MQMAS is considered.

To consider the effect of pulses in the hard and soft regimes, the evolution of the density operator needs to be determined. The Liouville-von Neumann equation, introduced in Chapter 2, describes the evolution of the density operator. For a hard pulse along the rotating frame x axis, the Hamiltonian is given by $\omega_1 I_x$, and so for an initial density operator at thermal equilibrium this equation takes the form

$$\frac{d\rho(t)}{dt} = -i\left[\omega_1 I_x, I_z\right]$$
$$= -\omega_1 I_y$$

(4.3)

This equation describes the nutation of the magnetization from the z axis to the $-y$ axis at a rate ω_1.

When a soft pulse is applied to a half-integer quadrupolar nucleus, only the central transition is excited. In such a situation, only two energy levels need

84

to be considered (those with $m_I = +1/2$ and $m_I = -1/2$) and so half-integer quadrupolar nuclei may be treated like spin $I = 1/2$ nuclei. In such cases, a convenient method for determining the effect of a soft pulse is the fictitious spin-1/2 operator formalism [223–226], which was introduced in 1977 for a spin $I = 1$ nucleus [224]. In this formalism, the matrix representations of the operators $I_x^{(1/2,-1/2)}$ and $I_y^{(1/2,-1/2)}$ are given by, for a spin $I = 3/2$ nucleus:

$$I_x^{(1/2,-1/2)} = \frac{1}{2}\begin{pmatrix} 0 & 0 & 0 & 0 \\ 0 & 0 & 1 & 0 \\ 0 & 1 & 0 & 0 \\ 0 & 0 & 0 & 0 \end{pmatrix}$$

$$I_y^{(1/2,-1/2)} = \frac{1}{2}\begin{pmatrix} 0 & 0 & 0 & 0 \\ 0 & 0 & -i & 0 \\ 0 & i & 0 & 0 \\ 0 & 0 & 0 & 0 \end{pmatrix}$$

. $\qquad$ (4.4)

The central 2×2 elements of these matrices are of course identical to the matrix representations of the angular momentum operators for a spin $I = 1/2$ nucleus given in Appendix A. Using these operators, the evolution of the density operator can be shown to be, for a nucleus with spin quantum number I:

$$\begin{aligned}\frac{d\rho(t)}{dt} &= -i\left[\left(I + \frac{1}{2}\right)\omega_1 I_x^{(1/2,-1/2)}, I_z\right] \\ &= -\left(I + \frac{1}{2}\right)\omega_1 I_y^{(1/2,-1/2)}\end{aligned}$$

. $\qquad$ (4.5)

A comparison of Eqs. (4.3) and (4.5) reveals that the nutation frequency is $(I +$
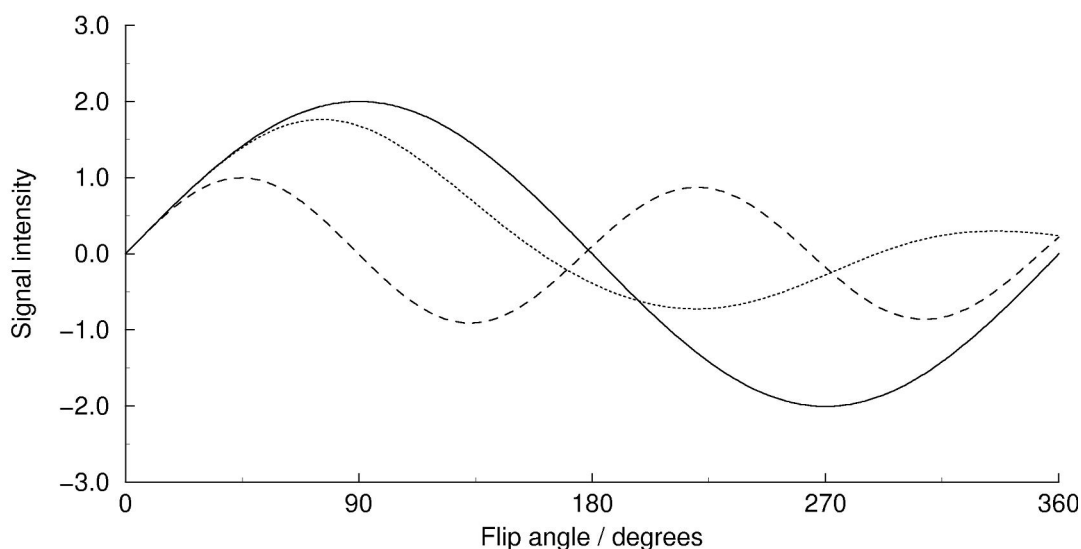
Figure 4.1. The dependence of signal intensity on the flip angle of an on-resonance excitation pulse for a spin I = 3/2 nucleus, shown for when ω_Q/ω_1 is equal to 0 (solid line), 1 (dotted line) and 25 (dashed line). Simulations were performed assuming the sample to be static and assuming the presence of a second-order quadrupolar interaction with η = 0. The simulations were performed by assuming 90 equally-spaced values of the angle β. The vertical scale is normalised with respect to the maximum single-quantum coherence obtained with a soft pulse.

1/2) times greater for a selective pulse compared to a non-selective one.

This variation in nutation frequency is demonstrated in Fig. 4.1 for a spin I = 3/2 nucleus, where the dependence of the central-transition signal intensity is shown as a function of the excitation pulse flip angle for ratios of ω_Q/ω_1 equal to 0, 1 and 25. The increase in nutation frequency for a soft pulse means that it leads to a maximum in signal intensity at a flip angle (for a spin I = 3/2 nucleus) of 45°, half the 90° observed in the hard pulse case. In addition, this also means that there is a null in signal intensity observed for a soft pulse at a flip angle of 90°, half the 180° observed for a hard pulse. The increase in nutation frequency shown in Fig. 4.1 also leads to an (I + 1/2) factor reduction in the signal intensity obtained when a pulse selective for the central transition is

used compared with a hard pulse.

4.2   Excitation of Multiple-Quantum Coherence

The excitation of multiple-quantum coherence [227, 228] plays an important role in a wide range of NMR experiments. Even though only single-quantum coherence may be directly detected in NMR, excitation of multiple-quantum coherence of spin I = 1/2 nuclei in liquids is found in a variety of experiments such as DQF-COSY [229, 230], HMQC [231] and INADEQUATE [232]. The use of double- and triple-quantum filtration methods as a means of measuring the relaxation rates of spin I = 3/2 nuclei in liquids and of differentiating between nuclear environments has also been shown [233, 234]. In the solid state, it was shown in 1981 that triple-quantum coherence may be excited for spin I = 3/2 nuclei [235].

When working in the liquid state, multiple-quantum excitation is typically achieved via a two-pulse method [84]. Likewise, in the original MQMAS experiment, two-pulse excitation was used [48, 49]. It has been shown, however, that a single-pulse excitation is more efficient when ω_1 < ω_Q^{PAS} [225] and excitation of triple-quantum coherence for spin I ≥ 3/2 nuclei has been shown [236, 237] and implemented into triple-quantum MAS [207] successfully using this method. Using the single-transition operator formalism, Wokaun and Ernst have shown that triple-quantum excitation in spin I = 3/2 nuclei yields a signal that may be quantified in terms of the expectation value of the operator

$I_y^{(3/2,-3/2)}$ [225]:

$$\left\rangle I_y^{(3/2,-3/2)} \right\langle (t) \approx -\frac{3}{2} \sin\left(\frac{3\omega_1^3}{8\omega_Q^2} t \right), \tag{4.6}$$

and consequently, the duration of a triple-quantum excitation pulse that yields the optimum amplitude of triple-quantum coherence, τ_{ex}^{max}, is given by

$$\tau_{ex}^{max} = \frac{8}{3} \left(\frac{\omega_Q}{\omega_1} \right)^2 \tau_{90}^{max}, \tag{4.7}$$

where the optimum signal amplitude obtained by a 90° pulse has a duration, τ_{90}^{max}, given by:

$$\tau_{90}^{max} = \frac{\pi}{2\omega_1}. \tag{4.8}$$

It can also be shown that the excitation of single-quantum coherence reaches its maximum value when the duration of the pulse, $\tau_{p=-1}^{max}$, is

$$\tau_{p=-1}^{max} = \frac{\tau_{90}^{max}}{2} = 45^0. \tag{4.9}$$

This is consistent with Section 4.1, in which it was shown that the nutation frequency of the central transition is (I + 1/2) times faster in the limit $\omega_1 < \omega_Q$.

The dependence of triple-quantum excitation on the pulse flip angle is shown as a function of the ratio ω_Q/ω_1 in Fig. 4.2, where the amplitude of triple-
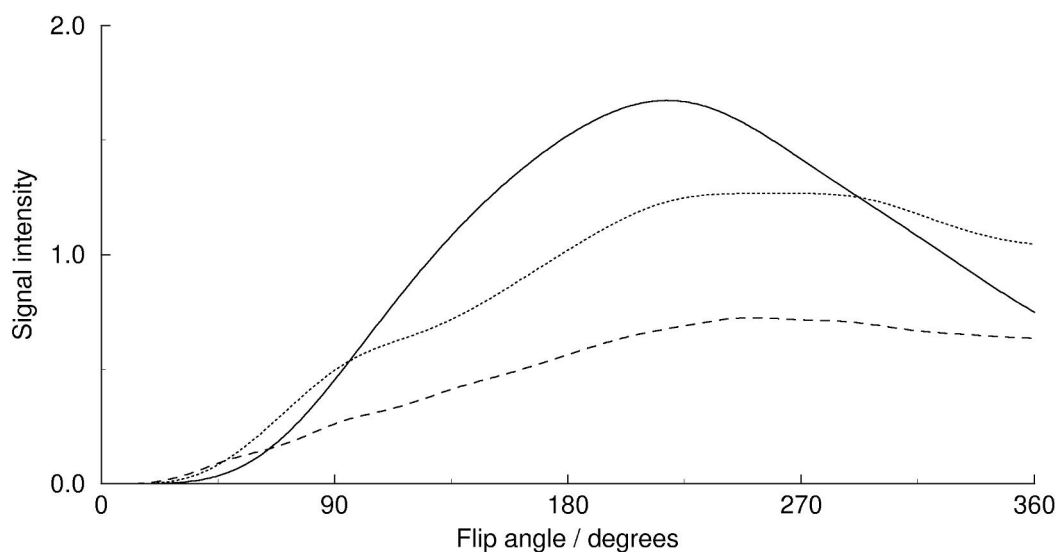
Figure 4.2. Dependence of the triple-quantum signal intensity on the flip angle of the excitation pulse, shown for a spin I = 3/2 nucleus for ω_Q/ω_1 equal to 2 (solid line), 4 (dotted line) and 8 (dashed line). The y axis scale is normalised as in Fig. 4.1 and all other simulation parameters are the same as those used in Fig. 4.1.

quantum coherence excited is defined as the magnitude of the tensor operator $T_{3,-3}$ (p = -3 coherence) obtained when single-pulse excitation is performed on the operator $T_{1,0}$. When ω_Q/ω_1 is 2, triple-quantum excitation reaches its optimum at a flip angle of 218°, whilst flip angles of 267° and 251° yield maximum triple-quantum signal intensity when this ratio is equal to 4 and 8, respectively. The triple-quantum amplitudes are comparable to the central transition amplitudes obtained in Fig 4.1, so indicating that triple-quantum excitation is a relatively efficient process.

The three curves in Fig. 4.2 show that a factor of four increase in the ratio ω_Q/ω_1 leads to an approximate 60% reduction in the triple-quantum signal intensity. Given that in a powder the quadrupolar coupling parameter ω_Q can take values ranging from zero to ω_Q^{PAS}, this means that each crystallite in a powder does not lead to equal triple-quantum excitation.

The observations made using Fig. 4.2 have been considered in greater detail in the literature [56, 237], where the triple-quantum excitation behaviour of half-integer quadrupolar nuclei has been demonstrated [56]. In addition, the effect of MAS has also been considered [238].

## 4.3   Conversion of Multiple-Quantum Coherence

The original MQMAS experiment [48, 49] consisted of two steps — the excitation of triple-quantum coherence and its conversion to observable central-transition coherence. The signal intensity obtained from this experiment when either the $-3 \rightarrow -1$ or $+3 \rightarrow -1$ coherence transfer pathway is selected is shown in Figs. 4.3a and 4.3b respectively, as a function of the flip angle of the conversion pulse when the ratio ω_Q/ω_1 is equal to 2, 4 and 8. Figure 4.3a shows that when the $-3 \rightarrow -1$ pathway is selected, the maximum signal intensity is obtained when the conversion pulse has a flip angle close to 60°. When the $+3 \rightarrow -1$ pathway is selected, Fig. 4.3b reveals maximum signal intensity to occur at a flip angle of approximately 95°. In both cases the reduction in signal intensity as the quadrupolar coupling parameter is increased, which was also observed for triple-quantum excitation in Fig. 4.2, is seen.

One obvious feature evident in both Figs. 4.3a and 4.3b is that the signal intensity is greatly reduced with respect to Fig. 4.2. This indicates that the conversion of triple-quantum coherences is a far less efficient process than triple-quantum excitation. Closer inspection reveals that, for a spin $I = 3/2$

a

b
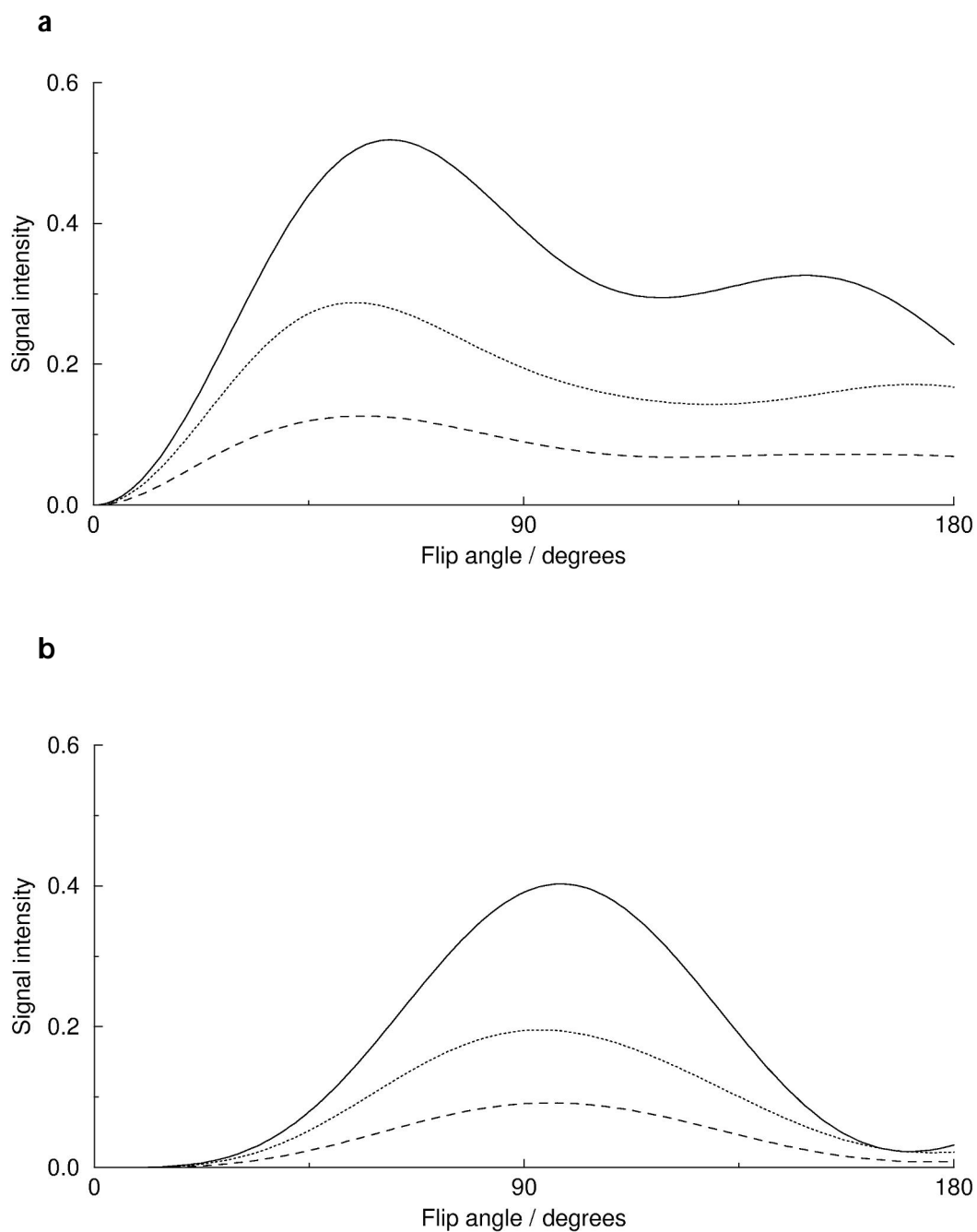
Figure 4.3. Dependence of the signal intensity obtained for a spin $I = 3/2$ nucleus in the (a) $-3 \rightarrow -1$ and (b) $+3 \rightarrow -1$ MQMAS experiments as a function of the flip angle of the conversion pulse, with the ratio ω_Q/ω_1 equal to 2 (solid line), 4 (dotted line) and 8 (dashed line). The flip angle of the triple-quantum excitation pulse is 240°; all other parameters are as in Fig. 4.2.

nucleus, the conversion of triple-quantum coherences via the $-3 \rightarrow -1$ and $+3 \rightarrow -1$ pathways is equally efficient when a pulse with a flip angle of 90° is used. This has the implication that, by performing an amplitude-modulated MQMAS

91
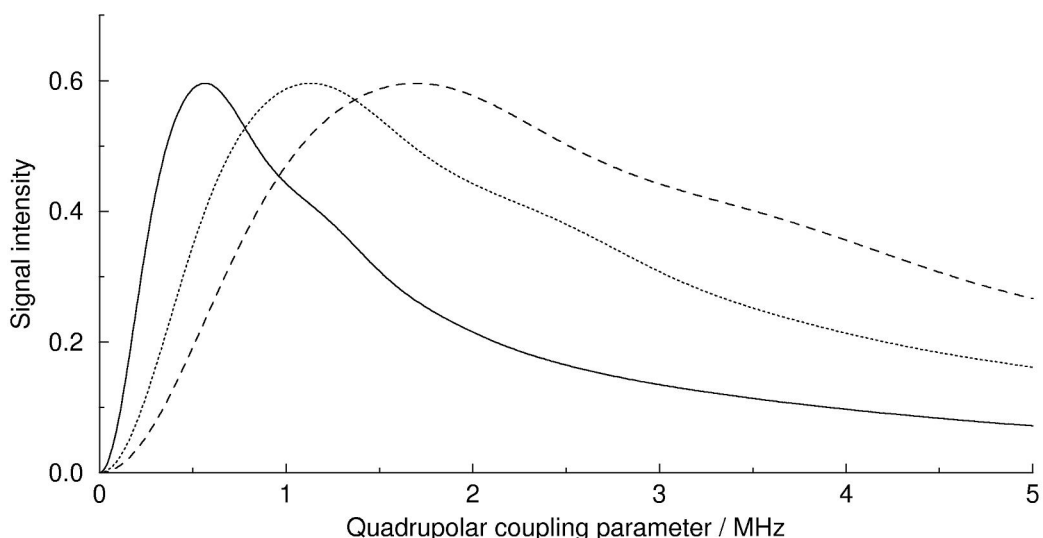
Figure 4.4. Dependence of the signal intensity on the quadrupolar coupling parameter, C_Q, using the two-pulse MQMAS experiment in Fig. 3.7 (selecting the $-3 \rightarrow -1$ pathway). The signal intensity is shown for the cases where the radiofrequency field strength is equal to 100 kHz (solid line), 200 kHz (dotted line) and 300 kHz (dashed line). The flip angles of the excitation and conversion pulses are 240° and 60°, respectively; all other parameters are as in Fig. 4.2.

experiment in which both $p = +3$ and $p = -3$ coherences are selected during the t_1 period (described earlier in Section 3.4.3.3), a two-dimensional spectrum may be obtained that contains pure- phase lineshapes [207]. Such behaviour is, however, only observed for spin $I = 3/2$ nuclei and hence such an experiment has not found widespread application.

The dependence of the signal intensity obtained from the MQMAS experiment used in Fig. 4.3a on the quadrupolar coupling is demonstrated in Fig. 4.4, where the signal intensity is shown as a function of the quadrupolar coupling parameter, C_Q. Figure 4.4 shows how the maximum signal intensity obtained occurs at a higher value of the quadrupolar coupling constant as the hard-pulse field strength is increased; this is consistent with Eq. (4.6). It is seen that, for a radiofrequency field strength $\omega_1/2\pi = 100$ kHz, the experiment is at

its most efficient when C_Q is ~0.6 MHz. Clearly, for significant signal intensity to be obtained for nuclei with C_Q greater than 2 MHz a much higher B_1 field is required. The highest B_1 field currently achievable with commercial MAS probes is ~300 kHz and as shown in Fig. 4.4, the maximum efficiency of the MQMAS experiment occurs when C_Q ~1.7 MHz in this case. Clearly, MQMAS performs poorly in the presence of large quadrupolar interactions. It is also evident from Fig. 4.4 that a single pulse will fail to excite multiple-quantum coherences if the field strength is too large [225].

Figure 4.4 demonstrates what is arguably the greatest limitation of the MQMAS experiment, specifically the lack of sensitivity for nuclei with large quadrupolar interactions. This has the consequence that the intensities of resonances arising from crystallographically inequivalent sites do not accurately reflect the site populations predicted from the crystal structure.

The non-uniform excitation and conversion of triple-quantum coherences also has the effect that it can lead to distortions in the quadrupolar lineshapes. The range of values of the quadrupolar coupling parameter ω_Q observed in a powder means that the multiple-quantum filtered spectrum of a static sample exhibits significant distortions. In particular, crystallites with $\omega_Q = 0$ do not yield any signal due to the failure to excite multiple-quantum coherence in the absence of a quadrupolar interaction. Under MAS conditions distortions are typically minimal as a result of the time dependence imposed on the quadrupolar interaction under spinning conditions, although they can be significant when the ratio ω_Q/ω_1 is large.

Figure 4.3 demonstrates the inefficiency of the conversion step in the MQMAS experiment. In STMAS, the conversion of satellite-transition to central-transition coherences is also an inefficient process [53, 54] and so, like MQMAS, the experiment can suffer from poor sensitivity in the presence of large quadrupolar interactions. In addition, the excitation and conversion of satellite-transition coherences is dependent on the magnitude of the quadrupolar interaction and so, like MQMAS, STMAS is a non-quantitative technique.

4.4 Methods for Enhanced Coherence Transfer

It was shown in the previous section that the inefficiency of the excitation and conversion processes is one of the major weaknesses of the MQMAS (and STMAS) experiments. The first efforts to remedy this situation focussed on improving the efficiency of the excitation of triple-quantum coherences in MQMAS. The use of composite pulses has been shown to yield a 30% increase in signal intensity with respect to single-pulse excitation [239], whilst shaped pulses have also been shown to provide useful enhancements [240]. More recent efforts have predominantly focussed on addressing the inefficiency of the conversion step in MQMAS. This has led to the development of several methods that increase the signal intensity obtained from MQMAS, such as fast amplitude-modulated (FAM) pulses [57, 241–243], hyperbolic secant pulses (HS) pulses [244], double frequency sweeps (DFS) [245, 246], rotationally-

induced adiabatic coherence transfer (RIACT) [247], shaped pulses [248] and soft-pulse added mixing (SPAM) pulses [58]. FAM pulses have been used most widely for enhancing the conversion of triple-quantum to single-quantum coherence in MQMAS of spin I = 3/2 nuclei and have, in addition, been successfully implemented into triple-quantum MQMAS of spin I = 5/2 [241, 249] and spin I = 7/2 [250] nuclei. SPAM pulses, which closely resemble FAM pulses, have only recently been introduced as a method of enhancing coherence transfer in the conversion step of MQMAS [58, 251, 252]. Their application in double-quantum filtered (DQF)-STMAS has also been reported [253, 254].

In this section, FAM and SPAM pulses are introduced and their implementation in MQMAS is discussed [255]. Computer-simulated spin I = 3/2 NMR spectra are shown and compared with [87]Rb (spin I = 3/2) NMR spectra of rubidium nitrate, $RbNO_3$, and ^{27}Al (spin I = 5/2) NMR spectra of aluminium acetylacetonate, $Al(acac)_3$, recorded using one-dimensional versions of the two-pulse MQMAS experiment. Two-dimensional [87]Rb NMR spectra of rubidium nitrate and ^{27}Al NMR spectra of bayerite, α-$Al(OH)_3$, acquired using two-pulse and whole-echo MQMAS methods with FAM and SPAM pulses are shown and the corresponding signal intensities and lineshapes are considered. Finally, the performance of FAM and SPAM pulses in STMAS and DQF-STMAS is shown.

4.4.1   FAM and SPAM Pulses

FAM pulses commonly come in two forms. FAM-I pulses involve a train of alternate phase hard pulses interleaved with delays; the pulses and delays being of equal duration [57, 241]. FAM-II pulses involve two alternate phase hard pulses of unequal duration, applied in succession [242]. These pulses may be used in enhancing the triple-quantum to single-quantum coherence conversion process if a change in coherence order $\left|\Delta p\right|$ = 2 (i.e., $\pm 3 \rightarrow \pm 1$) is required, although it has been reported that FAM-I pulses are more effective in enhancing coherence transfer where $\left|\Delta p\right|$ = 4 and that FAM-II pulses perform better when $\left|\Delta p\right|$ = 2 [241]. Only FAM-II pulses are considered in the experimental results shown in this chapter and so these will be referred to henceforth simply as FAM pulses.

SPAM pulses are, like FAM pulses, composite pulses [256], consisting of a hard pulse followed immediately by a soft pulse that acts as a selective 90° pulse on the central transition. The signal intensity yielded by SPAM pulses is at its maximum when the hard pulse duration is optimised to yield maximum $\pm 3 \rightarrow 0$ transfer [58, 251], and so is identical to the optimum value found in a z-filter experiment [135]. The relative phase of the two components of a SPAM pulse depends on whether the multiple-quantum coherence to central-transition coherence conversion step involves a change in sign of coherence order [58, 251].

The implementation of FAM and SPAM pulses in MQMAS is shown in
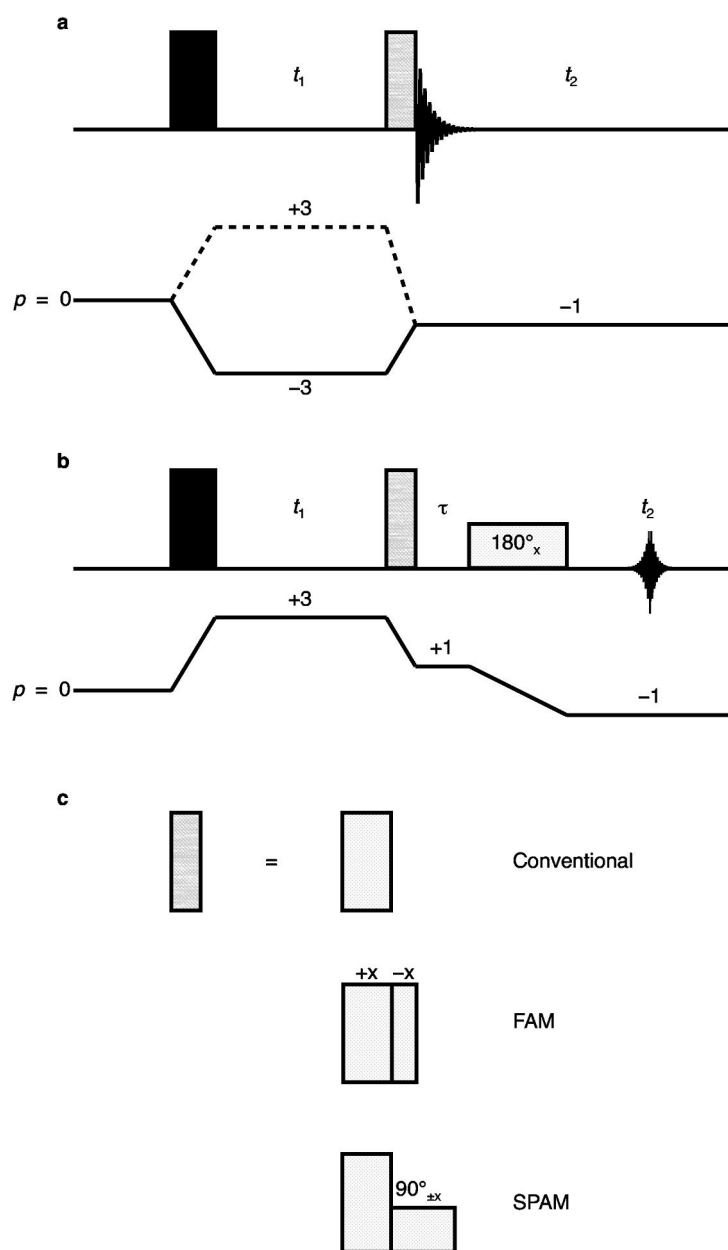
Figure 4.5. (a) Two-pulse sequence for the (triple-quantum) MQMAS experiment. (b) Phase-modulated version of the whole-echo (triple-quantum) MQMAS experiment. The shaded conversion pulse in (a) and (b) can either be a single hard pulse, a composite FAM pulse, or a composite SPAM pulse, as shown in (c). The two components of the SPAM pulse have the same phase for $\pm 3 \rightarrow \mu 1$ transfer and the opposite phase for $\pm 3 \rightarrow \pm 1$ transfer.

Fig. 4.5. As seen in Fig. 4.5a, FAM and SPAM pulses may easily be inserted into the conversion step of the two-pulse MQMAS experiment. They are also ideally suited to insertion into the $+3 \rightarrow +1$ conversion step of phase-modulated split-t_1
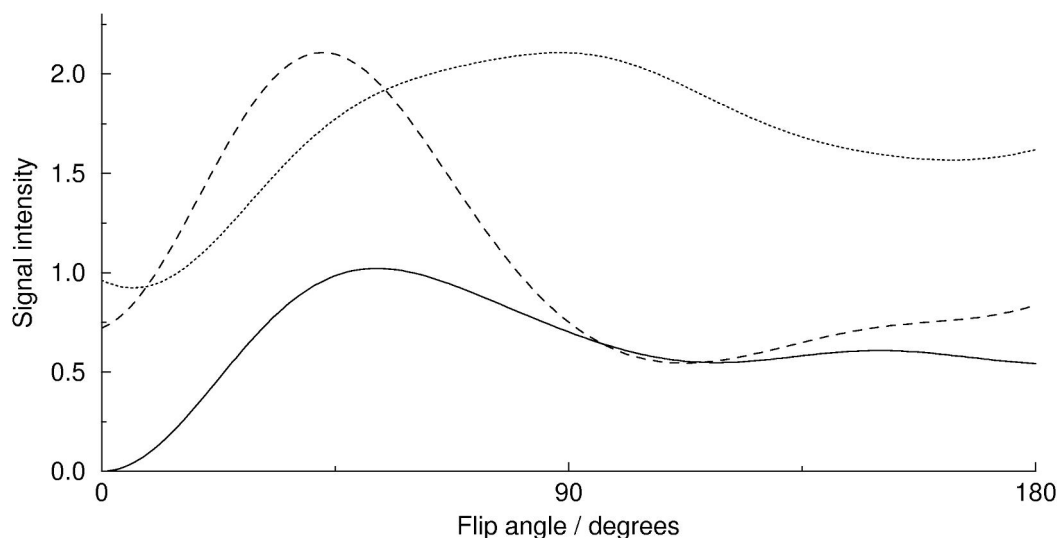
Figure 4.6. Dependence of the central-transition amplitude on the flip angle of the conversion pulse in the $-3 \rightarrow -1$ MQMAS experiment for a spin $I = 3/2$ nucleus. Plots are shown for when a single hard pulse is used (solid line) and for the first and second hard pulses in a FAM pulse (dotted and dashed lines, respectively). When the first FAM pulse is incremented, the second pulse has a flip angle of 43°, whilst a flip angle of 88° is used for the first pulse when the second one is being varied. The y axis scale is normalised with respect to the signal intensity obtained when an optimised single hard pulse is used. Simulations were performed assuming a radiofrequency field strength of 100 kHz, a quadrupolar coupling constant of 2.0 MHz and a Larmor frequency of 100 MHz. The excitation pulse flip angle is 240°. All other parameters are as in Fig. 4.2.

whole-echo methods, as shown in Fig. 4.5b. Aside from providing signal enhancement, it has been reported that SPAM pulses, when used in the echo and antiecho versions of the two-pulse MQMAS experiment, yield very similar signal intensities [58, 251]. This has led to the suggestion that combining data obtained from the SPAM-echo and SPAM-antiecho experiments is an effective method for recording high-resolution MQMAS spectra with enhanced sensitivity [251].

Figure 4.6 shows the dependence of the signal intensity obtained, for a
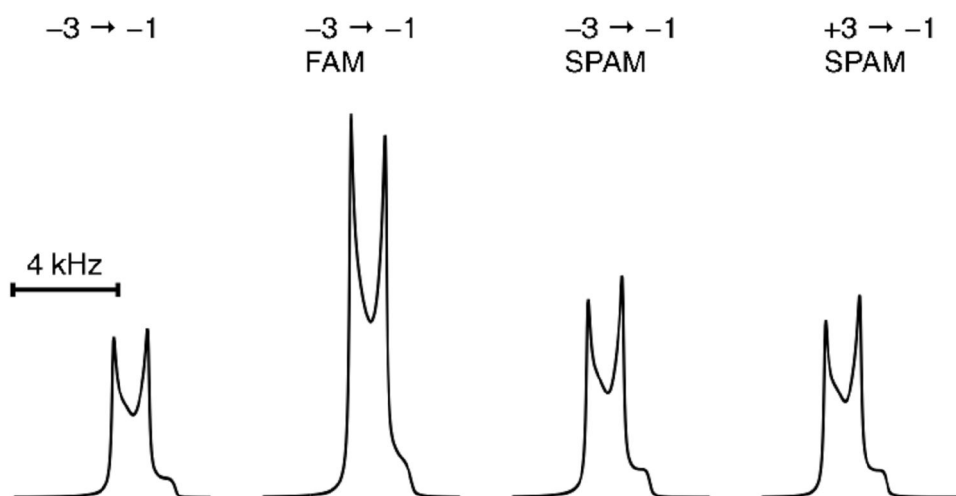
Figure 4.7. Computer-simulated spin I = 3/2 NMR spectra corresponding to one-dimensional versions of the two-pulse MQMAS experiment shown in Fig. 4.5a, using the conversion pulses and coherence transfer pathways indicated. Spectra were generated using the following parameters: 100 MHz Larmor frequency, 2.0 MHz quadrupolar coupling constant, 150 kHz hard-pulse radiofrequency field strength, 4.5 μs excitation pulse, 1.0 μs hard conversion pulse, 1.3 μs + 0.8 μs FAM pulse and 1.2 μs + 12.5 μs (v_1 = 10 kHz) SPAM pulse. Spectra were generated with η = 0 and by summing over 500 equally-spaced values of the angle β'.

spin I = 3/2 nucleus, from the two-pulse MQMAS experiment on the pulse flip angle when a FAM pulse is used for the conversion step, compared to when a single, hard pulse is used. The flip angles of the first and second pulses are seen to be in the ratio of approximately 2 : 1 and a signal enhancement of ~100% is observed. An analogous simulation (not shown) of the signal intensity observed in the $-3 \rightarrow -1$ and $+3 \rightarrow -1$ experiments when a SPAM pulse is used reveals a smaller signal enhancement of ~30% in the former experiment with respect to single-pulse conversion. In addition, a similar, but not identical, signal intensity is obtained when SPAM is implemented in these two experiments. Computer-simulated spectra have been generated to demonstrate the performance of FAM pulses in the echo version and of SPAM pulses in the echo and antiecho versions, of the one-dimensional two-pulse MQMAS experiment. These spectra,
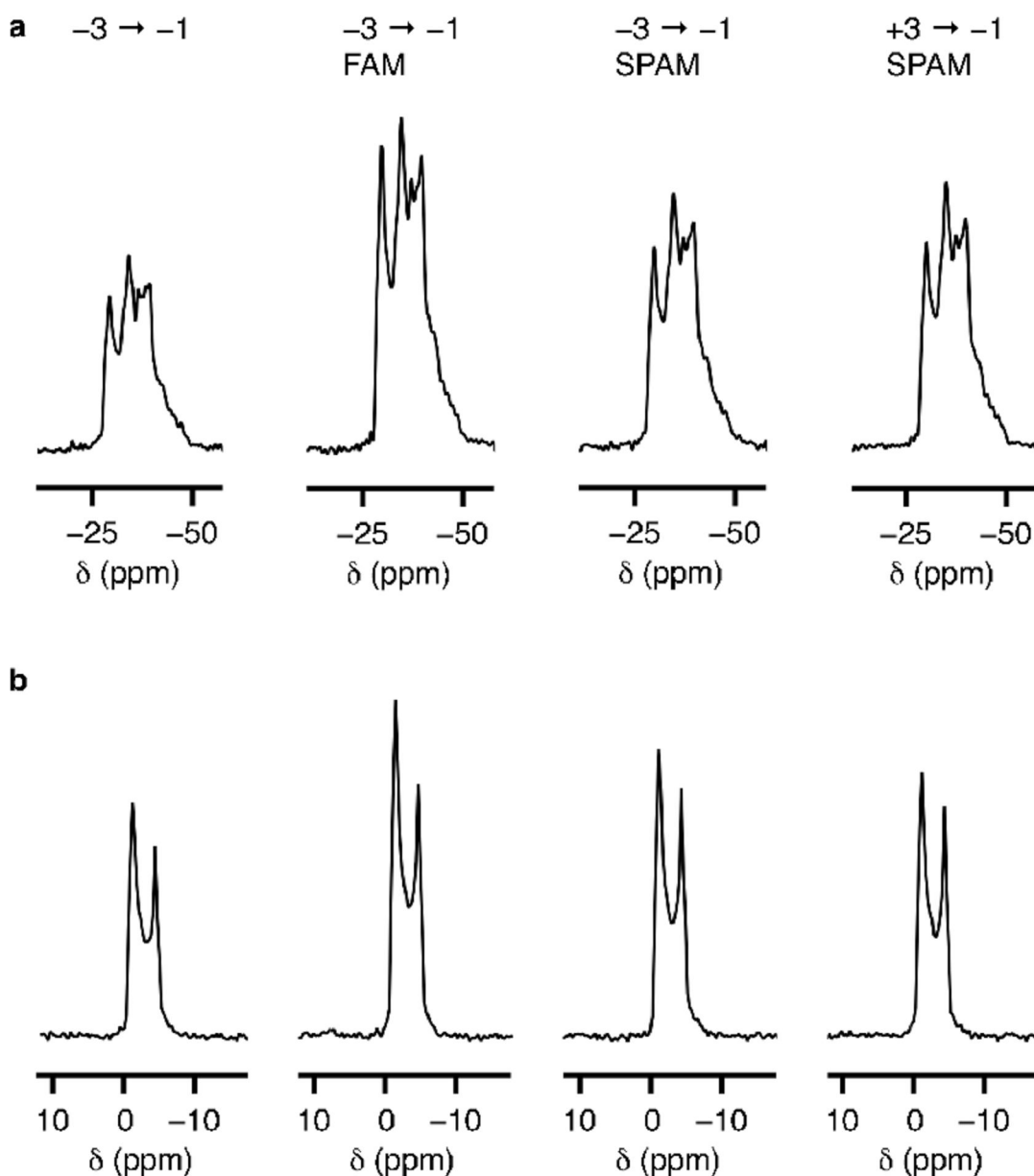
Figure 4.8. (a) ^{87}Rb NMR spectra of RbNO$_3$ and (b) ^{27}Al NMR spectra of Al(acac)$_3$ recorded using one-dimensional versions of the two-pulse MQMAS experiment in Fig. 4.5a using the coherence transfer pathways and conversion pulses shown. Experimental parameters: (a) 2.9 μs excitation pulse (corresponding to a hard-pulse radiofrequency field strength of ~150 kHz), 0.9 μs conventional conversion pulse, 1.3 μs + 0.75 μs FAM pulse, 1.3 μs + 13.7 μs (v_1 ≈ 9.1 kHz) SPAM pulse; (b) 4.0 μs excitation pulse (corresponding to a hard-pulse radiofrequency field strength of ~100 kHz), 1.1 μs conventional conversion pulse, 1.6 μs + 0.9 μs FAM pulse, 1.7 μs + 21 μs (v_1 ≈ 4.0 kHz) SPAM pulse.

shown in Fig. 4.7, reveal the expected signal enhancement from the FAM pulse and the lesser enhancement from the SPAM pulse, when used in the echo

version of the experiment. When implemented into the antiecho version, the SPAM pulse yields slightly less signal intensity than that obtained from the echo experiment. In the case of both FAM and SPAM pulses, minimal lineshape distortions are observed.

The performance of FAM and SPAM pulses in enhancing coherence transfer in MQMAS has been considered using two crystalline materials. Figure 4.8 shows one-dimensional MQMAS spectra of rubidium nitrate and aluminium acetylacetonate recorded using the conversion pulses and coherence transfer pathways indicated.

For both spin I = 3/2 and spin I = 5/2 nuclei, FAM pulses are shown to yield the most signal intensity. SPAM pulses result in a smaller, but still very useful, enhancement with respect to a single hard pulse, whilst the two versions of the SPAM pulse yield very similar, but not identical signal intensities for the echo and antiecho pathways. These observations confirm the validity of the spin I = 3/2 computer-simulated spectra in Fig. 4.7.

4.4.2   Two-Dimensional MQMAS NMR

The application of FAM and SPAM pulses to two-dimensional MQMAS NMR is now considered. Figure 4.9 presents two-dimensional [87]Rb MQMAS NMR spectra of rubidium nitrate. The spectra shown in Figs. 4.9a and 4.9b were recorded using the whole-echo experiment in Fig. 4.5b with split-t_1 acquisition, using either a single hard pulse (Fig. 4.9a) or a FAM pulse (Fig. 4.9b) for the
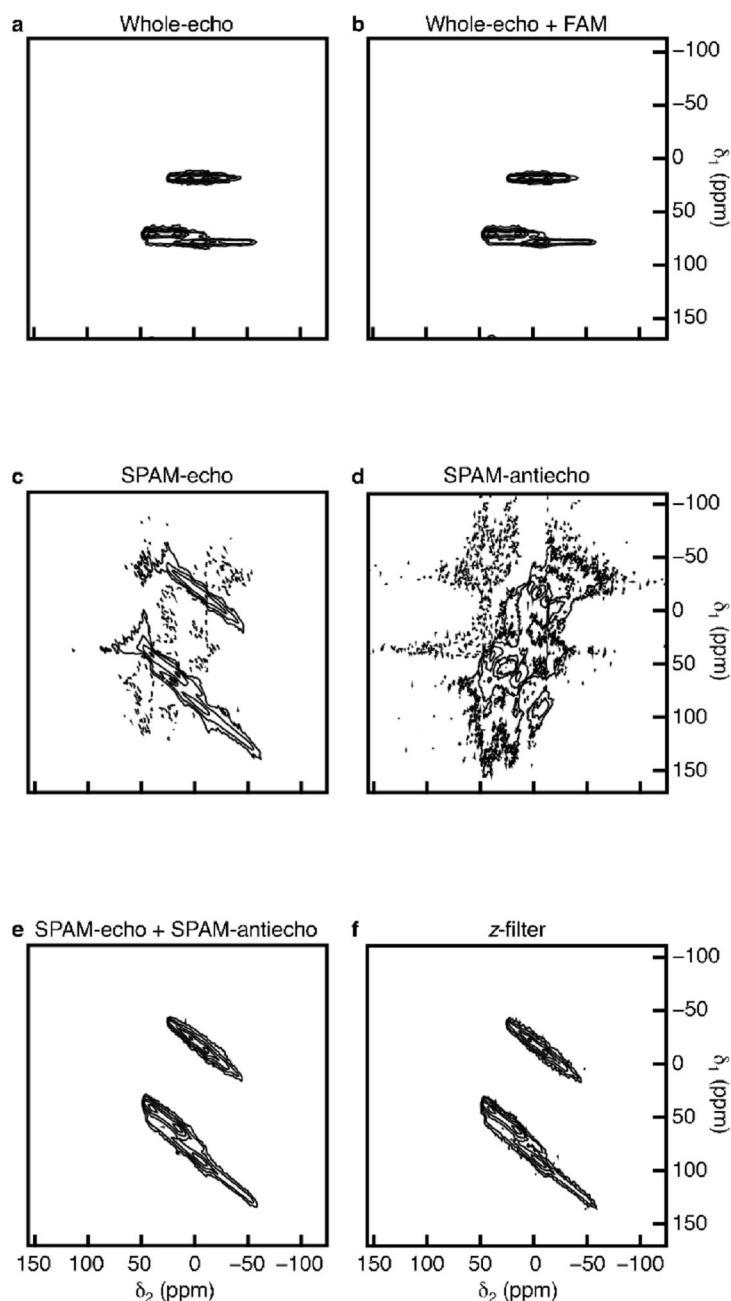
Figure 4.9. Two-dimensional ^{87}Rb MQMAS NMR spectra of RbNO$_3$ recorded using (a) a split-t_1 whole-echo experiment with a single hard conversion pulse, (b) a split-t_1 whole-echo experiment with a FAM conversion pulse, (c) a two-pulse experiment with a $-3 \rightarrow -1$ SPAM pulse, (d) a two-pulse experiment with a $+3 \rightarrow -1$ SPAM pulse, and (f) a z-filter experiment. Spectrum (e) was obtained by the summation of (c) and (d). Experimental parameters: (a and b) 96 transients (of 20.6 ms) averaged for each of 256 t_1 increments; (c and d) 48 transients averaged for each of 256 t_1 increments; (f) 48 transients averaged for each of 512 t_1 increments (TPPI method). All pulse durations were as in Fig. 4.8a. Contour levels are shown at 4, 8, 16, 32 and 64% of the maximum intensity in (a), (b), (e) and (f), 3, 9, 27 and 81% of the maximum intensity in (c) and 8, 24 and 72% of the maximum intensity in (d).
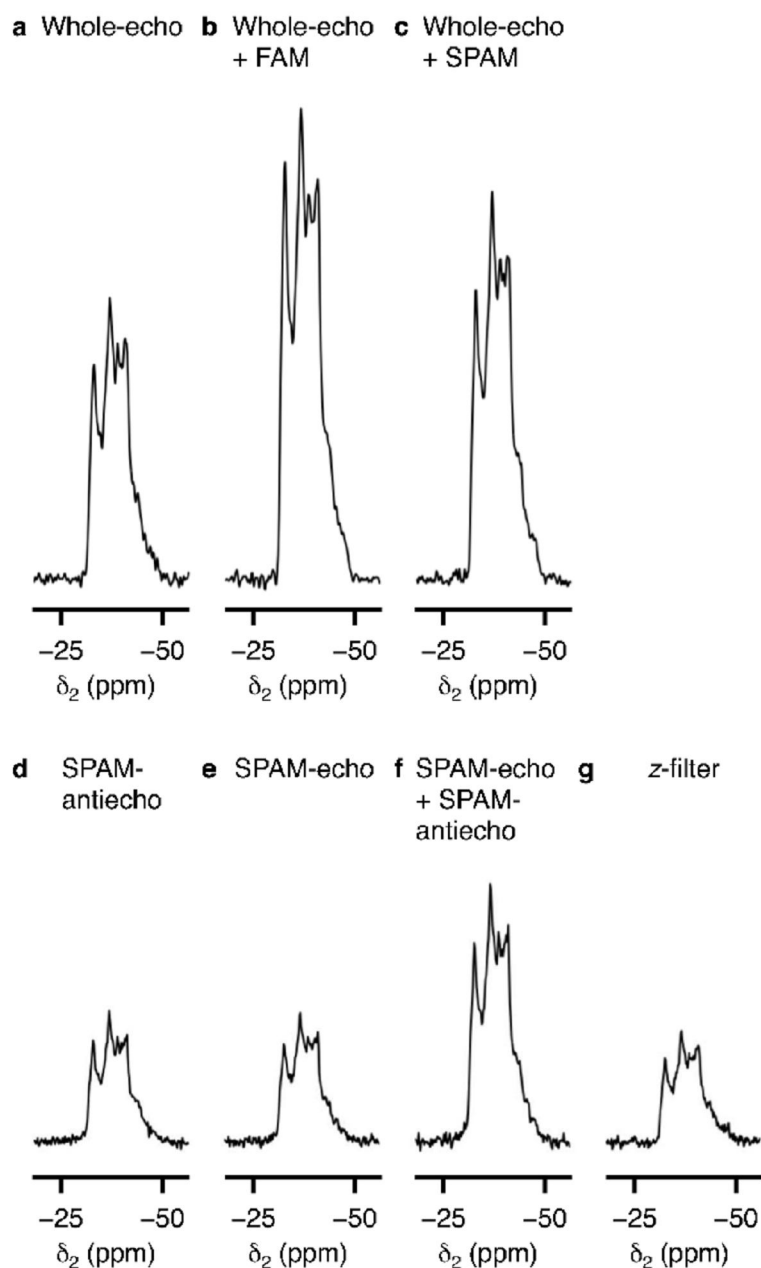
Figure 4.10. δ_2 projections of the spectra in Fig. 4.9, plus that of a spectrum recorded using a split-t_1 whole-echo experiment with a SPAM conversion pulse.

conversion step. A split-t_1 whole-echo experiment with a SPAM conversion pulse was also performed (spectrum not shown) and yielded a similar result to that seen in Figs. 4.9a and 4.9b. Two-pulse MQMAS experiments with $-3 \rightarrow -1$ SPAM and $+3 \rightarrow -1$ SPAM conversion pulses were also performed and the resultant spectra are shown in Figs. 4.9c and 4.9d, respectively. The spectrum in
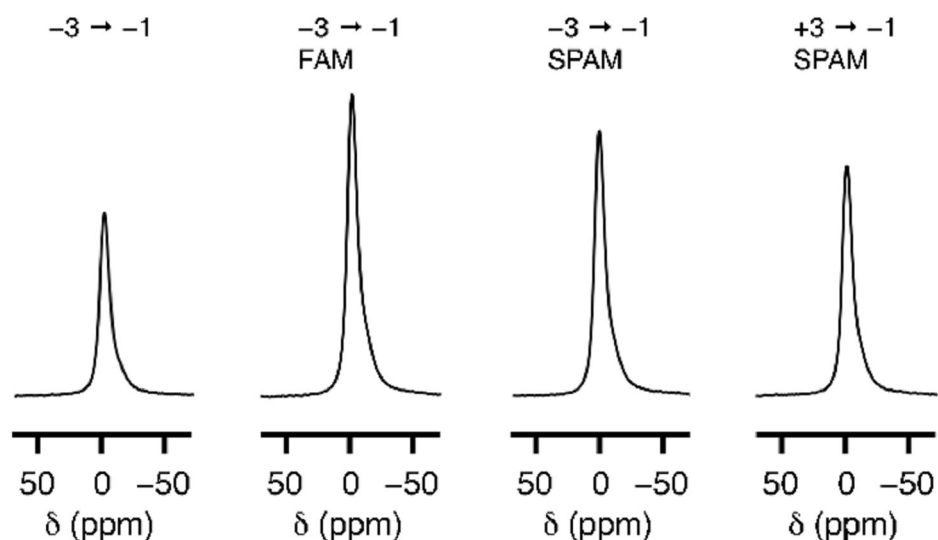
Figure 4.11. ^{27}Al NMR spectra of α-Al(OH)$_3$ recorded using one-dimensional versions of the two-pulse MQMAS experiment in Fig. 4.5a with the conversion pulses and coherence transfer pathways stated. Experimental parameters: 2.8 μs excitation pulse (corresponding to a hard-pulse radiofrequency field strength of ~150 kHz), 0.9 μs single, hard conversion pulse, 1.5 μs + 0.8 μs FAM pulse, 1.2 μs + 12.0 μs ($\nu_1 \approx$ 6.9 kHz) SPAM pulse.

Fig. 4.9e was obtained by adding the spectra in Figs. 4.9c and 4.9d, whilst the spectrum in Fig. 4.9f was recorded using a z-filter experiment.

Figure 4.9 reveals that, as expected, absorption-mode two-dimensional lineshapes are generated by the whole-echo and z-filter experiments, as well as by the combination of the two SPAM experiments. The spectra in Figs. 4.9c and 4.9d also show the phase-twist lineshapes expected for the SPAM-echo and SPAM-antiecho experiments, respectively; neither are suited to high-resolution NMR spectroscopy.

Figure 4.10 shows δ_2 projections of the spectra in Fig. 4.9, plus that obtained from a split-t_1 whole-echo experiment with a SPAM conversion pulse. The whole-echo experiments with either a FAM or SPAM conversion pulse are seen to yield the greatest signal intensity, though FAM pulses are, as

104

demonstrated in Fig. 4.8, superior to SPAM pulses in enhancing triple-quantum to single-quantum coherence transfer. The whole-echo experiment with a single hard conversion pulse and the sum of the SPAM-echo and SPAM-antiecho spectra yield considerably less signal, whilst the *z*-filter experiment yields spectra with the lowest signal intensity of all.

To demonstrate the use of FAM and SPAM pulses in MQMAS NMR of amorphous or disordered materials [257], ^{27}Al NMR spectra of bayerite, α-Al(OH)$_3$, were recorded. In this material there exists aluminium in an octahedrally coordinated environment, with a single ^{27}Al peak at δ ~0 ppm [179, 258]. The essentially featureless lineshape, possessing a "tail" to low frequency, is characteristic of the presence of distributions of both chemical shift and quadrupolar parameters [259–261]. Figure 4.11 shows spectra obtained using the same one-dimensional experiments used in Fig. 4.8 for the crystalline materials. As shown for both rubidium nitrate and aluminium acetylacetonate, the $-3 \rightarrow -1$ FAM pulse yields a greater signal enhancement than the $-3 \rightarrow -1$ SPAM pulse. There is, however, a greater disparity observed in the signal intensities obtained when SPAM is used in the $-3 \rightarrow -1$ and $+3 \rightarrow -1$ experiments than is seen with the crystalline materials. This most likely arises due to the presence of aluminium with a very small quadrupolar coupling constant, (a fact confirmed by the very similar signal intensities obtained from the $-3 \rightarrow -1$ and $+3 \rightarrow -1$ experiments (not shown) with a single hard conversion pulse), on which the selective 90° pulse in the SPAM composite pulse would have no effect.
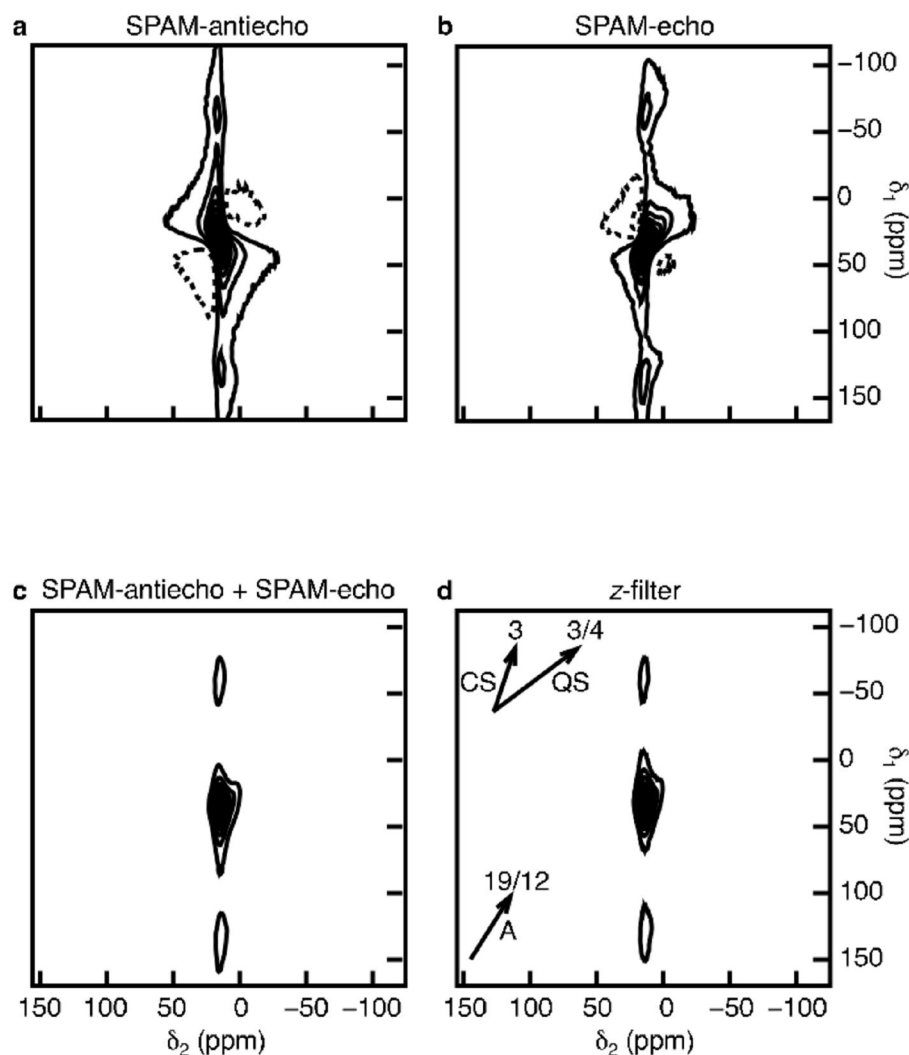
Figure 4.12. Two-dimensional ^{27}Al MQMAS NMR spectra of α-Al(OH)$_3$ recorded using (a) the two-pulse experiment with a $-3 \rightarrow -1$ SPAM conversion pulse, (b) the two-pulse experiment with a $+3 \rightarrow -1$ SPAM conversion pulse, and (d) a z-filter experiment. Spectrum (c) was obtained by adding (a) and (b). Experimental parameters: (a and b) 96 transients (of 7.3 ms) averaged for each of 48 t_1 increments; (d) 96 transients averaged for each of 96 t_1 increments (TPPI method). All pulse durations were as in Fig. 4.11. The gradients of the A, CS and QS axes are shown. Contour levels are shown at 10% increments in the range of 6–96% of the maximum value in (a) and (b) and at 10% increments in the range of 12–92% of the maximum value in (c) and (d).

Figure 4.12 shows two-dimensional ^{27}Al NMR spectra of bayerite. The spectra in Figs. 4.12a and 4.12b were obtained using the two-pulse MQMAS experiment with a $-3 \rightarrow -1$ SPAM and a $+3 \rightarrow -1$ SPAM pulse, respectively, and

the spectrum in Fig. 4.12c was obtained by adding Figs. 4.12a and 4.12b. The spectrum in Fig. 4.12d was obtained using a z-filter experiment. The spectrum in Fig. 4.12d reveals greatest broadening along the CS axis, which indicates that a distribution of chemical shifts makes the dominant contribution to the linewidth.

Whole-echo experiments analogous to those performed on the crystalline materials were also performed on bayerite (results not shown). The resultant spectra contain distorted two-dimensional lineshapes and greatly reduced signal intensities compared to that obtained from the z-filter experiment and so these results are not considered here.

As seen in Fig. 4.9, the SPAM-antiecho ($-3 \rightarrow -1$) and SPAM-echo ($+3 \rightarrow -1$) experiments yield highly phase-twisted lineshapes. The combination of the two SPAM experiments and the z-filter experiments both appear to yield two-dimensional spectra containing purely absorption-mode lineshapes, although there are some small differences. It is very difficult to say which of the lineshapes in Figs. 4.12c and 4.12d are closest to the "true" lineshape, but, given the difference in signal intensities observed between the two pathways in Fig. 4.11, it would seem likely that, despite its reduced signal-to-noise ratio, the z-filter spectrum is a more accurate representation.

4.4.3   *FAM and SPAM Pulses in STMAS*

The use of FAM and SPAM pulses in STMAS and DQF-STMAS [253, 254]
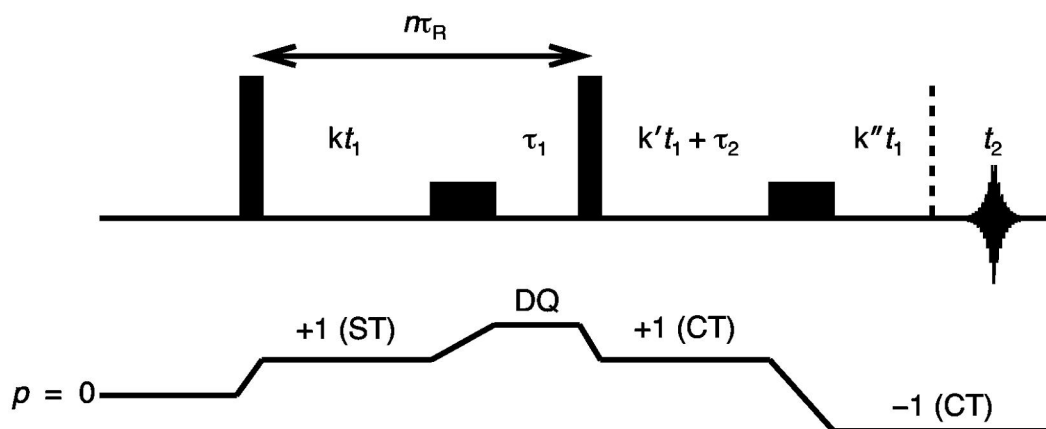
Figure 4.13. Pulse sequence and coherence transfer pathway for the phase-modulated whole-echo DQF-STMAS experiment. Phase cycling is used to ensure only double-quantum coherences evolve immediately after the second pulse. τ_1 is the period of double-quantum evolution and τ_2 is the echo interval.

has also been considered. The DQF-STMAS experiment [262] is a modification of the usual phase-modulated split-t_1 whole-echo method shown in Fig. 3.9 that enables the removal of the unwanted CT $\rightarrow$ CT autocorrelation signal. This is particularly useful for nuclei with spin $I > 3/2$, for which the separation between the CT $\rightarrow$ CT and ST $\rightarrow$ CT ridges is reduced. The pulse sequence, shown in Fig. 4.13, involves the insertion of a soft 180° pulse selective for the central transition between the satellite-transition excitation and conversion pulses. Phase cycling [86] is used to ensure that only double-quantum coherences evolve after the second pulse and the period of double-quantum evolution (τ_1) is typically only a few microseconds duration, to allow for pulse phase-shifting. DQF-STMAS typically yields ~80% of the signal intensity obtained from STMAS [53]. It has been reported that SPAM pulses, when implemented in the +2 $\rightarrow$ +1 conversion step of DQF-STMAS yield enhanced signal intensity [253, 254]. In particular, it has been shown that a signal enhancement of 100% can be achieved by the combination of echo and antiecho
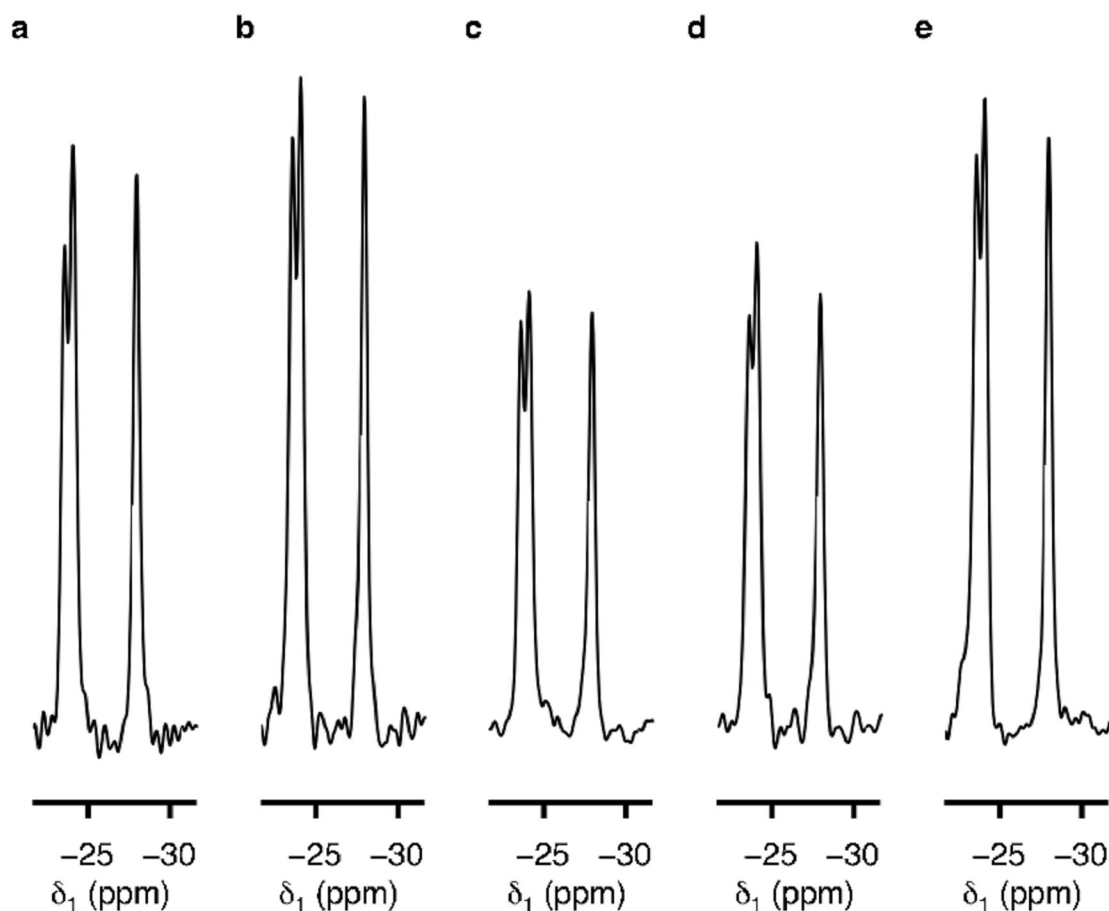
Figure 4.14. δ_1 projections obtained from two-dimensional ^{87}Rb STMAS NMR spectra of RbNO$_3$, recorded using (a–c) split-t_1 whole-echo STMAS and (d–e) split-t_1 whole-echo DQF-STMAS experiments, respectively. The ST → CT and DQ → CT conversion pulse is a single, hard pulse in (a) and (d) and a SPAM pulse in (c) and (e), respectively. A FAM pulse is used for ST → CT conversion in (b). Experimental parameters: 2.1 μs excitation pulse, 1.9 μs ST → CT conversion pulse, 1.2 μs DQ → CT conversion pulse, 2.0 μs + 0.7 μs FAM pulse, 2.5 μs + 17 μs SPAM pulse in (c) and 1.5 μs + 17 μs SPAM pulse in (e).

experiments where SPAM pulses are used in the conversion step, compared with a combination of the echo and anitecho signals obtained by using a conventional hard pulse [254]. To compare the performance of FAM and SPAM pulses in STMAS and DQF-STMAS, two-dimensional experiments were performed on rubidium nitrate. ^{87}Rb NMR spectra of rubidium nitrate were acquired using the split-t_1 whole-echo STMAS and DQF-STMAS methods,

using a hard pulse, a FAM pulse and a SPAM pulse for ST $\rightarrow$ CT conversion, and a hard pulse and a SPAM pulse for DQ $\rightarrow$ CT conversion, respectively. The δ_1 projections obtained from these experiments are shown in Fig. 4.14. When implemented in STMAS, a FAM pulse yields approximately 10% greater signal intensity (Fig. 4.14b) than a hard pulse (Fig. 4.14a), whilst SPAM pulses are ineffective and lead to a marked decrease in signal intensity (Fig. 4.14c). In DQF-STMAS, however, SPAM pulses are shown to yield about 40% more signal (Fig. 4.14e) than a hard pulse (Fig. 4.14d), whilst FAM pulses are ineffective (not shown). Given the loss of signal intensity that results from double-quantum filtration [53, 262], the signal-to-noise ratios obtained from STMAS with FAM and DQF-STMAS with SPAM are thus almost identical.

4.4.4   Conclusions

It has been shown that FAM and SPAM pulses are composite pulses that improve the efficiency of $\pm3 \rightarrow \pm1$ coherence transfer and, in the case of SPAM, also that of $\pm3 \rightarrow \mu1$ transfer. Experimental results and computer simulations have confirmed that FAM pulses consistently yield greater signal enhancements than SPAM pulses for spin I = 3/2 and spin I = 5/2 nuclei in a series of crystalline and amorphous materials. SPAM pulses have been shown to be a useful addition to the array of techniques available for enhancing the conversion step in MQMAS. They have the advantage over FAM pulses (where iterative optimization of two hard pulses is needed) that no additional

110

experimental optimization is required as the calibration of a soft pulse is performed elsewhere for use in z-filter and whole-echo methods. SPAM pulses have been shown to yield very similar, but not identical signal intensities when used for $\pm 3 \rightarrow \pm 1$ and $\pm 3 \rightarrow \mu 1$ coherence transfer.

When SPAM pulses are used in echo and antiecho two-dimensional MQMAS experiments, the summation of the resultant spectra yields approximately absorption-mode two-dimensional lineshapes, although the unequal signal intensities obtained from the two pathways means that caution should be exercised in their interpretation. SPAM pulses and $\pm 3 \rightarrow \pm 1$ FAM pulses have been shown to work effectively when implemented into phase-modulated whole-echo methods and, when used in this way, lead to spectra exhibiting absorption-mode lineshapes and a significantly higher signal-to-noise ratio than is obtained by the combination of SPAM-echo and SPAM-anti–echo spectra. SPAM pulses have also been demonstrated to be an effective method for enhancing the $\pm 2 \rightarrow \pm 1$ coherence transfer step in phase-modulated whole-echo DQF-STMAS, although they offer no greater signal intensity than is obtained when FAM pulses are implemented in the ± 1 (ST) $\rightarrow \pm 1$ (CT) conversion step of conventional STMAS.

The optimum use of FAM and SPAM pulses would appear to be in the phase-modulated whole-echo versions of the MQMAS and (DQF)-STMAS experiments, where, like DFS and HS pulses, they can easily be used. In amorphous and disordered materials (for which pure-phase two-dimensional lineshapes are of the utmost importance), the unequal efficiency of $\pm 3 \rightarrow \pm 1$

SPAM and $\pm 3 \to \mu 1$ SPAM coherence transfer may lead to distorted lineshapes. For such materials, the z-filter experiment is thus preferred, despite its lower signal-to-noise ratio with respect to the addition of SPAM-echo and SPAM-antiecho spectra.

Chapter 5

STARTMAS

5.1   Introduction

The DOR, DAS, MQMAS and STMAS techniques enable the acquisition of high-resolution NMR spectra of half-integer quadrupolar nuclei. The latter three techniques involve the acquisition of a two-dimensional dataset, whereas DOR yields isotropic spectra in real time, i.e., through acquisition of a one-dimensional dataset. The need for an entire phase cycle to be completed for each increment of the indirect (t_1) time period means that the acquisition of two-dimensional datasets is typically longer than that of one-dimensional datasets and hence is often the limiting factor on the duration of the experiment [263]. In this chapter, a new method will be introduced that, like DOR, enables acquisition of isotropic spin I = 3/2 NMR spectra in real time. In contrast to DOR, however, it may be performed on standard MAS probes and fast spinning rates and high radiofrequency field strengths may be achieved. This method involves, like the CRAMPS [15] and Carr-Purcell Meiboom-Gill (CPMG) [264] techniques, multiple-pulse sequences interleaved with real-time data acquisition.

5.2   Theoretical Basis

It was shown in Chapter 3 that by spinning at the magic angle, the second-rank contribution to second-order quadrupolar broadening is removed, whilst the fourth-rank contribution is only reduced. The DOR and DAS techniques achieve complete removal of the second-order quadrupolar interaction by exploiting the $d_{0,0}^2(\chi)$ and $d_{0,0}^4(\chi)$ terms in Eq. (3.29). The MQMAS and STMAS experiments achieve complete removal of residual second-order quadrupolar broadening by utilising the fourth-rank coefficients, $C^4(I, q)$, via coherence transfer. These coefficients correspond, in the t_1 period of an MQMAS experiment, to transitions with $m_I = \pm q \leftrightarrow \mu q$ and so q thus takes the value +3/2 for a triple-quantum MAS experiment. In an STMAS experiment, the fourth-rank coefficient pertaining to evolution in the t_1 period corresponds to a transition with $m_I = \pm(q-1) \leftrightarrow \pm q$ and so q is equal to +3/2 (for a spin $I = 3/2$ nucleus and for the inner satellite transitions of nuclei with spin $I \geq 5/2$).

Taking the example of MQMAS, by performing a two-dimensional experiment in which multiple- (usually triple-) quantum coherences and single-quantum central-transition coherences are allowed to evolve during two successive time periods, t_1 and t_2, the residual second-order quadrupolar broadening is refocussed as an echo when

$$t_2 = -\left(\frac{C^4(I, 3/2)}{C^4(I, 1/2)}\right) t_1 \ . \tag{5.1}$$

This leads to the question as to whether such a correlation could work in
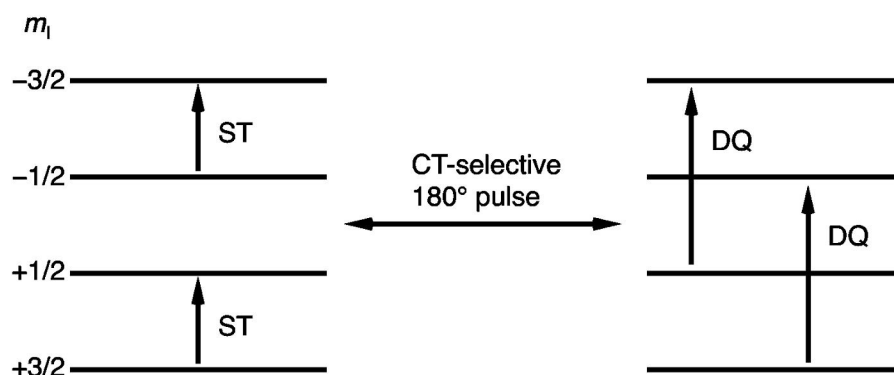
Figure 5.1. Energy-level diagram of a spin $I = 3/2$ nucleus demonstrating the interconversion between $p = -1$ ST coherences and $p = -2$ DQ coherences achieved by the application of a CT-selective 180° pulse.

real time. As in CPMG, in which a train of multiple echoes is acquired as a function of a single time variable, an experiment comprising excitation of multiple-quantum coherence and successive interconversion with central-transition coherence could be envisaged. For such an experiment to be successful, the pulses performing the excitation of triple-quantum coherences and their conversion to central-transition coherences need to be highly efficient. As shown in Chapter 4, both pulses are very inefficient, with the conversion pulse being particularly poor. Consequently, performing such an experiment would lead to a very large loss of signal intensity between successive echoes and hence an intolerably large line-broadening in the isotropic spectrum.

It is known that central-transition-selective pulses are highly effective and it has been reported that a selective inversion pulse applied to the central transition leads to the transfer of the adjacent satellite-transition coherences ($\pm 3/2 \leftrightarrow \pm 1/2$) into double-quantum coherences ($\pm 3/2 \leftrightarrow \mu 1/2$) with nearly 100% efficiency [262]. This coherence transfer, illustrated in Fig. 5.1, has been

exploited in the DQF-STMAS and DQF-SATRAS techniques [262, 265].

Considering the $C^4(I, q)$ coefficients of the satellite-transition and double-quantum coherences of a spin I = 3/2 nucleus, these take the values −48/35 and +6/35, respectively. These coefficients are given in Appendix E; the latter is obtained by a summation of the values for the central and satellite transitions (54/35 and −48/35, respectively). This means that an experiment in which selective central-transition conversion pulses are used for coherence transfer between satellite and double-quantum transitions will lead to refocussing of the residual second-order quadrupolar broadening for a spin I = 3/2 nucleus if the periods of evolution are in the ratio 6:48 = 1:8. This is the principle of the STARTMAS (*s*atellite *t*ransitions *a*cquired in *r*eal *t*ime MAS) experiment [266, 267], the details of which are given in the next section.

5.3   Pulse Sequence

The pulse sequence and coherence transfer pathway for the new STARTMAS experiment are shown in Fig. 5.2. The first pulse is a hard pulse optimized for excitation of satellite-transition coherences. Pairs of CT-selective inversion pulses then interconvert the satellite-transition and double-quantum coherences and, by spacing the pulses such that the periods of satellite-transition and double-quantum evolution are in the ratio 1:8, the residual second-order quadrupolar broadening is refocussed at the end of each τ period (the STARTMAS cycle). The τ period is rotor-synchronized, $\tau = n\tau_R = n/\nu_R$ and

116
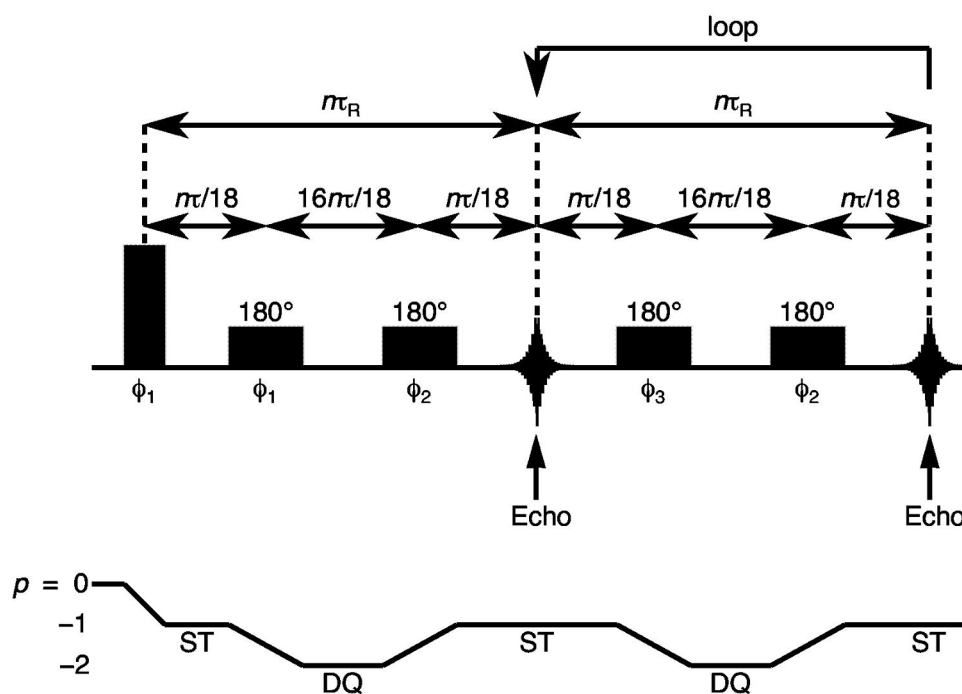
Figure 5.2. Pulse sequence and coherence transfer pathway for the STARTMAS experiment for spin $I = 3/2$ nuclei. The first two pulses are cycled with phase $\phi_1 = 0°, 45°, 90°, 135°, 180°, 225°, 270°, 315°$ and the receiver cycled with phase $\phi_{rx} = 0°, 90°, 180°, 270°$; this enables the suppression of central-transition coherences excited by the first pulse [268]. The subsequent 180° pulses are cycled with phases $\phi_2 = 180°$ and $\phi_3 = 0°$, respectively.

this ensures that the first- and second-order quadrupolar interactions are refocussed at the same point and that an isotropic echo is formed. Consequently, data sampling with a period equal to τ will ensure removal of quadrupolar broadening to second order. The number of rotor periods per τ period, n, is usually chosen to be either 9 or 18, the effect of a variation of this parameter is considered in Section 5.5.3. As in STMAS, the use of MAS to remove the effects of the large first-order quadrupolar interaction dictates the requirement for very accurate timings of the free precession intervals and, consequently, a stable spinning speed and accurately adjusted spinning angle are required. The excitation of central-transition coherences may occur, like in STMAS, as an unwanted by-product of the initial pulse; however, judicious
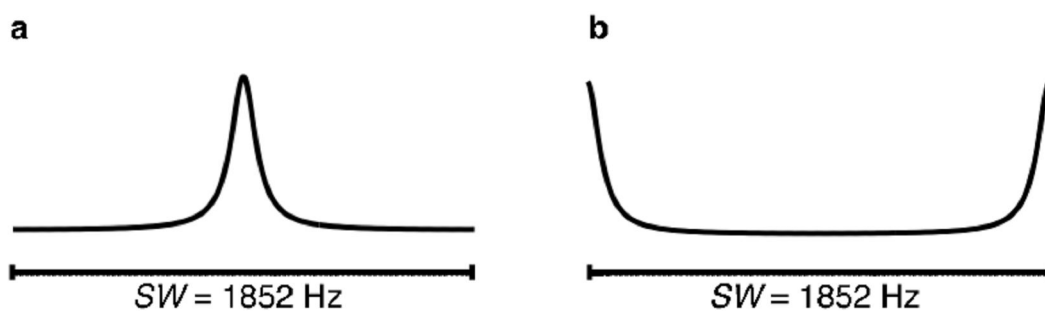
Figure 5.3. Computer-simulated spin $I = 3/2$ isotropic STARTMAS NMR spectra illustrating the spinor behaviour observed when the two inversion pulses in each STARTMAS unit are applied with (a) the opposite phase and (b) the same phase.

phase cycling of the first two pulses and of the receiver is sufficient to remove this [262, 265]. It should be noted that if the two CT-selective inversion pulses in each STARTMAS unit are applied with the same radiofrequency phase then alternate isotropic echoes are of opposite phase despite a net pulse flip angle of 360° being applied. This leads to an unwanted frequency shift of ($v_R/2n$) Hertz in the isotropic STARTMAS spectrum, as shown in Fig. 5.3, and is known as spinor behaviour [268]. This property is not exhibited by central-transition coherences, for which the application of two inversion pulses of the same phase does not effect a sign change. This difference in behaviour of the central and satellite transitions is a consequence of the former transition sharing two energy levels with the transition across which the inversion pulses are being applied and the latter only one. For satellite-transition coherences, the undesirable frequency shift that arises from spinor behaviour may be circumvented by applying two pulses with opposite phases, resulting in a net flip angle of 0°.

5.4   Data Sampling Schemes

There are several data sampling schemes that may be envisaged for STARTMAS, as illustrated in Fig. 5.4. Data points may be acquired by scheme (i), in which data is sampled continuously throughout the experiment over the wide spectral width needed for observation of spin I = 3/2 satellite transitions, by scheme (ii), sampling over the same large spectral width but only during the periods in which the satellite-transition signal is present and the first- and second-order quadrupolar interactions are refocussed, or by scheme (iii), sampling solely the points at the top of the isotropic echoes. Scheme (iii) yields a spectrum with a much smaller spectral width than schemes (i) and (ii) that is equal to the ratio of the MAS rate and the number of rotor periods in a τ period, i.e., $SW = \nu_R/n$. These schemes are illustrated in Fig. 5.4, in which computer-simulated time-domain signals and their Fourier transforms are shown.

As shown in Fig. 5.4a for the case of n = 18, scheme (i) produces a truncated time-domain signal and this leads to a spectrum containing the expected "sinc wiggles" [269]. Scheme (ii) yields a DOR-like spectrum containing isotropic sidebands whose manifold is given by the static spin I = 3/2 satellite-transition lineshape (Fig. 5.4b). It should be noted that, if the sideband spacing is given by $SW = \nu_R/n$, the spectral width is scaled by a factor of $x/9$, where x is the fraction of the satellite-transition acquisition window that is sampled. As shown in Fig. 5.4c, scheme (iii) yields an isotropic spectrum [270] that is devoid of sideband structure.
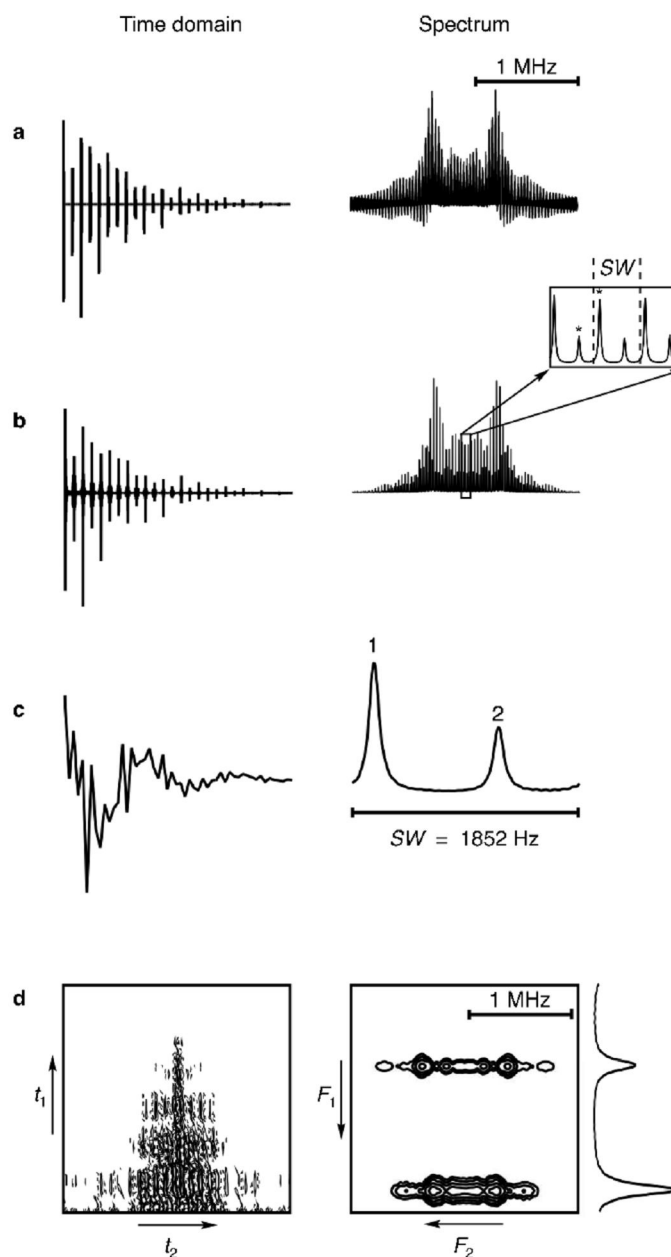
Figure 5.4. Computer-simulated time-domain and frequency-domain signals arising from four possible STARTMAS data sampling schemes. (a) Scheme (i) produces a highly truncated time-domain signal and spectrum. (b) Scheme (ii) yields a spectrum consisting of a series of isotropic spinning sidebands. The satellite-transition centrebands are indicated by asterisks. (c) Scheme (iii) yields an isotropic spectrum without a sideband manifold. (d) In scheme (iv) the whole echoes in (b) are reordered into a two-dimensional array which upon Fourier transformation yields an anisotropic-isotropic correlation spectrum. Spectra were simulated with the parameters: ν_0 = 100 MHz, ν_R = 33333 Hz, and in (b) and (d), x = 0.5. Two inequivalent sites with 2 : 1 relative populations were simulated, with the parameters C_Q = 1.6 MHz, η = 0 and δ_{CS} = 1.0 ppm (site 1) and C_Q = 2.0 MHz, η = 0 and δ_{CS} = 3.0 ppm (site 2). In the spectrum in (d) contour levels are shown at 4, 8, 16, 32 and 64% of the maximum intensity.

Of the schemes described above, (ii) and (iii) appear to be the most useful. Scheme (ii) enables the extraction of quadrupolar parameters from the envelope of the spinning sideband pattern, whilst scheme (iii) benefits from the sensitivity gain obtained when aliasing sideband intensity onto the satellite-transitions centreband. Scheme (iv), shown in Fig. 5.4d, involves using the train of echoes acquired in scheme (ii) to construct a two-dimensional array. This scheme is, of course, not a different method of data sampling, but is rather a different way of processing the data acquired using scheme (ii). The first STARTMAS whole echo forms the first row of the two-dimensional dataset, the second echo the second row, and so on. Two-dimensional Fourier transformation of this time-domain signal then yields the two-dimensional spectrum shown in Fig. 5.4d in which the static satellite-transition lineshape appears in the F_2 dimension (analogous to the ω_2 dimension defined in Section 2.7) and the isotropic spectrum in the F_1 dimension (analogous to the ω_1 dimension defined in Section 2.7). This method of data sampling (essentially analogous to methods reported for obtaining J spectra [271] and two-dimensional one-pulse (TOP) spectra [272]) would seem to be the optimum approach for acquiring STARTMAS NMR spectra, as it combines the information found in the spectra yielded by schemes (ii) and (iii).

Whilst STARTMAS suppresses the first- and second-order quadrupolar broadening, the isotropic chemical shift and second-order quadrupolar shift are not refocussed. Consequently, the isotropic STARTMAS shift, that is, the position of a given peak in the isotropic spectrum yielded by scheme (iii) and in

121

the F_1 dimension of the two-dimensional spectrum shown in Fig. 5.4d, δ_1, is given by:

$$\delta_1 = \frac{17}{9}\delta_{CS} + \frac{4}{9}\delta_Q ,$$

(5.2)

where δ_{CS} is the isotropic chemical shift and δ_Q is the quadrupolar shift, $[((\omega_Q^{PAS})^2 / \omega_0)(1 + \eta^2 / 3)]$, expressed as a ppm shift.

In the isotropic dimension of an STMAS or MQMAS spectrum obtained using either a shearing transformation, or by recording a split-t_1 experiment, both the isotropic chemical shift and quadrupolar shift are scaled. The isotropic chemical shift is scaled by a factor, x_{CS}, defined as [200]:

$$x_{CS} = -\frac{q + R(I, q)}{1 + |R(I, q)|} ,$$

(5.3)

where $R(I, q)$ is the MQMAS (or STMAS) ratio defined in Chapter 3. The coherence order of the transition evolving during the t_1 period of MQMAS or STMAS is again given by q and so takes the value $\pm 3/2$ for e.g., a triple-quantum MAS experiment. The quadrupolar shift is scaled by a factor, x_Q, given by [200]

$$x_Q = \frac{(A^0(I, q)/A^0(I, 1/2)) - R(I, q)}{1 + |R(I, q)|} .$$

(5.4)

For a split-t_1 STMAS experiment performed on a spin $I = 3/2$ nucleus, x_{CS} and x_Q thus take the values 1 and $-10/17$, respectively. Generally, these

quantities are related through the ratio

$$\frac{x_{\text{CS}}}{x_{\text{Q}}} = -\frac{17}{10} \, .$$

(5.5)

The chemical shift in the F_1 dimension of a split-t_1 MQMAS or STMAS spectrum may be expressed in the form [53]

$$\delta_1 = x_{\text{CS}}\delta_{\text{CS}} - A^0(I, 1/2)x_{\text{Q}}\delta_{\text{Q}} \, ,$$

(5.6)

and so, by comparison with Eq. (5.2), x_{CS} and x_{Q} thus have the values 17/9 and −10/9, respectively, for STARTMAS. The ratio $x_{\text{CS}}/x_{\text{Q}}$ is thus equal to −17/10, the same as is observed for MQMAS and STMAS. Consequently, the isotropic spectra produced by STARTMAS are related by a simple scaling factor to those obtained by MQMAS and STMAS.

5.5 Experimental Results

The results presented in this and the next section were processed using MATLAB programs written by Dr M. J. Thrippleton. The simulated spectra were also generated in MATLAB, by a stepwise integration of the Liouville-von Neumann equation with a summation over 3722 orientations according to the ZCW algorithm [273]. The spectra in Figs. 5.5a, 5.5b, 5.6, and 5.7 were recorded with the assistance of Dr S. Steuernagel (Bruker Biospin GmbH, Rheinstetten, Germany).

5.5.1   STARTMAS at High MAS Rates

STARTMAS NMR data were acquired at high spinning rates for four powdered solids, namely sodium oxalate, $Na_2C_2O_4$, sodium citrate dihydrate, $Na_3C_6H_5O_7 \cdot 2H_2O$, dibasic sodium phosphate, Na_2HPO_4, and rubidium nitrate. $RbNO_3$. Time-domain signals acquired with [87]Rb STARTMAS NMR of rubidium nitrate and ^{23}Na STARTMAS NMR of sodium citrate dihydrate are shown in Figs. 5.5a and 5.5b, along with their corresponding Fourier transforms (Figs. 5.5c and 5.5d), respectively. The one-dimensional DOR-like spectra shown in Figs. 5.5c and 5.5d have the expected appearance, consisting of an array of spinning sidebands which, for each crystallographically inequivalent site present in each solid (three in both rubidium nitrate [221] and sodium citrate dihydrate [164]), have an envelope corresponding to the static satellite-transition first-order quadrupolar broadened lineshape. It should be noted that in Fig. 5.5c, two of the sites in rubidium nitrate are coincident at this magnetic field strength due to the combined effect of the isotropic chemical shift and the second-order quadrupolar shift. The areas of intensity that fall below the baseline in Figs. 5.5c and 5.5d are consistent with the zero total integral of these spectra, this being a consequence of pulse-ringdown effects that preclude acquisition of the first half echo and so lead to a zero first point. Inspection of Figs. 5.5c and 5.5d reveals that the spinning sidebands are not spaced by the spinning speed, 33333 Hz. Owing to the non-continuous data sampling (points are collected only during part of the satellite-transition acquisition window), the sideband spacing is scaled by a factor $1/2x$ (where x is the fraction of the
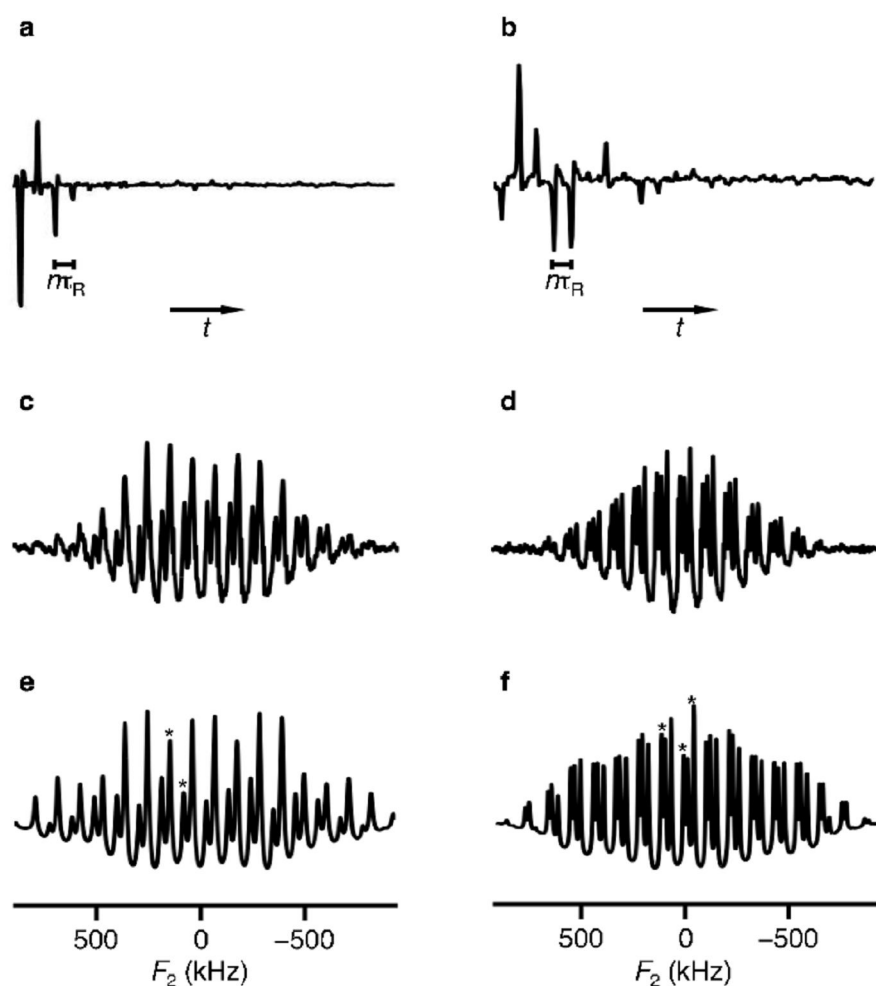
Figure 5.5. Time-domain data acquired using (a) ^{87}Rb STARTMAS NMR of rubidium nitrate and (b) ^{23}Na STARTMAS NMR of sodium citrate dihydrate and the corresponding one-dimensional spectra (c) and (d), respectively. Experiments were performed at B_0 = 11.7 T and a MAS rate of 33333 Hz. The n = 18 STARTMAS condition was used with x = 0.133, and 1584 and 1024 transients were averaged for rubidium nitrate and sodium citrate dihydrate, respectively. The initial excitation pulse had duration in the range 1.2–1.5 μs and the selective inversion pulses had duration 20 μs. Computer-simulated spectra in (e) and (f) were generated using literature NMR parameters [53, 164] for rubidium nitrate and sodium citrate dihydrate, respectively. The centrebands are indicated by asterisks.

satellite-transition acquisition window that is sampled, defined previously in Section 5.4), such that the separation of the sidebands is now 125 kHz. The computer-simulated spectra shown in Figs. 5.5e and 5.5f broadly agree with the experimental data.

It should be noted that the spectra in Figs. 5.5c–f are poorly suited to quantitative analysis, as a consequence of the baseline dip that results from the zero first point in the time domain data in Figs. 5.5a and 5.5b. This may be circumvented by a left shift of the time-domain data such that it begins at the top of the first whole echo. After one-dimensional Fourier transformation a large first-order phase correction is required, but this can easily be performed. This yields a spectrum like that shown in Fig. 5.4b, although the spectrum shown there was simulated by making the (experimentally unrealistic) assumption of infinitely short pulses, such that the first half echo could be acquired.

Figure 5.6 presents the two-dimensional ^{87}Rb STARTMAS NMR spectra of rubidium nitrate, generated by Fourier transformation of data acquired using the scheme shown in Fig. 5.4d. The simulated spectrum in Fig. 5.6a matches well the experimental spectrum in Fig. 5.6c, where the two coincident sites are seen to be partly aliased. Projections along the F_1 dimension of each spectrum are shown in Figs. 5.6b and 5.6d, where the isotropic spectral width equals $v_R/18$ = 1852 Hz. The three crystallographically inequivalent sites in rubidium nitrate have the quadrupolar parameters [53]: C_Q = 1.70 MHz, η = 0.6, C_Q = 1.70 MHz, η = 0.2 and C_Q = 2.00 MHz, η = 0.9 and are labelled 1, 2 and 3 in Fig. 5.6, respectively. The corresponding peaks of each site in the isotropic spectra have intensities that are consistent with their 1 : 1 : 1 population ratio [221].

Two-dimensional ^{23}Na STARTMAS NMR spectra of sodium citrate dihydrate are shown in Fig. 5.7, obtained via the data sampling scheme in Fig.
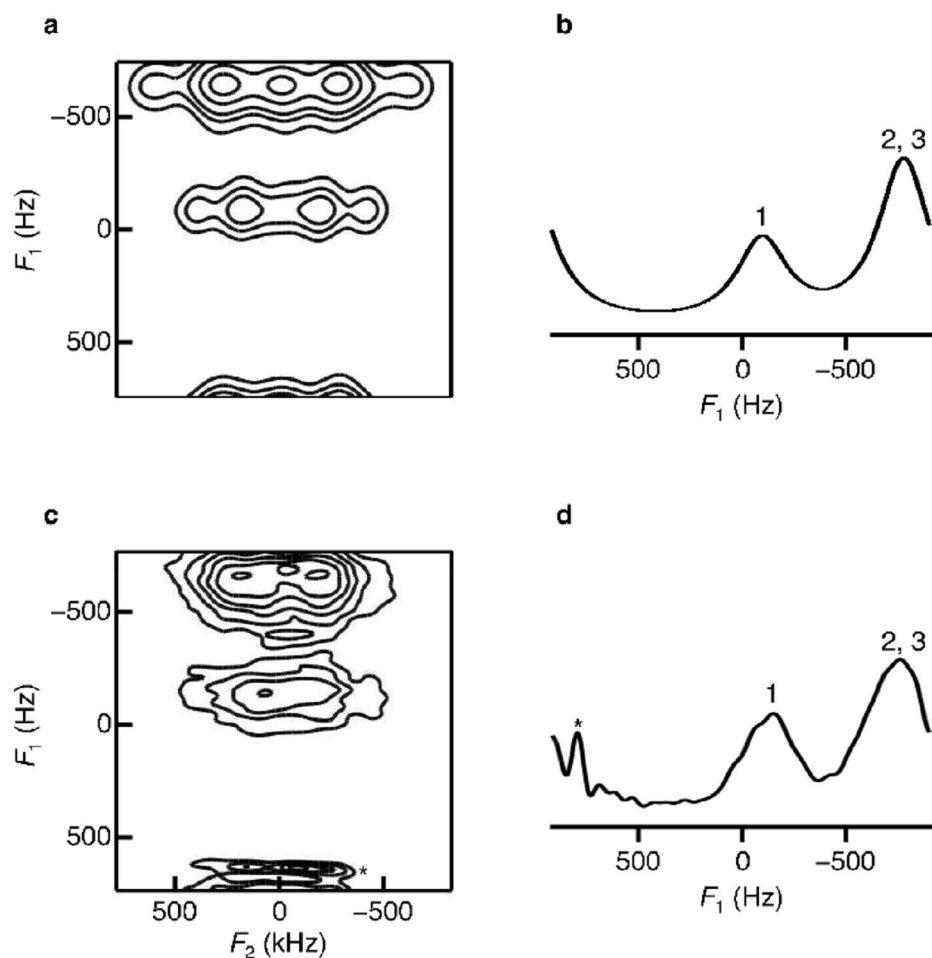
Figure 5.6. (a) Computer-simulated and (c) experimental two-dimensional ^{87}Rb STARTMAS NMR spectra of rubidium nitrate. The spectrum in (a) was generated using literature NMR parameters [53] and (c) was obtained from the one-dimensional time-domain data in Fig. 5.5a. The asterisked peak is present as a consequence of imperfections associated with the experimental implementation. Corresponding F_1 projections are shown in (b) and (d). Contour levels in (a) and (c) are shown at 20, 35, 50, 65, 80 and 95% of the maximum intensity.

5.4d. The three inequivalent ^{23}Na sites present in this material are seen to be well-resolved in the F_1 projections in Figs. 5.7b and 5.7d and have values of the quadrupolar product, P_Q [107], equal to 1.87 MHz, 1.65 MHz and 1.90 MHz for sites 1, 2 and 3, respectively [274]. As in rubidium nitrate, the relative peak intensities concur well with the 1 : 1 : 1 population ratio [164] for the three sites in the solid.
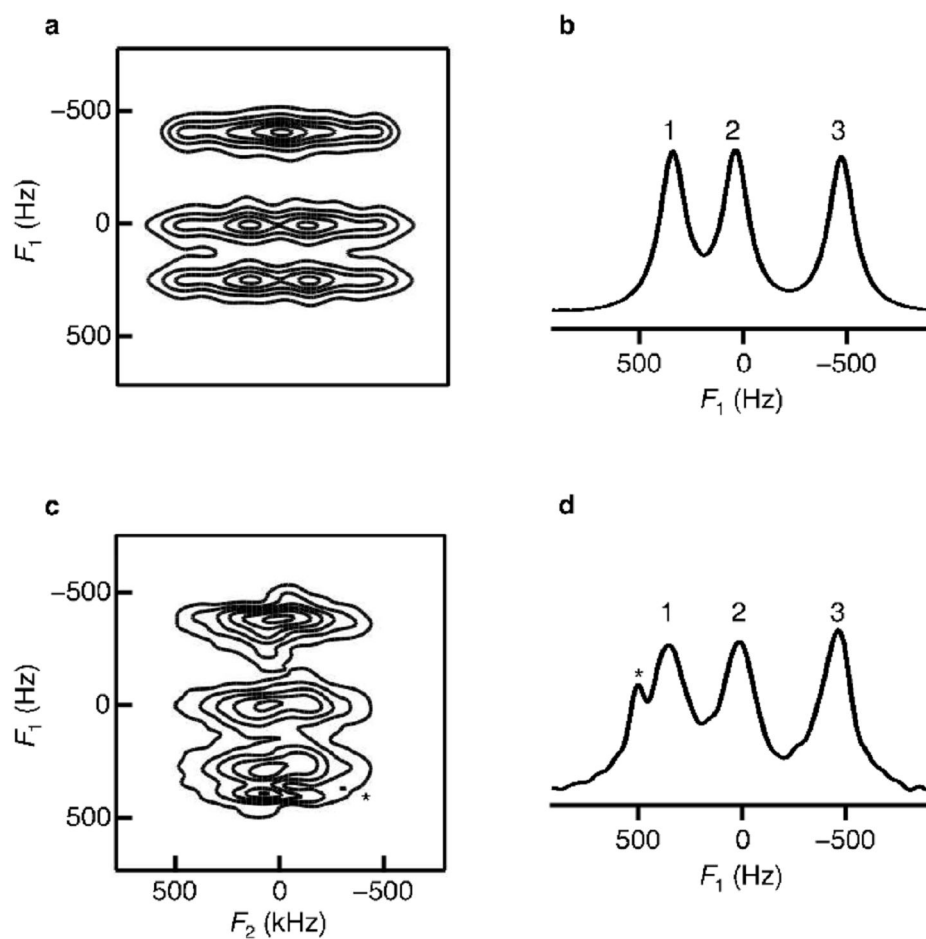
Figure 5.7. (a) Computer-simulated and (c) experimental two-dimensional ^{23}Na STARTMAS NMR spectra of sodium citrate dihydrate. The spectrum in (a) was generated using literature NMR parameters [274] and (c) was obtained from the one-dimensional time-domain data in Fig. 5.5b. Contour levels in (a) and (c) are shown at 20, 35, 50, 65, 80 and 95% of the maximum intensity. The "spike" marked with an asterisk arises due to imperfections in the experimental implementation. Corresponding F_1 projections are shown in (b) and (d).

^{23}Na STARTMAS NMR spectra of sodium oxalate and dibasic sodium phosphate were also acquired and are shown in Figs. 5.8a and 5.8c, respectively. The two-dimensional spectra and corresponding F_1 projections shown in Figs. 5.8b and 5.8d are consistent with the presence of one [275] and three [276] inequivalent sites, respectively. The three inequivalent sites in dibasic sodium phosphate have C_Q values of 3.8, 1.3 and 2.0 MHz for sites, 1, 2 and 3, respectively [248]. The odd F1 chemical shift scale in Figs. 5.8c and 5.8d

128
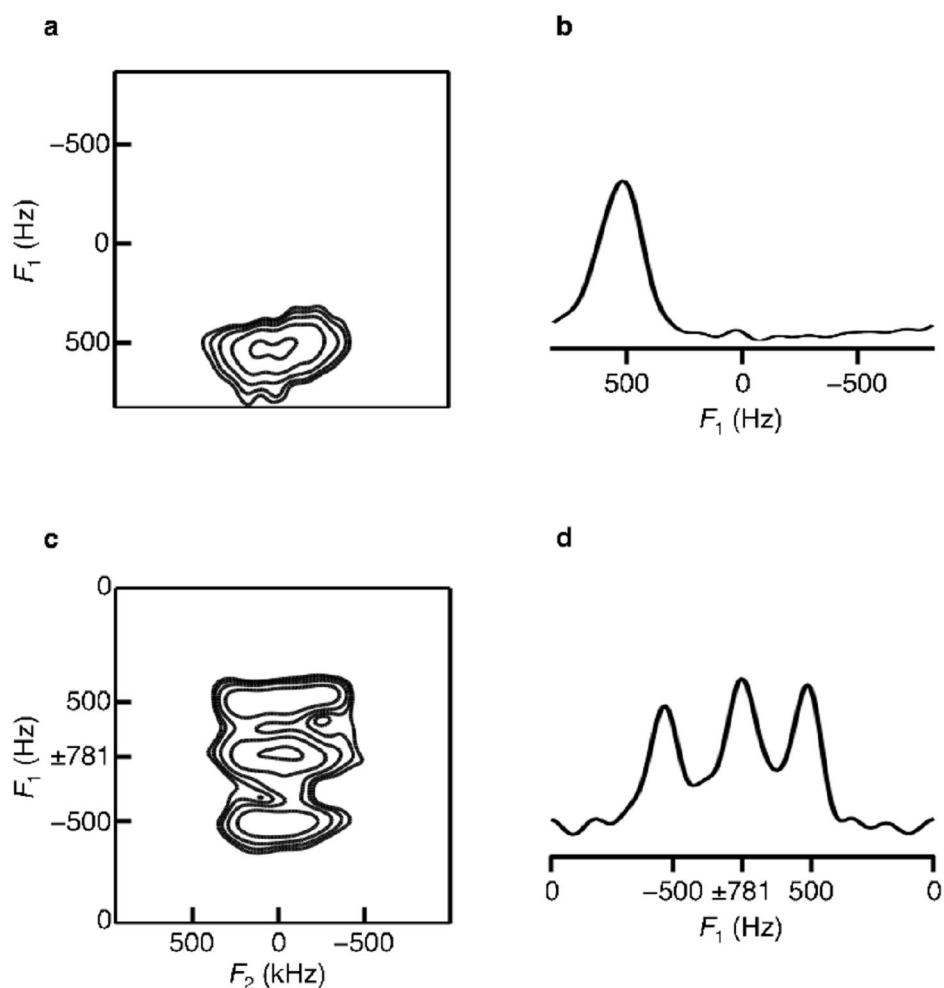
Figure 5.8. Two-dimensional ^{23}Na (n = 18) STARTMAS NMR spectra of (a) sodium oxalate and (c) dibasic sodium phosphate. Spectra were acquired at B_0 = 9.4 T and a MAS rate of (a) 30000 Hz and (c) 28125 Hz, so leading to isotropic spectral widths equal to 1666 Hz and 1562 Hz, respectively. F_1 projections are shown in (b) and (d). Satellite-transition excitation pulses of 2.0–2.2 μs were used and the CT-selective pulses had duration 30 μs. Contour levels in (a) and (c) are shown at 20, 35, 50, 65, 80 and 95% of the maximum intensity.

arises as a consequence of one of the peaks being at the edge of the spectral width such that half of it is aliases. Rearranging the spectrum in this way enables the 3 sites to be clearly seen.

It was shown in Chapter 4 that, for the case of MQMAS, the efficiency of both the excitation and conversion pulses varies with ω_Q. STMAS shows a similar, although less pronounced, variation in signal intensity with C_Q [53]

and, like MQMAS, is a non-quantitative technique. This has been illustrated using dibasic sodium phosphate, where the intensity ratio 1.1 : 1.0 : 0.7 (observed in STMAS) and 0.4 : 1.0 : 0.5 (in MQMAS) [53] does not concur with the 2 : 1 : 1 relative site population predicted from the crystal structure [275]. The F_1 projection of dibasic sodium phosphate shown in Fig. 5.8d reveals that the three sites yield peaks in the approximate intensity ratio 0.8 : 1.0 : 0.9. Given that STARTMAS involves the excitation of satellite-transition coherences, the similarity of this ratio to that obtained using STMAS is not surprising.

5.5.2   Ultrafast STARTMAS NMR

Under conditions of high sensitivity, such as at very high static magnetic fields or with large sample volumes, STARTMAS may be described as "ultrafast". In contrast to two-dimensional methods like MQMAS and STMAS, STARTMAS is not limited by data sampling requirements (such as that of the t_1 period in the former two techniques) and so is limited only by sensitivity considerations. To demonstrate the ability of STARTMAS to produce ultrafast spectra, ^{87}Rb STARTMAS NMR spectra of rubidium nitrate were recorded using a 4.0-mm MAS probe to maximise sample volume. As the achievable spinning speeds are much lower on this probe than on the 2.5-mm probe used for obtaining the spectra in Figs. 5.5–5.7, the $n = 9$ condition was used to maximise the isotropic spectral width. The two-dimensional spectra and corresponding F_1 projections are shown in Fig. 5.9 with that in Fig. 5.9a
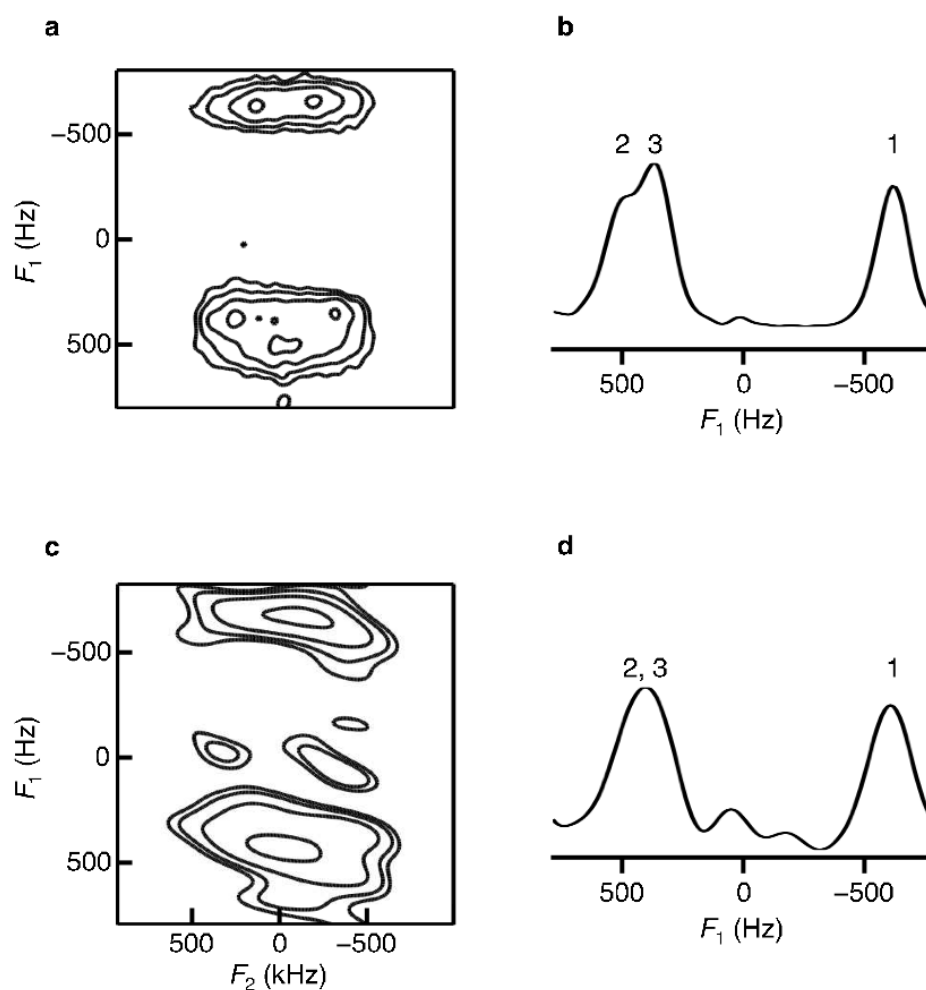
Figure 5.9. Two-dimensional ^{87}Rb STARTMAS NMR spectra of rubidium nitrate recorded at B_0 = 9.4 T with (a) 1024 transients and (c) 1 transient. The MAS rate was 14286 Hz and the n = 9 STARTMAS condition was used, so producing an isotropic spectral width of 1587 Hz. Inversion pulses of 30 μs were used and the satellite-transition excitation pulse had duration 1.8 μs. Corresponding F_1 projections are shown in (b) and (d), where the 3 sites are indicated by asterisks. Contour levels in (a) and (c) are shown at 15, 25, 45, and 85% of the maximum intensity.

recorded with 1024 transients and that in Fig. 5.9c recorded with a single transient. The spectrum in Fig. 5.9a reveals the expected three sites (labelled 1, 2 and 3, in the same way as in Fig. 5.6) present in rubidium nitrate (two of them no longer being coincident due to the experiment being performed at a different magnetic field strength than in Figs. 5.5 and 5.6). In Fig. 5.9c, these two sites again appear as one peak, this being due to the line broadening resulting from

the severe processing that was required to maximise the signal-to-noise ratio in this spectrum. Despite this, peaks are observed at the expected frequencies and so clearly STARTMAS can be used, under the right conditions, to produce ultrafast NMR spectra of spin $I = 3/2$ nuclei.

5.5.3   STARTMAS with $n \neq 18$

All of the STARTMAS spectra presented so far were obtained using either $n = 9$ or 18. It is highly desirable to rotor-synchronize pulses in experiments involving satellite transitions, as this ensures complete removal of the first-order quadrupolar broadening. The requirement for rotor-synchronization in STARTMAS limits the minimum value of n to 18 (for rotor-synchronization of all pulses) or to 9 (for the selective inversion pulses only).

Whilst all values of n between 1 and 18 are theoretically possible, no lower than $n = 5$ is realistically achievable. Commonly achievable MAS rates do not currently exceed ~35 kHz, leading to a STARTMAS cycle duration, $n\tau_R = 143$ μs, for $n = 5$. Any shorter duration of the STARTMAS cycle is likely to lead to pulse-ringdown effects affecting the acquisition windows and, whilst this may be alleviated by using slower MAS rates, the isotropic spectral width will be reduced. Consequently, higher MAS rates are to be preferred and so n should be no less than 5.

Two-dimensional STARTMAS NMR spectra of rubidium nitrate were acquired for different values of n and are shown in Fig. 5.10. The F_1 projections
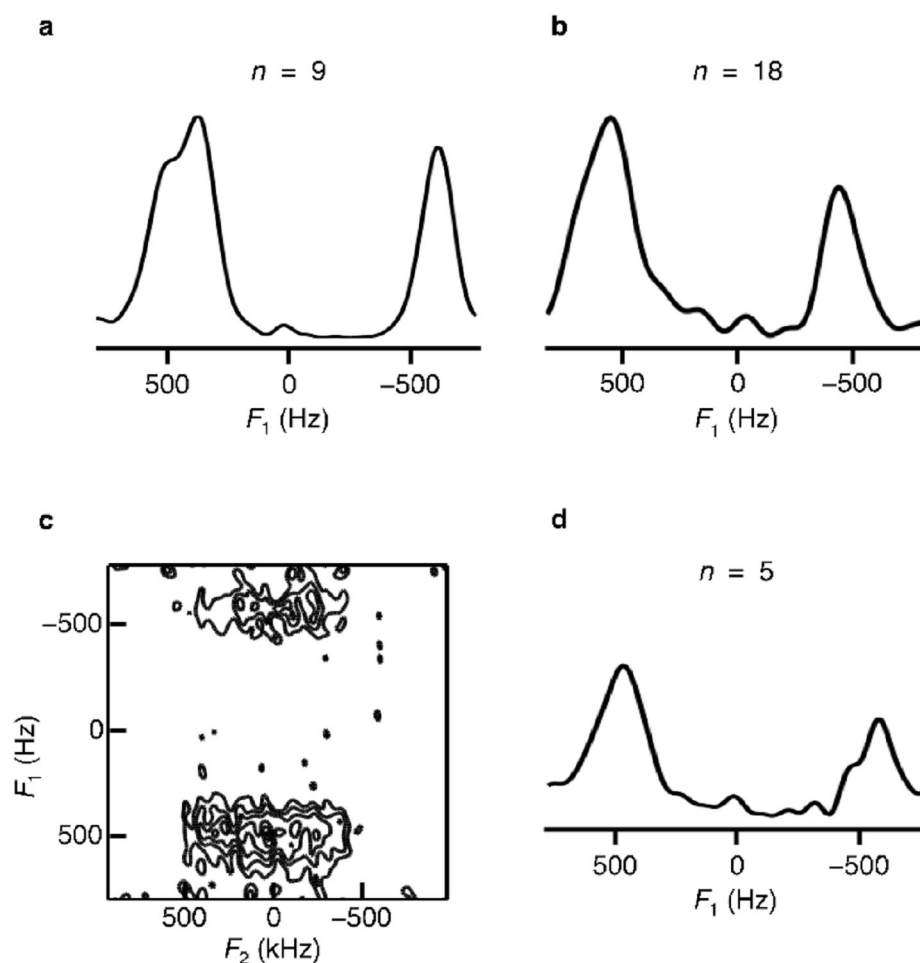
Figure 5.10. [87]Rb STARTMAS NMR spectra of rubidium nitrate, acquired using different values of n. (a) F_1 projection of the STARTMAS spectra recorded using (a) $n = 9$ and (b) $n = 18$. (c) Two-dimensional spectrum recorded with $n = 5$ and (d) the corresponding F_1 projection. The spectra were obtained at $B_0 = 9.4$ T, using MAS rates of (a) 14286 Hz, (b) 30000 Hz and (c) 7937 Hz. CT-selective pulses of duration 30 μs were used and the satellite-transition excitation pulse had duration 2.0–2.2 μs. Contour levels in (c) are shown at 20, 35, 50, 65, 80 and 95% of the maximum intensity.

obtained from the spectra acquired using $n = 9$ and 18 are shown in Figs. 5.10a and 5.10b, respectively. These two conditions, corresponding to complete ($n = 18$) and partial ($n = 9$) rotor-synchronization lead to isotropic STARTMAS spectra of comparable resolution and linewidths. The $n = 9$ condition appears to resolve the two [87]Rb sites that have very similar positions in the F_1 dimension, whilst in the $n = 18$ case, these two sites are not separated. There is

no obvious reason for this differing resolution, other than the different characteristics of the 2 different probes used for acquiring the $n = 9$ and $n = 18$ data. In both cases, good signal-to-noise ratios are obtained and peaks appear at the expected positions, so clearly, using either $n = 9$ or 18 is an acceptable way of recording STARTMAS spectra. In Fig. 5.10c, however, the spectrum acquired using $n = 5$ possesses a worse signal-to-noise ratio than the $n = 9$ and 18 spectra. This is clearly seen in the projection in Fig. 5.10d, where much broader and more distorted lineshapes are observed. It would thus seem that the performance of STARTMAS is optimum when rotor-synchronization ($n = 9$ or 18) is used.

5.5.4   *Extraction of Quadrupolar Parameters*

As is the case for MQMAS and STMAS, F_2 projections of two-dimensional STARTMAS spectra yield lineshapes whose width and shape are indicative of the size and asymmetry of the quadrupolar tensor. In contrast to MQMAS and STMAS, where the lineshapes typically have widths ~kHz, those obtained from STARTMAS are usually ~MHz wide. Consequently, F_2 lineshapes obtained from STARTMAS spectra are susceptible to probe bandwidth distortions and so quadrupolar parameters obtained using this method are likely to be less accurate than those obtained using other methods.

F_2 lineshapes extracted from the two-dimensional [87]Rb STARTMAS NMR spectrum of rubidium nitrate from which the F_1 projection in Fig. 5.10b was
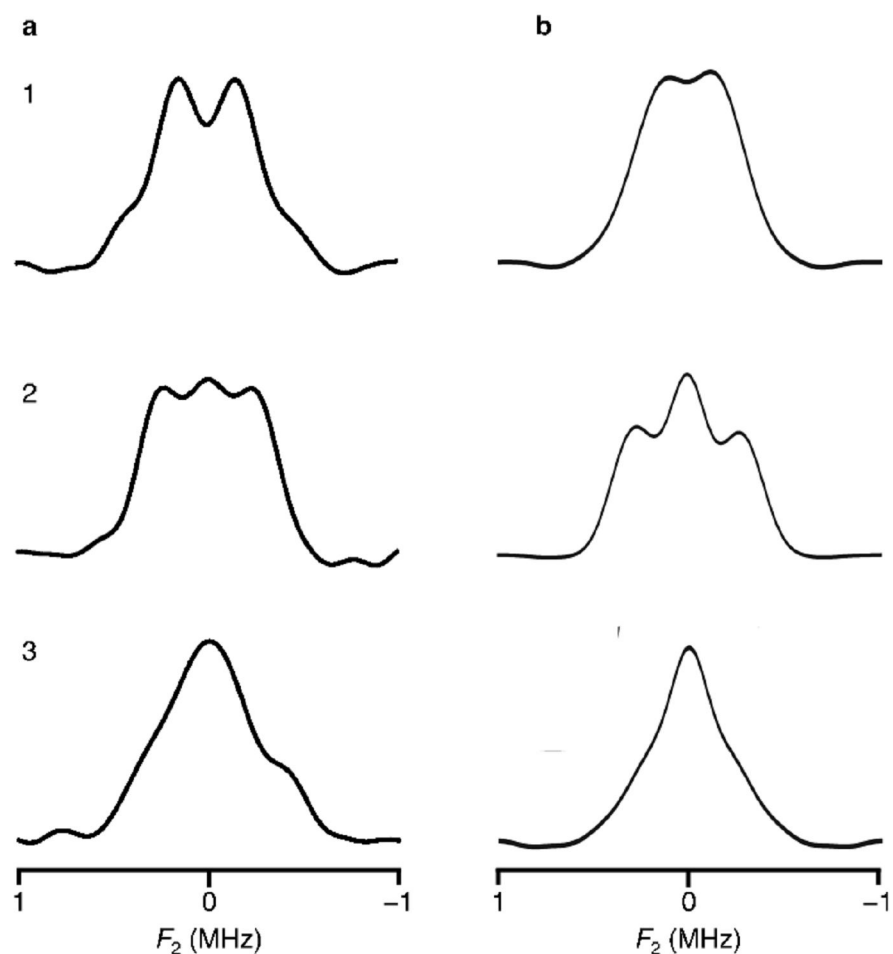
Figure 5.11. (a) Experimental and (b) simulated F_2 lineshapes from ^{87}Rb STARTMAS NMR spectra of rubidium nitrate. The lineshapes in (a) were obtained from the spectrum used for the F_1 projection in Fig. 5.10b.

extracted are shown in Fig. 5.11a. Computer-simulated spectra are shown in Fig. 5.11b for each site, labelled 1, 2 and 3. These sites have been previously found to have asymmetry parameters of 0.6, 0.2 and 0.9, respectively [53]. The experimental cross sections are seen to match well with the simulated spectra, although there are distortions evident in the former. A possible source of these distortions is the finite bandwidths of the probes used.

For the extraction of quadrupolar parameters, F_2 cross sections were simulated for a range of C_Q and η values for the rubidium nitrate $n = 9$
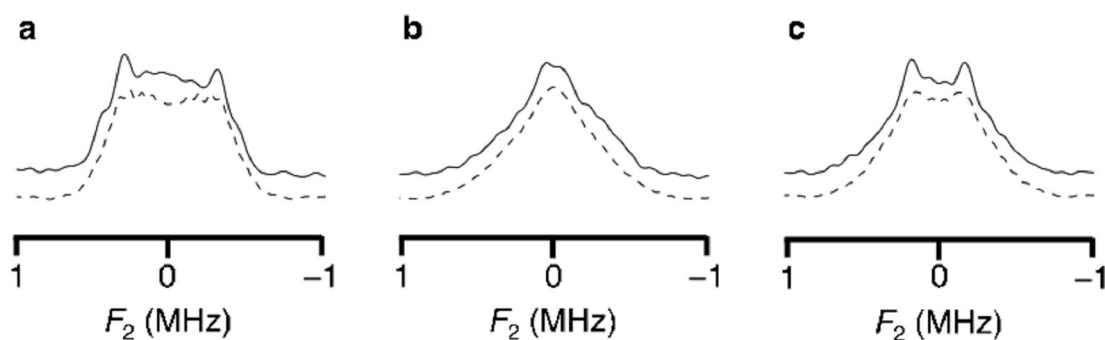
Figure 5.12. Experimental (solid line) and best-fit (dashed line) F_2 cross sections of rubidium nitrate $n = 9$ STARTMAS data used in Fig. 5.10a.

STARTMAS NMR data from which the F_1 projection in Fig. 5.10a was obtained. The spectra were generated using the experimental parameters, including finite pulse widths, and by applying an absorptive Lorentzian function (0.65 MHz linewidth at half-height) to simulate bandwidth effects. The resultant best-fit cross sections are shown in Fig. 5.12.

The best-fit spectra in Figs. 5.12a–c yield quadrupolar coupling constants of 1.75, 1.50 and 1.88 MHz, which compare favourably (with the exception of Fig. 5.12b) with the literature values [136] of 1.68, 1.94 and 1.72 MHz, respectively. The asymmetry parameters obtained from these cross sections have the values of 0.2, 0.85 and 0.55, which agree well with the literature values [136] of 0.2, 1.0 and 0.5, respectively. As in MQMAS and STMAS spectra, the peak positions in each dimension of a STARTMAS spectrum depend on δ_{CS} and δ_Q, from which the quadrupolar product, P_Q, may be obtained. Given the distortions that may exist in the broad F_2 lineshapes obtained from STARTMAS spectra, it would seem likely that extraction of quadrupolar parameters from a knowledge of the F_1 and F_2 peak positions (as shown in Chapter 3 for MQMAS

and STMAS) is a preferable method to the fitting procedure shown in Fig. 5.12.

5.6   Applications of STARTMAS

5.6.1   Isotropic-Isotropic Correlation

There have been several reports in the literature of experiments that enable connectivity information for quadrupolar nuclei in the solid state to be obtained [127, 277–281]. Magnetization transfer between inequivalent sites can provide site-specific information and this has enabled the relative orientation of quadrupolar tensors to be obtained via two-dimensional triple-quantum NOESY experiments [277, 280]. In addition, MQMAS has been incorporated into three-dimensional experiments and CSA and dipolar coupling parameters have been obtained [279]. The experiments detailed in Refs. [277–280] yield spectra in which there is an absence of anisotropic broadening (CSA, dipolar or quadrupolar in origin) in only one dimension. In Refs. [127] and [281], however, a two-dimensional correlation experiment derived from DOR is introduced that produces a spectrum that is isotropic in both dimensions. This is useful in cases where the overlap of peaks from inequivalent sites can limit the information that may be obtained from correlation spectra. Given the fact that STARTMAS can, like DOR, produce isotropic spectra in real time, a homonuclear correlation experiment derived from STARTMAS could thus prove a useful technique for establishing connectivities between quadrupolar nuclei in the solid state. Such an experiment would also not be hindered by the technical requirements that
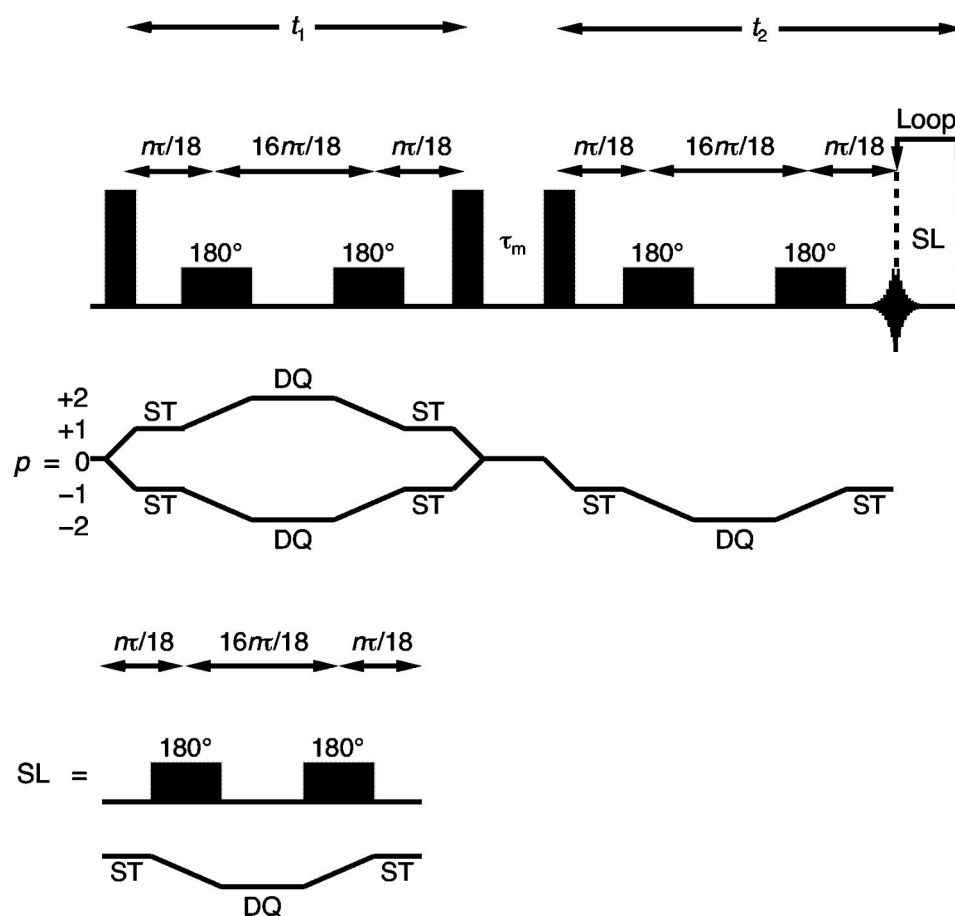
Figure 5.13. Pulse sequence and coherence transfer pathway for the STARTMAS isotropic-isotropic correlation experiment. The SHR method is used to ensure frequency discrimination in the F_1 dimension. The repeat STARTMAS unit during the t_2 period is denoted "SL".

limit the applicability of DOR.

The pulse sequence for a homonuclear correlation experiment is shown in Fig. 5.13. In this experiment, STARTMAS evolution during both time periods of a two-dimensional experiment yields a two-dimensional spectrum that is isotropic in both dimensions and so is akin to NOESY [282] spectra observed in solution-state NMR. The t_1 and t_2 periods sandwich a mixing time, τ_m, during which magnetization transfer between inequivalent sites can occur.

Two-dimensional ^{23}Na STARTMAS NMR correlation spectra of sodium

citrate dihydrate are shown in Fig. 5.14, recorded using the pulse sequence in Fig. 5.13. ^{1}H decoupling was applied during the t_1 and t_2 periods, but not during the mixing time, so as to enable proton-driven spin diffusion [283] to occur between the ^{23}Na nuclei. The spectrum in Fig. 5.14a, recorded with a zero mixing time, shows the expected 3 diagonal peaks for the 3 inequivalent sites in this material. In Fig. 5.14b, where the mixing time is 245 ms, there appears to be a cross peak between the two lowest frequency sites. F_2 cross sections taken at the F_1 frequency of this cross peak are shown alongside the spectra in Figs. 5.14a–d. It should be noted that these cross sections are not shown with the correct relative intensities; these have been adjusted so that the diagonal peak intensity appears constant and so that any changes in cross peak intensity may be more clearly observed. There is, of course, a significant loss of intensity between the experiments in Fig. 5.14a and 5.14d due to ^{23}Na T_1 relaxation.

The spectra in Fig. 5.14c and 5.14d, acquired at mixing times of 490 ms and 980 ms, respectively, reveal a continual growth in cross peak signal intensity, although in Fig. 5.14d this peak has an intensity not much greater than the background noise signal. A cross peak partner at a position obtained by reflection about the diagonal spectral axis is virtually absent, until the spectrum in Fig. 5.14d, where it appears with much lesser intensity. This feature is unsurprising if the intensity of the diagonal peaks in Fig. 5.14a is considered. The diagonal peak shown in the F_2 cross sections alongside Figs. 5.14a–d has much greater intensity than that arising from the 2 other sites in sodium citrate dihydrate, this of course being a consequence of the non-quantitative nature of
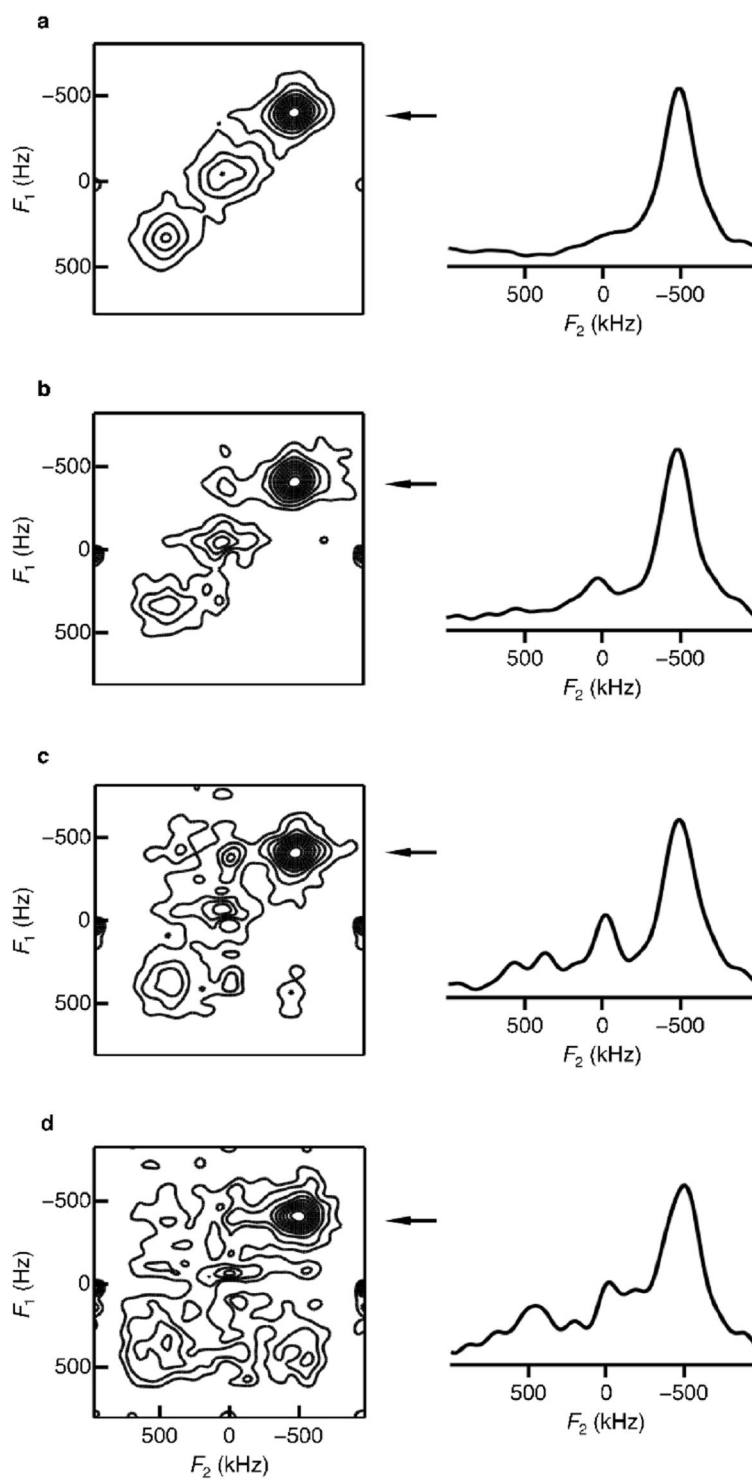
Figure 5.14. Two-dimensional ^{23}Na STARTMAS NMR correlation spectra of sodium citrate dihydrate recorded with a mixing time of (a) 0, (b) 245 ms, (c) 490 ms and (d) 980 ms. Alongside each spectrum is the F_2 cross section corresponding to the most intense diagonal peak. All experiments were performed at B_0 = 9.4 T, a MAS rate of 14286 Hz and with n = 9. The CT-selective, satellite-transition excitation and z-filter pulses had duration 30 µs, 2.0 µs and 2.0 µs, respectively. Contour levels in (a–d) are shown in 10% increments in the range of 5–95% of the maximum intensity.

satellite-transition excitation. Given that the intensity of the cross peaks is dependent on the amount of magnetization present at the end of the t_1 period on the spin from which the magnetization was transferred during the mixing time, the greater intensity of cross peaks arising from transfer from the spin yielding the most intense diagonal peak is not surprising.

This experiment was repeated on rubidium nitrate and sodium metasilicate pentahydrate, $Na_2SiO_3 \cdot 5H_2O$, (results not shown). No cross peaks were observed for rubidium nitrate; this is most likely a consequence of (i) the relatively short T_1 relaxation times in this material (less than 200 ms for all 3 sites), (ii) the 40% natural abundance of ^{87}Rb nuclei that increases the average distance between adjacent ^{87}Rb nuclei and (iii) the absence of ^1H nuclei that removes the possibility of enhanced spin diffusion between ^{87}Rb nuclei. In sodium metasilicate pentahydrate, for which exchange peaks between the two inequivalent sites have been reported previously [280], a pair of cross peaks was observed. As in the case of sodium citrate dihydrate, a significant disparity in the intensity of the cross peaks was observed, this most likely being attributable once again to the non-quantitative nature of satellite-transition excitation.

Reports of magnetization transfer between quadrupolar nuclei have generally yielded cross peaks of low intensity [277–280], although the absence of anisotropic broadening in correlation spectra obtained using STARTMAS would suggest that any cross peaks observed would have greater relative intensity. The spectra shown in Fig. 5.14 do not confirm this view, although

they do demonstrate the ease with which isotropic-isotropic correlation spectra may be obtained. In the absence of real-time data acquisition, such spectra may only be obtained via three-dimensional experiments, which, in many cases, may require a prohibitively long duration.

5.7   Conclusions

The new STARTMAS experiment has been shown to produce isotropic spectra of spin I = 3/2 nuclei in real time; this could only previously be achieved using specialist DOR probes. STARTMAS has been demonstrated on a range of powdered solids and, in cases of high sensitivity, spectra may be obtained using very few transients, or even just a single transient. It has been shown that STARTMAS can be performed at any value of n ≥ 5 but, for optimum results, the n = 9 or 18 conditions should be used. In addition, lineshape fitting procedures have been used to demonstrate the utility of STARTMAS spectra in obtaining quadrupolar parameters, although the susceptibility of the lineshapes to distortions due to probe and filter bandwidth effects means that such parameters are likely to be less reliable than those obtained by other means. The ability of STARTMAS to produce isotropic-isotropic correlation spectra has been shown and this application of the technique would appear to offer much promise.

One of the greatest challenges remaining for STARTMAS is to extend the method to spin I = 5/2 nuclei. The fourth-rank coefficients, $A^4(I, q)$, for the

inner satellite ($m_I = \pm1/2 \leftrightarrow \pm3/2$) and inner double-quantum ($m_I = \pm3/2 \leftrightarrow \mp1/2$) transitions of all nuclei with spin $I > 3/2$ are of the same sign and so the current approach to STARTMAS will fail in such cases. For nuclei with spin $I > 3/2$, interconversion of satellite and double-quantum coherences of opposite sign is thus needed. There are currently no known pulse schemes that can perform this conversion with the high efficiency required for real-time data acquisition.

The isotropic spectral width obtained in STARTMAS is small compared to that typically seen in MQMAS and STMAS spectra. This can, in many cases, lead to considerable aliasing and unwanted peak overlap may occur. Another improvement which would prove useful for STARTMAS is thus an increase in spectral width, which is constrained by the spinning frequency, the length of the selective pulses and the rotor-synchronization requirements. Finally, the use of MAS probes with larger bandwidths would enable extraction of F_2 lineshapes that are a more accurate reflection of the quadrupolar tensors characterising the satellite transitions.

Chapter 6

NOE Studies of Borane Adducts

6.1   Introduction

The nuclear Overhauser effect (NOE) [59, 61] is one of the most widely exploited phenomena in NMR and is well known as a means of determining molecular structure in solution. The effect arises through cross-relaxation driven by the modulation of the dipolar interaction between two spatially proximate spins, conventionally labelled I and S. Upon perturbation of the populations of the S-spin energy levels, cross-relaxation processes act to return the populations of the energy levels to their equilibrium values. This has the simultaneous effect of altering the population differences across the I-spin transitions, so leading to the observed increase or decrease in I-spin signal intensity.

Modulation of the dipole-dipole interaction arises due to the presence of molecular motion on the correct timescale. In the solution state, this motion exists as a result of the rapid, random tumbling. In the solid state, such motion is rarely observed due to the structural rigidity imposed on the molecules and consequently NOEs are typically not observed. The exceptions to this have mainly been in polymeric hydrocarbon derivatives, where the rapid rotation of methyl groups about their C_3 axes leads to $^{13}C\{^1H\}$ NOEs [64–66], and in the

case of adamantane and other "plastic crystals", where modulation of the heteronuclear dipolar interaction by isotropic molecular tumbling leads to enhancement of the ^{13}C signal intensity.

NOEs to quadrupolar nuclei are rarely observed, this being due to the typically much greater efficiency of quadrupolar relaxation than dipolar cross-relaxation. Given that quadrupolar spin-lattice relaxation is proportional to the square of C_Q, solution-state NOEs are only likely to be observed for nuclei with small quadrupole moments (e.g., ^{2}H and ^{6}Li, both with spin I = 1), or for quadrupolar nuclei in highly symmetric environments. Reports of NOEs to quadrupolar nuclei have been mainly confined to ^{6}Li [67, 284, 285] and ^{7}Li (spin I = 3/2) [286] nuclei.

Unusually, the presence of a ^{11}B{^{1}H} transient NOE in solid borane triphenylphosphine, $BH_3 \cdot PPh_3$, has recently been reported in an MAS NMR experiment [287]. The existence of an NOE in this case has been attributed to the presence of rapid rotation of the BH_3 group about its C_3 axis that modulates the ^{11}B{^{1}H} dipolar interaction. The absence of strong quadrupolar relaxation in this case is most likely due to the coincidence of the ^{11}B quadrupolar tensor and the C_3 symmetry axis. This has the effect that rotation of the BH_3 group leads to very little modulation of the ^{11}B quadrupolar interaction and thus inefficient quadrupolar relaxation.

In this chapter, ^{11}B{^{1}H} NOE results are presented for a series of borane adducts. ^{11}B{^{1}H} transient NOE experiments are used to obtain ^{11}B NMR

enhancements in a range of phosphine- and amine-derived borane adducts under MAS conditions and the results are compared and a rationale proposed for the trends seen. The ^{11}B{^{1}H} enhancement of the ^{11}B satellite transitions is obtained and a triple-quantum filtered transient NOE experiment is used for the analogous measurement for the ^{11}B triple-quantum transition. Variable-temperature NMR results are presented that demonstrate the variation of the ^{11}B{^{1}H} NOE enhancement in borane triphenylphosphine and the results obtained are considered in terms of the measured spin-lattice relaxation times and with the aid of theoretical calculations. A comparison of the NOE enhancements observed under static and MAS conditions is also made and theoretical arguments are used to rationalise the behaviour in the former case.

6.2   Theory

6.2.1   The Heteronuclear NOE

The nuclear Overhauser effect may be explained simply by considering the nuclear spin energy levels involved. Take, for example, the case of a heteronuclear IS dipolar-coupled spin pair, where I = ^{13}C (spin I = 1/2) and S = ^{1}H (spin I = 1/2). The energy levels of such a system are shown in Fig. 6.1, where the numbers shown above each energy level signify the relative deviations of their populations from a fully saturated state by assuming that γ_S/γ_I = 4. Shown in Fig. 6.1a are the energy levels at thermal equilibrium with the I- and S-spin transitions indicated. In Fig. 6.1b the energy levels are shown
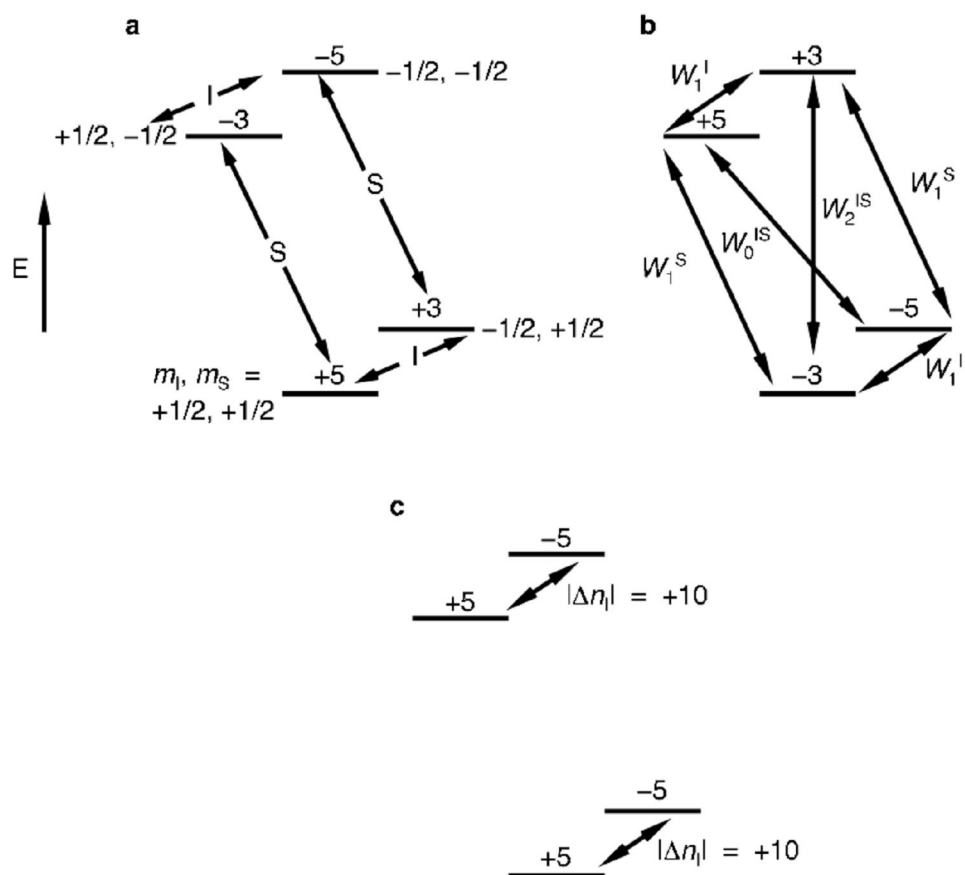
Figure 6.1. Energy levels of an IS heteronuclear spin pair for the case where I = ^{13}C and S = ^{1}H, depicted at (a) thermal equilibrium, (b) after inversion of the populations of the S-spin energy levels and (c) after cross-relaxation via the double-quantum (W_2^{IS}) pathway has restored the population difference between the energy levels indicated.

for the case where the populations of the S-spin energy levels are inverted (as in a transient NOE experiment). After perturbation of the populations of the S-spin energy levels, which leaves the population difference across the I-spin transitions unaffected, relaxation pathways act to return the populations of certain energy levels to their equilibrium values, as indicated in Fig. 6.1b. The W_1^I and W_1^S pathways correspond to a transition between the I- and S-spin energy levels, respectively, with the one subscript indicating that the transition involves a net change of magnetic quantum number, $|\Delta m_I|$, of one. Relaxation via this pathway simply corresponds to spin-lattice relaxation of the I and S

spins and so leads to the energy levels being populated as in Fig. 6.1a. There are two other pathways that can restore populations of the energy levels and these are denoted W_0^{IS} and W_2^{IS}, as they involve a net change in magnetic quantum number of zero and two, respectively. Relaxation via these pathways is known as cross-relaxation as it involves a simultaneous change of the populations of the energy levels of both spins. By restoring the populations of the energy levels indicated to their equilibrium values, relaxation via these two pathways leads to a simultaneous change of the population difference across the I-spin transitions. This is shown in Fig. 6.1c, where the populations of the energy levels are shown after hypothetical cross-relaxation solely via the W_2^{IS} pathway has occurred. It is shown that the population difference across the I-spin transitions, $|\Delta n_I|$, has increased to 10 from its value of 2 at thermal equilibrium. This increase in I-spin signal intensity is referred to as the NOE enhancement. The effect of cross-relaxation via the zero-quantum, W_0^{IS} pathway is not indicated in Fig. 6.1. This is because, for small molecules in solution, this pathway makes a very small contribution to cross-relaxation. This will be explained further in the next section.

6.2.2   The Solomon Equations

It was shown by Solomon [61] that the behaviour of the I- and S-spin magnetizations after perturbation of the populations of the S-spin energy levels may be expressed using the following rate equations:

$$\frac{d\overline{\langle I_z \rangle}(t)}{dt} = -\rho_I \left(\overline{\langle I_z \rangle}(t) - \overline{\langle I_z \rangle}_0 \right) - \sigma_{IS} \left(\overline{\langle S_z \rangle}(t) - \overline{\langle S_z \rangle}_0 \right)$$

$$\frac{d\overline{\langle S_z \rangle}(t)}{dt} = -\rho_S \left(\overline{\langle S_z \rangle}(t) - \overline{\langle S_z \rangle}_0 \right) - \sigma_{SI} \left(\overline{\langle I_z \rangle}(t) - \overline{\langle I_z \rangle}_0 \right) \qquad (6.1)$$

where $\overline{\langle I_z \rangle}(t)$ and $\overline{\langle S_z \rangle}(t)$ are ensemble averages of the expectation values of the z-components of the spin angular momentum operators at time t of the I and S spins, respectively. $\overline{\langle I_z \rangle}_0$ and $\overline{\langle S_z \rangle}_0$ are the expectation values of the same operators at equilibrium. Equation (6.1) is often simplified such that the expectation value and ensemble average are implied, which yields:

$$\frac{dI_z(t)}{dt} = -\rho_I \left(I_z(t) - I_z^0 \right) - \sigma_{IS} \left(S_z(t) - S_z^0 \right)$$

$$\frac{dS_z(t)}{dt} = -\rho_S \left(S_z(t) - S_z^0 \right) - \sigma_{SI} \left(I_z(t) - I_z^0 \right) \qquad (6.2)$$

where $I_z^0 = \overline{\langle I_z \rangle}_0$ and $S_z^0 = \overline{\langle S_z \rangle}_0$. Equation (6.2) would seem to imply that the operators are time dependent. This of course is not the case, as it is actually the populations and wavefunctions of the spin systems that are changing.

In Eqs. (6.1) and (6.2) the cross-relaxation rate constant is denoted σ_{IS}, whilst the self-relaxation rate constants for the I and S spins are given by ρ_I and ρ_S, respectively. These equations show that the behaviour of the I- and S-spin magnetizations is dependent on both the spin-lattice relaxation of each spin, and on the cross-relaxation. Note that the term involving σ is directly proportional to the change in the magnetization of the coupled spin in each case — this shows that the evolution of the I-spin magnetization is dependent on the

perturbation of the S-spin magnetization (and vice versa) and so is an equivalent way of describing what was shown in Fig. 6.1.

In the transient NOE experiment, shown in Fig. 6.2, the populations of the S-spin energy levels are inverted by the application of a 180° pulse to the S spins. Cross-relaxation then occurs during the NOE build-up interval, τ, before a 90° pulse on the I spin excites I-spin single-quantum coherence. The experiment is repeated using different values of τ and the change in I-spin signal intensity is observed. In such an experiment, directly after the S-spin inversion pulse ($\tau = 0$) the I- and S-spin magnetizations take the values:

$$\begin{aligned} I_z(0) &= I_z^{\,0} \\ S_z(0) &= -S_z^{\,0} \end{aligned} \quad . \tag{6.3}$$

If the approximation is made that the I- and S-spin magnetizations take the values given in Eq. (6.3) (the initial rate approximation), then these boundary conditions may be used to obtain the following behaviour of the I-spin magnetization, where t is now replaced by τ:

$$\frac{dI_z(\tau)}{d\tau} = 2\sigma_{IS}S_z^0 \, , \tag{6.4}$$

which yields the following solution:

$$I_z(\tau) = 2\sigma_{IS}\tau S_z^{\,0} + I_z^{\,0} \, . \tag{6.5}$$

Equation (6.4) states that the I-spin magnetization is dependent on τ and on the

cross-relaxation rate constant σ_{IS}, the latter of course being responsible for the NOE.

The behaviour of the S-spin magnetization may also be obtained by solving the second part of Eq. (6.1), which yields the equation:

$$S_z(\tau) = 2\rho_S \tau S_z^{\ 0} - S_z^{\ 0} . \qquad (6.6)$$

The S-spin magnetization thus returns to its equilibrium value at a rate characterised by its self-relaxation rate constant.

Using Eq. (6.5), an NOE enhancement, η, is defined as:

$$\eta = \frac{I_z(\tau) - I_z^{\ 0}}{I_z^{\ 0}}$$

$$= \frac{2\sigma_{IS} \tau S_z^{\ 0}}{I_z^{\ 0}} \qquad . \qquad (6.7)$$

$$= \frac{2\sigma_{IS} \tau \gamma_S}{\gamma_I}$$

Given that η is directly proportional to the gyromagnetic ratio of the S spin, this nucleus is typically chosen to be high-γ, i.e., ^{1}H or ^{19}F.

Equations (6.1–6.7) are only valid in the initial rate approximation, in which the NOE does not reach its maximum, and the conditions $\sigma_{IS}\tau \ll 1$ and $\rho_S \tau \ll 1$ are satisfied. At longer mixing times, the solutions of Eq. (6.1) are more difficult to obtain, but nevertheless, the following expressions may be obtained for the time dependence of the I- and S-spin magnetizations, assuming
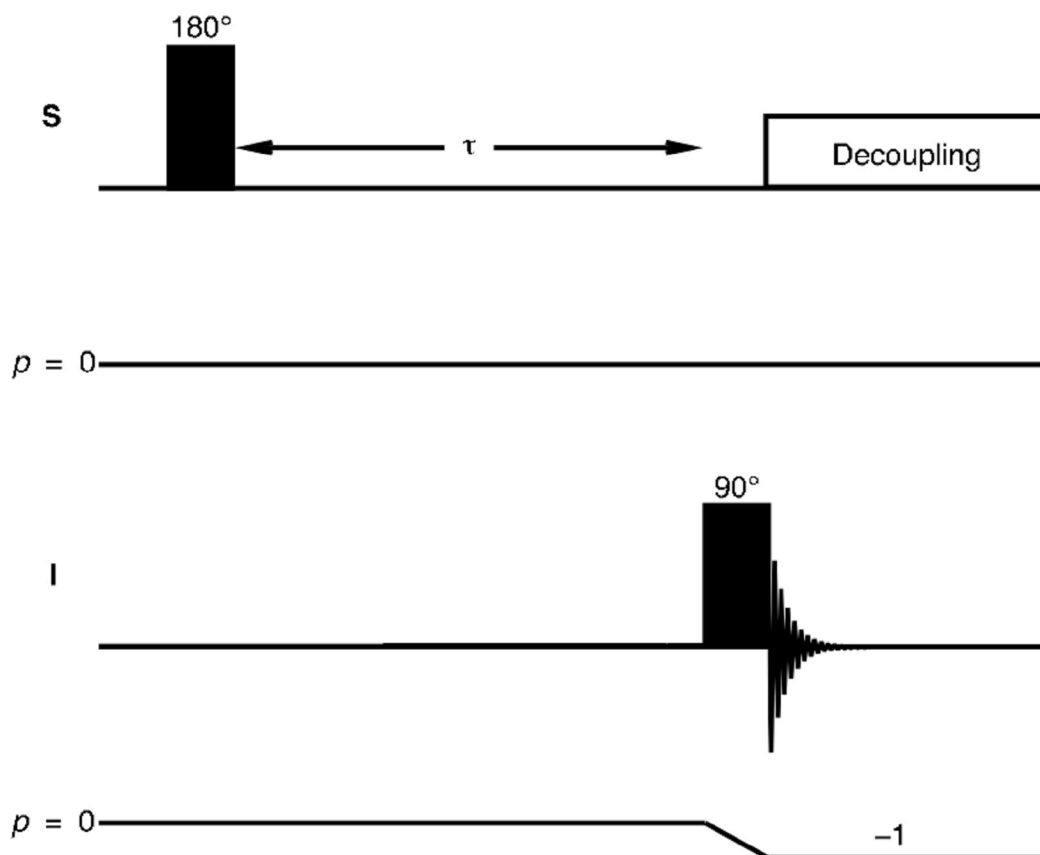
Figure 6.2. Pulse sequence and coherence transfer pathway for the transient NOE experiment that measures the heteronuclear NOE enhancement experienced by the central transition of spin I upon inversion of the populations of the S-spin energy levels. The NOE build-up interval is denoted τ.

that $\sigma_{IS} = \sigma_{SI}$ (an assumption that holds when the spin quantum numbers of the I and S spins are equal) [288]:

$$I_z(\tau) = I_z^0 + \frac{2\sigma_{IS}I_z^0\gamma_S}{A\gamma_I}\left\{\exp(-C\tau/2) - \exp(-B\tau/2)\right\}$$

$$S_z(\tau) = S_z^0 + \frac{2\sigma_{IS}S_z^0}{A}\left\{\frac{\left(\frac{C}{2} - \rho_I\right)}{2}\exp(-C\tau/2)\right.$$

$$\left. - \frac{\left(\frac{B}{2} - \rho_I\right)}{2}\exp(-B\tau/2)\right\} \qquad , \qquad (6.8)$$

152

where

$$A = \sqrt{\left(\rho_I - \rho_S\right)^2 + 4\sigma_{IS}^2}$$

$$B = \left(\rho_I + \rho_S\right) + \sqrt{\left(\rho_I - \rho_S\right)^2 + 4\sigma_{IS}^2} \; , \tag{6.9}$$

$$C = \left(\rho_I + \rho_S\right) - \sqrt{\left(\rho_I - \rho_S\right)^2 + 4\sigma_{IS}^2}$$

from which the NOE enhancement becomes:

$$\eta = \frac{2\gamma_S\sigma_{IS}}{A\gamma_I} \left\{\exp(-C\tau/2) - \exp(-B\tau/2)\right\} . \tag{6.10}$$

The value of τ for which the I-spin signal intensity has its greatest value, τ_{max}, may easily be obtained from Eq. (6.8) and is given by:

$$\tau_{max} = \frac{1}{A} \ln\left\{\frac{B}{C}\right\} , \tag{6.11}$$

When the I-spin signal intensity has its greatest value, $\tau = \tau_{max}$ and so, by substituting Eq. (6.11) into Eq. (6.10), the following expression for the maximum NOE enhancement, η_{max}, is obtained:

$$\eta_{max} = \frac{2\gamma_S\sigma_{IS}}{A\gamma_I} \left[\left(\frac{B}{C}\right)^{-\frac{C}{2A}} - \left(\frac{B}{C}\right)^{-\frac{B}{2A}}\right] . \tag{6.12}$$

For the case of a homonuclear spin pair, Eq. (6.12) reduces to

$$\eta_{max} = \left| \left(\frac{\rho + \sigma}{\rho - \sigma} \right)^{-\frac{(\rho - \sigma)}{2\sigma}} - \left(\frac{\rho + \sigma}{\rho - \sigma} \right)^{-\frac{(\rho + \sigma)}{2\sigma}} \right| ,$$ (6.13)

and likewise the I-spin signal intensity reaches its maximum value when

$$\tau_{max} = \frac{1}{(2\sigma)} \ln \left\{ \frac{(\rho + \sigma)}{(\rho - \sigma)} \right\} ,$$ (6.14)

where $\rho_I = \rho_S = \rho$ and $\sigma_{IS} = \sigma$.

The self-relaxation and cross-relaxation rate constants for a heteronuclear IS spin pair (both with spin $I = 1/2$), ρ_I, ρ_S and σ_{IS}, are directly related to the rate constants defined in Section 6.2.1, W_0^{IS}, W_1^I, W_1^S and W_2^{IS}, as follows:

$$\begin{aligned} \sigma_{IS} &= \frac{K^2}{20} \left[6j(\omega_I + \omega_S) - j(\omega_I - \omega_S) \right] \\ &= W_2^{IS} - W_0^{IS} \end{aligned}$$ (6.15)

and

$$\begin{aligned} \rho_I &= \frac{K^2}{20} \left[6j(\omega_I + \omega_S) + 3j(\omega_I) + j(\omega_I - \omega_S) \right] \\ &= W_2^{IS} + 2W_1^I + W_0^{IS} \\ \rho_S &= \frac{K^2}{20} \left[6j(\omega_I + \omega_S) + 3j(\omega_S) + j(\omega_I - \omega_S) \right] \\ &= W_2^{IS} + 2W_1^S + W_0^{IS} \end{aligned}$$ (6.16)

where

$$W_0{}^{IS} = \frac{K^2}{20} \, j(\omega_I - \omega_S)$$

$$W_1{}^{I} = \frac{3K^2}{40} \, j(\omega_I)$$

$$W_1{}^{S} = \frac{3K^2}{40} \, j(\omega_S) \qquad \qquad \text{(6.17)}$$

$$W_2{}^{IS} = \frac{3K^2}{10} \, j(\omega_I + \omega_S)$$

and

$$K = -\frac{\mu_0 \gamma_I \gamma_S \hbar}{4\pi r_{IS}^3} \, , \qquad \qquad \text{(6.18)}$$

where $j(\omega)$ are reduced spectral density functions, defined as:

$$j(\omega) = \frac{2\tau_c}{1 + (\omega\tau_c)^2} \, . \qquad \qquad \text{(6.19)}$$

Non-reduced spectral-density functions are usually expressed in the form [289]

$$J(\omega) = \overline{B_{loc}^2(t)} \, \frac{2\tau_c}{1 + (\omega\tau_c)^2} \, , \qquad \qquad \text{(6.20)}$$

where $\overline{B_{loc}^2(t)}$ is the average of the square of a time-dependent local magnetic field experienced by a given spin, in this case given by:

$$\overline{B_{loc}^2(t)} = K^2 = \left(\frac{\mu_0 \gamma_I \gamma_S \hbar}{4\pi r_{IS}^3} \right)^2 . \qquad \qquad \text{(6.21)}$$

Generally $\overline{B_{loc}^2(t)}$ can take positive integer or half-integer values which are

equally distributed about zero, such that the average over the entire sample is zero.

In Eqs. (6.19) and (6.20), τ_c is the correlation time (in seconds); this is defined as the time constant characterising the decay rate of the correlation function, $G(t)$ [289]:

$$G(t) = \overline{B_{loc}^2(t)} \exp(-|t| / \tau_c) . \qquad (6.22)$$

The correlation function describes the variation over time of the average of the square of the local magnetic field, $\overline{B_{loc}^2(t)}$, and its Fourier transform yields the spectral density function in Eq. (6.20).

For small molecules in solution, the correlation time is typically very short, such that the condition $\omega_0 \tau_c \ll 1$ is satisfied. This condition is known as the fast-motion or extreme-narrowing limit. Conversely, for large molecules in solution the correlation time is usually much longer and so the condition $\omega_0 \tau_c \gg 1$ is satisfied. This limit is referred to as the slow-motion or spin-diffusion limit. For the results to be presented in this Chapter, only the fast-motion limit is applicable and so the slow-motion limit will not be considered further here.

In the fast-motion limit, the reduced spectral density function defined in Eq. (6.19) becomes independent of frequency and is given by

$$j(\omega) = 2\tau_c , \qquad (6.23)$$

and so the cross-relaxation rate constant becomes

$$\begin{aligned} \sigma_{IS} &= \frac{K^2}{20} \left[12\tau_c - 2\tau_c \right] \\ &= \frac{K^2 \tau_c}{2} \end{aligned}$$

$$(6.24)$$

and hence $W_0{}^{IS}$ and $W_2{}^{IS}$ are given by

$$\begin{aligned} W_0{}^{IS} &= \frac{K^2 \tau_c}{10} \\ W_2{}^{IS} &= \frac{3K^2 \tau_c}{5} \end{aligned}$$

$$(6.25)$$

For small molecules in solution, the double-quantum pathway thus makes the dominant contribution to cross-relaxation, as was stated in Section 6.2.1. The self-relaxation rate constants are also simplified to:

$$\rho_I = \rho_S = K^2 \tau_c ,$$

$$(6.26)$$

and so, in the fast-motion limit, the cross- and self-relaxation rate constants are related by

$$\rho = 2\sigma .$$

$$(6.27)$$

Figure 6.3 shows the behaviour of the I- and S-spin magnetizations in a transient NOE experiment, directly after an inversion pulse has been applied to the S spins. A homonuclear spin system (spin $I = 1/2$) in the fast-motion regime is assumed and so, using Eq. (6.26), the maximum NOE enhancement in Eq.
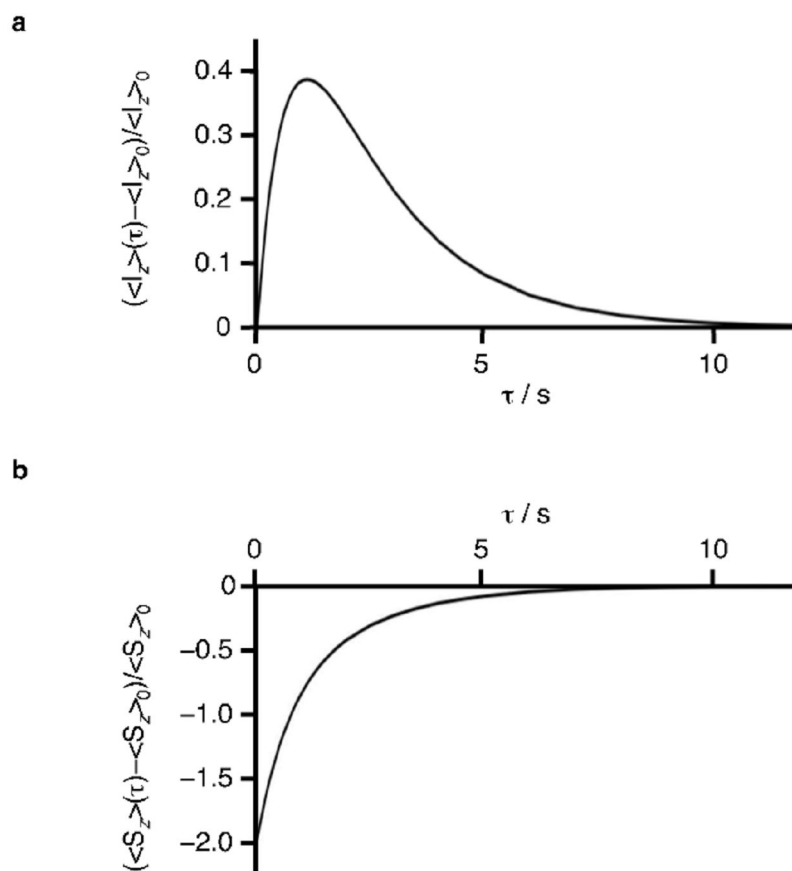
Figure 6.3. The behaviour of the (a) I-spin and (b) S-spin magnetizations in a transient NOE experiment during the NOE build-up interval τ for a pair of homonuclear spin $I = 1/2$ nuclei. Motion in the extreme-narrowing limit has been assumed and $\rho = 1.0\,\text{s}^{-1}$ and $\sigma = 0.5\,\text{s}^{-1}$.

(6.13) reduces to

$$\eta_{\max} = \frac{2}{3\sqrt{3}}\,.$$

$$= 0.385$$

(6.28)

More generally, the maximum transient NOE enhancement in the fast-motion limit for a pair of spin $I = 1/2$ nuclei is given by

$$\eta_{\max} = \frac{2}{3\sqrt{3}}\left(\frac{\gamma_S}{\gamma_I}\right).$$

(6.29)

For an IS spin pair where $I = {}^{11}\text{B}$ and $S = {}^{1}\text{H}$, the maximum NOE

enhancement is, by treating ^{11}B as a spin I = 1/2 nucleus (a valid approximation, as the quadrupolar interaction renders the satellite transitions virtually unobservable in an MAS experiment), 1.20.

Figure 6.3a shows that the I-spin signal intensity increases until τ = τ_{max}, at which point the maximum NOE enhancement for a homonuclear spin pair of 0.385 is achieved, before I-spin self-relaxation then returns it to its equilibrium value. The curve shown in Fig. 6.3a is referred to as an "NOE build-up" curve. The recovery of the S-spin magnetization to its equilibrium value after the inversion pulse has been applied is shown in Fig. 6.3b.

6.3   NOEs to Quadrupolar Nuclei

As described in Section 6.1, NOEs to quadrupolar nuclei are rarely observed as a consequence of the quadrupolar contribution being by far the most dominant one to spin-lattice relaxation. This can be illustrated by considering the NOE build-up curves when cross-relaxation is achieved via just a dipolar mechanism, and when both dipolar and quadrupolar mechanisms are operative.

NOE build-up curves may be obtained by calculating the Redfield relaxation matrix [290]. This calculation may be illustrated with the simple case of a homonuclear spin I = 1/2 pair. The equation of motion describing such a system is given by [290]:

$$\frac{d}{d\tau}\begin{pmatrix}\sigma_{11}\\ \sigma_{22}\\ \sigma_{33}\\ \sigma_{44}\end{pmatrix} = \begin{pmatrix}R_{1111} & R_{1122} & R_{1133} & R_{1144}\\ R_{2211} & R_{2222} & R_{2233} & R_{2244}\\ R_{3311} & R_{3322} & R_{3333} & R_{3344}\\ R_{4411} & R_{4422} & R_{4433} & R_{4444}\end{pmatrix}\begin{pmatrix}\sigma_{11}\\ \sigma_{22}\\ \sigma_{33}\\ \sigma_{44}\end{pmatrix}$$

$$= R\begin{pmatrix}\sigma_{11}\\ \sigma_{22}\\ \sigma_{33}\\ \sigma_{44}\end{pmatrix}$$

(6.30)

where R is the relaxation matrix and R_{abcd} ($1 \leq a, b, c, d \leq 4$) the corresponding matrix elements. The vector elements σ_{11}, σ_{22}, σ_{33} and σ_{44} correspond to the relative populations of the four Zeeman states with m_I, m_S = +1/2, +1/2; –1/2, +1/2; +1/2, –1/2 and –1/2, –1/2; labelled 1, 2, 3 and 4, respectively. The off-diagonal relaxation matrix elements may be calculated using the equation

$$R_{abcd} = \sum_{q=-2}^{2} 2J(\omega_{ac})\left\langle a\left|V_{IS}^{q}\right|c\right\rangle\left\langle d\left|V_{IS}^{-q}\right|b\right\rangle,$$

(6.31)

where the spectral density function $J(\omega_{ac})$ is defined according to:

$$J(\omega_{ac}) = \frac{3K^2}{20}\left(\frac{2\tau_c}{1 + (\omega_{ac}\tau_c)^2}\right),$$

(6.32)

and where the frequencies ω_{ac} take the values (for a homonuclear spin pair) 0 (for ω_{23}); ω_0 (for ω_{12}, ω_{13}, ω_{24} and ω_{34}) and $2\omega_0$ (for ω_{14}) and where the relation $\omega_{ac} = \omega_{ca}$ is satisfied. The summation of the elements in each row and column of the relaxation matrix is zero and so the diagonal elements can be obtained through knowledge of the off-diagonal elements. V_{IS}^{q} are tensors and $\left\langle a\left|V_{IS}^{q}\right|c\right\rangle$

and $\left\langle d \left| V_{IS}^q \right| b \right\rangle$ their corresponding matrix elements; these tensors are defined according to

$$
\begin{aligned}
V_{IS}^0 &= -\left(\frac{1}{6}\right)^{\frac{1}{2}} \left(4I_z^I I_z^S - I_+^I I_-^S - I_-^I I_+^S \right) \\
V_{IS}^{\pm 1} &= \left(I_\pm^I I_z^S + I_z^I I_\pm^S \right) \qquad\qquad , \qquad\qquad (6.33) \\
V_{IS}^{\pm 2} &= -I_\pm^I I_\pm^S
\end{aligned}
$$

in terms of the Cartesian operators, I_z and the raising and lowering operators I_+ and I_-, respectively:

$$
\begin{aligned}
I_x &= \frac{1}{2}\left(I_+ + I_- \right) \\
I_y &= -\frac{i}{2}\left(I_+ - I_- \right)
\end{aligned}
\qquad . \qquad (6.34)
$$

The relaxation matrix R is thus:

$$
\begin{pmatrix}
-J(\omega) - 2J(2\omega) & \dfrac{J(\omega)}{2} & \dfrac{J(\omega)}{2} & 2J(2\omega) \\[2mm]
\dfrac{J(\omega)}{2} & -J(\omega) - \dfrac{J(0)}{3} & \dfrac{J(0)}{3} & \dfrac{J(\omega)}{2} \\[2mm]
\dfrac{J(\omega)}{2} & \dfrac{J(0)}{3} & -J(\omega) - \dfrac{J(0)}{3} & \dfrac{J(\omega)}{2} \\[2mm]
2J(2\omega) & \dfrac{J(\omega)}{2} & \dfrac{J(\omega)}{2} & -J(\omega) - 2J(2\omega)
\end{pmatrix}
\quad . \quad (6.35)
$$

The matrix now needs to be transformed into a suitable basis set. For a pair of spin $I = 1/2$ nuclei, products of Cartesian spin angular momentum operators (so-called "product operators" [76], referred to in Section 2.5 of Chapter 2) are particularly useful. In this case, the 4 operators E, I_z, S_z and $2I_zS_z$ are required,

where E is the unity operator. A transformation matrix, U, is then formed where each row is derived from the diagonal elements of the 4 basis operators (note that E, I_z and S_z have to be multiplied by E to yield the required 4 × 4 matrices):

$$U = \frac{1}{2}\begin{pmatrix} 1 & 1 & 1 & 1 \\ 1 & 1 & -1 & -1 \\ 1 & -1 & 1 & -1 \\ 1 & -1 & -1 & 1 \end{pmatrix}, \tag{6.36}$$

and a new relaxation matrix R′ in the Zeeman order basis set is now obtained by multiplying R by U and its transpose U^T (where $U = U^T$):

$$R' = URU^T$$

$$= \begin{pmatrix} 0 & 0 & 0 & 0 \\ 0 & -\dfrac{J(0)}{3} - J(\omega) - 2J(2\omega) & \dfrac{J(0)}{3} - 2J(2\omega) & 0 \\ 0 & \dfrac{J(0)}{3} - 2J(2\omega) & -\dfrac{J(0)}{3} - J(\omega) - 2J(2\omega) & 0 \\ 0 & 0 & 0 & -2J(\omega) \end{pmatrix}. \tag{6.37}$$

The equation of motion is now modified to:

$$\frac{d}{d\tau}\begin{pmatrix} \langle E\rangle(\tau) \\ \langle I_z\rangle(\tau) \\ \langle S_z\rangle(\tau) \\ \langle 2I_zS_z\rangle(\tau) \end{pmatrix} = R'\begin{pmatrix} \langle E\rangle(\tau) - \langle E\rangle_0 \\ \langle I_z\rangle(\tau) - \langle I_z\rangle_0 \\ \langle S_z\rangle(\tau) - \langle S_z\rangle_0 \\ \langle 2I_zS_z\rangle(\tau) - \langle 2I_zS_z\rangle_0 \end{pmatrix}, \tag{6.38}$$

where the expectation values of these operators have the same meaning as those in Eq. (6.1).

Equation (6.38) can be easily solved to yield expressions for the expectation values of the operators I_z and S_z:

$$\langle I_z \rangle(\tau) = \left(\langle I_z \rangle(\tau) - \langle I_z \rangle_0\right)\left(-\frac{J(0)}{3} - J(\omega) - 2J(2\omega)\right)\tau$$

$$+ \left(\langle S_z \rangle(\tau) - \langle S_z \rangle_0\right)\left(\frac{J(0)}{3} - 2J(2\omega)\right)\tau + c$$

$$\langle S_z \rangle(\tau) = \left(\langle I_z \rangle(\tau) - \langle I_z \rangle_0\right)\left(\frac{J(0)}{3} - 2J(2\omega)\right)\tau$$

$$+ \left(\langle S_z \rangle(\tau) - \langle S_z \rangle_0\right)\left(-\frac{J(0)}{3} - J(\omega) - 2J(2\omega)\right)\tau + c$$

$$(6.39)$$

where c is a constant of integration. If the boundary conditions given in Eq. (6.3) are assumed (i.e., the initial rate limit), then the expressions in Eq. (6.39) are identical to those in Eqs. (6.5) and (6.6).

For the case of a spin $I = 3/2$, spin $I = 1/2$ pair the relaxation matrix was constructed using a basis set consisting of the products of 2 spherical tensor operators ($T_{0,0}$ and $T_{1,0}$) for the spin $I = 1/2$ nucleus (spin S) and 4 spherical tensor operators ($T_{0,0}$, $T_{1,0}$, $T_{2,0}$ and $T_{3,0}$) for the spin $I = 3/2$ nucleus (spin I). This resulted in 8 operators ($T_{0,0}(S)T_{0,0}(I)$, $T_{0,0}(S)T_{1,0}(I)$, $T_{0,0}(S)T_{2,0}(I)$, $T_{0,0}(S)T_{3,0}(I)$, $T_{1,0}(S)T_{0,0}(I)$, $T_{1,0}(S)T_{1,0}(I)$, $T_{1,0}(S)T_{2,0}(I)$ and $T_{1,0}(S)T_{3,0}(I)$) and a relaxation matrix of dimensions 8×8 was obtained with the aid of the MathNMR Mathematica program [291]. The matrix was calculated directly in the spherical tensor operator basis set (i.e., without the need for any transformation as described in the case of a homonuclear spin $I = 1/2$ pair) and, due to the block diagonal nature of 4 operators in the matrix (i.e., these 4 operators showed correlations

only with each other), the equation of motion was modified to one containing a relaxation matrix of dimensions 4×4. This equation can then easily be solved with the boundary condition $\rangle S_z \langle (0) = \rangle S_z \langle_0$.

The modified equation of motion describes the time dependence of the expectation values of the operators $T_{0,0}(S)T_{1,0}(I)$, $T_{0,0}(S)T_{3,0}(I)$, $T_{1,0}(S)T_{0,0}(I)$ and $T_{1,0}(S)T_{2,0}(I)$. The expectation values of these tensors are defined as $\rangle \Delta T \langle$, the deviation of these tensors from their equilibrium values:

$$\rangle \Delta T \langle = \rangle T \langle (\tau) - \rangle T \langle_0 . \tag{6.40}$$

The evolution of the I-spin magnetization is represented by the operator $T_{0,0}(S)T_{1,0}(I)$; the magnitude of the expectation value of this operator ($<\Delta T_{0,0}(S)T_{1,0}(I)>$) is plotted in Fig. 6.4 for the case of an IS spin pair, where $I = {}^{11}B$ and $S = {}^{1}H$.

NOE build-up curves are shown in Fig. 6.4 when just dipolar and a combination of dipolar and quadrupolar mechanisms are present to effect cross-relaxation. Motion in the extreme-narrowing limit is assumed. In Fig. 6.4a, the maximum NOE enhancement of 0.43 is achieved when solely dipolar contributions are incorporated into the calculation of the relaxation matrix (solid line), whilst the addition of the quadrupolar mechanism with a quadrupolar coupling parameter, C_Q, equal to 0.5 MHz, leads to a significant reduction of the enhancement to just 0.04 (dashed line). The strong effect of a quadrupolar coupling is demonstrated further in Fig. 6.4b, where the presence
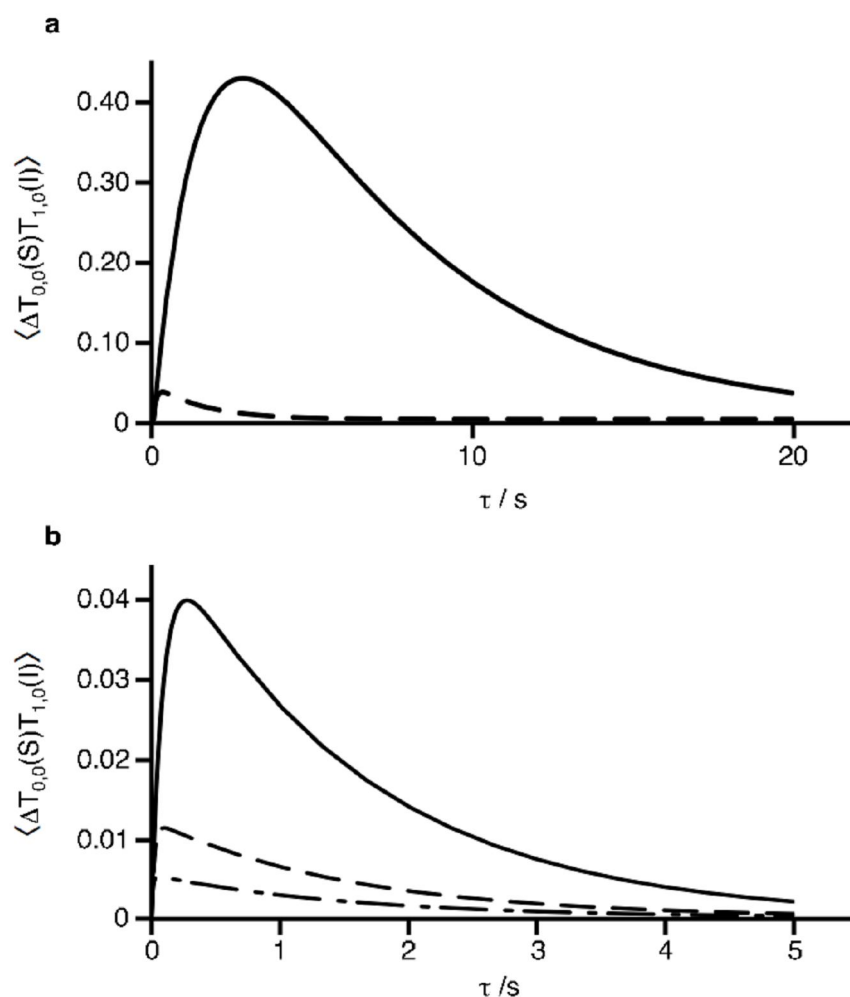
Figure 6.4. NOE build-up curves for an I = ^{11}B, S = ^{1}H spin pair shown for when the mechanism for cross-relaxation is (a) solely dipolar (solid line) and dipolar and quadrupolar (dashed line, C_Q = 0.5 MHz) in origin and (b) when both dipolar and quadrupolar contributions are present and C_Q = 0.5 MHz (solid line), 1.0 MHz (dashed line) and 1.5 MHz (dot dashed line). The MathNMR Mathematica program [291] was used for calculating the curves when a quadrupolar contribution was included. The correlation time τ_c = 100 ps.

of a quadrupolar interaction with C_Q = 0.5 MHz (solid line), 1.0 MHz (dotted line) and 1.5 MHz (dot dashed line) is shown. The increase in C_Q continues to decrease significantly the enhancement to the point where, at C_Q = 1.5 MHz, an enhancement of just 0.006 is expected. The magnitude of this effect, even when C_Q is modest, is thus so great that NOEs to quadrupolar nuclei are typically too small to be detected.

6.4   Transient NOE Enhancement of Borane Adducts

6.4.1   *Central Transition* $^{11}B\{^{1}H\}$ *NOE*

Transient NOE experiments have been performed on a series of solid borane adducts, using the pulse sequence shown in Fig. 6.2 under MAS conditions. This experiment is used instead of the steady-state NOE method commonly used in the solution state as the long periods of high-power decoupling needed make it unsuitable for use in solid-state NMR. In each case, a range of τ values was used such that an NOE build-up curve like that shown in Fig. 6.3a was obtained. For each material, the maximum enhancement was obtained and the value of τ for which the maximum ^{11}B signal intensity was seen, τ_{max}, was determined. In these results, the NOE enhancement is expressed as a percentage and so is defined as

$$f_{\mathrm{I}}\{\mathrm{S}\} = \frac{I(\tau_{\max}) - I_0}{I_0} \times 100 \, , \qquad\qquad (6.41)$$

where $I(\tau_{max})$ and I_0 are the I-spin signal intensities at $\tau = \tau_{max}$ and $\tau = 0$, respectively. Figure 6.5 shows ^{1}H-decoupled ^{11}B MAS spectra of borane triphenylphosphine for the cases of $\tau = 0$ and $\tau = \tau_{max} = 650$ ms. The ^{11}B central transition MAS lineshape is broadened by the residual second-order quadrupolar interaction (the quadrupolar coupling parameter, $C_Q = 1.2$ MHz and the asymmetry parameter, $\eta = 0$ [293]) and also shows evidence of ^{11}B-^{31}P *J* coupling ($J_{11B\text{-}31P} = 60$ Hz [293]). The increase in signal intensity in Fig. 6.5 is evidence of a heteronuclear NOE with an NOE enhancement $f_{\mathrm{I}}\{\mathrm{S}\} = 155\%$.
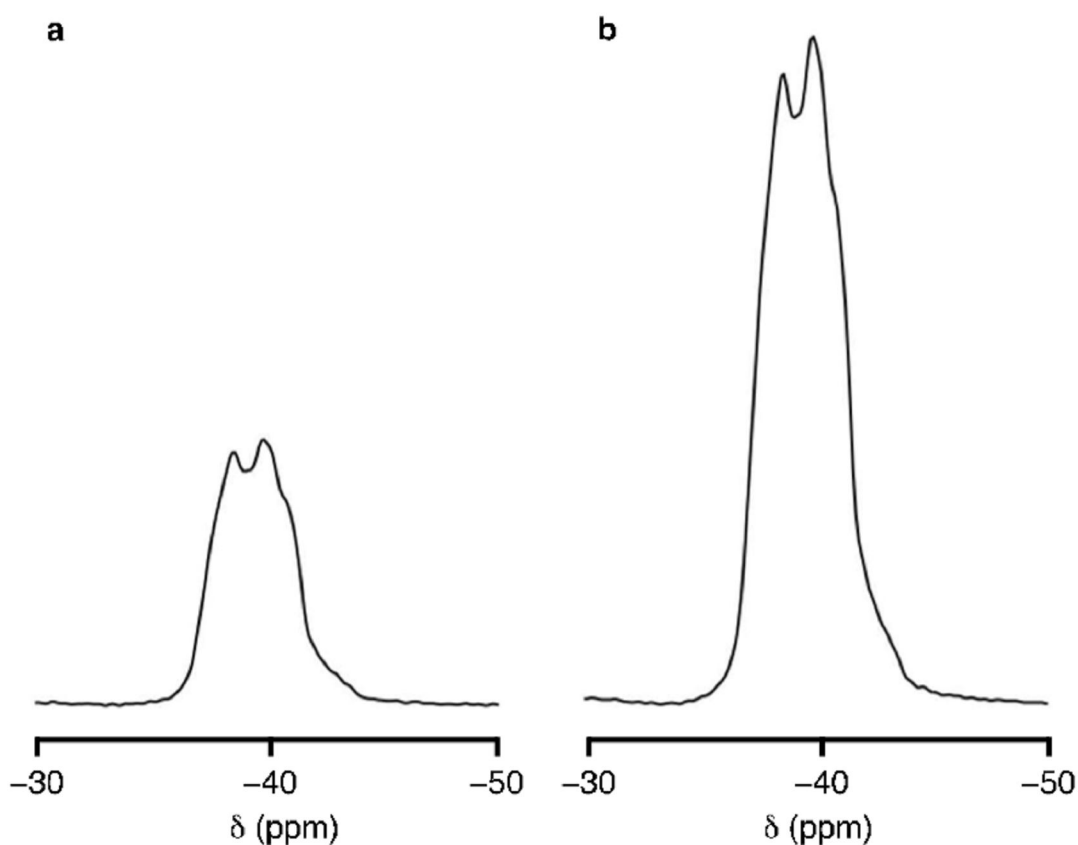
Figure 6.5. ^{1}H-decoupled ^{11}B MAS spectra of borane triphenylphosphine acquired using the transient NOE experiment in Fig. 6.2, shown for values of (a) τ = 0 and (b) τ = 650 ms. The experiment was performed at B_0 = 9.4 T and the MAS rate was 10 kHz. The chemical shift scale is referenced to solid BPO$_4$ at −3.3 ppm [292]. The ^{11}B 90° pulse had duration 1.1 µs and the ^{1}H inversion pulse was 2.9 µs. The ^{1}H decoupling field strength was ~65 kHz.

When this experiment is performed on the same material in the solution state, no NOE is observed [287].

The presence of a transient NOE in this material is intriguing given that ^{11}B is a quadrupolar nucleus and that an enhancement is observed only in the solid state. A likely source of motion on the fast timescale is the rapid rotation of the BH$_3$ group about its C_3 axis that causes a random modulation of the ^{1}H-^{11}B dipole-dipole interaction. The close proximity of the ^{11}B and ^{1}H nuclei (r_{IS} = 0.117 nm in borane ammonia complex, BH$_3$·NH$_3$ [294]) leads to a strong dipolar

interaction and hence a large NOE enhancement. T_1 relaxation of quadrupolar nuclei is often very efficient and usually takes effect more rapidly than any dipolar-driven cross-relaxation. The presence of an NOE in this material is thus likely to be due to the absence of a modulation of the ^{11}B quadrupolar interaction that would lead to efficient quadrupolar relaxation. This arises because, as the ^{11}B quadrupole tensor is axially symmetric, it is aligned along the BH_3 C_3 axis and so rapid reorientation of the BH_3 group about this axis alters very little the ^{11}B quadrupolar interaction. The validity of this rationale is demonstrated with the absence of a transient ^{11}B{^{1}H} NOE in solid *ortho*-carborane, $B_{10}H_{10}C_2H_2$. Rapid isotropic tumbling of this cage molecule [295] causes the modulation of the ^{1}H-^{11}B and ^{1}H-^{13}C dipole-dipole interactions that is required for NOE enhancement of the ^{11}B and ^{13}C nuclei, respectively. However, whilst a ^{13}C{^{1}H} NOE enhancement of 63% is observed [287], a ^{11}B{^{1}H} NOE enhancement is not. This is because the isotropic tumbling also modulates the ^{11}B quadrupolar interaction, so leading to efficient quadrupolar relaxation and hence no ^{11}B{^{1}H} NOE. The absence of a transient ^{11}B{^{1}H} NOE of borane triphenylphosphine in the solution state may be similarly explained. In this case, the rapid tumbling about all Cartesian axes seen in solution modulates the ^{11}B quadrupolar interaction and destroys the NOE.

Equation (6.29) reveals that a maximum ^{11}B{^{1}H} transient NOE enhancement of 1.20 would be expected (if ^{11}B is treated as a spin I = 1/2 nucleus). Expressed as a percentage according to Eq. (6.41), the maximum NOE enhancement of 120% is less than the 155% observed experimentally in borane
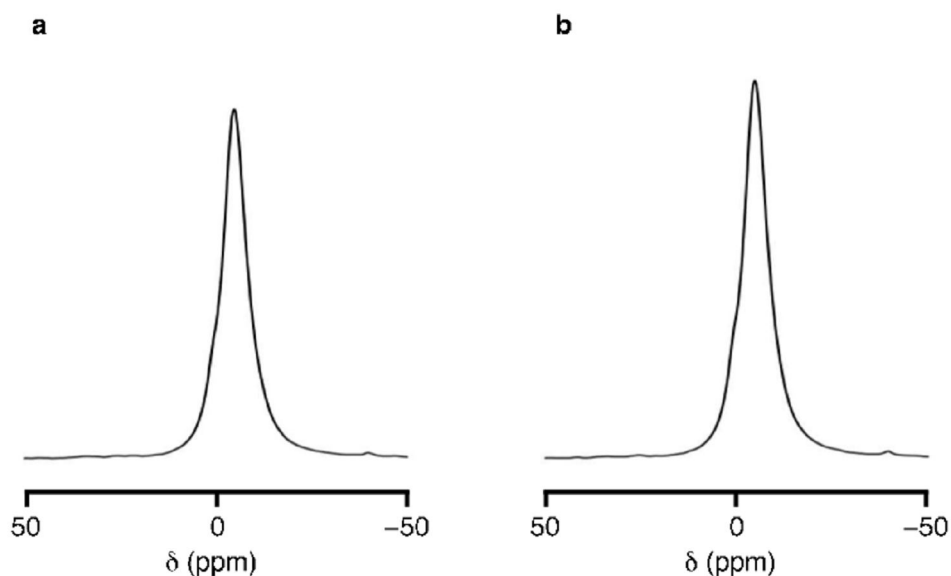
Figure 6.6. [1]H-decoupled ^{31}P MAS spectra of borane triphenylphosphine recorded (a) without an NOE enhancement and (b) with τ = 2.75 s in the sequence in Fig. 6.2. The experiment was performed at B_0 = 9.4 T and the MAS rate was 10 kHz. The [31]P 90° pulse had duration 2.5 μs and the ^{1}H inversion pulse was 2.9 μs.

triphenylphosphine. In contrast to the steady-state NOE, however, the maximum transient NOE enhancement increases with the number of S spins equidistant from the I spin. It can be shown that, for three non-interacting S spins, all equidistant from the *I* spin (where I and S both have spin *I* = 1/2), the maximum transient NOE enhancement in the fast-motion limit is given by $f_I\{3 \times S\}$ = $0.601(\gamma_I/\gamma_S) \times 100$ = 187% if I = [11]B and S = [1]H [287]. The discrepancy between this value and that observed experimentally most likely arises as a result of enhanced ^{1}H spin-lattice relaxation resulting from [1]H-^{1}H dipolar interactions that are ignored in the theoretical calculation. In addition, there is likely to be a quadrupolar contribution to the [11]B spin-lattice relaxation.

[1]H-decoupled ^{31}P MAS spectra of borane triphenylphosphine with and without an NOE are shown in Fig. 6.6. At τ = 2.75 s, the ^{31}P signal intensity

Adduct	$f_I\{S\}$ (%)	τ_{max} /ms	$f_I\{S\}$ (%)	τ_{max} /ms	$T_1(^1H)$ /s	$T_1(^{11}B)$ /s	$T_1(^{31}P)$ /s
	I = ^{11}B		I = ^{31}P				
$BH_3 \cdot PPh_3$	155	600	8.6	2750	1.28	0.62	20.28
$BH_3 \cdot PHPh_2$	128	300	8.5	1500	0.54	0.32	12.69
$BH_3 \cdot NMe_3$	34	750	—	—	1.67	0.38	—
$BH_3 \cdot NH^tBu_2$	32	400	—	—	1.10	0.24	—
$BH_3 \cdot NH_2{}^tBu$	32	350	—	—	0.94	0.21	—
$BR_3 \cdot NH_3$ (R = p-MeOC$_6$H$_4$)	8.9	3000	—	—	7.01	0.99	—

Table 6.1. Fractional NOE enhancements of ^{11}B and ^{31}P in a series of phosphine- and amine-derived adducts of borane, along with T_1 times of the ^{1}H, ^{11}B and ^{31}P nuclei. All experiments were performed at either B_0 = 4.7 T or 9.4 T and a MAS rate of 10 kHz.

reaches its maximum and a heteronuclear NOE enhancement of 8.5% is observed. The much smaller enhancement observed for ^{31}P compared with ^{11}B is, given the r^{-6} dependence of the NOE, consistent with the greater distance to the protons in the BH_3 group ($r_{IS} \approx 0.25$ nm [296]). In contrast to the case of ^{11}B, performing this experiment in the solution state yields an NOE enhancement of $f_I\{S\}$ = 53%.

Transient NOE results for borane triphenylphosphine and a series of other phosphine- and amine-derived borane adducts are summarised in Table 6.1. T_1 relaxation times for ^{1}H, ^{11}B and ^{31}P nuclei are also shown. The ^{11}B$\{^1$H$\}$ NOE enhancement of borane diphenylphosphine, BH$_3$·PHPh$_2$, is smaller than that observed in borane triphenylphosphine. This concurs with the more efficient ^{1}H and ^{11}B spin-lattice relaxation shown by the T_1 values in Table 6.1.

The ^{11}B$\{^1$H$\}$ NOE enhancements observed for borane trimethylamine, BH$_3$·NMe$_3$, borane *tert*-butylamine, BH$_3$·NH$_2^t$Bu, and borane di-*tert*-butylamine, BH$_3$·NH^{t}Bu$_2$, are very similar, which is not surprising given the chemical similarity of these materials. The slightly smaller enhancements observed with the *tert*-butylamine and di-*tert*-butylamine adducts are consistent with the more efficient ^{1}H and ^{11}B T_1 relaxation observed in these solids. The much smaller enhancement observed for borane tri-*para*-methoxyphenylamine, B(*p*-MeOC$_6$H$_4$)$_3$·NH$_3$, is consistent with the source of the NOE being the more distant protons attached to the nitrogen atom.

6.4.2   Satellite and Triple-Quantum Transition ^{11}B$\{^1$H$\}$ NOE

The results shown in the previous section were concerned with the ^{11}B$\{^1$H$\}$ NOE enhancement of the ^{11}B central transition. By performing the transient NOE experiment in Fig. 6.2 over a large spectral width and by modifying the technique to incorporate triple-quantum filtration, the enhancement of the satellite and triple-quantum transitions may be obtained, respectively. The
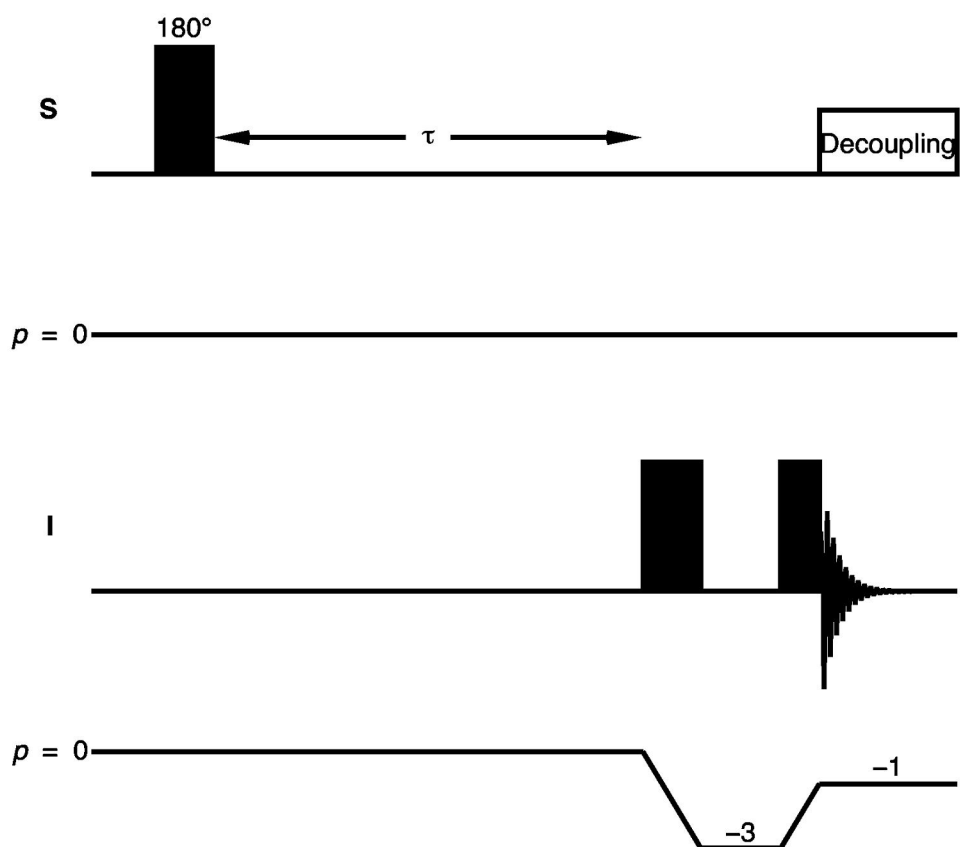
Figure 6.7. Pulse sequence and coherence transfer pathway for the transient NOE experiment that measures the heteronuclear NOE enhancement experienced by the triple-quantum transition of spin I upon inversion of the populations of the S-spin energy levels. The NOE build-up interval is denoted τ.

pulse sequence for the triple-quantum filtered transient NOE experiment is shown in Fig. 6.7.

^{1}H-decoupled ^{11}B MAS spectra of borane triphenylphosphine recorded with a spectral width of ~1 MHz are shown in Fig. 6.8, both in the absence of an NOE (Fig. 6.8a) and with τ = 550 ms (Fig. 6.8b), when the maximum NOE enhancement was obtained. The spectra show the expected manifold of spinning sidebands whose envelope approximately corresponds to the axially symmetric static satellite-transition lineshape expected for this material. The maximum NOE enhancement is obtained at τ = 550 ms (Fig. 6.8b), where an
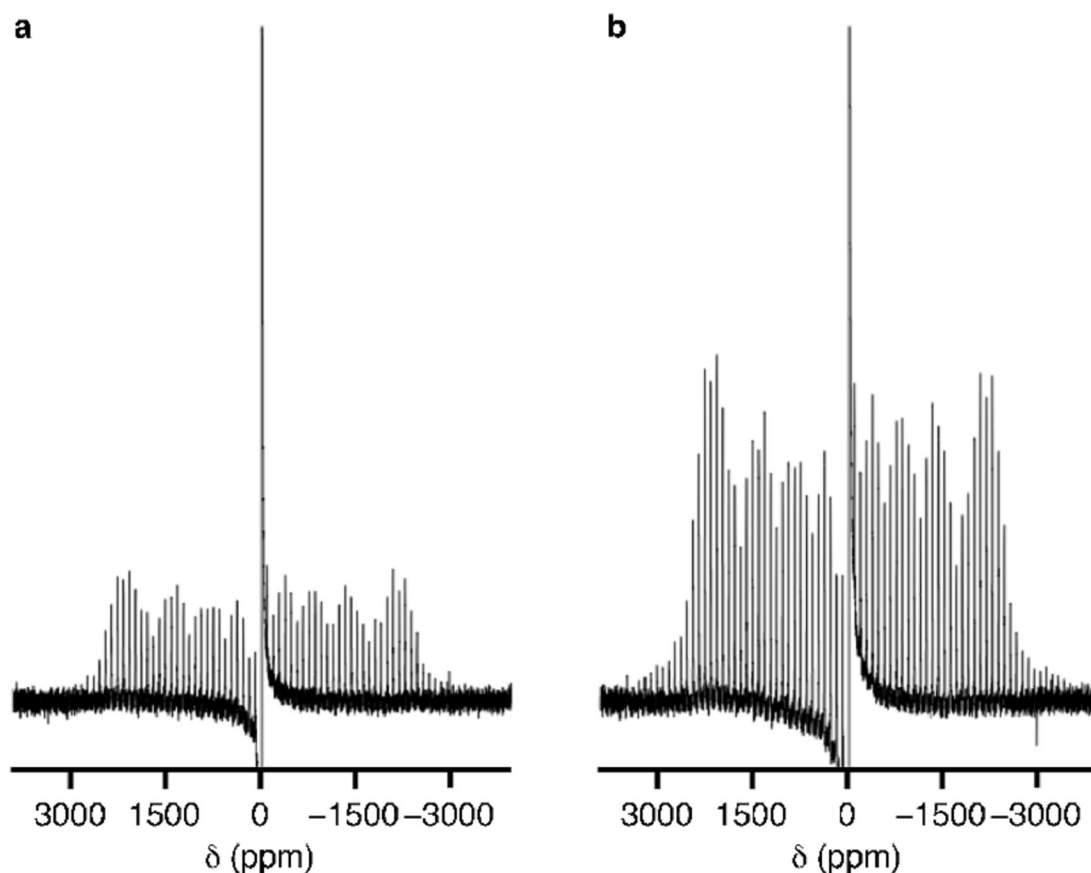
Figure 6.8. ^{1}H-decoupled ^{11}B MAS spectra of borane triphenylphosphine recorded using the pulse sequence in Fig. 6.2 with (a) $\tau = 0$ and (b) $\tau = 550$ ms. Spectra were acquired at $B_0 = 9.4$ T and a MAS rate of 10 kHz. A pulse length of duration 2.25 μs, optimised for ^{11}B satellite-transition excitation, was used, and accounts for the partly dispersive nature of the central-transition centreband.

increase in signal intensity of 155% is observed, as was seen for the central transition in Fig. 6.5. Closer analysis of a range of sidebands in the spectrum reveals that the enhancement is uniform across the entire powder pattern.

Figure 6.9 shows ^{1}H-decoupled ^{11}B MAS spectra of borane triphenyl-phosphine obtained using the triple-quantum filtered transient NOE experiment in Fig. 6.7. The spectra show, as expected, minimal distortion from triple-quantum filtration, although the ^{11}B-^{31}P J coupling is more apparent than in the central transition lineshapes shown in Fig. 6.5. Comparison of the
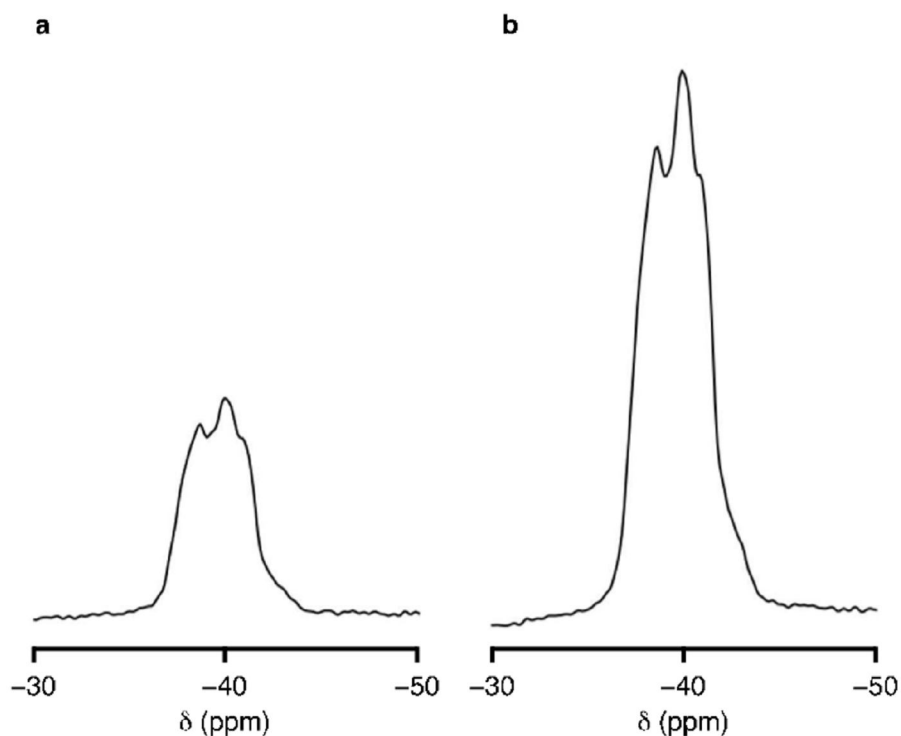
Figure 6.9. ^{1}H-decoupled ^{11}B MAS spectra of borane triphenylphosphine, recorded using the triple-quantum filtered transient NOE experiment in Fig. 6.6, shown for values of (a) $\tau = 0$ and (b) $\tau = 650$ ms. Experiments were performed at $B_0 = 9.4$ T and a MAS rate of 10 kHz. The triple-quantum excitation and conversion pulses had durations 4.75 μs and 1.5 μs, respectively.

spectrum obtained with $\tau = 0$ (Fig. 6.9a) and that obtained with $\tau = 650$ ms (Fig. 6.9b) reveals a maximum NOE enhancement of 155%, as is observed for the central and satellite transitions. The uniform enhancement observed for the central, satellite and triple-quantum transitions has also been observed in borane *tert*-butylamine (results not shown).

The uniform enhancement of the three ^{11}B transitions shown in Figs. 6.5, 6.8 and 6.9 is, at first glance, rather surprising. Given the different population differences that exist across these transitions, it may have been expected that different NOE enhancements would result. Consider the energy levels of a dipolar-coupled spin $I = 3/2$ (spin I), spin $I = 1/2$ (spin S) pair, shown in Fig.
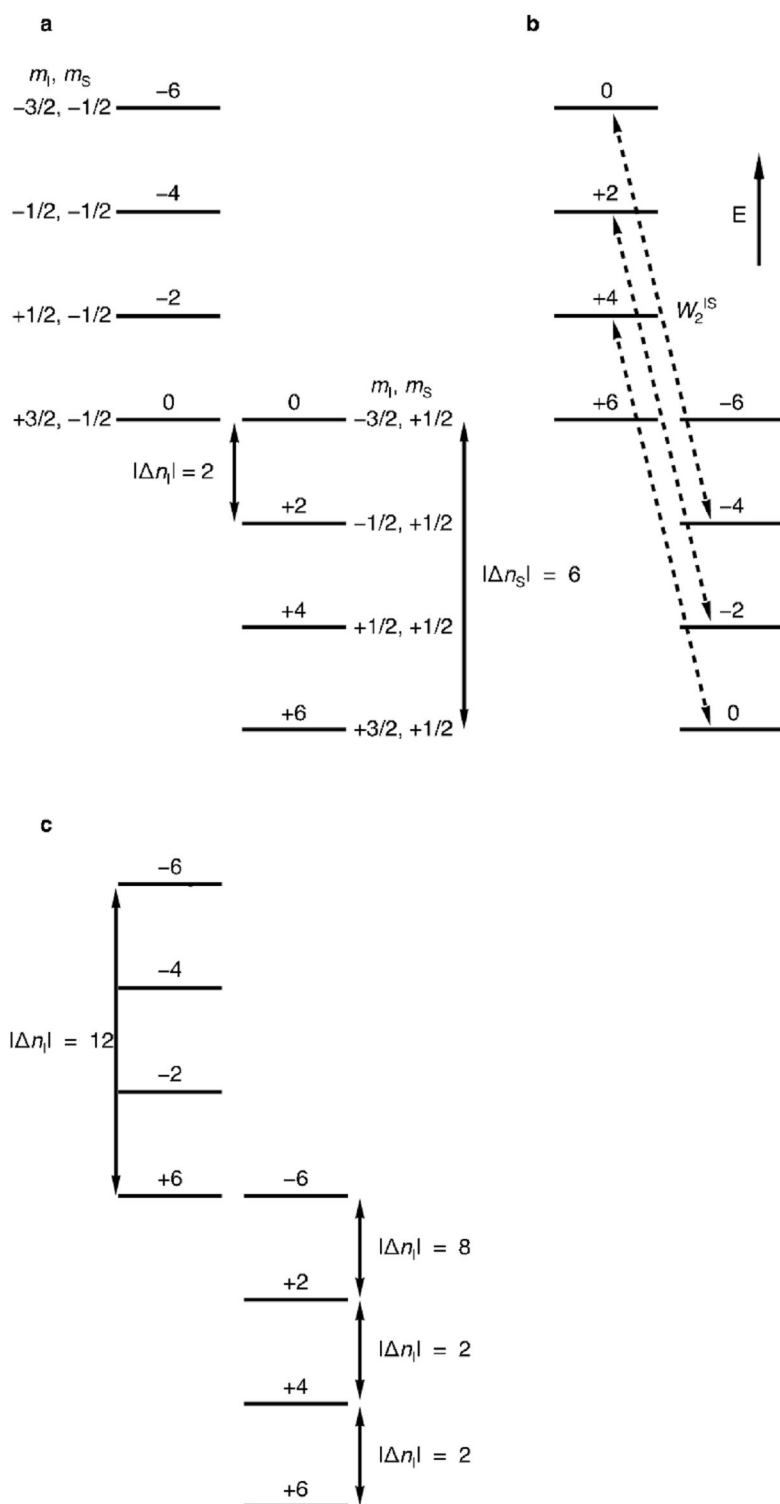
Figure 6.10. Energy level diagram for a dipolar-coupled heteronuclear spin pair consisting of a spin $I = 3/2$ nucleus (I) and a spin $I = 1/2$ nucleus (S) shown (a) at thermal equilbrium, (b) after a 180° pulse has been applied to the S spins and (c) after cross-relaxation via solely the double-quantum pathway. The energy levels are marked with their relative populations with the assumption that $\gamma_S/\gamma_I = 3$.

6.10. In Fig. 6.10a, the energy levels are shown with their relative populations at thermal equilibrium. By making the approximation that $\gamma_S/\gamma_I = 3$ (on the basis that spin I is ^{11}B and spin S is ^{1}H), the I and S spins have relative population differences, $|\Delta n_I|$ and $|\Delta n_S|$, of 2 and 6, respectively. The relative populations after an inversion pulse has been applied to the S spins are shown in Fig. 6.10b. Indicated in Fig. 6.10b, by the rate constant W_2^{IS}, are double-quantum pathways that may be utilised by cross relaxation to return the populations of the energy levels involved to their equilibrium values. The zero-quantum pathways are not shown as they make, for small molecules in solution, a minor contribution to cross-relaxation when there is motion present in the extreme-narrowing limit. Figure 6.10c shows the energy levels after hypothetical cross-relaxation (solely via the double-quantum pathway) has acted between the levels indicated in Fig. 6.10b. The population differences across the central, triple-quantum and two satellite transitions are shown in Fig. 6.10c and reveal that the population difference across the central transition remains the same at 2, the triple-quantum transition population difference increases from 6 to 12 and the difference across the two satellite transitions remain the same at 2 and increase to 8, respectively.

The perturbations to the populations of the energy levels in an I = ^{11}B, S = ^{1}H spin pair shown in Fig. 6.10 suggest that an NOE enhancement is expected for neither the central transition nor one of the satellite transitions, whilst enhancements of 300% and 100% are expected for the other satellite transition and the triple-quantum transition, respectively. Whilst the energy

level illustration in Fig. 6.10 of such a spin system is only intended as a qualitative guide to the outcome of transient NOE experiments of the various ^{11}B transitions, the uniform enhancements observed experimentally are still surprising. A possible reason for this discrepancy is the presence of MAS-induced spin diffusion [297]. Under MAS, the energies of the $2I + 1$ spin angular momentum states of a given spin vary with time, and, assuming that these energies are not changing too rapidly, different spins can interact such that, in this case, the different perturbations to the population differences across the central, triple-quantum and satellite transitions shown in Fig. 6.10 are averaged to a common value. This is the basis of the spin diffusion effect. This interaction can be mediated by, for example, the strong ^{1}H-^{1}H and ^{1}H-^{11}B dipolar interactions. One possible way of observing different NOE enhancements under MAS conditions is to use a more selective (lower rf field strength) excitation pulse. ^{11}B{^{1}H} transient NOE experiments on borane triphenylphosphine were performed using a series of central-transition excitation pulses with rf field strengths in the range 13–89 kHz (spectra not shown). The absence of any significant changes in NOE enhancement, seen also when a similar analysis was performed using variable-field strength triple-quantum excitation pulses in the triple-quantum filtered transient NOE experiment, supports further the suggestion of spin diffusion effects. Such effects are absent under static conditions and so nonequivalent NOE enhancements for the different transitions would be expected in such cases. Transient NOE results obtained under static conditions are presented in Section 6.6.

6.5   Variable-Temperature NOE Studies

Variable-temperature $^{11}B\{^1H\}$ transient NOE experiments were performed on borane triphenylphosphine. By increasing the temperature, it would be expected that the correlation time describing the rotation of the BH_3 group about its C_3 axis would decrease, so enhancing the efficiency of dipolar-driven cross-relaxation and increasing the NOE enhancement. Conversely, reducing the temperature would be expected to increase the correlation time and so result in a decrease in the enhancement.

Transient NOE enhancements for borane triphenylphoshine over the temperature range 223–353 K are shown in Fig. 6.11a. At temperatures of 293 K and above, the enhancement is essentially constant with $f_I\{S\}$ ~155%. Below room temperature, the enhancement remains constant until 273 K, beyond which point the enhancement decreases such that, at 223 K, it is substantially reduced to 94%. The τ_{max} values obtained from these experiments are shown in Fig. 6.11b and show a steady decrease as the temperature is reduced.

In the theoretical derivation of the NOE in Sections 6.2.2 and 6.3 the simplification that the correlation time, τ_c, is in the fast-motion limit ($\omega_0\tau_c$ << 1) was made. This typically corresponds to values of τ_c in the range 10^{-12}–10^{-9} s. Given that a variation in temperature causes a change of the correlation time and hence a change of the NOE enhancement, a comparison of the NOE build-up curves for a range of values of τ_c should enable an estimate of its value to be made. NOE build-up curves for a range of values of τ_c between 50 ps and 100 ns
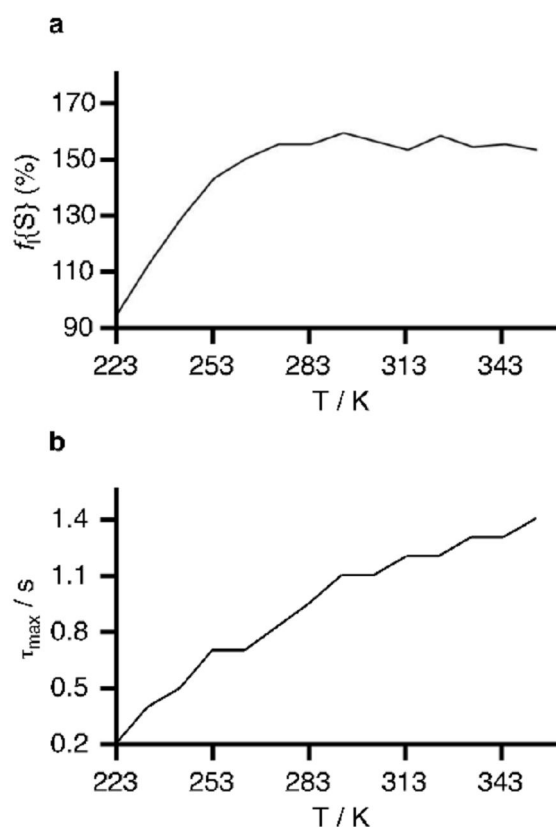
Figure 6.11. (a) $^{11}B\{^1H\}$ transient NOE enhancements of borane triphenylphosphine as a function of temperature obtained by performing the transient NOE experiment in Fig. 6.2 at 10 K increments in the range 223–353 K (except at T = 303 K). All experiments were performed at B_0 = 9.4 T and the MAS rate was 10 kHz. (b) τ_{max} values corresponding to the experiments in Fig. 6.11a.

are shown in Fig. 6.12. These curves were generated using the method described in Section 6.3, assuming only a dipolar contribution to cross-relaxation. The I-spin signal intensity is thus again expressed as the magnitude of the expectation value of the tensor operator $T_{0,0}(S)T_{1,0}(I)$. Figure 6.12 reveals that, in the fast-motion limit, the NOE enhancement reaches its maximum value and remains constant for shorter τ_c. By noting that in this same range of correlation times τ_{max} continues to increase, a comparison of Figs. 6.11a and 6.12 confirms that, at temperatures of 283 K and above, there is motion present in
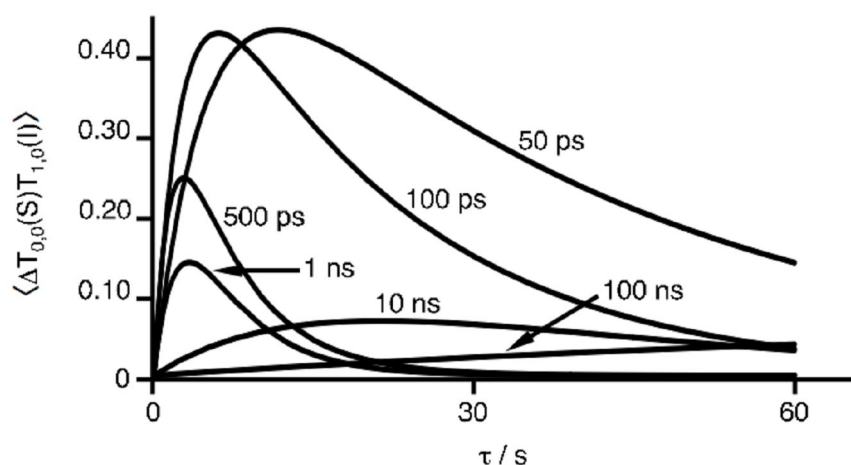
Figure 6.12. NOE build-up curves for an I = ^{11}B, S = ^{1}H spin pair for a range of correlation times. The ^{11}B nucleus is treated as a spin I = 1/2 nucleus (C_Q = 0). The MathNMR Mathematica program was again used for calculating these curves. Due to the large number of curves shown, each one is individually labelled with the correlation time with which it was obtained.

the extreme-narrowing limit. In addition, the decrease in NOE enhancement seen at longer correlation times qualitatively matches the trend seen in Fig. 6.11a.

The variation in NOE enhancement shown in Fig. 6.11 may also be rationalised by considering the I- and S-spin self-relaxation rates. The ^{1}H and ^{11}B T_1 relaxation times in borane triphenylphosphine are shown in Fig. 6.13. Both nuclei show the same trend of decreasing T_1 times as temperature is decreased, although there is a much greater change in the case of the protons. The enhanced self-relaxation of the ^{1}H and ^{11}B nuclei takes effect progressively more rapidly than cross-relaxation as the temperature is decreased and so accounts for the decrease in NOE enhancement shown in Fig. 6.11a.
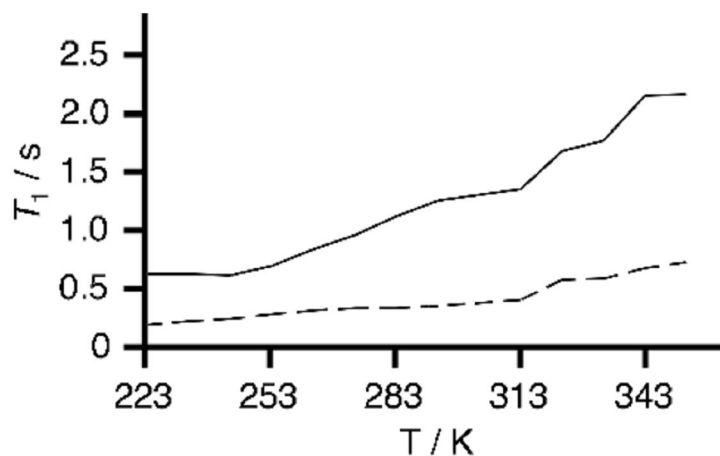
Figure 6.13. ^{1}H (solid line) and ^{11}B (dashed line) T_1 relaxation times as a function of temperature in borane triphenylphosphine.

6.6   NOE Enhancement under Static Conditions

The transient ^{11}B{^{1}H} NOE experiment was performed on borane triphenylphosphine under non-spinning (static) conditions. The ^{11}B spectrum of this material is shown in Fig. 6.14, recorded at applied magnetic field strengths of 4.7 T and 9.4 T. As expected, the spectrum in Fig. 6.14b, obtained at B_0 = 4.7 T, features a second-order quadrupolar broadened central-transition lineshape with a width of ~100 ppm, twice the 50 ppm width seen in the spectrum in Fig. 6.14a, recorded at B_0 = 9.4 T. Neither of the spectra in Fig. 6.14 appear like the static central-transition lineshape shown in Fig. 3.4a in Chapter 3. This is because the presence of the ^{11}B-^{31}P dipolar coupling (ω_D^{PAS} ~1 kHz), combined with the second-order quadrupolar interaction, yields a spectrum consisting of two overlapping central-transition powder patterns, one narrowed and the other broadened with respect to the single powder pattern that would be obtained if only quadrupolar broadening was present. The broader powder
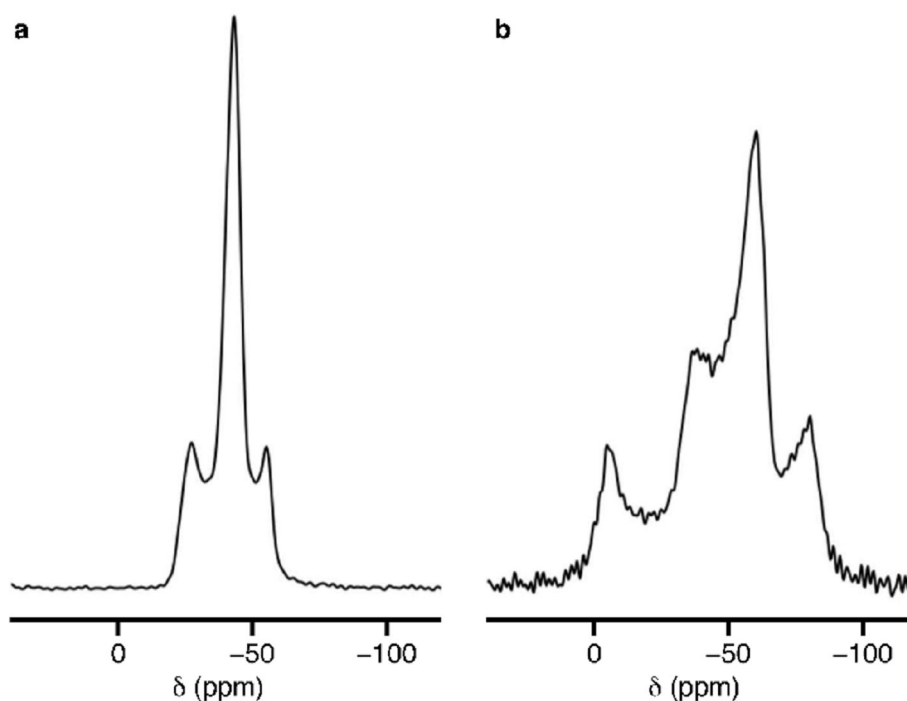
Figure 6.14. ^{1}H-decoupled ^{11}B NMR spectra of borane triphenylphosphine at B_0 = (a) 9.4 T and (b) 4.7 T. In each case a spin-echo sequence was used to remove unwanted signal from the stator block in the probe. The excitation and inversion pulses had duration 1.4 µs and 19 µs in (a) and 1.8 µs and 21 µs in (b), respectively.

pattern arises from a simultaneous increase in the splitting of the central-transition energy levels from both the second-order quadrupolar interaction and the ^{11}B-^{31}P dipolar coupling. In the case of the narrower pattern, there is a simultaneous decrease in the splitting of the central-transition energy levels by the second-order quadrupolar interaction and an increase in the splitting by the ^{11}B-^{31}P dipolar coupling (and vice versa). Under MAS, line broadening due to heteronuclear dipolar couplings is removed and so this effect is not observed. In the spectrum in Fig. 6.14a, the narrowed powder pattern, centred at ~−40 ppm, is narrowed to the extent that the characteristic second-order quadrupolar broadened lineshape is not observed. For the purposes of observing the transient NOE, performing the experiment at B_0 = 4.7 T is preferable as, given
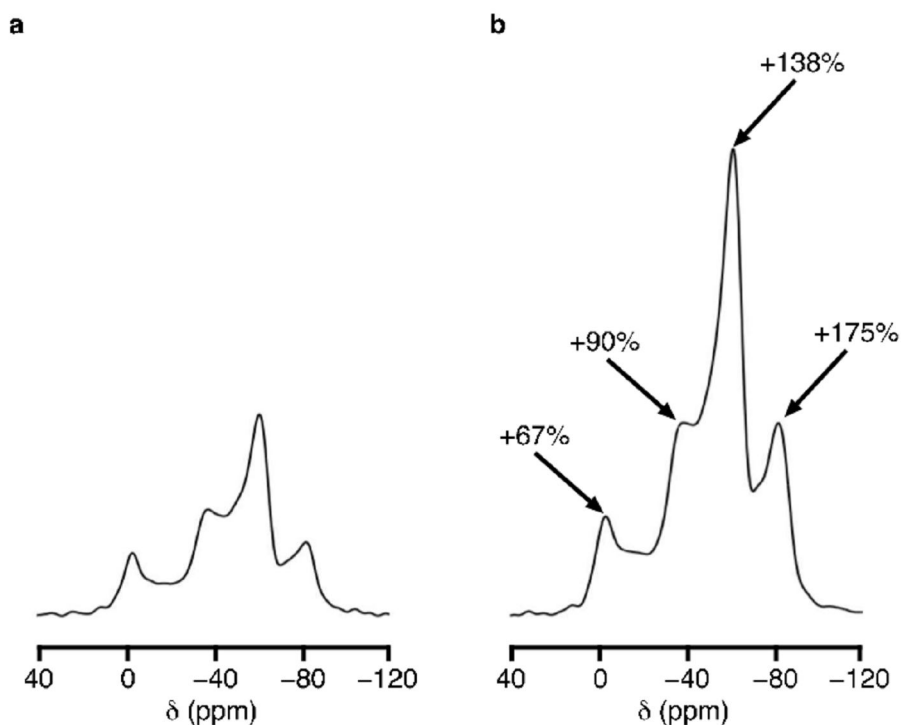
Figure 6.15. ^{1}H-decoupled ^{11}B NMR spectra of borane triphenylphosphine, recorded using the transient NOE experiment in Fig. 6.2 at B_0 = 4.7 T with (a) τ = 0 and (b) τ = 700 ms. The numbers indicated correspond to the maximum transient NOE enhancements observed at these points of the powder pattern.

the greater breadth of the spectrum at this magnetic field strength, it enables the enhancement across the powder pattern to be more closely analysed.

^{11}B NMR spectra of borane triphenylphosphine recorded using the transient NOE experiment are shown in Fig. 6.15. In Fig. 6.15a the spectrum obtained without an NOE is shown, whilst the spectrum recorded with τ = 700 ms is shown in Fig. 6.15b. The maximum signal intensity is obtained across the entire powder pattern at this value of τ and, clearly, a non-uniform enhancement is observed. The enhancements observed at the extremities of each of the two overlapping powder patterns are indicated in Fig. 6.15b and vary strongly in the range $f_I\{S\}$ = 67–175%, compared with the uniform
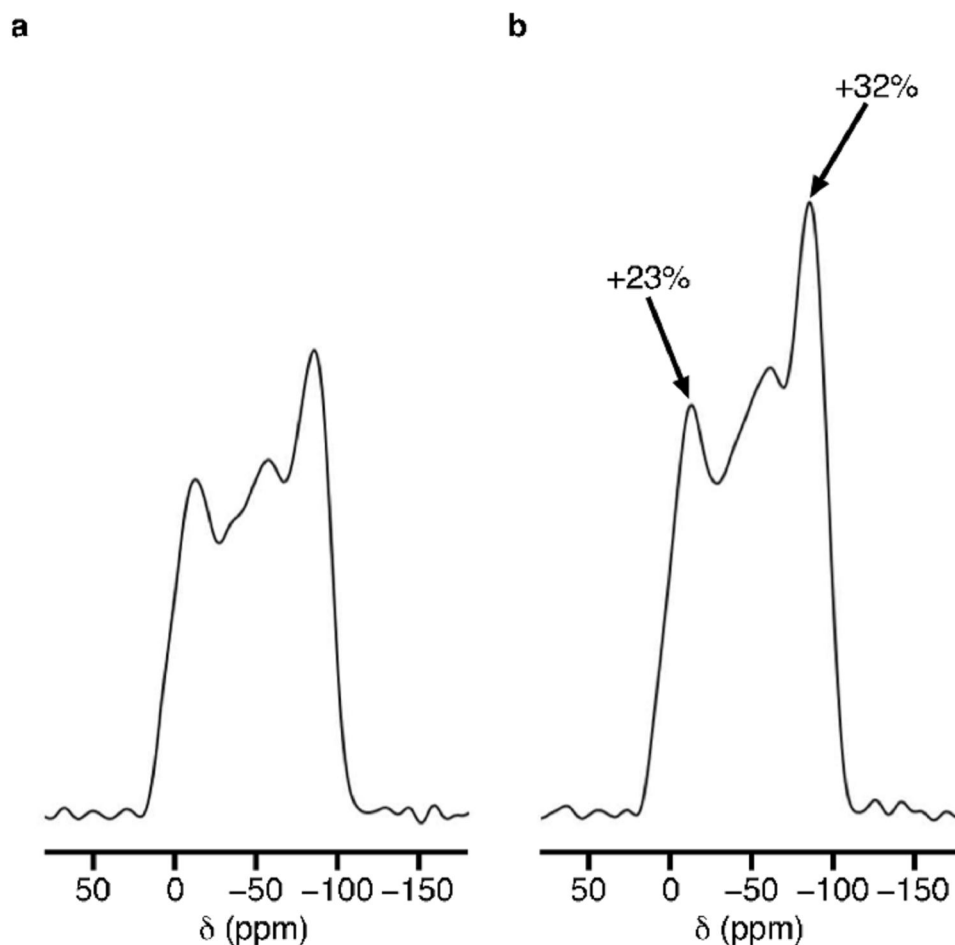
Figure 6.16. ^{1}H-decoupled ^{11}B NMR spectra of borane di-*tert*-butylamine recorded at B_0 = 4.7 T using the transient NOE experiment in Fig. 6.2 with (a) τ = 0 and (b) τ = 300 ms. The numbers indicated correspond to the maximum transient NOE enhancements observed at these points of the powder pattern.

enhancement of 155% observed under MAS conditions. The NOE build-up curves seen for these four features of the lineshape (not shown) reveal, unsurprisingly, that the signal intensity increases at a greater rate the larger the enhancement.

This variation in transient NOE enhancement under static conditions is also seen in the ^{11}B NMR spectrum of borane di-*tert*-butylamine, shown in Fig. 6.16. The lower gyromagnetic ratios of ^{14}N and ^{15}N compared to ^{31}P, and the low natural abundance of ^{15}N (0.37%), means that the significant dipolar

Transition	ν_1 / kHz	$f_I\{S\}$ (%)
CT	118	67, 90, 138, 175
TQ	118	38, 58, 113, 129
CT	7	52, 76, 115, 155

Table 6.2. ^{11}B$\{^1$H$\}$ transient NOE enhancements observed under static conditions for borane triphenylphosphine for the transitions indicated. The experiments were performed at B_0 = 4.7 T and the enhancements, $f_I\{S\}$, are given in the sequence of decreasing chemical shift and correspond to the four singularities indicated in Fig. 6.15b.

coupling seen in borane triphenylphosphine is not present and that the expected static central-transition lineshape is observed, as shown in Fig. 6.16a. A distorted lineshape is again observed at τ = τ_{max} = 300 ms, as shown in Fig. 6.16b. As indicated in Fig. 6.16b, the NOE enhancement varies within the range $f_I\{S\}$ = 23–32%, compared with the enhancement under MAS conditions of 34%. The enhancement observedfollows the same trend as was observed for borane triphenylphosphine, namely that it increases with decreasing chemical shift.

The triple-quantum filtered transient NOE experiment was also performed on borane triphenylphosphine under static conditions. The enhancements observed are given in Table 6.2 and refer to the same four singularities in the powder pattern indicated for the central-transition enhancements in Fig. 6.15b. As was seen for the central transition, the enhancements vary enormously, falling within the range 38–129%. In contrast
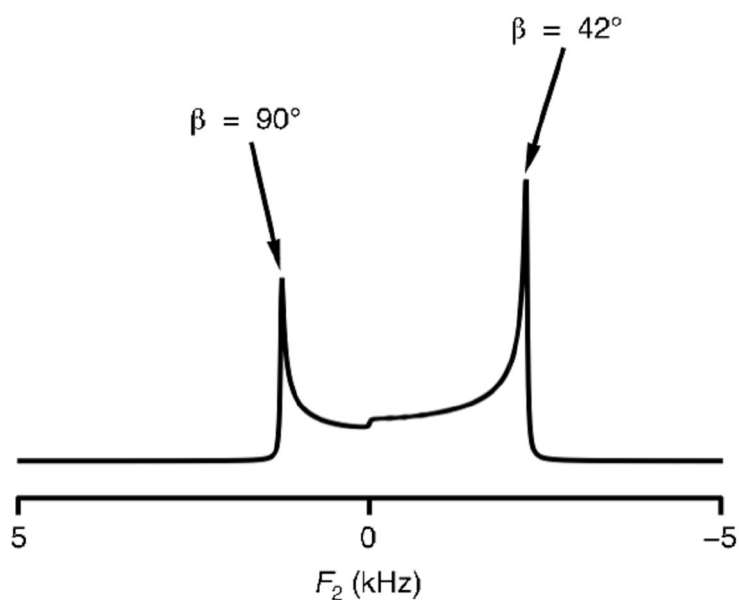
Figure 6.17. Computer-simulated static spin $I = 3/2$ central-transition lineshape. The spectrum was generated with a quadrupolar coupling parameter $C_Q = 2$ MHz, a Larmor frequency $\nu_0 = 100$ MHz and by averaging over 500 equally-spaced values of the angle β. Axial symmetry is assumed.

to the trend observed under MAS conditions, the enhancements observed for the triple-quantum transition are thus significantly different to those observed for the central transition. This is in accordance with Fig. 6.10 and with the suggestion in Section 6.4.2 that spin diffusion effects, not present under static conditions, account for the identical enhancements observed for the central and triple-quantum transitions under MAS conditions. Performing the transient NOE experiment with a reduced rf field strength, ν_1, for the central-transition excitation pulse also causes the NOE enhancements to change. As shown in Table 6.2, when a field strength of 7 kHz is used the enhancements now cover the range 52–155%. Again, the absence of an analogous effect under MAS conditions would appear to indicate the presence of spin diffusion effects.

It was shown in Chapter 3 that the characteristic static central-transition

lineshape arises as a consequence of the different perturbation experienced by each crystallite as a result of the second-order quadrupolar interaction. The powder pattern observed is thus the result of a summation of a range of frequencies that depend on the angles α, β and γ, as described by Eq. (3.23) in Chapter 3. In Fig. 6.17 the static spin $I = 3/2$ central-transition lineshape is shown, annotated with values of the angle β (one of the Euler angles defined in Section 3.3.1) that give rise to the largest and smallest resonance frequencies. The greatest positive second-order perturbation to the central-transition frequency is observed when $\beta = 90°$, whilst the largest negative second-order perturbation is observed when $\beta = 42°$. The presence of an NOE enhancement that varies across the powder pattern is thus an indication that the NOE is dependent on crystallite orientation. This is considered using theoretical arguments in the next section.

6.7   Theoretical Studies of Relaxation

In attempting to rationalise the NOE enhancements shown in the previous section, an obvious comparison to be made is the T_1 relaxation behaviour under static and MAS conditions. The anisotropy of spin-lattice relaxation is well-known, with one of the first reported examples being the orientational dependence of ^{13}C spin-lattice relaxation in powdered benzene under static conditions [298]. The presence of enhanced spin diffusion effects under MAS conditions has been used to demonstrate the observation of a common T_1 value

Adduct	^{1}H T_1	^{11}B T_1	^{1}H T_1	^{11}B T_1	$f_I\{S\}$
	/ s	/ s	/ s	/ s	(%)
	static	static	MAS	MAS	static
$BH_3 \cdot PPh_3$	1.28	0.42, 0.34, 0.37, 0.32	1.28	0.62	67, 90, 138, 175
$BH_3 \cdot NH^tBu_2$	0.21	0.85, 0.94	0.24	1.10	23, 32

Table 6.3. ^{1}H and ^{11}B T_1 relaxation times in borane triphenylphosphine and borane di-*tert*-butylamine measured under static and MAS conditions. The static ^{11}B$\{^1$H$\}$ NOE enhancements are also shown. The multiple values shown for the ^{11}B T_1 times and maximum NOE enhancements for each molecule correspond, in order of decreasing chemical shift, to the same powder pattern features used to indicate the enhancements for borane triphenylphosphine and borane di-*tert*-butylamine in Figs. 6.15b and 6.16b, respectively.

between inequivalent deuterons in ^{2}H MAS NMR [297]. ^{1}H and ^{11}B relaxation times have been measured for borane triphenylphosphine and borane di-*tert*-butylamine under static and MAS conditions and are shown in Table 6.3; the corresponding NOE enhancements under static conditions are also shown. The T_1 values quoted in Table 6.3 refer to the four and two singularities in the spectra of these materials indicated in Figs. 6.15b and 6.16b, respectively, and so follow the sequence of decreasing chemical shift. For the case of borane triphenylphosphine, the general decrease of ^{11}B T_1 times does not concur with the increase in NOE enhancement; enhanced self-relaxation should reduce the contribution of cross-relaxation to the process of returning the ^{11}B magnetization to its equilibrium value. For borane di-*tert*-butylamine, the reverse trend is observed and so the ^{11}B T_1 relaxation times under static

conditions are consistent with the NOE enhancements. For both materials, very little change is seen in the ^{1}H T_1 relaxation times measured under static conditions compared with those under MAS. Whilst T_1 relaxation clearly has a role to play in the observed NOE enhancements, the trends observed under static conditions may not be explained by a consideration solely of the T_1 values given in Table 6.3.

To rationalise the static NOE enhancements, a consideration of all the sources of relaxation is needed. To do this, the Hamiltonian describing the dipolar interaction between two non-equivalent spins I and S, H_{dd}, is required. A convenient formalism with which to express this Hamiltonian is the spherical tensor form, where an interaction B is described by a Hamiltonian, H_B:

$$H_B = \sum_{p=-l}^{l} \sum_{l=0}^{2} (-1)^p A_{l,-p}^B T_{l,p}^B ,$$ (6.42)

where $A_{l,-p}^B$ and $T_{l,p}^B$ are referred to as the spatial and spin tensor components of the Hamiltonian, respectively. The latter are identical to the spherical tensor operators, $T_{l,p}$, introduced in Chapter 2. For the dipolar interaction, the only non-zero component of the tensor $A_{l,-p}^B$ is, when expressed in the PAS of the dipolar coupling tensor, $A_{2,0}^{PAS}$. Terms with $l = 0$ and ± 1 are zero as a consequence of the dipolar coupling tensor being (like the electric field gradient tensor) traceless. Components of the spatial tensor with $p = \pm 1$ and ± 2 are neglected as a consequence of the "high-field" approximation being made. In this approximation, the Zeeman interaction is assumed to be dominant and

only those terms which commute with the Zeeman Hamiltonian are considered; these terms are described as "secular". The component $A_{2,0}^{PAS}$ is given by:

$$A_{2,0}^{PAS} = \sqrt{6}\omega_D^{PAS} ,$$
(6.43)

where ω_D^{PAS} is the dipolar coupling parameter in the PAS of the dipolar coupling tensor and is defined as in Eq. (2.50) in Chapter 2. Given the simplification described in Eq. (6.43), the first-order average Hamiltonian in the laboratory frame, H_{dd}, is thus

$$\begin{aligned} H_{dd} &= A_{2,0}^{PAS}T_{2,0} \\ &= \sqrt{6}\omega_D^{PAS}T_{2,0} \end{aligned}$$
(6.44)

Equation (6.44) is only sufficient for describing the dipolar interaction experienced by the range of crystallite orientations in a powder if the IS internuclear vector is coincident with the laboratory frame *z* axis, i.e., if the dipolar coupling PAS and laboratory frames are coincident. Generally, this condition does not hold for the majority of crystallites and so the following transformation is required, where α, β and γ are Euler angles relating the PAS and laboratory frames of reference and $D_{m',m}^2(\alpha, \beta, \gamma)$ are Wigner rotation matrix elements:

$$A_{2,m}^{Lab} = \sum_{m'=-2}^{2} D_{m',m}^2(\alpha, \beta, \gamma)A_{2,m'}^{PAS} ,$$
(6.45)

and if only secular components of the dipolar coupling tensor in the high-field

approximation (i.e., $m' = m = 0$) are used, this reduces to

$$A_{2,0}^{\text{Lab}} = D_{0,0}^2(\alpha, \beta, \gamma)A_{2,0}^{\text{PAS}} . \qquad (6.46)$$

Equation (6.44) thus becomes:

$$H_{dd} = \sqrt{6}\,\frac{\omega_D^{\text{PAS}}}{2}\,(3\cos^2\beta - 1)T_{2,0} . \qquad (6.47)$$

Given that the tensor operator $T_{2,0}$ may also be expressed in the form

$$T_{2,0} = \frac{1}{\sqrt{6}}\,(3I_zS_z - I \cdot S) , \qquad (6.48)$$

Eq. (6.47) is thus identical to the Hamiltonian in Eq. (2.48) in Chapter 2, where the former is expressed in spherical tensor operators and the latter in terms of Cartesian operators.

The neglect of second-rank components of the spatial tensor with $m, m' \neq 0$ leads to the Hamiltonians in Eqs. (6.47) and, in Chapter 2, Eq. (2.48) being referred to as "truncated" or secular. In an attempt to rationalise the static NOE results in the previous section, these terms (i.e., those that do not commute with the Zeeman Hamiltonian and that are termed "non-secular") need to be considered. To do this, two rotations are needed to obtain the components of the dipolar coupling tensor in the laboratory frame, $A_{2,m}^{\text{Lab}}$, in terms of those defined in the dipolar coupling PAS, $A_{2,m}^{\text{PAS}}$. To perform this transformation, an intermediate frame of reference is used and is referred to as the molecular
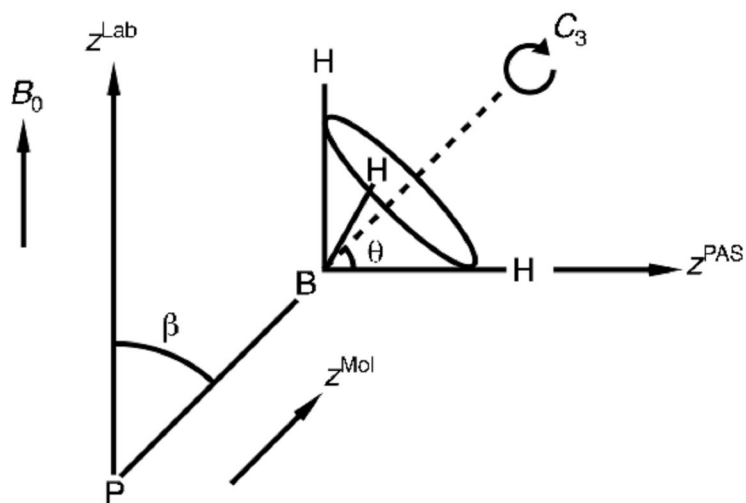
Figure 6.18. Illustration of the angles β and θ that relate the dipolar coupling PAS, molecular and laboratory frames of reference (shown for the case of a borane phosphine adduct). The angle χ (not shown) is the azimuthal angle that the ^{1}H nuclei subtend as they rotate about the BH_3 C_3 axis in the cone indicated.

frame. The three frames of reference are shown in Fig. 6.18, where the molecular frame is defined such that its z axis is coincident with (in the case of borane triphenylphosphine) the BP axis, i.e., it is aligned along the BH_3 C_3 axis. The rotation from the PAS of the ^{1}H-^{11}B dipolar coupling tensor to the molecular frame is defined using the angles θ and χ, where θ is the (polar) angle between the BH internuclear vector and the BH_3 C_3 axis and χ is the corresponding azimuthal angle. The transformation from the molecular frame to the laboratory frame is described solely by the angle β, which is defined as the angle between the BP bond and the static magnetic field (i.e., the laboratory frame z axis). Given the reference frames shown in Figure 6.18, Eq. (6.46) thus becomes

$$A_{2,m}^{Lab} = \sum_{n=-2}^{2} \sum_{m'=-2}^{2} D_{m',n}^{2}(0, \theta, -\chi) D_{n,m}^{2}(0, -\beta, 0) A_{2,m'}^{PAS} , \qquad (6.49)$$

192

and by remembering that in its PAS the dipolar coupling tensor has non-zero components only when $m' = 0$, this reduces to

$$A_{2,m}^{Lab} = \sum_{n=-2}^{2} D_{0,n}^{2}(0, \theta, -\chi)D_{n,m}^{2}(0, -\beta, 0)A_{2,0}^{PAS} \, . \tag{6.50}$$

The angle β in Fig. 6.18 is analogous to the angle β used with the other Euler angles α and γ to describe the transformation of the quadrupole tensor from its PAS to the laboratory frame in Chapter 3 and that is used in Fig. 6.17 to indicate the extremities of the static central-transition lineshape. Consequently, evaluation of Eq. (6.50) enables the modulation of the ^{1}H-^{11}B dipolar interaction for a range of crystallite orientations to be considered, so providing a possible rationale for the results in the previous section.

Evaluation of Eq. (6.50) with $m = 0, \pm 1$ and ± 2 yields the following expressions for $A_{2,0}^{Lab}$, $A_{2,\pm 1}^{Lab}$ and $A_{2,\pm 2}^{Lab}$:

$$\begin{aligned} A_{2,0}^{Lab} = \sqrt{6}\omega_Q^{PAS}\Bigg[&\left(\frac{3}{4}\right)\sin^2\theta\sin^2\beta\cos 2\chi \\ &+\left(\frac{1}{4}\right)(3\cos^2\theta - 1)(3\cos^2\beta - 1) \\ &+3\sin\theta\cos\theta\sin\beta\cos\beta\cos\chi\Bigg] \end{aligned} \tag{6.51}$$

$$A_{2,\pm1}^{\text{Lab}} = \sqrt{6}\omega_Q^{\text{PAS}} \left[\exp\{2i\chi\}\sqrt{\frac{3}{32}}\,\sin^2\theta\,\sin\beta(1 \pm \cos\beta) \right.$$

$$\mp \exp\{i\chi\}\sqrt{\frac{3}{8}}\,\sin\theta\cos\theta\,\sin\beta(1 \mp 2\cos\beta)(1 \pm \cos\beta)$$

$$\mp\sqrt{\frac{3}{8}}(3\cos^2\theta - 1)\sin\beta\cos\beta \qquad , \qquad (6.52)$$

$$\mp \exp\{-i\chi\}\sqrt{\frac{3}{8}}\,\sin\theta\cos\theta\,\sin\beta(1 \pm 2\cos\beta)(1 \mp \cos\beta)$$

$$\left. - \exp\{-2i\chi\}\sqrt{\frac{3}{32}}\,\sin^2\theta\,\sin\beta(1 \mp \cos\beta) \right]$$

and

$$A_{2,\pm2}^{\text{Lab}} = \sqrt{6}\omega_Q^{\text{PAS}} \left[\exp\{\pm2i\chi\}\sqrt{\frac{3}{8}}\,\sin^2\theta\,\cos^4\!\left(\frac{\beta}{2}\right) \right.$$

$$\mp \exp\{i\chi\}\sqrt{\frac{3}{8}}\,\sin\theta\cos\theta\,\sin\beta(1 \pm \cos\beta)$$

$$\pm\sqrt{\frac{3}{32}}(3\cos^2\theta - 1)\sin^2\beta \qquad . \qquad (6.53)$$

$$\pm \exp\{-i\chi\}\sqrt{\frac{3}{8}}\,\sin\theta\cos\theta\,\sin\beta(1 \mp \cos\beta)$$

$$\left. + \exp\{\mp2i\chi\}\sqrt{\frac{3}{8}}\,\sin^2\theta\,\sin^4\!\left(\frac{\beta}{2}\right) \right]$$

The inclusion of components of the dipolar coupling tensor with non-zero coherence order means that the Hamiltonian describing the interaction between spins I and S, H_{dd}^{Lab}, is given by:

$$H_{dd}^{\text{Lab}} = A_{2,0}^{\text{Lab}}T_{2,0} + A_{2,-1}^{\text{Lab}}T_{2,-1} + A_{2,1}^{\text{Lab}}T_{2,1} + A_{2,-2}^{\text{Lab}}T_{2,-2} + A_{2,2}^{\text{Lab}}T_{2,2} . \qquad (6.54)$$

The physical interpretation of Eq. (6.54) and its meaning in the context of relaxation may be shown by considering the evolution of the density operator, $\rho(t)$, under a Hamiltonian, H. This may be accomplished by using the Liouville-von Neumann equation, introduced in Chapter 2:

$$\frac{d\rho(t)}{dt} = -i[H, \rho(t)] .$$
(6.55)

The Hamiltonian is commonly expressed as the sum of a static part, H_0, and a random time-dependent part, $H_1(t)$. For the case of two dipolar-coupled spins I and S, H_0 and $H_1(t)$ are thus defined as:

$$
\begin{aligned}
H_0 &= \omega_0 I_z + \omega_0 S_z \\
H_1(t) &= H_{dd}^{Lab}(t)
\end{aligned}
$$
(6.56)

The time dependence of $H_{dd}^{Lab}(t)$, whilst not stated in Eq. (6.54), is obviously the result of the rotation of the BH_3 group about its C_3 axis with a correlation time of $2\pi\tau_c$ seconds such that the ^1H nuclei subtend the azimuthal angle $\chi = 2\pi t/\tau_c$ degrees. This is analogous to the definition of the angle $\omega_R t$ in Chapter 3 that was used for determining the effect of sample rotation on the second-order quadrupolar perturbation of the energy levels of half-integer quadrupolar nuclei.

To consider the effect of an interaction such as dipolar coupling, perturbation theory is often used. In an analogous manner to the quadrupolar interaction in Chapter 3, the dipolar interaction is treated as a perturbation of

the dominant Zeeman Hamiltonian. A transformed density operator, $\rho^T(t)$, and

a transformed time-dependent Hamiltonian, $H_1^T(t)$, are defined as

$$\rho^T(t) = \exp\left(iH_0 t\right)\rho(t)\exp\left(-iH_0 t\right)$$
$$H_1^T(t) = \exp\left(iH_0 t\right)H_1(t)\exp\left(-iH_0 t\right) \quad, \tag{6.57}$$

in which case the equation of motion of $\rho^T(t)$ is

$$\frac{d\rho^T(t)}{dt} = -i\left[H_1^T(t), \rho^T(t)\right]. \tag{6.58}$$

In this transformed representation, known as the interaction representation, $\rho(t)$ evolves under solely the action of the random Hamiltonian $H_1^T(t)$; evolution under the much larger static Hamiltonian, $H_0(t)$, is factored out.

The spherical tensor operators in Eq. (6.54), which make up the spin part of the dipolar Hamiltonian, may also be expressed in terms of Cartesian operators:

$$T_{2,0} = \sqrt{\frac{1}{6}}\left(3I_z S_z - I \cdot S\right)$$
$$= \sqrt{\frac{2}{3}}\left[I_z S_z - \frac{1}{4}\left(I_+ S_- + I_- S_+\right)\right] \quad, \tag{6.59}$$
$$T_{2,\pm 1} = \mp\frac{1}{2}\left(I_\pm S_z + I_z S_\pm\right)$$
$$T_{2,\pm 2} = \frac{1}{2}I_\pm S_\pm$$

where the definitions of the operators I_x and I_y in terms of the raising and lowering operators I_+ and I_- have been used:

$$I_x = \frac{1}{2}\left(I_+ + I_-\right)$$
$$I_y = -\frac{i}{2}\left(I_+ - I_-\right)$$

(6.60)

The Cartesian operators in Eq. (6.59) evolve under the static Hamiltonian at characteristic frequencies, ω_C; this is described by the equation

$$\exp\left(iH_0 t\right)C \exp\left(-iH_0 t\right) = \exp\left(i\omega_C t\right)C ,$$

(6.61)

for the general case of an operator C. The characteristic frequencies for the operators given in Eq. (6.59) are shown in Table 6.4, where the former are labelled ω_C^{dd} and the latter C_{dd}. Oscillations at the Larmor frequencies of the I and S spins, ω_I and ω_S, respectively, lead to spin-lattice relaxation of the I and S spins and so correspond to the $W_1{}^I$ and $W_1{}^S$ pathways indicated in Fig. 6.1b. The I_+S_z and I_-S_z terms thus lead to relaxation via the former pathway and the I_zS_+ and I_zS_- terms relaxation via the latter. Table 6.4 shows that the terms I_+S_- and I_-S_+ lead to oscillations at frequencies of $-\omega_I + \omega_S$ and $\omega_I - \omega_S$, respectively, and so these terms are responsible for the zero-quantum cross-relaxation pathway indicated $W_0{}^{IS}$ in Fig. 6.1b. Finally, cross-relaxation via the double-quantum pathway $W_2{}^{IS}$ arises by oscillation at frequencies of $(\omega_I + \omega_S)$ and $-(\omega_I + \omega_S)$ and so is due to the presence the terms I_-S_- and I_+S_+, respectively. The implications of these characteristic frequencies is that the $T_{2,\pm1}$ tensor operators form the spin

C_{dd}	ω_C^{dd}
$I_z S_z$	0
$I_+ S_-$	$-\omega_I + \omega_S$
$I_- S_+$	$\omega_I - \omega_S$
$I_+ S_z$	ω_I
$I_- S_z$	$-\omega_I$
$I_z S_+$	ω_S
$I_z S_-$	$-\omega_S$
$I_+ S_+$	$-(\omega_I + \omega_S)$
$I_- S_-$	$(\omega_I + \omega_S)$

Table 6.4. Characteristic frequencies at which the operators comprising the dipolar Hamiltonian, C_{dd}, evolve at under the effects of H_0.

part of the Hamiltonian that is responsible for I- and S-spin T_1 relaxation, whilst the $T_{2,0}$ and $T_{2,\pm2}$ operators form the spin components of the parts of the Hamiltonian responsible for zero- and double-quantum cross-relaxation, respectively. Analysis of the corresponding spatial components of the Hamiltonian, $A_{2,0}^{Lab}$, $A_{2,\pm1}^{Lab}$ and $A_{2,\pm2}^{Lab}$, will thus enable the orientational dependence of these relaxation processes to be determined and so enable the static $^{11}B\{^1H\}$ NOE results to be explained. Equations (6.51–6.53) reveal that
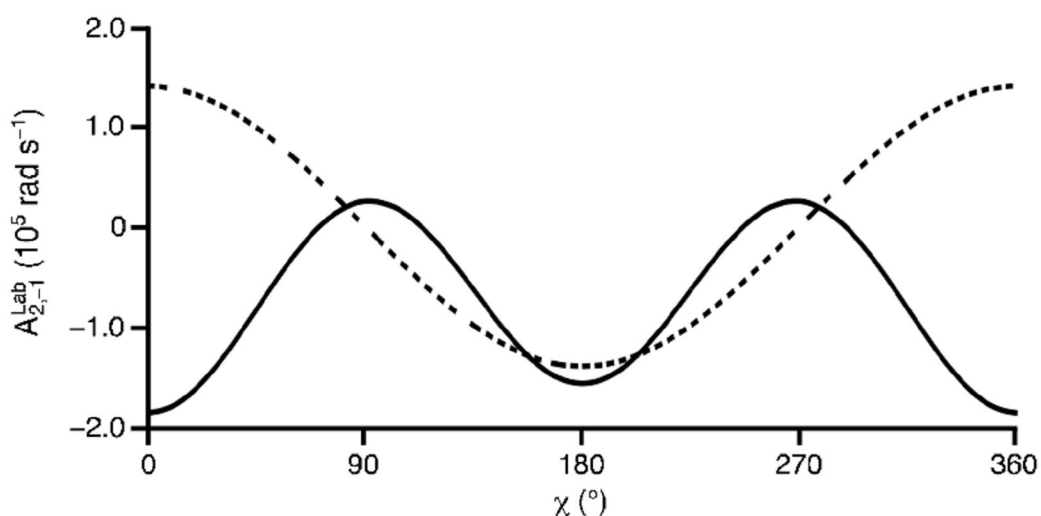
Figure 6.19. Amplitude of the real part of the component indicated with increasing χ, shown for values of β = 42° (solid line) and 90° (dashed line). The angle θ is fixed at 70.5°.

these tensors are complex functions. In the subsequent discussion, only the real components of each will be considered.

The amplitude of the component $A_{2,-1}^{\text{Lab}}$ as χ is incremented (i.e., as the BH_3 group rotates) is shown in Fig. 6.19, for values of β = 42° and 90°. As described in Section 6.6, these values of the Euler angle β yield the greatest negative and positive second-order quadrupolar perturbations to the central-transition frequency, respectively. It is clear that, over the course of a rotation, this component experiences a much greater modulation when β = 90° than when β = 42°. Given that this component comprises the part of the Hamiltonian responsible for I (and S) spin T_1 relaxation, Fig. 6.19 indicates that, by virtue of the greater modulation of this function when β = 90°, ^{11}B T_1 relaxation is more efficient at this crystallite orientation. More efficient T_1 relaxation reduces the NOE and hence, this observation concurs with the experimental results in Figs. 6.15 and 6.16.
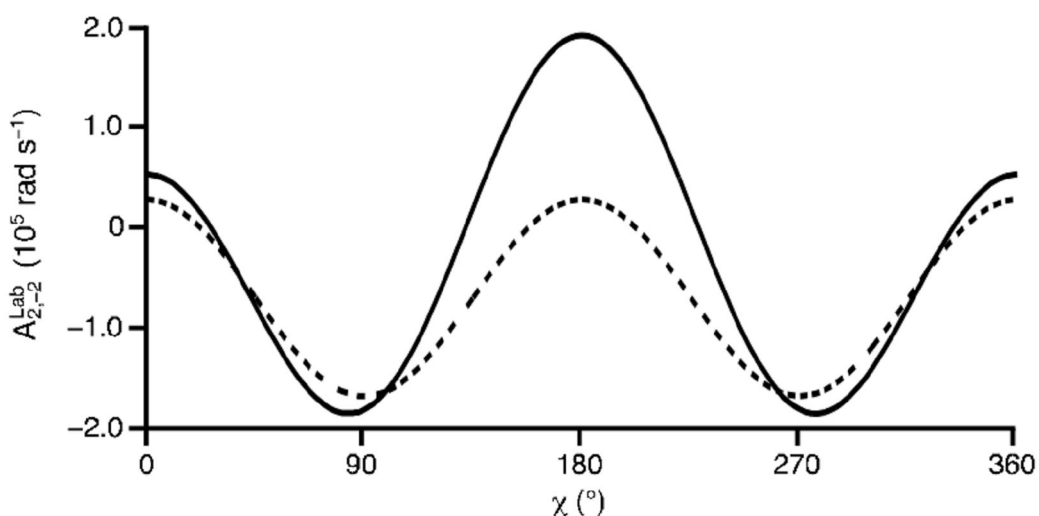
Figure 6.20. Magnitude of the real part of the component indicated with increasing χ, shown for values of β = 42° (solid line) and 90° (dashed line). The angle θ is fixed at 70.5°.

A similar analysis may be performed for the $A_{2,\pm2}^{\text{Lab}}$ components of the Hamiltonian. The amplitude of the $A_{2,-2}^{\text{Lab}}$ operator is shown in Fig. 6.20, again for values of β = 42° and 90°. As shown earlier, this spatial tensor comprises the part of the Hamiltonian responsible for cross-relaxation via the double-quantum pathway and so a consideration of the orientational dependence of this function enables further corroboration of the experimental NOE results to be obtained. Figure 6.20 shows that there is greater modulation of this function during a complete rotation of the BH_3 group when β = 42° than when β = 90°. This corresponds to more efficient cross-relaxation at the former orientation and so agrees with the experimental results shown earlier.

The orientational dependence of the $A_{2,-1}^{\text{Lab}}$ and $A_{2,-2}^{\text{Lab}}$ components of the dipolar Hamiltonian shown in Figs. 6.19 and 6.20 provide an explanation for the static $^{11}B\{^1H\}$ NOE results shown in the previous section. The $A_{2,0}^{\text{Lab}}$ component, which could provide an insight into the orientational dependence
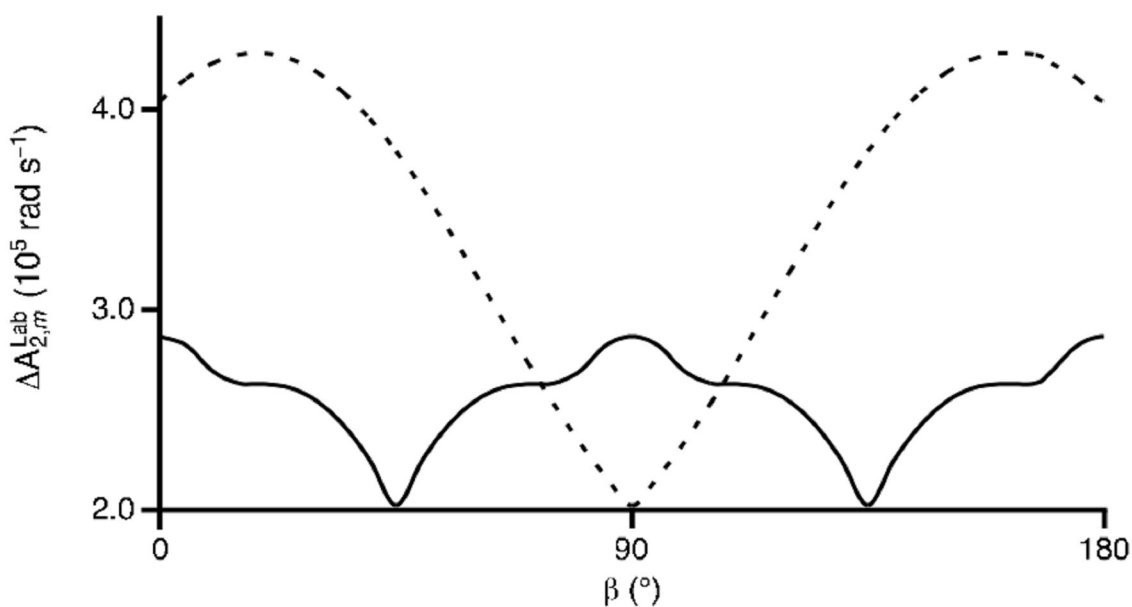
Figure 6.21. Amplitude of the real part of the component indicated when $m = -1$ (solid line) and -2 (dashed line) as a function of the angle β.

of cross-relaxation via the zero-quantum pathway, is not considered here as this pathway makes (for small molecules in solution) only a minor contribution to the NOE in the fast-motion limit.

A more complete consideration of the modulation of the $A_{2,-1}^{\text{Lab}}$ and $A_{2,-2}^{\text{Lab}}$ components over the range of orientations present in a powdered solid is shown in Fig. 6.21. The modulation of each component is defined as

$$\Delta A_{2,m}^{\text{Lab}} = \left(A_{2,m}^{\text{Lab}}\right)^{\text{max}} - \left(A_{2,m}^{\text{Lab}}\right)^{\text{min}} , \qquad (6.62)$$

where $\left(A_{2,m}^{\text{Lab}}\right)^{\text{max}}$ and $\left(A_{2,m}^{\text{Lab}}\right)^{\text{min}}$ are the maximum and minimum values of these functions for $0 \leq \chi \leq 360°$. Figure 6.21 reveals that the modulation of these functions repeat every 90° for the $A_{2,-1}^{\text{Lab}}$ component and every 180° for the $A_{2,-2}^{\text{Lab}}$ component. Maximum and minimum values are reached in the former case at β

= 0° and 90° and at β = 45° and 135°, respectively. Likewise, for the $A_{2,-2}^{Lab}$ components, maxima and minima are seen at β = 18° and 162° and at β = 90°, respectively.

6.8   Conclusions

The presence of ^{11}B{^{1}H} NOEs in a range of borane adducts have been shown. NOEs in the solid state are rare and NOEs to quadrupolar nuclei are even more scarce; their observation here is due to the rapid rotation of the BH$_3$ group about its C_3 axis that modulates very little the ^{11}B quadrupolar interaction. ^{31}P{^{1}H} NOEs in a series of phosphine-derived borane adducts have confirmed the protons attached to the boron atom to be the source of the NOE; the resultant enhancements in these and a range of amine-derived adducts have been rationalised in terms of the measured ^{1}H, ^{11}B and ^{31}P T_1 relaxation times. ^{11}B{^{1}H} central-transition, satellite-transition and triple-quantum transition NOE enhancements have been measured and been shown to be equivalent under MAS conditions. This unexpected result has been rationalised as being due to MAS-enhanced spin diffusion effects. The observation of an NOE to a quadrupolar nucleus in the solid state is a very interesting one, especially given its absence in the solution state. Whilst it may be that such an observation is limited to this particular group of materials, the presence of an NOE enhancement does, nevertheless, indicate that the nuclear Overhauser effect may be a useful source of insight into the dynamics of quadrupolar nuclei in the

solid state.

Variable-temperature $^{11}B\{^1H\}$ transient NOE experiments have revealed a reduction in signal enhancement with decreasing temperature. Such an observation has been shown to be consistent with an increased correlation time and more efficient ^1H and ^{11}B T_1 relaxation at lower temperatures.

Transient NOE experiments performed under static conditions have revealed a variable enhancement across the powder pattern. In addition, different central-transition and triple-quantum enhancements have been observed. Calculations of the orientational dependence of the spatial tensor components of the dipolar Hamiltonian with coherence order ±1 and ±2 have been used to explain this behaviour. A consideration of the former has shown there to be more efficient T_1 relaxation when the angle $\beta = 90°$, whilst analysis of the latter has demonstrated cross-relaxation to be more efficient when $\beta = 42°$. Both of these observations concur with the trends observed experimentally.

Appendix A

Matrix Representations of Spin Angular Momentum Operators

Spin *I* = 1/2

$$I_x = \frac{1}{2}\begin{pmatrix} 0 & 1 \\ 1 & 0 \end{pmatrix} \qquad I_y = \frac{i}{2}\begin{pmatrix} 0 & -1 \\ 1 & 0 \end{pmatrix} \qquad I_z = \frac{1}{2}\begin{pmatrix} 1 & 0 \\ 0 & -1 \end{pmatrix}$$

Spin *I* = 3/2

$$I_x = \frac{1}{2}\begin{pmatrix} 0 & \sqrt{3} & 0 & 0 \\ \sqrt{3} & 0 & 2 & 0 \\ 0 & 2 & 0 & \sqrt{3} \\ 0 & 0 & \sqrt{3} & 0 \end{pmatrix} \quad I_y = \frac{i}{2}\begin{pmatrix} 0 & -\sqrt{3} & 0 & 0 \\ \sqrt{3} & 0 & -2 & 0 \\ 0 & 2 & 0 & -\sqrt{3} \\ 0 & 0 & \sqrt{3} & 0 \end{pmatrix} \quad I_z = \frac{i}{2}\begin{pmatrix} 3 & 0 & 0 & 0 \\ 0 & 1 & 0 & 0 \\ 0 & 0 & -1 & 0 \\ 0 & 0 & 0 & -3 \end{pmatrix}$$

Spin *I* = 5/2

$$I_x = \frac{1}{2}\begin{pmatrix} 0 & \sqrt{5} & 0 & 0 & 0 & 0 \\ \sqrt{5} & 0 & \sqrt{8} & 0 & 0 & 0 \\ 0 & \sqrt{8} & 0 & 3 & 0 & 0 \\ 0 & 0 & 3 & 0 & \sqrt{8} & 0 \\ 0 & 0 & 0 & \sqrt{8} & 0 & \sqrt{5} \\ 0 & 0 & 0 & 0 & \sqrt{5} & 0 \end{pmatrix} \quad I_y = \frac{i}{2}\begin{pmatrix} 0 & -\sqrt{5} & 0 & 0 & 0 & 0 \\ \sqrt{5} & 0 & -\sqrt{8} & 0 & 0 & 0 \\ 0 & \sqrt{8} & 0 & -3 & 0 & 0 \\ 0 & 0 & 3 & 0 & -\sqrt{8} & 0 \\ 0 & 0 & 0 & \sqrt{8} & 0 & -\sqrt{5} \\ 0 & 0 & 0 & 0 & \sqrt{5} & 0 \end{pmatrix}$$

$$I_z = \frac{1}{2}\begin{pmatrix} 5 & 0 & 0 & 0 & 0 & 0 \\ 0 & 3 & 0 & 0 & 0 & 0 \\ 0 & 0 & 1 & 0 & 0 & 0 \\ 0 & 0 & 0 & -1 & 0 & 0 \\ 0 & 0 & 0 & 0 & -3 & 0 \\ 0 & 0 & 0 & 0 & 0 & -5 \end{pmatrix}$$

Appendix B

Matrix Representations of Spherical Tensor Operators, $T_{l,p}$

This appendix contains matrix representations of spherical tensor operators of spin $I = 1/2$, spin $I = 1$ and spin $I = 3/2$ nuclei. Only second-rank operators are shown for spin $I = 3/2$ nuclei, the remaining operators may be found in Ref. [76].

Spin $I = 1/2$

$$T_{0,0} = \frac{1}{\sqrt{2}} \begin{pmatrix} 1 & 0 \\ 0 & 1 \end{pmatrix}$$

$$T_{1,-1} = \begin{pmatrix} 0 & 0 \\ 1 & 0 \end{pmatrix} \qquad T_{1,0} = \frac{1}{\sqrt{2}} \begin{pmatrix} 1 & 0 \\ 0 & -1 \end{pmatrix} \qquad T_{1,1} = \begin{pmatrix} 0 & -1 \\ 0 & 0 \end{pmatrix}$$

Spin $I = 1$

$$T_{0,0} = \frac{1}{\sqrt{3}} \begin{pmatrix} 1 & 0 & 0 \\ 0 & 1 & 0 \\ 0 & 0 & 1 \end{pmatrix}$$

$$T_{1,0} = \frac{1}{\sqrt{2}} \begin{pmatrix} 1 & 0 & 0 \\ 0 & 0 & 0 \\ 0 & 0 & -1 \end{pmatrix}$$

$$T_{1,-1} \;=\; \frac{1}{\sqrt{2}}\begin{pmatrix} 0 & 0 & 0 \\ 1 & 0 & 0 \\ 0 & 1 & 0 \end{pmatrix} \qquad\qquad T_{1,1} \;=\; \frac{1}{\sqrt{2}}\begin{pmatrix} 0 & -1 & 0 \\ 0 & 0 & -1 \\ 0 & 0 & 0 \end{pmatrix}$$

$$T_{2,0} \;=\; \frac{1}{\sqrt{6}}\begin{pmatrix} 1 & 0 & 0 \\ 0 & -2 & 0 \\ 0 & 0 & 1 \end{pmatrix}$$

$$T_{2,-1} \;=\; \frac{1}{\sqrt{2}}\begin{pmatrix} 0 & -1 & 0 \\ 0 & 0 & 1 \\ 0 & 0 & 0 \end{pmatrix} \qquad\qquad T_{2,1} \;=\; \frac{1}{\sqrt{2}}\begin{pmatrix} 0 & 0 & 0 \\ 1 & 0 & 0 \\ 0 & -1 & 0 \end{pmatrix}$$

$$T_{2,-2} \;=\; \frac{1}{\sqrt{2}}\begin{pmatrix} 0 & 0 & 0 \\ 0 & 0 & 0 \\ 1 & 0 & 0 \end{pmatrix} \qquad\qquad T_{2,2} \;=\; \frac{1}{\sqrt{2}}\begin{pmatrix} 0 & 0 & 1 \\ 0 & 0 & 0 \\ 0 & 0 & 0 \end{pmatrix}$$

Spin I = 3/2

$$T_{2,0} \;=\; \frac{1}{2}\begin{pmatrix} 1 & 0 & 0 & 0 \\ 0 & -1 & 0 & 0 \\ 0 & 0 & -1 & 0 \\ 0 & 0 & 0 & 1 \end{pmatrix}$$

$$T_{2,-1} \;=\; \frac{1}{\sqrt{2}}\begin{pmatrix} 0 & 0 & 0 & 0 \\ 1 & 0 & 0 & 0 \\ 0 & 0 & 0 & 0 \\ 0 & 0 & -1 & 0 \end{pmatrix} \qquad\qquad T_{2,1} \;=\; \frac{1}{\sqrt{2}}\begin{pmatrix} 0 & -1 & 0 & 0 \\ 0 & 0 & 0 & 0 \\ 0 & 0 & 0 & 1 \\ 0 & 0 & 0 & 0 \end{pmatrix}$$

$$T_{2,-2} \;=\; \frac{1}{\sqrt{2}}\begin{pmatrix} 0 & 0 & 0 & 0 \\ 0 & 0 & 0 & 0 \\ 1 & 0 & 0 & 0 \\ 0 & 1 & 0 & 0 \end{pmatrix} \qquad\qquad T_{2,2} \;=\; \frac{1}{\sqrt{2}}\begin{pmatrix} 0 & 0 & 1 & 0 \\ 0 & 0 & 0 & 1 \\ 0 & 0 & 0 & 0 \\ 0 & 0 & 0 & 0 \end{pmatrix}$$

Appendix C

Reduced Rotation Matrix Elements, $\mathrm{d}^{l}_{p',p}(\beta)$

This appendix lists single-, second- and fourth-rank reduced rotation matrix elements. Only fourth-rank elements relevant to calculations in Chapter 3 are shown.

l = 1

$$\mathrm{d}^{1}_{1,1} = \mathrm{d}^{1}_{-1,-1} = \frac{1}{2}(1 + \cos \beta)$$

$$\mathrm{d}^{1}_{1,-1} = \mathrm{d}^{1}_{-1,1} = \frac{1}{2}(1 - \cos \beta)$$

$$\mathrm{d}^{1}_{1,0} = -\mathrm{d}^{1}_{-1,0} = -\mathrm{d}^{1}_{0,1} = \mathrm{d}^{1}_{0,-1} = -\frac{1}{\sqrt{2}}\sin \beta$$

$$\mathrm{d}^{1}_{00} = \cos \beta$$

l = 2

$$\mathrm{d}^{2}_{2,2} = \mathrm{d}^{2}_{-2,-2} = \frac{1}{4}(1 + \cos \beta)^2$$

$$\mathrm{d}^{2}_{2,-2} = \mathrm{d}^{2}_{-2,2} = \frac{1}{4}(1 - \cos \beta)^2$$

$$\mathrm{d}^{2}_{2,1} = -\mathrm{d}^{2}_{-2,-1} = -\mathrm{d}^{2}_{1,2} = \mathrm{d}^{2}_{-1,-2} = -\frac{1}{2}\sin \beta(1 + \cos \beta)$$

$$\mathrm{d}^{2}_{2,-1} = -\mathrm{d}^{2}_{-2,1} = -\mathrm{d}^{2}_{-1,2} = \mathrm{d}^{2}_{1,-2} = -\frac{1}{2}\sin \beta(1 - \cos \beta)$$

$$\mathrm{d}^{2}_{2,0} = \mathrm{d}^{2}_{-2,0} = \mathrm{d}^{2}_{0,2} = \mathrm{d}^{2}_{0,-2} = \sqrt{\frac{3}{8}}(\sin^2 \beta)$$

$$d_{11}^{2} = d_{-1,-1}^{2} = -\frac{1}{2}(1 - 2\cos\beta)(1 + \cos\beta)$$

$$d_{-1,1}^{2} = d_{1,-1}^{2} = \frac{1}{2}(1 + 2\cos\beta)(1 - \cos\beta)$$

$$d_{1,0}^{2} = -d_{-1,0}^{2} = -d_{0,1}^{2} = d_{0,-1}^{2} = -\sqrt{\frac{3}{2}}\,\sin\beta\cos\beta$$

$$d_{0,0}^{2} = \frac{1}{2}(3\cos^{2}\beta - 1)$$

l = 4

$$d_{0,0}^{4} = \frac{1}{8}(35\cos^{4}\beta - 30\cos^{2}\beta + 3)$$

$$d_{0,2}^{4} = d_{0,-2}^{4} = -\frac{\sqrt{10}}{64}(7\cos^{4}\beta - 4\cos^{2}\beta - 3)$$

$$d_{3,0}^{4} = d_{0,-3}^{4} = -d_{-3,0}^{4} = -d_{0,3}^{4} = -\frac{\sqrt{35}}{4}\cos\beta\sin^{3}\beta$$

$$d_{0,4}^{4} = d_{0,-4}^{4} = d_{4,0}^{4} = d_{-4,0}^{4} = \frac{\sqrt{70}}{128}(\cos^{4}\beta - 4\cos^{2}\beta + 3)$$

Appendix D

Coefficients, $c_{l',l}^p(\tau)$, Quantifying the Evolution of Spherical Tensor Operators under a First-Order Quadrupolar Splitting

Spin $I = 1$

$$c_{1,1}^{-1}(\tau) = c_{1,1}^1(\tau) = c_{2,2}^{-1}(\tau) = c_{2,2}^1(\tau) = \cos \omega_Q \tau$$

$$c_{2,1}^{-1}(\tau) = c_{1,2}^{-1}(\tau) = -c_{2,1}^1(\tau) = -c_{1,2}^1(\tau) = i \sin \omega_Q \tau$$

Spin $I = 3/2$

$$c_{1,1}^{-1}(\tau) = c_{1,1}^1(\tau) = \frac{1}{5}(2 + 3 \cos 2\omega_Q \tau)$$

$$c_{2,1}^{-1}(\tau) = c_{1,2}^{-1}(\tau) = -c_{2,1}^1(\tau) = -c_{1,2}^1(\tau) = i\left(\sqrt{3/5}\right)\sin 2\omega_Q \tau$$

$$c_{3,1}^{-1}(\tau) = c_{1,3}^{-1}(\tau) = c_{3,1}^1(\tau) = c_{1,3}^1(\tau) = i\left(\sqrt{6}/5\right)\cos 2\omega_Q \tau - 1)$$

$$c_{2,2}^{-1}(\tau) = c_{2,2}^1(\tau) = \cos 2\omega_Q \tau$$

$$c_{3,2}^{-1}(\tau) = c_{2,3}^{-1}(\tau) = -c_{3,2}^1(\tau) = -c_{2,3}^1(\tau) = i\left(\sqrt{2/5}\right)\sin 2\omega_Q \tau$$

$$c_{3,1}^{-1}(\tau) = c_{1,3}^{-1}(\tau) = c_{3,1}^1(\tau) = c_{1,3}^1(\tau) = \left(1/5\right)(2 \cos 2\omega_Q \tau + 3)$$

$$c_{2,2}^{-2}(\tau) = c_{2,2}^2(\tau) = c_{3,3}^{-2}(\tau) = c_{3,3}^2(\tau) = \cos 2\omega_Q \tau$$

$$c_{3,2}^{-2}(\tau) = c_{2,3}^{-2}(\tau) = -c_{3,2}^2(\tau) = -c_{2,3}^2(\tau) = i \sin 2\omega_Q \tau$$

Appendix E

Zeroth-, Second- and Fourth-Rank Coefficients, $A^0(I, q)$, $B^2(I, q)$ and $C^4(I, q)$, for Spin I = 3/2 and Spin I = 5/2 Nuclei

This appendix lists values of the zeroth-, second- and fourth-rank coefficients introduced in Chapter 3. These coefficients are labelled according to the transition they refer to.

I	q	$A^0(I, q)$	$B^2(I, q)$	$C^4(I, q)$
3/2	1/2 (CT)	−2/5	−8/7	54/35
	3/2 (ST)	4/5	4/7	−48/35
	3/2 (TQ)	6/5	0	−6/5
5/2	1/2 (CT)	−16/15	−64/21	144/35
	3/2 (ST_1)	2/15	−4/3	6/5
	3/2 (TQ)	−4/5	−40/7	228/35
	5/2 (ST_2)	56/15	80/21	−264/35
	5/2 (5Q)	20/3	40/21	−60/7

Appendix F

MQMAS and STMAS Ratios, R(*I*, *q*), for Spin *I* = 3/2, Spin *I* = 5/2 and Spin *I* = 7/2 Nuclei

In this appendix values of the MQMAS and STMAS ratios are shown for the transitions indicated.

I	*q*	R(*I*, *q*)
3/2	3/2 (ST)	−8/9
	3/2 (TQ)	−7/9
5/2	3/2 (ST$_1$)	7/24
	3/2 (TQ)	19/12
	5/2 (ST$_2$)	−11/6
	5/2 (5Q)	−25/12
7/2	3/2 (ST$_1$)	28/45
	5/2 (ST$_2$)	−23/45
	7/2 (ST$_3$)	−12/5

Appendix G

Coefficients k, k′ and k″, for Split-t_1 MQMAS and STMAS Experiments of Half-Integer Quadrupolar Nuclei

I	q	k	k′	k″
3/2	3/2 (ST)	9/17	8/17	0
	3/2 (TQ)	9/16	7/16	0
5/2	3/2 (ST$_1$)	24/31	0	7/31
	3/2 (TQ)	12/31	0	19/31
	5/2 (ST$_2$)	6/17	11/17	0
	5/2 (5Q)	12/37	25/37	0
7/2	3/2 (ST$_1$)	45/73	0	28/73
	5/2 (ST$_2$)	45/68	23/68	0
	7/2 (ST$_3$)	5/17	12/17	0

Appendix H

The peak positions in the F_1 and F_2 dimensions, given by δ_1 and δ_2, respectively, for MQMAS and STMAS experiments of spin I = 3/2 and spin I = 5/2 nuclei in terms of the isotropic chemical shift, δ_{CS}, and the isotropic second-order quadrupolar shift, δ_Q.

I	q	δ	Unsheared spectra	Sheared / split-t_1 spectra
3/2	1/2	δ_2	$\delta_{CS} - (2/5)\delta_Q$	$\delta_{CS} - (2/5)\delta_Q$
	3/2 (ST)	δ_1	$\delta_{CS} + (4/5)\delta_Q$	$\delta_{CS} + (4/17)\delta_Q$
	3/2 (TQ)	δ_1	$3\delta_{CS} + (6/5)\delta_Q$	$(17/8)\delta_{CS} + (1/2)\delta_Q$
5/2	3/2	δ_2	$\delta_{CS} - (16/15)\delta_Q$	$\delta_{CS} - (16/15)\delta_Q$
	3/2 (ST_1)	δ_1	$\delta_{CS} + (2/15)\delta_Q$	$(17/31)\delta_{CS} + (32/93)\delta_Q$
	3/2 (TQ)	δ_1	$3\delta_{CS} - (4/5)\delta_Q$	$(17/31)\delta_{CS} + (32/93)\delta_Q$
	3/2 (ST_1)	δ_1	$\delta_{CS} + (56/15)\delta_Q$	$\delta_{CS} + (16/17)\delta_Q$
	5/2 (TQ)	δ_1	$5\delta_{CS} + (20/3)\delta_Q$	$(85/37)\delta_{CS} + (160/111)\delta_Q$

References

1. I. I. Rabi, J. R. Zacharias, S. Millman, and P. Kusch, *Phys. Rev.* **53,** 318 (1938).

2. I. I. Rabi, S. Millman, and P. Kusch, *Phys. Rev.* **55,** 526 (1939).

3. E. M. Purcell, H. C. Torrey, and R. V. Pound, *Phys. Rev.* **69,** 37 (1946).

4. F. Bloch, W. W. Hansen, and M. Packard, *Phys. Rev.* **69,** 127 (1946).

5. M. Packard, W. W. Hansen, and F. Bloch, *Phys. Rev.* **69,** 680 (1946).

6. F. Bloch, *Phys. Rev.* **70,** 460 (1946).

7. J. Virlet, in "Encyclopedia of Nuclear Magnetic Resonance" (D. M. Grant and R. K. Harris, Eds.), Vol. 4, p. 2694, Wiley, Chichester, 1996.

8. E. R. Andrew, A. Bradbury, and R. G. Eades, *Nature* **182,** 1659 (1958).

9. I. J. Lowe, *Phys. Rev. Lett.* **2,** 285 (1959).

10. E. R. Andrew, A. Bradbury, and R. G. Eades, *Nature* **183,** 1802 (1959).

11. M. M. Maricq and J. S. Waugh, *J. Chem. Phys.* **70,** 3300 (1979).

12. M. Lee and W. I. Goldburg, *Phys. Rev.* **140,** A1261 (1965).

13. J. S. Waugh, L. M. Huber, and U. Haeberlen, *Phys. Rev. Lett.* **20,** 180 (1968).

14. U. Haeberlen and J. S. Waugh, *Phys. Rev.* **175,** 453 (1968).

15. B. C. Gerstein, R. G. Pemberton, R. C. Wilson, and L. M. Ryan, *J. Chem. Phys.* **66,** 361 (1977).

16. C. E. Bronnimann, B. L. Hawkins, M. Zhang, and G. E. Maciel, *Anal. Chem.* **60,** 1743 (1988).

17. A. Pines, M. G. Gibby, and J. S. Waugh, *J. Chem. Phys.* **56,** 1776 (1972).

18. S. R. Hartmann and E. L. Hahn, *Phys. Rev.* **128,** 2042 (1962).

19. A. Pines, M. G. Gibby, and J. S. Waugh, *J. Chem. Phys.* **59,** 569 (1973).

20. J. Schaefer, E. O. Stejskal, and R. Buchdahl, *Macromolecules* **8,** 291 (1975).

21. J. Schaefer and E. O. Stejskal, *J. Am. Chem. Soc.* **98,** 1031 (1976).

22. J. Schaefer, E. O. Stejskal, and R. Buchdahl, *Macromolecules* **10,** 384 (1977).

23. E. O. Stejskal and J. Schaefer, *J. Magn. Reson.* **28,** 105 (1977).

24. F. Bloch, *Phys. Rev.* **111,** 841 (1958).

25. M. Mehring, A. Pines, W. K. Rhim, and J. S. Waugh, *J. Chem. Phys.* **54,** 3239 (1971).

26. A. J. Vega, *J. Magn. Reson.* **96,** 50 (1992).

27. A. J. Vega, *Solid State Nucl. Magn. Reson.* **1,** 17 (1992).

28. L. van Wüllen, L. Züchner, W. Müller-Warmuth, and H. Eckert, *Solid State Nucl. Magn. Reson.* **6,** 203 (1996).

29. T. H. Walter, G. L. Turner, and E. Oldfield, *J. Magn. Reson.* **76,** 106 (1988).

30. J. Haase and E. Oldfield, *Solid State Nucl. Magn. Reson.* **3,** 171 (1994).

31. R. K. Harris and G. J. Nesbitt, *J. Magn. Reson.* **78,** 245 (1988).

32. J. M. Egan and K. T. Mueller, *J. Phys. Chem.* **B104,** 9580 (2000).

33. P. J. Barrie, *Chem. Phys. Lett.* **208,** 486 (1993).

34. R. G. Bryant, S. Ganapathy, and S. D. Kennedy, *J. Magn. Reson.* **72,** 376 (1987).

35. J. C. Edwards and P. D. Ellis, *Magn. Reson. Chem.* **28,** S59 (1990).

36. S. Hayashi and K. Hayamizu, *Chem. Phys. Lett.* **203,** 319 (1993).

37. E. R. Andrew, in "Encyclopedia of Nuclear Magnetic Resonance" (D. M. Grant and R. K. Harris, Eds.), Vol. 5, p. 2891, Wiley, Chichester, 1996.

38. E. Kundla, A. Samoson, and E. Lippmaa, *Chem. Phys. Lett.* **83,** 229 (1981).

39. E. Oldfield, S. Schramm, M. D. Meadows, K. A. Smith, R. A. Kinsey, and J. Ackerman, *J. Am. Chem. Soc.* **104,** 919 (1982).

40. A. Llor and J. Virlet, *Chem. Phys. Lett.* **152,** 248 (1988).

41. A. Samoson, E. Lippmaa, and A. Pines, *Mol. Phys.* **65,** 1013 (1988).

42. A. Samoson and E. Lippmaa, *J. Magn. Reson.* **84**, 410 (1989).

43. K. T. Mueller, B. Q. Sun, G. C. Chingas, J. W. Zwanziger, T. Terao, and A. Pines, *J. Magn. Reson.* **86,** 470 (1990).

44. K. T. Mueller, E. W. Wooten, and A. Pines, *J. Magn. Reson.* **92,** 620 (1991).

45. P. Grandinetti, J. H. Baltisberger, A. Llor, Y. K. Lee, U. Werner, M. A. Eastman, and A. Pines, *J. Magn. Reson.* **A103,** 72 (1993).

46. S. Ganapathy, S. Schramm, and E. Oldfield, *J. Chem. Phys.* **77,** 4360 (1982).

47. F. Lefebvre, J. P. Amoureux, C. Fernandez, and E. G. Derouane, *J. Chem. Phys.* **86,** 6070 (1987).

48. L. Frydman and J. S. Harwood, *J. Am. Chem. Soc.* **117,** 5367 (1995).

49. A. Medek, J. S. Harwood, and L. Frydman, *J. Am. Chem. Soc.* **117**, 12779 (1995).

50. Z. Gan, *J. Am. Chem. Soc.* **122**, 3242 (2000).

51   Z. Gan, *J. Chem. Phys.* **114,** 10845 (2001).

52. S. E. Ashbrook and S. Wimperis, *J. Magn. Reson.* **156**, 269 (2002).

53. S. E. Ashbrook and S. Wimperis, *Prog. Nucl. Magn. Reson. Spectrosc.* **45**, 53 (2004).

54. N. G. Dowell, S. E. Ashbrook, and S. Wimperis, *J. Phys. Chem.* **B108**, 13292 (2004).

55. S. E. Ashbrook, S. Antonijevic, A. J. Berry, and S. Wimperis, *Chem. Phys. Lett.* **364,** 634 (2002).

56. J. P. Amoureux, C. Fernandez, and L. Frydman, *Chem. Phys. Lett.* **259,** 347 (1996).

57. P. K. Madhu, A. Goldbourt, L. Frydman, and S. Vega, *Chem. Phys. Lett.* **307,** 41 (1999).

58. Z. Gan and H. T. Kwak, *J. Magn. Reson.* **168**, 346 (2004).

59. A. Overhauser, *Phys. Rev.* **92,** 411 (1953).

60. T. R. Carver and C. P. Slichter, *Phys. Rev.* **92**, 212 (1953).

61. I. Solomon, *Phys. Rev.* **99,** 559 (1955).

62. T. R. Carver and C. P. Slichter, *Phys. Rev.* **102**, 975 (1956).

63. D. Neuhaus and M. P. Williamson, in "The Nuclear Overhauser Effect in Structural and Conformational Analysis", VCH, New York, 1989.

64. A. Findlay and R. K. Harris, *J. Magn. Reson.* **87,** 605 (1990).

65. J. L. White and J. F. Haw, *J. Am. Chem. Soc.* **112,** 5896 (1990).

66. J. L. White, *Solid State Nucl. Magn. Reson.* **10,** 79 (1997).

67. A. G. Avent, C. Eaborn, M. N. A. El-Kheli, M. E. Molla, J. D. Smith, and A. C. Sullivan, *J. Am. Chem. Soc.* **108,** 3854 (1986).

68. F. Bloch, *Phys. Rev.* **70,** 460 (1946).

69. A. E. Derome, in "Modern NMR Techniques for Chemistry Research", p. 77, Pergamon Press, Oxford, 1991.

70. R. R. Ernst, G. Bodenhausen, and A. Wokaun, in "Principles of Nuclear Magnetic Resonance in One and Two Dimensions", p. 104, Clarendon Press, Oxford, 1987.

71. R. R. Ernst and W. A. Anderson, *Rev. Sci. Instr.* **37,** 93 (1966).

72. A. E. Derome, in "Modern NMR Techniques for Chemistry Research", p. 13, Pergamon Press, Oxford, 1991.

73. P. W. Atkins and R. S. Friedman, in "Molecular Quantum Mechanics", Chap. 8, Oxford University Press, Oxford, 1997.

74. C. P. Slichter, in "Principles of Magnetic Resonance", p. 157–165, Springer-Verlag, Berlin, 1990.

75. A. Abragam, in "Principles of Nuclear Magnetism", p. 26, Oxford Science Publications, 1961.

76. O. W. Sørensen, G. W. Eich, M. H. Levitt, G. Bodenhausen, and R. R. Ernst, *Prog. NMR. Spectrosc.* **16,** 163 (1983).

77. N. Müller, G. Bodenhausen, and R. R. Ernst, *J. Magn. Reson.* **75,** 297 (1987).

78. P. J. Hore, in "Nuclear Magnetic Resonance", p. 9, Oxford University Press, Oxford, 1995.

79. M. Duer, in "Introduction to Solid-State NMR Spectroscopy", Chap. 3, Blackwell Publishing Ltd, Oxford, 2004.

80. M. Duer, in "Introduction to Solid-State NMR Spectroscopy", Chap. 4, Blackwell Publishing Ltd, Oxford, 2004.

81. R. R. Ernst, G. Bodenhausen, and A. Wokaun, in "Principles of Nuclear Magnetic Resonance in One and Two Dimensions", p. 104, Clarendon Press, Oxford, 1987.

82. J. McManus, R. Kemp-Harper, and S. Wimperis, *Chem. Phys. Lett.* **311,** 292 (1999).

83. J. Jeener, Ampère International Summer School, Basko Polje, Yugoslavia, 1971.

84. W. P. Aue, E. Barthodi, and R. R. Ernst, *J. Chem. Phys.* **64,** 2229 (1976).

85. R. R. Ernst, G. Bodenhausen, and A. Wokaun, in "Principles of Nuclear Magnetic Resonance in One and Two Dimensions", p. 316, Clarendon Press, Oxford, 1987.

86. G. Bodenhausen, H. Kogler, and R. R. Ernst, *J. Magn. Reson.* **58,** 370 (1984).

87. R. R. Ernst, G. Bodenhausen, and A. Wokaun, in "Principles of Nuclear Magnetic Resonance in One and Two Dimensions", p. 294–301, Clarendon Press, Oxford, 1987.

88. U. Piantini, O. W. Sørensen, and R. R. Ernst, *J. Am. Chem. Soc.* **104,** 6800 (1982).

89. D. J. States, R. A. Haberkorn, and D. J. Ruben, *J. Magn. Reson.* **48,** 286 (1982).

90. D. Marion and K. Wüthrich, *Biochem. Biophys. Res. Commun.* **113,** 967 (1983).

91. R. V. Pound, *Phys. Rev.* **79,** 685 (1950).

92. P. P. Man, in "Encyclopedia of Nuclear Magnetic Resonance" (D. M. Grant and R. K. Harris, Eds.), Vol. 6, p. 3838, Wiley, Chichester, 1996.

93. A. J. Vega, in "Encyclopedia of Nuclear Magnetic Resonance" (D. M. Grant and R. K. Harris, Eds.), Vol. 6, p. 3869, Wiley, Chichester, 1996.

94. J. P. Amoureux, *Solid State Nucl. Magn. Reson.* **2,** 83 (1993).

95. P. W. Atkins and R. S. Friedman, in "Molecular Quantum Mechanics", Chap. 6, Oxford University Press, Oxford, 1997.

96. A. Abragam, in "Principles of Nuclear Magnetism", p. 232, Oxford Science Publications, 1961.

97. R. N. Zare, in "Angular Momentum", Chap. 5, Wiley, Chichester, 1987.

98. R. N. Zare, in "Angular Momentum", Chap. 3, Wiley, Chichester, 1987.

99. H. A. Buckmaster, *Can. J. Phys.* **42,** 386 (1964).

100. R. N. Zare, in "Angular Momentum", Chap. 2, Wiley, Chichester, 1987.

101. J. Herzfeld and A. E. Berger, *J. Chem. Phys.* **73,** 6021 (1980).

102. M. H. Levitt, *J. Magn. Reson.* **82,** 427 (1989).

103. R. E. Youngman and J. W. Zwanziger, *J. Phys. Chem.* **100,** 16720 (1996).

104. B. F. Chmelka, K. T. Mueller, A. Pines, J. Stebbins, Y. Wu and J. W. Zwanziger, *Nature* **339,** 42 (1989).

105. K. T. Mueller, Y. Wu, B. F. Chmelka, J. Stebbins, and A. Pines, *J. Am. Chem. Soc.* **113,** 32 (1991).

106. I. Farnan, P. J. Grandinetti, J. H. Baltisberger, J. F. Stebbins, U. Werner, M. A. Eastman, and A. Pines, *Nature* **358,** 31 (1992).

107. K. T. Mueller, J. H. Baltisberger, E. W. Wooten, and A. Pines, *J. Phys. Chem.* **96,** 7001 (1992).

108. P. Florian, K. E. Vermillion, P. J. Grandinetti, I. Farnan, and J. F. Stebbins, *J. Am. Chem. Soc.* **118,** 3493 (1996).

109. K. T. Mueller, Y. Wu, B. F. Chmelka, J. Stebbins, and A. Pines, *J. Am. Chem. Soc.* **113,** 32 (1991).

110. M. E. Smith, C. Jaeger, R. Schoenhofer, and S. Steuernagel, *Chem. Phys. Lett.* **219,** 75 (1994).

111. K. J. Pike, V. Lemaître, A. Kukol, T. Anupõld, A. P. Howes, A. Watts, M. E. Smith, and R. Dupree, *J. Phys. Chem.* **B108,** 9256 (2004).

112. A. P. Howes, T. Anupõld, V. Lemaître, A. Kukol, A. Watts, A. Samoson, M. E. Smith, and R. Dupree, *Chem. Phys. Lett.* **421,** 42 (2006).

113. A. Wong, A. P. Howes, K. J. Pike, V. Lemaître, A. Watts, T. Anupõld, J. Past, A. Samoson, R. Dupree, and M. E. Smith, *J. Am. Chem. Soc.* **128,** 7744 (2006).

114. D. Prochnow, A. R. Grimmer, and D. Freude, *Solid State Nucl. Magn. Reson.* **30,** 69 (2006).

115. A. Wong, I. Hung, A. P. Howes, T. Anupõld, J. Past, A. Samoson, S. P. Brown, M. E. Smith, and R. Dupree, *Magn. Reson. Chem.* **45,** S68 (2007).

116. G. Englehardt, H. Koller, P. Sieger, W. Depmeier, and A. Samoson, *Solid State Nucl. Magn. Reson.* **1,** 127 (1992).

117. M. Hunger, G. Engelhardt, H. Koller, and J. Weitkamp, *Solid State Nucl. Magn. Reson.* **2,** 111 (1993).

118. H. A. M. Verhulst, W. J. J. Welters, G. Vorbeck, L. J. M. van de Ven, V. H. J. de Beer, R. A. van Santen, and J. W. de Haan, *J. Chem. Soc., Chem. Commun.* 639 (1994).

119. H. A. M. Verhulst, W. J. J. Welters, G. Vorbeck, L. J. M. van de Ven, V. H. J. de Beer, R. A. van Santen, and J. W. de Haan, *J. Phys. Chem.* **98,** 7056 (1994).

120. M. Feuerstein, M. Hunger, G. Engelhardt, and J. P. Amoureux, *Solid State Nucl. Magn. Reson.* **7,** 95 (1996).

121. H. Koller, A. R. Overweg, R. A. van Santen, and J. W. de Haan, *J. Phys. Chem.* **B101,** 1754 (1997).

122. G. Engelhardt, A. P. M. Kentgens, H. Koller, and A. Samoson, *Solid State Nucl. Magn. Reson.* **15,** 171 (1999).

123. K. J. D. MacKenzie, M. E. Smith, M. Schmücker, H. Schneider, P. Angerer, Z. Gan, T. Anupõld, A. Reinhold, and A. Samoson, *Phys. Chem. Chem. Phys.* **3,** 2137 (2001).

124. J. Jänchen, M. P. J. Peeters, J. W. de Haan, L. J. M. van de Ven, and J. H. C. van Hooff, *J. Phys. Chem.* **97,** 12042 (1993).

125. G. J. Kennedy, J. B. Higgins, C. F. Ridenour, H. X. Li, and M. E. Davis, *Solid State Nucl. Magn. Reson.* **4,** 173 (1995).

126. M. Kovalakova and P. J. Grobet, *Solid State Nucl. Magn. Reson.* **9,** 107 (1997).

127. I. Hung, A. P. Howes, T. Anupõld, A. Samoson, D. Massiot, M. E. Smith, S. P. Brown, and R. Dupree, *Chem. Phys. Lett.* **432,** 152 (2006).

128. J. McManus, R. Kemp-Harper, and S. Wimperis, *Chem. Phys. Lett.* **311,** 292 (1999).

129. S. Wi and L. Frydman, *J. Chem. Phys.* **112,** 3248 (2000).

130. C. Fernandez and J. P. Amoureux, *Chem. Phys. Lett.* **242**, 449 (1995).

131. G. Wu, D. Rovnyak, B. Sun, and R. G. Griffin, *Chem. Phys. Lett.* **249,** 210 (1996).

132. C. Fernandez and J. P. Amoureux, *Solid State Nucl. Magn. Reson.* **5,** 315 (1996).

133. O. W. Sørensen, M. Rance, and R. R. Ernst, *J. Magn. Reson.* **56,** 527 (1984).

134. S. P. Brown, S. J. Heyes, and S. Wimperis, *J. Magn. Reson.* **A119,** 280 (1996).

135. J. P. Amoureux, C. Fernandez and S. Steuernagel, *J. Magn. Reson.* **A123,** 116 (1996).

136. D. Massiot, B. Touzo, D. Trumeau, J. P. Coutures, J. Virlet, P. Florian, and P. J. Grandinetti, *Solid State Nucl. Magn. Reson.* **6,** 73 (1996).

137. S. P. Brown and S. Wimperis, *J. Magn. Reson.* **124,** 279 (1997).

138. S. P. Brown and S. Wimperis, *J. Magn. Reson.* **128,** 42 (1997).

139. P. J. Grandinetti, J. H. Baltisberger, J. Stebbins, U. Werner, M. A. Eastman, and A. Pines, *Mol. Phys.* **81,** 1109 (1994).

140. S. J. Hwang, C. Fernandez, J. P. Amoureux, J. Cho, S. W. Martin, and M. Pruski, *Solid State Nucl. Magn. Reson.* **8,** 109 (1997).

141. S. J. Hwang, C. Fernandez, J. P. Amoureux, J. W. Han, J. Cho, S. W. Martin, and M. Pruski, *J. Am. Chem. Soc.* **120,** 7337 (1998).

142. K. Kanehashi, K. Saito, and H. Sugisawa, *Chem. Lett.* **29,** 588 (2000).

143. L. van Wüllen and G. Schwering, *Solid State Nucl. Magn. Reson.* **21,** 134 (2002).

144. M. R. Hansen, T. Vosegaard, H. J. Jakobsen, and J. Skibsted, *J. Phys. Chem.* **A108,** 586 (2004).

145. S. K. Lee, K. Mibe, Y. Fei, G. D. Cody, and B. O. Mysen, *Phys. Rev. Lett.* **94,** 165507 (2005).

146. P. J. Dirken, S. C. Kohn, M. E. Smith, and E. R. H. van Eck, *Chem. Phys. Lett.* **266,** 568 (1997).

147. J. F. Stebbins, J. V. Oglesby, and Z. Xu, *Am. Mineral.* **82,** 1116 (1997).

148. G. Wu, D. Rovnyak, P. C. Huang, and R. G. Griffin, *Chem. Phys. Lett.* **277,** 79 (1997).

149. J. P. Amoureux, F. Bauer, H. Ernst, C. Fernandez, D. Freude, D. Michel, and U. T. Pingel, *Chem. Phys. Lett.* **285,** 10 (1998).

150. S. Wang and J. F. Stebbins, *J. Non-Cryst. Solids.* **231,** 286 (1998).

151. Z. Xu, H. Maekawa, J. V. Oglesby, and J. F. Stebbins, *J. Am. Chem. Soc.* **120,** 9894 (1998).

152. S. Wang and J. F. Stebbins, *J. Am. Ceram. Soc.* **82,** 1519 (1999).

153. J. F. Stebbins, S. K. Lee, and J. V. Oglesby, *Am. Mineral.* **84,** 983 (1999).

154. J. F. Stebbins, P. Zhao, S. K. Lee, and X. Cheng, *Am. Mineral.* **84,** 1680 (1999).

155. S. K. Lee and J. F. Stebbins, *J. Phys. Chem.* **B104,** 4091 (2000).

156. S. E. Ashbrook, A. J. Berry, and S. Wimperis, *J. Am. Chem. Soc.* **123,** 6360 (2001).

157. D. Freude, T. Loeser, D. Michel, U. Pingel, and D. Prochnow, *Solid State Nucl. Magn. Reson.* **20,** 46 (2001).

158. G. Wu and S. Dong, *J. Am. Chem. Soc.* **123,** 9119 (2001).

159. S. E. Ashbrook, A. J. Berry, and S. Wimperis, *J. Phys. Chem.* **B106,** 773 (2002).

160. J. E. Readman, N. Kim, M. Ziliox, and C. P. Grey, *Chem. Commun.* 2808 (2002).

161. A. Wong, K. J. Pike, R. Jenkins, G. J. Clarkson, T. Anupõld, A. P. Howes, D. H. G. Crout, A. Samoson, R. Dupree, and M. E. Smith, *J. Phys. Chem.* **A110,** 1824 (2006).

162. J. V. Hanna, M. E. Smith, and H. J. Whitfield, *J. Am. Chem. Soc.* **118,** 5772 (1996).

163. D. Massiot, R. Conanec, W. Feldmann, R. Marchand, and Y. Laurent, *Inorg. Chem.* **35,** 4957 (1996).

164. G. Wu, D. Rovnyak, and R. G. Griffin, *J. Am. Chem. Soc.* **118,** 9326 (1996).

165. M. J. Duer and C. Stourton, *J. Magn. Reson.* **124,** 189 (1997).

166. M. Hanaya and R. K. Harris, *Solid State Nucl. Magn. Reson.* **8,** 147 (1997).

167. L. Delevoye, S. Liu, M. Welch, C. Fernandez, J. P. Amoureux, and J. Klinowski, *J. Chem. Soc. Faraday Trans.* **93,** 2591 (1997).

168. F. Angeli, T. Charpentier, P. Faucon, and J. C. Petit, *J. Phys. Chem.* **B103,** 10356 (1999).

169. S. Ding and C. A. McDowell, *Chem. Phys. Lett.* **320,** 316 (2000).

170. K. H. Lim and C. P. Grey, *J. Am. Chem. Soc.* **122,** 9768 (2000).

171. R. J. Accardi, R. F. Lobo, and M. Kalwei, *J. Phys. Chem.* **B105,** 5883 (2001).

172. S. Antonijevic, S. E. Ashbrook, R. I. Walton, and S. Wimperis, *J. Mater. Chem.* **12,** 1469 (2002).

173. H. Yang, R. I. Walton, S. Antonijevic, and S. Wimperis, *J. Phys. Chem.* **B108,** 8208 (2004).

174. S. Sham and G. Wu, *Inorg. Chem.* **39,** 4 (2000).

175. C. V. Grant, V. Frydman, and L. Frydman, *J. Am. Chem. Soc.* **122,** 11743 (2000).

176. C. Fernandez, J. P. Amoureux, L. Delmotte, and H. Kessler, *Microporous Materials* **6,** 125 (1996).

177. C. Fernandez, J. P. Amoureux, J. M. Chezeau, L. Delmotte, and H. Kessler, *Microporous Materials* **6,** 331 (1996).

178. J. H. Baltisberger, Z. Xu, J. F. Stebbins, S. H. Wang, and A. Pines, *J. Am. Chem. Soc.* **118,** 7209 (1996).

179. H. Kraus, R. Prins, and A. P. M. Kentgens, *J. Phys. Chem.* **100,** 16336 (1996).

180. J. Rocha, Z. Lin, C. Fernandez, and J. P. Amoureux, *Chem. Commun.* 2513 (1996).

181. J. Rocha, A. P. Esculcas, C. Fernandez, and J. P. Amoureux, *J. Phys. Chem.* **100,** 17889 (1996).

182. P. Sarv, C. Fernandez, J. P. Amoureux, and K. Keskinen, *J. Phys. Chem.* **100,** 19223 (1996).

183. B. Ollivier, R. Retoux, P. Lacorre, D. Massiot, and G. Férey, *J. Mater. Chem.* **7,** 1049 (1997).

184. S. R. Jansen, H. T. Hintzen, R. Metselaar, J. W. de Haan, L. J. M. van de Ven, A. P. M. Kentgens, and G. H. Nachtegaal, *J. Phys. Chem.* **B102,** 5969 (1998).

185. S. P. Brown, S. E. Ashbrook, and S. Wimperis, *J. Phys. Chem.* **B103,** 812 (1999).

186. S. E. Ashbrook, J. McManus, K. J. D. MacKenzie, and S. Wimperis, *J. Phys. Chem.* **B104,** 6408 (2000).

187. J. McManus, S. E. Ashbrook, K. J. D. MacKenzie, and S. Wimperis, *J. Non-Cryst. Solids* **282,** 278 (2001).

188. C. A. Fyfe, J. L. Bretherton, and L. Y. Lam, *J. Am. Chem. Soc.* **123,** 5285 (2001).

189. C. J. Fontenot, J. W. Wiench, G. L. Schrader, and M. Pruski, *J. Am. Chem. Soc.* **124,** 8435 (2002).

190. S. E. Ashbrook, A. J. Berry, and S. Wimperis, *J. Am. Chem. Soc.* **125**, 11824 (2003).

191. K. Kanehashi and K. Saito, *Energy and Fuels* **18,** 1732 (2004).

192. H. Yang, R. I. Walton, S. Antonijevic, S. Wimperis, and A. C. Hannon *J. Phys. Chem.* **B108,** 8208 (2004).

193. S. Antonijevic, S. E. Ashbrook, S. Biedasek, R. I. Walton, S. Wimperis, and H. Yang, *J. Am. Chem. Soc.* **128,** 8054 (2006).

194. S. E. Ashbrook, A. J. Berry, D. J. Frost, A. Gregorovic, C. J. Pickard, J. E. Readman, and S. Wimperis, *J. Am. Chem. Soc.* **129,** 13213 (2007).

195. K. Shimoda, Y. Tobu, K. Kanehashi, T. Nemoto, and K. Saito, *Chem. Lett.* **34,** 1588 (2005).

196. K. Shimoda, Y. Tobu, K. Kanehashi, and K. Saito, *Solid State Nucl. Magn. Reson.* **30,** 198 (2006).

197. K. Shimoda, Y. Tobu, Y. Shimoikeda, T. Nemoto, and K. Saito, *J. Magn. Reson.* **186,** 156 (2007).

198. D. Laurencin, A. Wong, J. V. Hanna, R. Dupree, and M. E. Smith, *J. Am. Chem. Soc.* **130,** 2412 (2008).

199. S. H. Wang, Z. Xu, J. H. Baltisberger, L. M. Bull, J. F. Stebbins, and A. Pines, *Solid State Nucl. Magn. Reson.* **8,** 1 (1997).

200. K. J. Pike, R. P. Malde, S. E. Ashbrook, J. McManus, and S. Wimperis, *Solid State Nucl. Magn. Reson.* **16,** 203 (2000).

201. U. G. Nielsen, A. Boisen, M. Brorson, C. J. H. Jacobsen, H. J. Jakobsen, and J. Skibsted, *Inorg. Chem.* **41,** 6432 (2002).

202. U. G. Nielsen, H. J. Jakobsen, and J. Skibsted, *Solid State Nucl. Magn. Reson.* **23,** 107 (2003).

203. A. Samoson, *J. Magn. Reson.* **A121,** 209 (1996).

204. T. Charpeutier and J. Virlet, *Solid State Nucl. Magn. Reson.* **12,** 227 (1998).

205. U. G. Nielsen, H. J. Jakobsen, and J. Skibsted, *Solid State Nucl. Magn. Reson.* **20,** 23 (2001).

206. S. Kroeker and R. E. Wasylishen, *Can. J. Chem.* **77,** 1962 (1999).

207. C. Fernandez and J. P. Amoureux, *Solid State Nucl. Magn. Reson.* **5,** 315 (1996).

208. H. J. Kim, M. Pruski, J. W. Wiench, D. Y. Jeong, and S. H. Choh, *Phys. Rev.* **B63,** 064107 (2001).

209. L. P. Cruz, J. Rocha, J. D. Pedrosa de Jesus, J. M. Savariault, and J. Galy, *Solid State Nucl. Magn. Reson.* **15,** 153 (1999).

210. S. Prasad, P. Zhao, J. Huang, J. J. Fitzgerald, and J. S. Shore, *Solid State Nucl. Magn. Reson.* **19,** 45 (2001).

211. D. Zhou, G. L. Hoatson, and R. L. Vold, *J. Magn. Reson.* **167,** 242 (2004).

212. O. B. Lapina, D. F. Khabibulin, K. V. Romanenko, Z. Gan, M. G. Zuev, V. N. Krasil'nikov, and V. E. Fedorov, *Solid State Nucl. Magn. Reson.* **28,** 204 (2005).

213. R. L. Vold, G. L. Hoatson, and M. Vijayakumar, *Phys. Rev.* **B75,** 134105 (2007).

214. A. Flambard, L. Montagne, L. Delevoye, and S. Steuernagel, *Solid State Nucl. Magn. Reson.* **32,** 34 (2007).

215. J. Trebosc, J. P. Amoureux, and Z. Gan, *Solid State Nucl. Magn. Reson.* **31,** 1 (2007).

216. K. J. Pike, S. E. Ashbrook, and S. Wimperis, *Chem. Phys. Lett.* **345,** 400 (2001).

217. J. P. Amoureux, C. Huguenard, F. Engelke, and F. Taulelle, *Chem. Phys. Lett.* **356,** 497 (2002).

218. S. Wi, S. E. Ashbrook, S. Wimperis, and L. Frydman, *J. Chem. Phys.* **118,** 3131 (2003).

219. S. E. Ashbrook, A. J. Berry, W. O. Hibberson, S. Steuernagel, and S. Wimperis, *Am. Mineral.* **90,** 1861 (2005).

220. S. E. Ashbrook, A. J. Berry, D. J. Frost, A. Gregorovic, C. J. Pickard, J. E. Readman, and S. Wimperis, *J. Am. Chem. Soc.* **129,** 13213 (2007).

221. C. Dean, T. W. Hambley, and M. R. Snow, *Acta Cryst.* **C40,** 1512 (1984).

222. P. R. Bodart, *J. Magn. Reson.* **133,** 207 (1998).

223. V. H. Schmidt, Proc. Ampère. Int. Summer School II 75 (1971).

224. S. Vega and A. Pines, *J. Chem. Phys.* **66,** 5624 (1977).

225. A. Wokaun and R. R. Ernst, *J. Chem. Phys.* **67,** 1752 (1977).

226. S. Vega, *J. Chem. Phys.* **68,** 5518 (1977).

227. G. Bodenhausen, *Prog. Nucl. Magn. Reson. Spectrosc.* **14,** 137 (1981).

228. T. J. Norwood, *Prog. Nucl. Magn. Reson. Spectrosc.* **24,** 295 (1992).

229. U. Piantini, O. W. Sørensen, and R. R. Ernst, *J. Am. Chem. Soc.* **104,** 6800 (1982).

230. A. J. Shaka and R. Freeman, *J. Magn. Reson.* **51,** 169 (1983).

231. A. Bax, R. H. Griffey, and B. L. Hawkins, *J. Magn. Reson.* **55,** 301 (1983).

232. A. Bax, R. Freeman, and T. A. Frenkiel, *J. Am. Chem. Soc.* **103,** 2102 (1981).

233. G. Jaccard, S. Wimperis, and G. Bodenhausen, *J. Chem. Phys.* **85,** 6282 (1986).

234. S. Wimperis, in "Encyclopedia of Nuclear Magnetic Resonance" (D. M. Grant and R. K. Harris, Eds.), Vol. 6, p. 4078, Wiley, Chichester, 1996.

235. S. Vega and Y. Naor, *J. Chem. Phys.* **75,** 75 (1981).

236. N. C. Nielsen, H. Bildsøe, and H. Jakobsen, *J. Magn. Reson.* **97,** 149 (1992).

237. J. P. Amoureux and C. Fernandez, *Solid State Nucl. Magn. Reson.* **10,** 211 (1998).

238. J. P. Amoureux, M. Pruski, D. P. Lang, and C. Fernandez, *J. Magn. Reson.* **131,** 170 (1998).

239. L. Marinelli, A. Medek, and L. Frydman, *J. Magn. Reson.* **132,** 88 (1998).

240. S. Ding and C. A. McDowell, *Chem. Phys. Lett.* **270,** 81 (1997).

241. P. K. Madhu, A. Goldbourt, L. Frydman, and S. Vega, *J. Chem. Phys.* **112,** 2377 (2000).

242. A. Goldbourt, P. K. Madhu, and S. Vega, *Chem. Phys. Lett.* **320,** 448 (2000).

243. C. M. Morais, M. Lopes, C. Fernandez, and J. Rocha, *Magn. Reson. Chem.* **41,** 679 (2003).

244. R. Siegel, T. T. Nakashima, and R. E. Wasylishen, *Chem. Phys. Lett.* **403,** 353 (2004).

245. A. P. M. Kentgens and R. Verhagen, *Chem. Phys. Lett.* **300,** 435 (1999).

246. D. Iuga and A. P. M. Kentgens, *Chem. Phys. Lett.* **343,** 556 (2001).

247. G. Wu, D. Rovnyak and R. G. Griffin, *J. Am. Chem. Soc.* **118,** 9326 (1996).

248. S. Ding and C. A. McDowell, *J. Magn. Reson.* **135,** 61 (1998).

249. J. Gu and W. G. Power, *Solid State Nucl. Magn. Reson.* **27,** 192 (2005).

250. P. K. Madhu, O. G. Johannessen, K. J. Pike, R. Dupree, M. E. Smith, and M. H. Levitt, *J. Magn. Reson.* **163,** 310 (2003).

251. J. P. Amoureux, L. Delevoye, S. Steuernagel, Z. Gan, S. Ganapathy, and L. Montagne, *J. Magn. Reson.* **172**, 268 (2005).

252. N. Malicki, L. Mafra, A. A. Quoineaud, J. Rocha, F. Thibault-Starzyk, and C. Fernandez, *Solid State Nucl. Magn. Reson.* **28**, 13 (2005).

253. J. P. Amoureux, A. Flambard, L. Delevoye, and L. Montagne, *Chem. Commun.* **27**, 3472 (2005).

254. J. P. Amoureux, L. Delevoye, G. Fink, F. Taulelle, A. Flambard, and L. Montagne, *J. Magn. Reson.* **175**, 285 (2005).

255. T. J. Ball and S. Wimperis, *J. Magn. Reson.* **187,** 343 (2007).

256. M. H. Levitt and R. Freeman, *J. Magn. Reson.* **33,** 473 (1979).

257. J. McManus, S. E. Ashbrook, K. J. D. MacKenzie, and S. Wimperis, *J. Non-Cryst. Solids* **282,** 278 (2001).

258. G. Kunath-Fandrei, T. J. Bastow, J. S. Hall, C. Jäger, and M. E. Smith, *J. Phys. Chem.* **99,** 15138 (1995).

259. C. Jäger, G. Kunath, P. Losso, and G. Scheler, *Solid State Nucl. Magn. Reson.* **2,** 73 (1993).

260. A. P. M. Kentgens, *Geoderma* **80,** 271 (1997).

261. S. E. Ashbrook, K. J. D. MacKenzie, and S. Wimperis, *Solid State Nucl. Magn. Reson.* **20,** 87 (2001).

262. H. T. Kwak and Z. Gan, *J. Magn. Reson.* **164,** 369 (2003).

263. M. H. Levitt, G. Bodenhausen, and R. R. Ernst, *J. Magn. Reson.* **58,** 462 (1984).

264. S. Meiboom and D. Gill, *Rev. Sci. Instrum.* **29,** 688 (1958).

265. S. E. Ashbrook and S. Wimperis, *J. Magn. Reson.* **177,** 44 (2005).

266. M. J. Thrippleton, T. J. Ball, S. Steuernagel, S. E. Ashbrook, and S. Wimperis, *Chem. Phys. Lett.* **431,** 390 (2006).

267. M. J. Thrippleton, T. J. Ball, and S. Wimperis, *J. Chem. Phys.* **128,** 034507 (2008).

268. D. Suter, A. Pines, and M. Mehring, *Phys. Rev. Lett.* **57,** 242 (1986).

269. R. R. Ernst, G. Bodenhausen, and A. Wokaun, in "Principles of Nuclear Magnetic Resonance in One and Two Dimensions", p. 101, Clarendon Press, Oxford, 1987.

270. M. Maricq and J. S. Waugh, *Chem. Phys. Lett.* **47,** 327 (1977).

271. A. Bax, A. F. Mehlkopf, and J. Smidt, *J. Magn. Reson.* **40,** 213 (1980).

272. B. Blümich, P. Blümler, and J. Jansen, *Solid State Nucl. Magn. Reson.* **1,** 111 (1992).

273. S. K. Zaremba, *Ann. Mat. Pura. Appl.* **73,** 293 (1966).

274. S. E. Ashbrook and S. Wimperis, *J. Magn. Reson.* **147,** 238 (2000)

275. G. A. Jeffrey and G. S. Parry, *J. Am. Chem. Soc.* **76,** 5283 (1954).

276. M. Baldus, B. H. Meier, R. R. Ernst, A. P. M. Kentgens, H. Meyer zu Altenschildesche, and R. Nesper, *J. Am. Chem. Soc.* **117,** 5141 (1995).

277. N. G. Dowell, S. E. Ashbrook, J. McManus, and S. Wimperis, *J. Am. Chem. Soc.* **123,** 8135 (2001).

278. M. Edén, J. Grinshtein, and L. Frydman, *J. Am. Chem. Soc.* **124,** 9708 (2002).

279. S. Wi, H. Heise, and A. Pines, *J. Am. Chem. Soc.* **124,** 10652 (2002).

280. N. G. Dowell, S. E. Ashbrook, and S. Wimperis, *J. Phys. Chem.* **A106,** 9470 (2002).

281. A. P. M. Kentgens, E. R. H van Eck, T. G. Ajithkumar, T. Anupõld, J. Past, A. Reinhold, and A. Samoson, *J. Magn. Reson.* **178,** 212 (2006).

282. J. Jeener, B. H. Meier, P. Bachmann, and R. R. Ernst, *J. Chem. Phys.* **71,** 4546 (1979).

283. B. H, Meier, *Adv. Magn. Opt. Reson.* **18,** 1 (1994).

284. F. W. Wehrli, *Org. Magn. Reson.* **11,** 106 (1978).

285. S. Berger and F. Müller, *Chem. Ber.* **128,** 799 (1995).

286. L. D. Field, M. G. Gardiner, C. H. L. Kennard, B. A. Messerie, and C. L. Raston, *Organometallics* **10,** 3167 (1991).

287. S. E. Ashbrook, N. G. Dowell, I. Prokes, and S. Wimperis, *J. Am. Chem. Soc.* **128,** 6782 (2006).

288. J. H. Noggle and R. E. Schirmer, in "The Nuclear Overhauser Effect: Chemical Applications", p. 113–120, Academic Press, New York, 1971.

289. J. Keeler, in "Understanding NMR Spectroscopy", Chap. 9, Wiley, Chichester, 2005.

290. A. G. Redfield, *Adv. Magn. Reson.* **1,** 1 (1965).

291. A. Jerschow, *J. Magn. Reson.* **176,** 7 (2005).

292. G. L. Turner, K. A. Smith, R. J. Kirkpatrick, and E. Oldfield, *J. Magn. Reson.* **67,** 544 (1986).

293. W. P. Power, *J. Am. Chem. Soc.* **117,** 1800 (1995).

294. W. T. Klooster, T. F. Koetzle, P. E. M. Siegbahn, T. B. Richardson, and R. H. Crabtree, *J. Am. Chem. Soc.* **121,** 6337 (1999).

295. R. H. Baughman, *J. Chem. Phys.* **53,** 3781 (1970).

296. J. C. Huffman, W. A. Skupinski, K. G. Caulton, *Cryst. Struct. Commun.* **11,** 1435 (1982).

297. M. Alla, R. Eckman, and A. Pines, *Chem. Phys. Lett.* **71,** 148 (1980).

298. M. G. Gibby, A. Pines, and J. S. Waugh, *Chem. Phys. Lett.* **16,** 296 (1972).